Electronic and structural characterizations of a transparent conductive oxide/organic interface: Towards applications for organic electronic devices

Quentin Arnoux

UNIVERSITÉ PIERRE ET MARIE CURIE

PhD Thesis in Chemistry

Chimie Physique et Chimie Analytique de Paris-Centre (ED 388)

LCPMR/FES – IPCM/e-POM – IRAMIS/NIMBE/LICSEN

presented by

Quentin ARNOUX

to obtain the diploma of:

Doctor of the UNIVERSITÉ PIERRE ET MARIE CURIE

Thesis subject:

Electronic and structural characterizations of a transparent conductive oxide/organic interface:

Towards applications for organic electronic devices

presented on September 15th, 2017

Jury composition:

Andreas KLEIN	Professor	Referee
Francine SOLAL	Professor	Referee
Matthieu SOLLOGOUB	Professor	Examiner
Luca FLOREANO	Scientific Director	Examiner
Valérie MARVAUD	Scientific Director	Examiner
François ROCHET	Professor	PhD Director
Ludovic TORTECH	Assistant Professor	PhD Supervisor

Contents

Acknowledgement

Pour commencer ces remerciements, je voudrais remercier tout d'abord mes deux encadrants Ludovic Tortech et François Rochet pour leur apport scientifique et humain tout au long de ce doctorat. Leur collaboration a donné naissance à un beau projet alliant chimie et physique, des sciences fondamentales à l'application. Sans eux, je ne serais pas parti au quatre coins de l'Europe pour les différents runs synchrotrons. Je remercie François pour ces longues discussions sur la physique du solide, l'alignement des niveaux énergétiques et la photoémission. Je remercie Ludovic pour les longues discussions sur la science des couches minces et sur le photovoltaïque, discussions qui parfois avaient la chance de se passer autour d'une bonne bière ou de bons vins Italiens. Tout ceci nous a permis d'obtenir de beaux résultats et d'écrire de belles publications dans le domaine.

Tout ceci n'aurait d'ailleurs pas pu être possible sans le soutien financier du Labex MiChem que je tiens à remercier aussi ici. Grâce à ces financements, j'ai pu avancer sans me soucier des besoins annexes comme le matériel dont nous avions besoin, mais aussi les déplacements lors de conférences et congrès. Le Labex m'a ainsi permis de discuter avec des scientifiques du monde entier dans des domaines très variés et il me semble qu'aujourd'hui, la pluridisciplinarité au sein des sciences est primordial.

Je voudrais ensuite remercier les laboratoires qui m'ont accueilli au sein de leurs locaux : le LCPMR à l'UPMC et le LICSEN au CEA. Je tiens donc à remercier Alain Dubois et Vincent Derycke qui ont participé à leur niveau à la réussite de ce doctorat. Sans cet accueil, je n'aurais pas pu préparer sereinement mes échantillons, traiter les données, écrire diverses rapports et une thèse.

Je ne peux continuer sans remercier tous les collaborateurs que j'ai pu rencontrer sur les lignes synchrotrons : Fausto Sirotti et Mathieu Silly sur la ligne TEMPO à SOLEIL, Luca Floreano et Albano Cossaro sur la ligne ALOISA à ELETTRA, Jörg Raabe et Benjamin Watts sur la ligne POLLUX au PSI. Je tiens d'ailleurs à remercier Sufal Swaraj et Stefan Stanescu de la ligne HERMES à SOLEIL, de m'avoir accompagné dans cette Suisse lointaine et pour le temps qu'ils m'ont consacrés lors des expériences. Je voudrais à la suite de cela remercier chaleureusement Adam Hitchcock. Cela a été une rencontre

très enrichissante sur la spectroscopie d'absorption et sans lui je n'aurais pu aller jusqu'au bout du traitement des données de STXM.

Bien qu'ils aient été déjà remerciés pour certains, je voudrais remercier les membres de mon jury de doctorat qui ont pris le temps d'évaluer mon travail : Andreas Klein, Francine Solal en tant que rapporteurs, et Valérie Marvaud et Matthieu Sollogoub en tant qu'examinateurs.

Par le biais de ces deux derniers je voudrais remercier l'IPCM pour le soutien scientifique et en particulier Etienne Derat pour les calculs effectués en DFT. A ces remerciements, s'ajoutent ceux pour Stéphane Carniato du LCPMR : je le remercie chaleureusement d'avoir accepté de pousser jusqu'au bout les calculs théoriques. Sans lui, nous ne serions par parvenus à conclure sur nos résultats expérimentaux.

Je tiens aussi à remercier tous les membres du LCPMR pour les discussions humaines et scientifiques, et pour m'avoir écouté lors des journées scientifiques du laboratoire bien que mon sujet était parfois bien loin de ce qu'ils peuvent étudier. Je remercie toute mon équipe : Jean-Jacques Gallet, Fabrice Bournel, Ahmed Naitabdi et Rabah Benbalagh pour leur soutien tout au long de ce doctorat. Un soutien que j'ai retrouvé aussi au CEA avec Nick Barrett, Claire Mathieu et Christophe Lubin.

Je voudrais remercier aussi ici mes collègues du Palais de la Découverte : Sok pour m'avoir accueilli au sein de l'équipe puis Frédérique, Véronique, Claire et Ludovic. Sans eux, la pédagogie de ma présentation n'aurait pas été appréciée.

Je pense qu'il est temps de remercier maintenant tous mes amis, doctorants, docteurs, ou non, qui m'ont permis de souffler aussi : Anthony, car sans lui pas de chanson à 3h du matin en synchrotron, François, car sans lui pas de soirée dub et bière, Pierre, car sans lui pas de soirée billard, Antoine, car je le reverrai sans doute tour 65, Sevan, car sans lui ni soirée impro, ni Grand Corps Malade, Marie, car sans elle pas de soirée huître, Marie-Charlotte, car sans elle pas de soirée dessin sur frigo avec Antoine, Olivier, car sans lui pas de soirée PolyTech, tous mes amis de Chimie Paris (Arnaud, Madeleine, Sophie, Héloïse, Charlie, Bruno, Maxime, Hafssa, Luc, Diane), car sans eux, pas de houmousgate, pas de BBQ, pas de weekend-end au Mans, pas d'ostréicole, pas de bières à Bruxelles, pas de rugby, pas de pleins de choses en fait...

Et pour conclure ces remerciements, j'embrasse fortement mes parents sans qui je ne serais peut-être pas arrivé jusque là (et surtout je n'aurais pas pu faire un si beau pot de fin de doctorat), et comme maintenant elle fait partie de ma famille, je souhaite finir cette partie avec des remerciements tout particuliers à mon petit chat : à notre rencontre, à toi, mon amour.

Abbreviations

AEY	Auger electron yield
AFM	Atomic force microscopy
BHJ	Bulk heterojunction
C	Conductor
CB	Conduction band
CS-AFM	Current-sensing atomic force microscopy
CT	Charge transfer
DFT	Density functional theory
DIP	Dipyranylidene
DOS	Density of state
ESCA	Electron spectroscopy for chemical analysis
FWHM	Full width at half maximum
HF	Hartree-Fock
HOMO	Highest occupied molecular orbital
IFL	Interfacial layer
IMFP	Inelastic mean free path
ITO	Tin-doped indium oxide
LUMO	Lowest unoccupied molecular orbital
MO	Molecular orbital

NMR	Nuclear magnetic resonance
OFET	Organic field effect transistor
OLED	Organic light-emitting diode
OSC	Organic solar cell
$P^{+/-}$	Positive/Negative polaron
PCA	Principal component analysis
PSC	Perovskite solar cell
PV	Photovoltaic
QB	Quartz balance
ResPES	Resonant photoemission electron spectroscopy
SC	Semiconductor
SEEDC	Secondary electron energy distribution curve
SOMO	Singly occupied molecular orbital
STXM	Scanning transmission X-ray microscopy
SUMO	Singly unoccupied molecular orbital
TCO	Transparent conductive oxide
TEY	Total electron yield
UPS	Ultraviolet photoemission spectroscopy
UV	Ultraviolet
VB	Valence band
XPS	X-ray photoemission spectroscopy
XRD	X-ray diffraction

Introduction

Organic electronic and optoelectronic devices have been investigated in recent years as a potentially competitive alternative to the current inorganic semiconductor technology for applications such as organic light-emitting diodes (OLEDs), [1] organic field effect transistors (OFETs), [2] bulk-heterojunction [3] or dye sensitized solar cells, [4] or chemical sensors. [5] While some of these applications are already in the market (OLEDs, OFETs), others are still far from real applications, despite the rising strides in efficiency registered in the last decades (bulk heterojunction solar cells). [6]

Improving the efficiency of such devices requires control over many parameters, such as the chemical nature and electronic structure of the molecular building blocks, the degree of order of the organic molecules in the active layer, the presence of dopants and impurities, or the nanoscale morphology of the organic films. [7] The interface between the organic active layer and the metallic contacts is of paramount importance in determining the efficiency of the device: for example, the alignment of the molecular orbital levels of the organic layer with the Fermi level of the metallic substrates determines the electron- and hole-injection barriers. [8, 9, 10] Alongside the purely electronic effects, the molecular organization at the interface will also determine the morphology and structure of the organic molecules in thicker films and, thus, will play an important role in steering the physical behavior of the device. [11]

Thus, from the 90's and during two decades, research on the structure of organic monolayers deposited on metallic or passivated semiconductor surfaces progressed at a very fast pace. [12, 13, 14, 15] This research was driven by the observation that, if the nature of the organic molecules and the substrate were properly chosen, many of the concepts developed by supramolecular chemistry in solution phase [16] could be directly exported to the 2D organic adlayers. For supramolecular chemistry, molecule-molecule interactions are numerous: hydrogen bonding, metal coordination, hydrophobic forces, Van der Waals forces, π-π interactions, and electrostatic effects. These interactions also play a detrimental role in organic layers on surfaces. It is worth mentioning that even in the limit of weak molecule-substrate interactions, small changes in the electronic structure

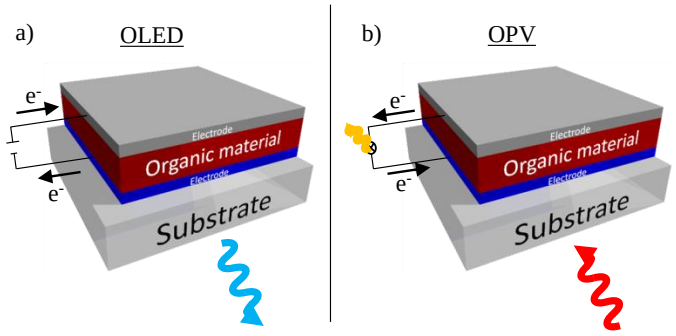

Figure 1 – Schematic process of a) organic light-emitting diode (OLED) and b) organic photovoltaic (OPV) devices.

and morphology of both adsorbates and substrate have been reported. [12, 13, 14, 15] If we now consider the functions that electronic and optoelectronic devices must perform, we often find that molecules with a strong donor or acceptor electronic character, or mixtures of them both, are required to separate regions with opposite sign of the charge carriers, electrons (e^-), and holes (h^+). This requirement must be met, for example, by OLEDs, [1] since the light-emitting mechanism is ultimately related to the recombination of electrons and holes in the active layer (Figure 1a)). Similarly, the working principle underlying bulk-heterojunction solar cells requires the splitting of the tightly bound excitons formed by light absorption on the organic molecules, into electrons and holes that can be later on driven to different metallic electrodes (Figure 1b)). [6]

Since the molecules interesting for electronic and optoelectronic applications turn out to be strong donors or acceptors, charge transfer between the substrate and the adsorbate is to be expected, especially when the substrates are metallic. The properties of such charged adsorbates in terms of molecule-molecule or molecule-substrate interactions cannot be expected to be the same as when they are in solution.

For this reason, during the last few years many groups have directed their attention to organic donor and acceptor species deposited on metal surfaces, and their investigations have shown many new phenomena. [17, 18, 19, 20, 21] Such effects have their origin in, but are not limited to, the charge-rearrangement at the interface and the concomitant realignment of the energy levels. Moreover, the transfer of electrons across the inorganic/organic interface leads to the formation of dispersive delocalized electron states [22] or may even confer magnetic properties to the organic adlayers. [23, 24]

During this 3-year project, we studied a metal/organic interface. The research community works highlighted specific interface geometric and electronic rules, and impact on the overall behaviour. Several synchrotron experiments have been performed at the

TEMPO beamline (SOLEIL synchrotron, France), the ALOISA beamline (ELETTRA synchrotron, Italy), and the PolLux beamline (SLS synchrotron, Switzerland). The results offer an understanding of the structural and electronic properties of a metal/organic interface, based on indium tin oxide (ITO), the metal, and dipyranylidene (DIP), the organic material. ITO, a transparent conducting oxide, remains the dominant material used as an electrode for organic electronics. DIPs have shown to be great donors [25] and are already used in different organic electronic devices. [26, 27, 28] In these systems, DIP layer electronic properties have not been fully characterized regarding the electronic mechanism at a metal/organic interface. Therefore, we performed a precise morphological and electronic study of this interface. The results are summarized in the five chapters below.

In Chapter I, we will recall the basis on the (inorganic and organic) semiconductor properties. We will then present the different interactions at a metal/organic interface, and the growth modes of an organic layer on a substrate. We will discuss the process of charge-transfer by itself, to understand the alignment of the electronic levels at the interface between metals and organic donors and acceptors. Finally, X-ray basis and experiments will be presented as a tool to determine both morphology (absorption) and electronic properties (photoemission) of the interface.

The morphology of the ITO/DIPO-Ph_4 samples will be presented in Chapter II. Atomic force microscopy (AFM) and scanning X-ray microscopy (STXM) have been performed to determine the growth mode and the molecular orientation. Thermal annealing treatments allow us to tailor the organic layer morphology. This study will help us to understand the measurements performed via X-ray photoemission spectroscopy (XPS) presented in Chapter III.

Indeed, in the latter, we will make a complete description of the ITO electronic properties. XPS data on the ITO/DIPO-Ph_4 interface will be then presented. These results have been confronted to density functional theory (DFT) calculations. A charge transfer from the organic material to the substrate is observed. To complete this chapter, we will also present resonant photoemission spectroscopy (ResPES), a tool to access the charge transfer time, and pump-probe results that have been performed to gain insight on the DIPO-Ph_4 de-excitation time.

The DIPO-Ph_4 layer fully characterized, we integrated the system in photovoltaic devices. We will present in Chapter IV the energetic alignment of a typical organic solar cell with DIPO-Ph_4 as interfacial layer. The photovoltaic response has been measured and we will comment on the efficiency increase regarding both the morphology and the electronic properties of the organic layer.

In the last chapter, Chapter V, we will present the effect of a change in the DIP

heteroatom on the morphology and electronic properties. In this thesis, these data will be presented as preliminary results and further XPS experiments and DFT calculations will be performed to allow a complete discussion on DIP derivatives.

Chapter I

Metal/organic interfaces: morphology and electronic study

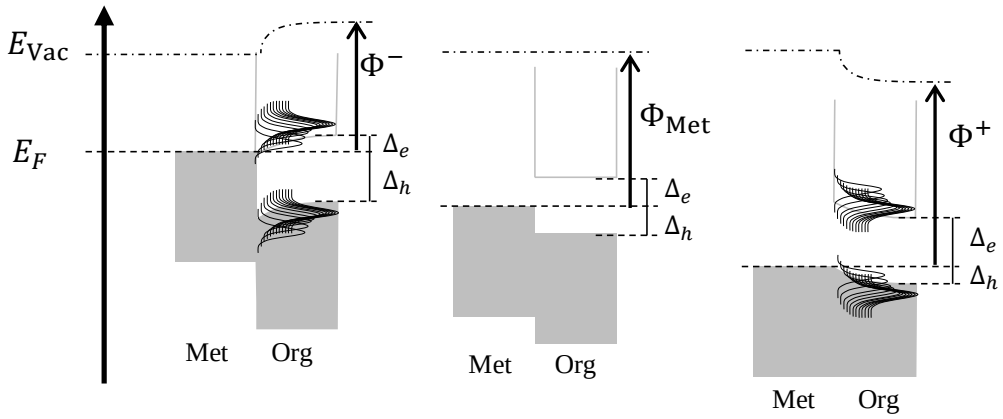

LUMO pinning Schottky-Mott limit HOMO pinning

I.1 Semiconductor description

In this section, we will present the electronic description of a semiconductor and the state-of art on metal/organic level alignment.

To understand molecular electronics, we must first consider the electronic properties of a semiconductor and how molecules grow on a surface. We will recall the fundamentals of energy placement in a solid and the growth mode of an organic layer.

I.1.1 Inorganic semiconductor

a) Theoretical description

Within an isolated atom, the energy levels are discrete and we speak of an atomic orbital. Their values are obtained by solving the Shrödinger equation: [29]

$$\left[-\frac{\hbar^2}{2m^*}\nabla^2 + V\right]\psi\left(\mathbf{r},\mathbf{k}\right) = E\psi\left(\mathbf{r},\mathbf{k}\right)$$

where $\hbar$ is the reduced Planck constant, m^* the effective mass, V the potential energy, $\mathbf{r}$ the position vector, ψ the wave function, $\mathbf{k}$ the wave vector and E the energetic level.

From this energetic description, an ionization potential (IP) is defined, which corresponds to the energy to be supplied to the system for withdrawing an electron from an occupied state. On the other hand, the electronic affinity (EA) corresponds to the energy required for adding an electron to an unoccupied state.

In a crystalline material, the studied entity is not isolated. Indeed, there is a periodic repetition of a pattern. Consequently, the energy levels are no more discretized. This repetition generates a band energy structure. Two bands are key parameters for a material description: the last band filled with electrons, called the valence band (VB), and the first band constituted with unoccupied state, the conduction band (CB). From this description, IP_v is thus the difference between the vacuum level (E_{Vac}), which is the zero of energy, and the maximum of the valence band. EA_c is the difference between E_{Vac} and the minimum of the conduction band. The energy gap (E_G), which is equal to the difference between EA_c and IP_v (Figure), defines the electronic properties of the material and corresponds to the minimum energy required to form an electron-hole pair, called an exciton.

Depending on the E_G value, the materials properties will be different and there are three types of behaviour:

- $E_G \gg 0$: insulator
- $E_G > 0$: semiconductor (SC)

I.1 Semiconductor description

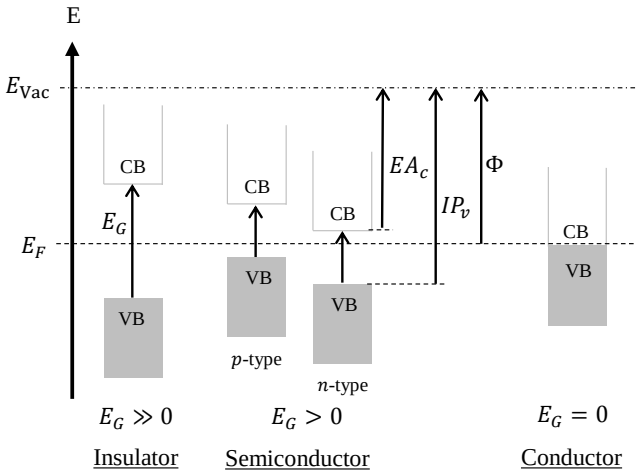

Figure I.1 – Energetic representation of insulator, semiconductor, and metallic materials.

- $E_G = 0$: conductor (C)

At room temperature, an electron can be easily promoted from the VB to the CB. A pseudo-energy state, the Fermi level (E_F) is defined as the energy level for which the probability of having an electron is equal to $\frac{1}{2}$. This is called the Fermi-Dirac statistic (P). [29] This probability is then expressed in the form of a sigmoid which verifies $P(E_F) = \frac{1}{2}$ and $P_{T\to 0}(E) = 1$. P is expressed as:

$$P(E) = \frac{1}{1 + \exp^{\frac{E-E_F}{k_B T}}}$$

where k_B is the Boltzmann constant and T the temperature.

For an insulator, the Fermi level is situated between VB and CB. For a conductor, the Fermi level is at the VB maximum (Figure I.1).

For a doped semiconductor, there are two cases:

- p-type SC: the material is doped with acceptor elements; therefore, the hole concentration is larger than the electron one. The Fermi level is close to the VB. The SC has an affinity for hole conduction through the VB (hole donor or electron acceptor).

- n-type SC: the material is doped with donor elements; therefore, the electron concentration is larger than the hole one. The Fermi level is then close to the CB. The SC has an affinity for electron conduction through the CB (electron donor).

From the Fermi level, the work function (Φ) is defined as the energy between E_{Vac} and E_F.

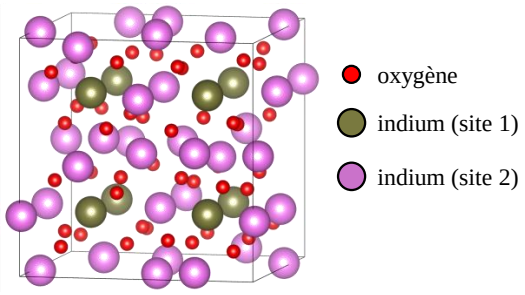

Figure I.2 – Bixbyite structure of indium oxide determined via X-ray diffraction.

b) Electrode for organic electronics

To highlight the semiconductor description, we can focus on the practical study of transparent conductive oxides (TCO) that are mainly used in electronic devices.

The materials of the transparent electrodes (used for anodes) in the organic electronic devices are mainly oxides, [30, 31, 32] although a replacement with alternative materials, for instance polymers [33] and graphene, [34, 35, 36] starts to be explored. Among oxides, Sn-doped In_2O_3 (indium tin oxide, ITO) remains the dominant material used as an electrode for organic electronics despite its high cost in front of alternative oxides like aluminum-doped zinc oxides, mainly because of a better resistance to degradation in outdoor environments. [37] Its wide utilization is attributed to its remarkable properties such as high conductivity, excellent transmittance, and suitable work function. [38] But the finite availability of element indium and chemical and electrical drawbacks of ITO, impel the development of new electrode candidates, such as solution-processed silver nanowire, [39] conducting polymer films, [40] carbon nanotube films, [41] as well as transparent graphene-constructed films. [42] For the cathode, vacuum evaporated metal films such as aluminium or silver are usually used.

ITO is formed thanks to a doping with tin oxide (SnO_2) of indium oxide (In_2O_3). The doping is typically 10 % weight of SnO_2. The structure is based on a bixbyite structure of In_2O_3 with a substitution of In^{3+} cations by Sn^{4+} (Figure I.2). [43] In this case, theoretical atomic ratios are: In 0.356, Sn 0.036, O 0.607.

A variety of techniques have been developed for ITO deposition, including sputtering, evaporation, spray pyrolysis and screen printing. The sputtering method now prevails in the production of ITO films since it can deposit films over large areas at rates comparable to electron-beam evaporation, without the degree of radiation heating typical of thermal sources. Impact of gas partial pressure and substrate temperature have been widely studied to understand ITO growth. [44] Structure is a key for resistivity and optical properties.

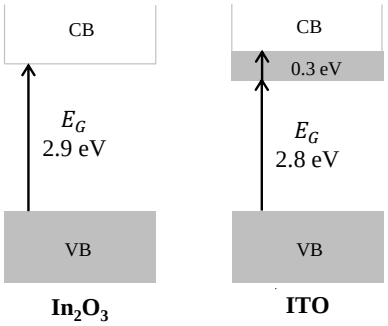

Figure I.3 – Energetic diagram of indium oxide and ITO.

Concerning electronic properties, ITO is often depicted as an "ordinary" metal. In fact, it is a *n*-type degenerate wide gap semiconductor. The value of the direct gap E_G of In_2O_3 has evolved with time, from ∼3.6 eV in earlier publications (based on optical spectra, see Ref. 45, 46) to a much smaller value of ∼2.9 eV (X-ray photoelectron spectroscopy (XPS), *ab initio* band structure calculations [47] and scanning tunneling spectroscopy [48]). The filling of the conduction band, according to the Burstein-Moss model, [49, 50] is made via the presence of Sn donors substituting In atoms, up to ∼0.3 eV from its bottom (Figure I.3). [51]

In contrast to the conclusions of the UV photoelectron spectroscopy (UPS) work of Gassenbauer *et al.* (Ref. 46) where an E_G of ∼3.6 eV was considered, the most recent high energy XPS study of the valence-band, at 3.6 keV photon energy, [47] points to a flat band situation extending deeply in the bulk (the electron escape depth is ∼6 nm) together with a low E_G value of ∼2.8 eV. A subsequent high energy XPS analysis at 6 keV of the In 3d core levels is indicative of a slight carrier depletion in the layers closer to the surface. [52] The ITO work function (Φ_{ITO}) is ∼4.2 eV. It could change with deposition conditions but also post-surface treatment. Cleaning solvents and UV-ozone treatment can modify the ITO surface, which leads to a modification of the electronic properties and thus of the work function. [53] A too long ozone exposure will move the Fermi level above the CB and results in non-conductive ITO.

I.1.2 Organic semiconductor

For organic electronics, we cannot go further without describing the electronic schema of the organic materials. In comparison with the inorganic material, when an organic molecule is formed, the atomic orbitals interact with each other to form molecular orbitals. Two levels are particularly interesting: the highest occupied molecular orbital (HOMO) and lowest unoccupied molecular orbital (LUMO).

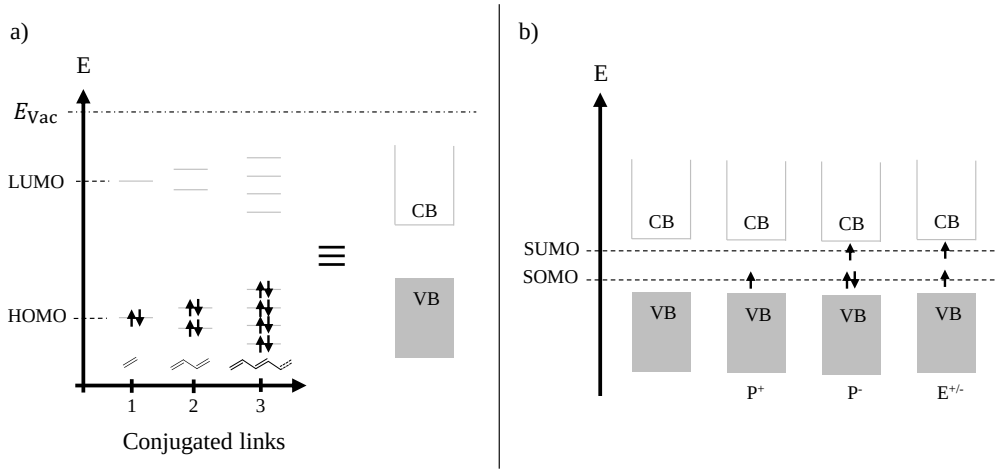

Figure I.4 – a) Energetic representation of an organic semiconductor; b) Energetic representation of SOMO and SUMO levels for organic semiconductor.

The organic materials in molecular electronics are carbon-based. Other atoms with low atomic numbers, such as oxygen or sulphur, are used as structural elements. The carbon skeleton is formed by alternating single and double bonds to establish the conjugation. The carbons are then at the center of three sp^2 orbitals in the plane and one p orbital perpendicular to the previous plane. The overlap between p orbitals leads to a delocalization of the electronic states. The continuum of the binding π orbitals thus constitutes the HOMO, HOMO-1, HOMO$-n$, and can be assimilated to the VB of the material, and similarly the LUMO, LUMO$+1$, LUMO$+n$ are constituted by the continuum of the antibonding π^* orbitals, and it can be assimilated to the CB as described in Figure I.4a)).

Molecules can be either good electron donor or good electron acceptor. When a charge transfer occurs, we speak of polaron (P^- or P^+). The formation of a molecular ion leads to a relaxation to minimize the system energy. As shown in Figure I.4b), the newly occupied (for P^-) or unoccupied (for P^+) level is a semi-occupied molecular orbital (SOMO) or semi-unoccupied molecular orbital (SUMO). [9] These energetic level positions are obtained after stabilization of an excess charge in the organic semiconductor, by geometric relaxation of the charged molecule itself (internal relaxation) and of the surrounding lattice (external relaxation). Yet, the energetic difference between the polaronic states (SOMO and SUMO) and the neutral states (HOMO and LUMO, respectively) is typically smaller than 0.1 eV. [54] Polaronic effects will, therefore, no longer be considered in the following.

In organic electronics, the organic materials are classified as hole-transport, or electron-

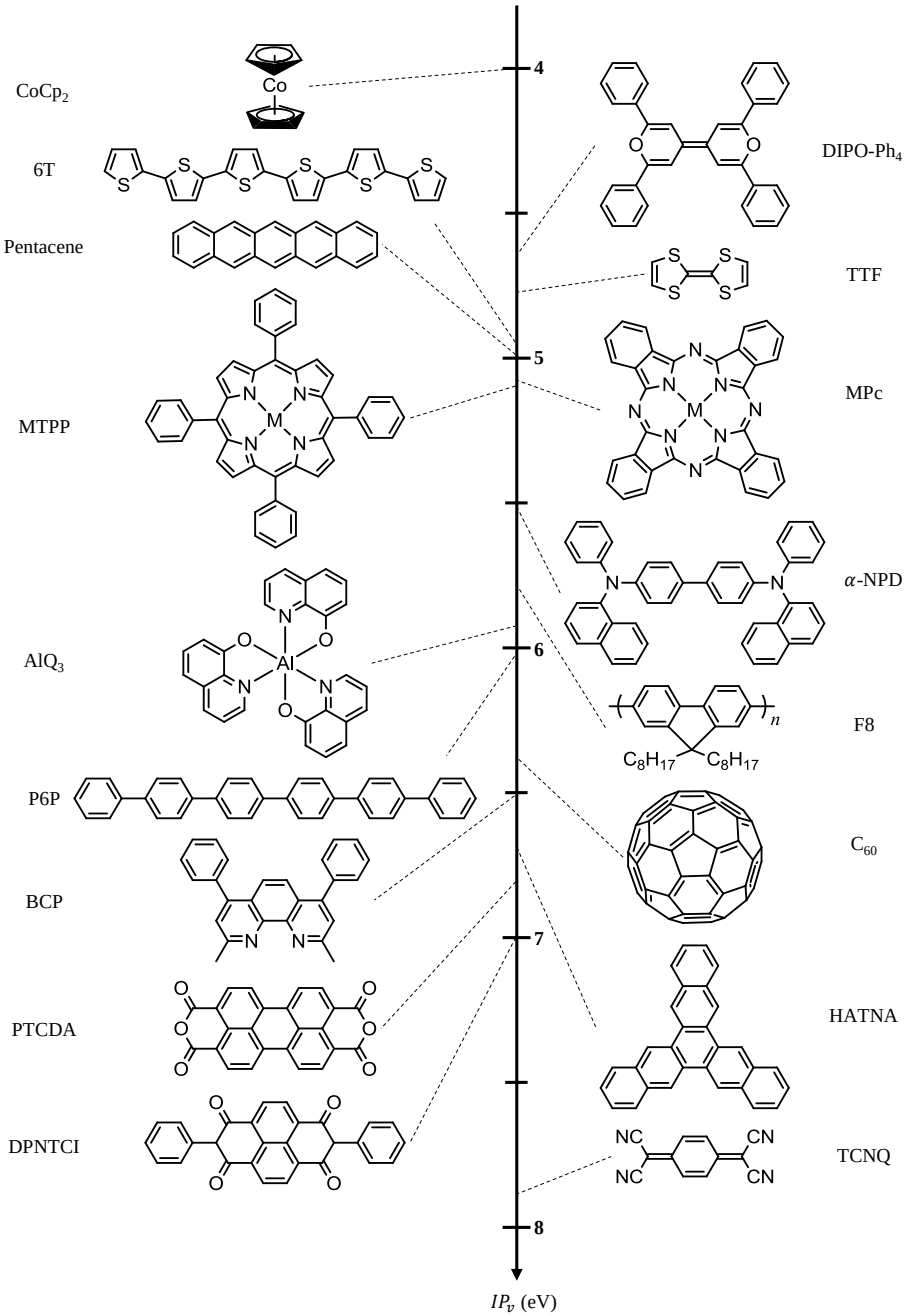

Figure I.5 – The structure and ionization energy IP_v (in eV) of common materials used for organic electronics study. The full names of the compounds are: cobaltocene ($CoCp_2$), tetraphenyl-dipyranylidene (DIPO-Ph_4), tetrathiafulvalene (TTF), sexithiophene (6T), metal phtalocyanine (MPc), metal tetraphenyl-porphyrin (MTPP), N,N'-di(1-naphthyl)-N,N'-diphenyl-(1,1'-biphenyl)-4,4'-diamine (α-NPD), poly(9,9-di-n-octylfluorenyl-2,7-diyl) (F8), fullerene (C60), bathocuproine (BCP), hexaazatrinaphthylene (HATNA), perylenetetracarboxylic dianhydride (PTCDA), N,N'-diphenyl-1,4,5,8-napthyltetracarboxyldiimide (DPNTCI), tetracyanoquinodimethane (TCNQ).

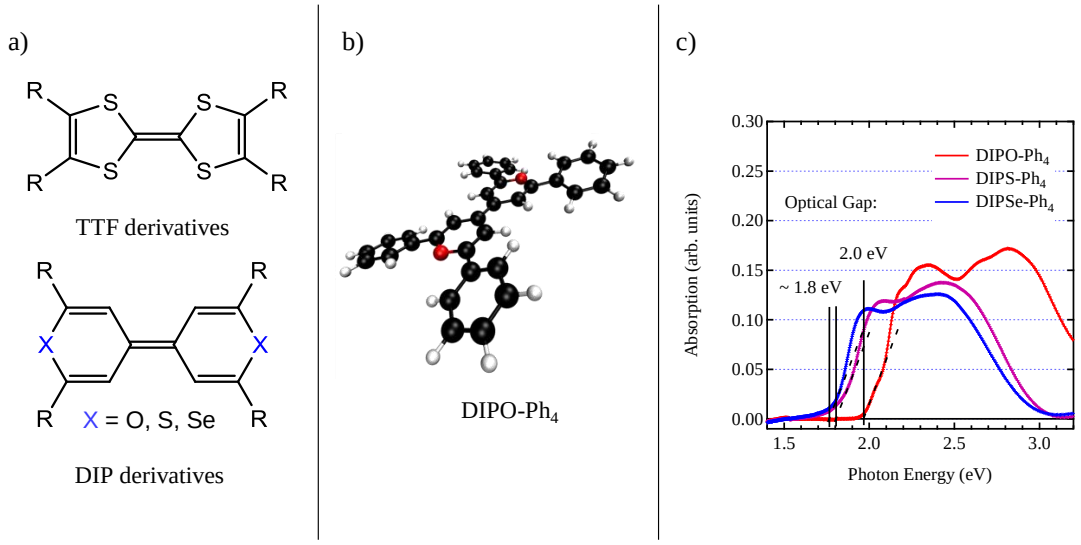

Figure I.6 – a) Structure comparison between TTF and DIP family; b) Optimized geometry of DIPO-Ph_4 derivative; c) UV absorption of solid state DIPX-Ph_4 layer.

transport, for electron donor, or acceptor, respectively. A lot have already been developed (Figure I.5) and all starts with tetrathiafulvalene (TTF) as electron donor and with tetracyanoquinodimethane (TCNQ) as electron acceptor. [55]

Among the organic semiconductors, dipyranylidenes (DIP) are promising molecules (structure presented in Figure I.6a)). The quinoid structure of the DIP core is reminiscent of TTF, a well-known family of π donors with potential applications in molecular electronics. However, in sharp contrast with TTF and its analogues, whose properties have been extensively studied, DIP derivatives remain almost unexplored today. Alizon *et al.* shows that DIP forms a high-conductivity donor-acceptor complex with TCNQ. [25] The DIP oxidation potentials are around 0.2 V which makes it a better electron donor than TTF (0.34 V both relative to Ag/AgCl in acetonitrile). This value leads to an ionization potential (IP_v) of ~4.6 eV, according to the Forrest's relationship. [56]

The DIP synthesis has been optimized during previous works. [57] In this study we will focus on the phenyl (Ph) derivatives (DIPX-Ph_4 with X = O, S or Se). In the solid state, the optical gap of the molecular material deposited as a thin layer is $\leq$ 2 eV (Figure I.6c)). Concerning the geometry of the free molecule (Figure I.6b), oxygen DIP derivative), the four phenyls are almost parallel to the DIP core, the dihedral angle being ~17° for the oxygen derivative. This value increases to ~39° for the sulphur derivative and ~42° for the selenium one. The heteroatom volume increases from O to Se which increases repulsive forces. The tilted angle between the DIP core and the Ph groups may lead to a change in the electronic behaviour of the molecular material as the molecular

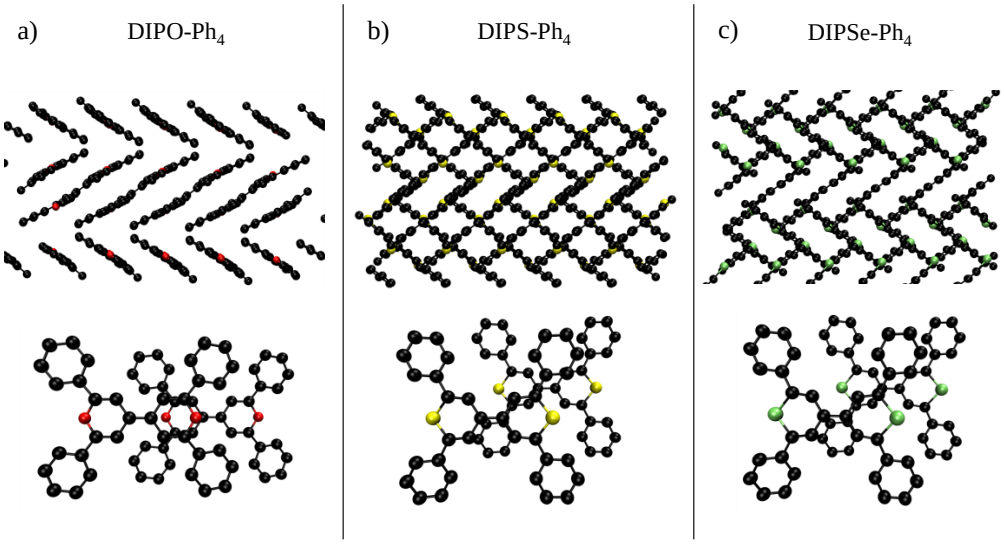

Figure I.7 – Crystallization mode for a) DIPO-Ph_4, b) DIPS-Ph_4 and c) DIPSe-Ph_4. The upper view is along the DIP core plan. The bottom view is along the normal of the DIP plan.

orbital localization changes. However, the molecule behaviour deposited as thin films can be different due to the intermolecular interactions. In the solid-state, X-ray diffraction (XRD) measurements have been performed: molecules pack plane-to-plane in columns and the dihedral angle of the phenyl groups reduces to 7.8° for oxygen derivatives. [58] For DIPS-Ph_4, the angle is 12.4° and for DIPSe-Ph_4, it reduces to 14°. [59, 60]

Molecules are V-shaped at solid state (Figure I.7). The molecules do not pack one molecule on top of the other. For the DIPO-Ph_4 there is a shift along the O – O direction of 4.8 Å. For the DIPS-Ph_4 and DIPSe-Ph_4 as there is a bigger dihedral angle between the phenyls and the DIP core, molecules are also shifted along the perpendicular X – X direction in the DIP core plan. This crystallized morphology has been also confirmed in thin layers after thermal evaporation. [61, 27]

DIP derivatives have already been used in organic devices such as organic solar cells (OSCs) [28, 26] or organic field effect transistors (OFETs) [61, 27] but the electronic process and properties have not been clearly demonstrated. During this work, we thus aim to gain a better understanding of the interface formed by DIP layers on ITO substrates, which are typical metal/organic interfaces.

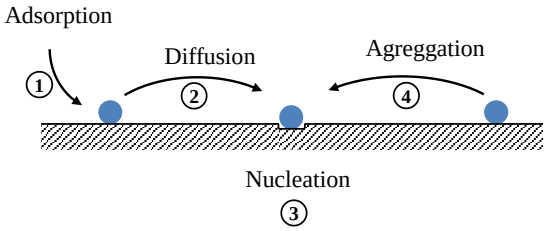

Figure I.8 – Four-step-model for the growth mode of a layer formed via thermal evaporation.

I.2 Metal/organic interface

I.2.1 Layer interactions

Two sets of interactions are to be considered to describe the metal/organic interfaces: [8]

- Substrate/molecule interactions: interactions between the first deposited layer and the substrate.
- Intermolecular interactions: interactions between molecules within the layer.

Substrate/molecule interactions:

The production thin layers is usually achieved by several nucleation and growth steps. [62] These steps involve adsorption, diffusion to a nucleation point, and aggregation between the manipulated entities (Figure I.8). The film growth thus depends on a trihedral, including the surface state (adsorption sites, potential barrier), the nature of the manipulated entities (polarization, interaction) and the deposition conditions (speed, time). In the case of physisorption, molecules are anchored to the substrate by Van der Waals interactions of low energy. In the case of chemisorption, the bond with the substrate is established through covalent bonds.

Due to substrate/molecule interactions, a charging rearrangement can be observed. [8] This charging effect is of different nature, depending on the involved interactions.

The factors affecting the interface are presented in Figure I.9:

- Charge transfer between the metal and the organic layer with formation of a cation (donor) or an anion (acceptor).
- Mirror force due to a charge concentration at the substrate surface.
- Chemical bonds leading to a chemical modification.

I.2 Metal/organic interface

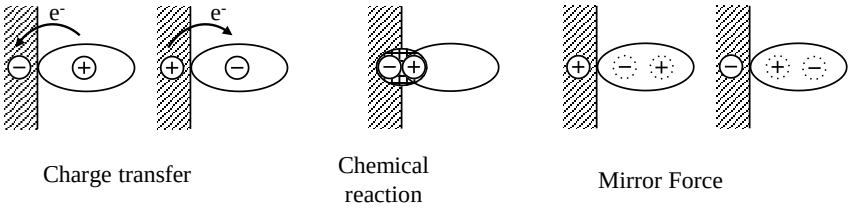

Figure I.9 – Charge effect at the molecular: substrate interface.

Intermolecular interactions:

Within a thin layer, intermolecular interactions allow to establish cohesion between the molecules by minimizing the total system energy. Some are directional and make it possible to structure the layer. These interactions are commonly classified according to their bond energy (Table I.1).

Table I.1 – Main intermolecular interactions.

Interaction	**Description**	**Energy** $(\mathbf{kcal \cdot mol^{-1}})$	**Example**
Hydrogen bond	$H \cdots A$	2-30	DNA
Electrostatic	Anion-Cation	1-20	Salt (LiF)
Orbital	π-stacking	0-10	Polyaromatic layer
Van der Waals	Weak interaction	0.1-1	Alkyl layer

Growth mode:

Concerning the layer growth mode, substrate/molecule and molecule/molecule interactions are competing which leads to three possible modes of crystal growth on a surface (Figure I.10): [62]

- The island type, or Volmer-Weber mode, is a three-dimensional growth during which islets form. This growth mode is usually favoured when the entities forming the deposited layer are more strongly bonded to one another than to the substrate.
- The Frank Van der Merwe mode, or layer type, is a two-dimensional growth which is favoured when the energy of interactions between the deposited entities is less than or equal to that between the thin layer and the substrate. In this case, the films are formed layer by layer.
- The last mode, the Stranski-Krastanov mode, is a combination of the two previous modes. After the two-dimensional growth has begun, a change in growth mode is observed, where the island formation becomes energetically favourable.

Figure I.10 – Three growth modes for layer formation on a surface.

I.2.2 Energetic level alignment

The electronic levels of an organic material deposited on a metal are most often placed against each other by aligning the vacuum levels (the so-called Schottky-Mott limit). A vast literature on metal/organic or inorganic semiconductor/organic interfaces shows that it is far to be always the case. [9, 10, 17, 21, 63, 64, 65, 66] Various models were proposed to describe the actual situation. They differ not only in their intended range of applicability (from a single organic semiconductor layer to thick films) but also in the envisioned regimes of electronic coupling strength between the organic material and the electrode (from weak coupling with a passivated electrode to intermediate coupling with an atomically clean metal) as well as in the assumed energy distribution of the electronic states in the organic material (from discrete to continuous).

In the integer charge transfer model, according to the respective energies of the metal work function and of donor/acceptor polaronic levels related to, but not confounded with, the highest occupied molecular orbital (HOMO)/lowest unoccupied molecular orbital (LUMO) levels, charge can be transferred across the interface or not. When charge transfer occurs, the energy levels are pinned by the acceptor/donor polaronic levels. A change in the work function is seen and the Schottky-Mott alignment is not observed. [9]

The concept of the polaronic level, on which the integer charge transfer model was based, was recently challenged by the electrostatic model of Oehzelt and coworkers [10] who considered the polaronic energy as almost negligible. Relying heavily on the density of state (DOS) of the organic film, the spatial profile of the electrostatic potential in the organic layer was calculated via the Poisson equation. The DOS shape and the energy distribution of electronic states tailing into the fundamental gap is found to determine both the minimum value of practically achievable injection barriers as well as their spatial profile, ranging from abrupt interface dipoles to extended band-bending regions.

The different energetic level alignment regimes are presented in Figure I.11.

Three regimes are possible:

- HOMO pinning.
- Schottky-Mott limit.

I.2 Metal/organic interface

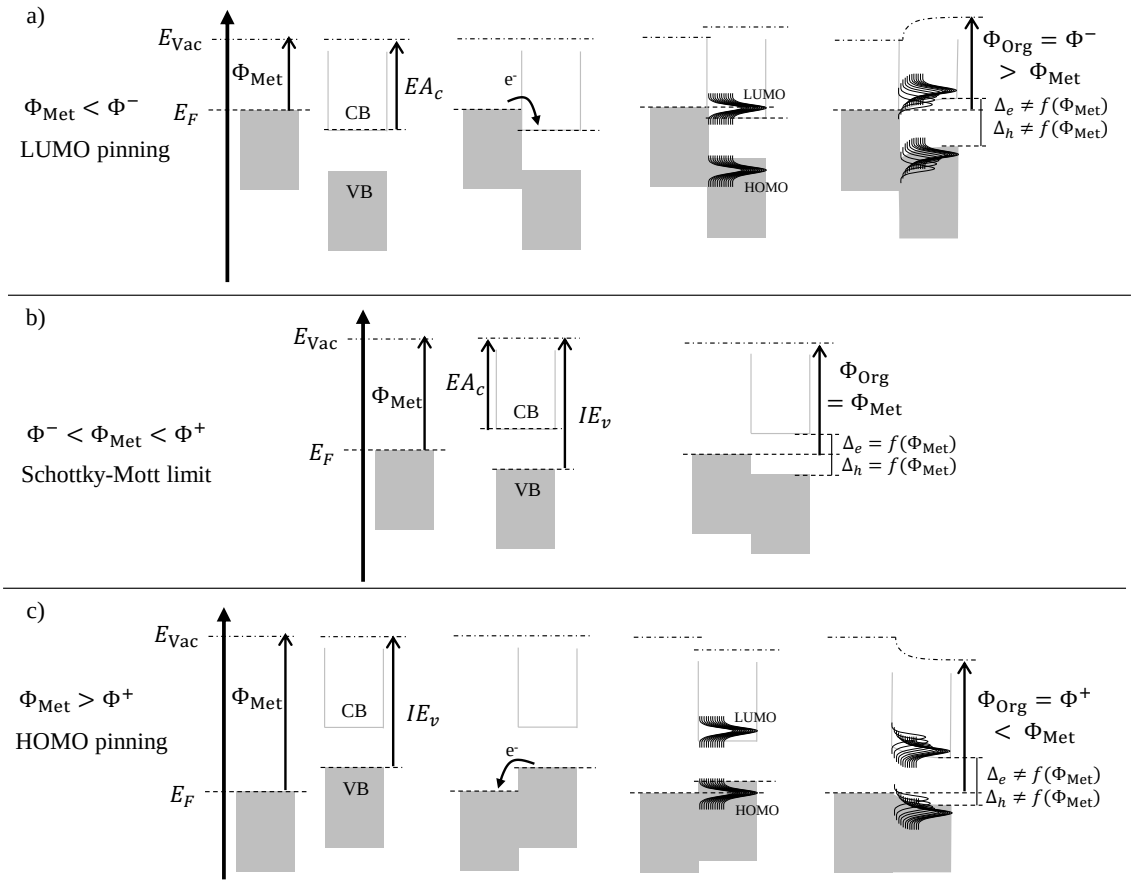

Figure I.11 – Energetic representations of a metal/organic interface and alignment after a) LUMO pinning, b) Schottky-Mott limit, and c) HOMO pinning.

- LUMO pinning.

Each one depends on the metal work function (Φ_{Met}) position in comparison with two virtual states Φ^+ and Φ^-. It corresponds to the work function value for which a charge transfer (positive or negative) is observed. These states are positioned in the organic band gap. Between the two values, there is no charge transfer from and to the metal substrate (Figure I.11b)). The alignment follows the typical Schottky-Mott limit which is based on the vacuum level (E_{Vac}) alignment. In this case, the organic work function (Φ_{Org}) value is equal to Φ_{Met}. Therefore, the electron barrier (Δ_e) and the hole barrier (Δ_h), which are key parameters for organic electronics devices, are depending on Φ_{Met}. These values can be plotted as a function of Φ_{Met} in a Z-shaped curve (Figure I.12).

In the two other regimes, charge transfer occurs. For $\Phi_{\mathrm{Met}} < \Phi^-$ (see Figure I.11a)), there is a charge transfer (e^-) from the metal substrate to the organic material which leads to an anionic formation at the interface. The Fermi level aligns with the LUMO

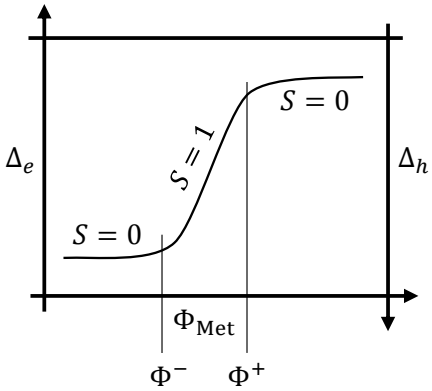

Figure I.12 – Z-shaped curve representing the hole and electron barriers as a function of the metal work function.

level (LUMO pinning). The interface dipole leads to an upward band bending. Finally, the Δ_e only depends of the organic layer thickness ($\Delta_e = 0$ for a monolayer) and does not rely on Φ_{Met} (slope $S = 0$ for the Z-shaped curve). The Φ^- value can be determined measuring the work function for a thick organic layer (Φ_{Org}), far from the metal/organic interface. In a similar way, for $\Phi_{\text{Met}} > \Phi^+$ (see Figure I.11c)), there is a charge transfer from the organic material to the metal substrate. After HOMO pinning, a downward band bending is seen and $\Delta_h = 0$ for a monolayer. Φ^+ is then determined thanks to the value of the thick organic layer work function.

To summarize, when charge transfer occurs the HOMO, donor case, (or LUMO, for the acceptor case) aligns with the Fermi level of the metal very close to the surface, and further apart an extended "band-bending" region appears, according to the value of the DOS. The electrostatic model of Ref. 10 reproduces the experimental behaviour of the hole- and electron-injection barriers versus the substrate work function, distinguishing cases obeying the Schottky-Mott limit from those where the HOMO or LUMO of the molecular solid pin the work function.

To determine the energetic level alignment, X-ray characterizations can be performed.

I.3 X-ray characterizations

The history of X-ray experiments can be considered to begin in 1887, with the discovery of the photoelectric effect by Herzt. [67] Already in 1907, Innes described a kinetic energy spectrum of photoelectrons excited by radiation of an X-ray tube with a platinum anode and registered by a spectrometer consisting of a magnetic analyzer and photographic detection (see Appendix B.3.3). [68] Siegbahn *et al.* developed a high-resolution

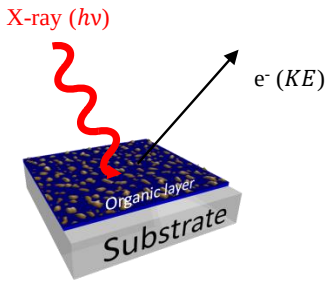

Figure I.13 – Schematic representation of photoelectron emission.

spectrometer which allowed to measure accurately the binding energy of photoelectron peaks.([69] Subsequently, the same group observed the chemical shift effect for the binding energy of core level electrons, which led to a development of the whole field of electron spectroscopy named ESCA (electron spectroscopy for chemical analysis). Siegbahn was awarded a Nobel Prize in 1981 "for his contribution to the development of high-resolution electron spectroscopy". In 1969-1970, commercial X-ray instruments began to appear thanks to the development of ultra-high vacuum (UHV) routine methods. X-ray experiments are now widely-used methods for investigation of solid sample surfaces. The possibility of chemical composition estimation, and of element chemical states, together with a depth information, make it an important method for microelectronics, metallurgy, heterogeneous catalysis, polymer technology and corrosion science. [70]

Depending on the energy of the light source, two types of spectroscopy are distinguished: the photoemission in the ultraviolet (UV) region (ultraviolet photoelectron spectroscopy, UPS) that allows ejecting the electrons from the valence band and X-ray photoemission (X-ray photoelectron spectroscopy, XPS) that allows ejecting electrons from core levels (Figure I.13).

Experimentally, we obtain from the detector an intensity (N_{counts}) curve as a function of the photoelectrons kinetic energy KE (from photoemission cut-off ($KE = 0\,\text{eV}$) to the last photoelectrons at Fermi level ($KE = E_F$)).

I.3.1 Physical principles

Berglund and Spicer developed the theoretical model of the photoemission process in 1964. [71] The photoemission process is described as a three-step model. In this approach, the optical excitation between two Bloch states, the transport of the electron to the surface and the escape of the electron through the surface into the vacuum, are treated separately.

A simple explanation of the three-step model can be given as follows:

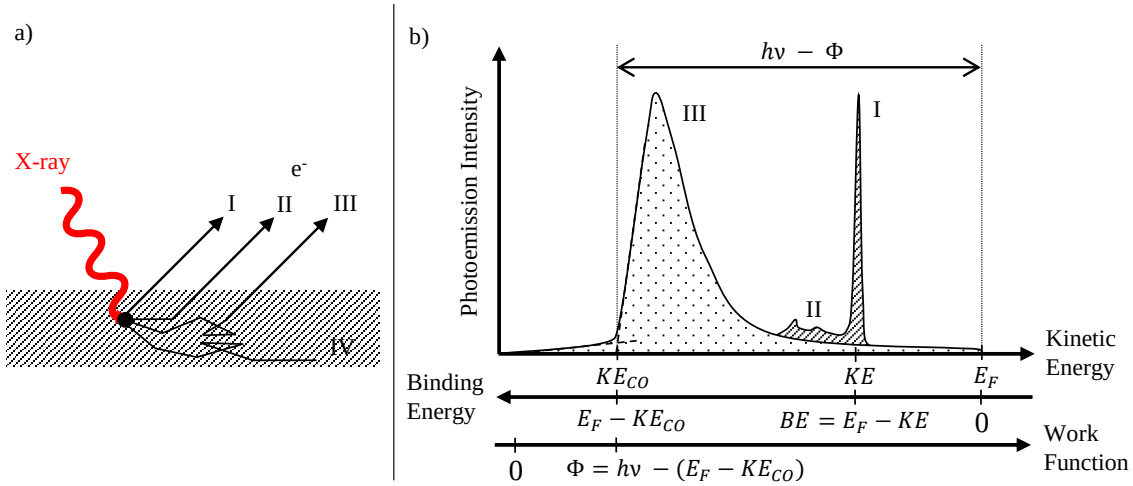

Figure I.14 – a) Photoelectron-matter interaction after X-ray irradiation; b) Schematic representation of a photoemission spectrum.

Step 1. Photon ionization:

When an atom absorbs a photon with sufficient energy, it can be ionized, causing an electron to escape from a bound state to a free state. The transition probability is related to the cross-section of the interaction process, which depends on the photon energy, the atom from which the electron is extracted from, and the electronic shell from which the photoelectron is ejected.

Step 2. Photoelectron transport to the surface:

The surface sensitivity of this technique arises from the strong interaction of electrons with matter. Before escaping from a solid the electron can interact with the matter in different ways, giving rise to different photoemission structures (Figure I.14):

- Elastically scattered electrons which have escaped from the solid without suffering energy loss. These lead to the main photoemission peak (case I).
- Inelastically scattered electrons which have lost kinetic energy on their way out of the solid. Such kinetic energy losses may arise due to electron-phonon (broadening), electron-electron (intra or interband transitions; few eV) or electron plasmon (few eV up to about 30 eV) transitions. These types of electrons give rise to a peak broadening or to satellites peaks (case II).
- Electrons that have undergone many inelastic scattering processes and lost the energy information of their original levels. They are termed as secondary electrons (case III).

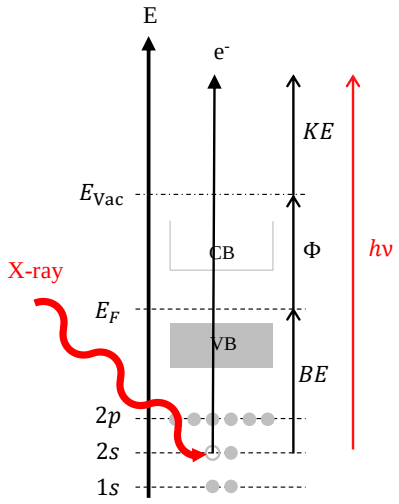

Figure I.15 – Energetic diagram of the photoemission process.

- Electrons that have lost too much energy due to inelastic scattering processes and cannot escape from the surface (case IV).

Step 3. Crossing the surface:

At the surface, electrons must overcome the work function (Φ) of the material.

The energetic diagram of the photoemission process is presented in Figure I.15:

The elastic photoelectron kinetic energy (KE) is related to the energy of the photons ($h\nu$), the binding energy of the energetic level the photoelectron is extracted from (BE), and the work function (Φ) of the sample which give:

$$KE = h\nu - BE - \Phi \tag{I.1}$$

As KE is a function of the photon energy $h\nu$, the photoemission intensity curve is plotted as a function of BE with $BE = E_F - KE$. E_F is used as a reference for the XPS and UPS curve and is the 0 of the BE energy. In addition, note that with this description, IP can be defined for any occupied states (from the core to the valence levels) and $IP = BE + \Phi$.

The binding energy (BE) of an electron is the difference between the energy of the initial state ($E_i\,(n)$, atom with n electrons) and of the final state ($E_f\,(n-1)$, atom with $n-1$ electrons (ion) and a free photoelectron).

$$BE = E_f\,(n-1) - E_i\,(n)$$

In the approximation of frozen orbitals, *i.e.* in the absence of relaxation due to electronic rearrangement following the photoemission process, according to the Koopmans theorem,

BE corresponds to the orbital energy (ϵ_{orb}).

However, after the photoionization process, the surrounding orbitals relax around the core hole to screen it. Therefore, the BE of an electron depends on the chemical environment of the element. The energies of the core electrons, which are measured with XPS, are influenced by the Coulomb interaction with the other electrons and the attractive potential of the nuclei. Changes in the chemical environment cause a spatial redistribution of the valence electrons, which influences the measured BE of the core electrons. The variation of BE results in the shift of the corresponding XPS peak. The BE change of an element core electron due to a change in the chemical bonding of that element is called a chemical shift ($\Delta\xi$):

$$\Delta\xi = -\Delta\epsilon_{\text{orb}} - \Delta E_R + \Delta E_F$$

where:

- $\Delta\epsilon_{\text{orb}}$ is the initial state contribution, and it is the real chemical shift. This term expresses potential modification due to the chemical bond between atoms, acting on the electrons. This could be analysed using a simple physical model. We consider a punctual charge e (which represent the core hole) surrounded by the valence charge at a distance r (approximately the distance from the nucleus). Thanks to the Gauss theorem we have:

  $$\Delta\epsilon_{\text{orb}} \propto \frac{C\partial q}{r}$$

  where C (constant) > 0 and ∂q is the charge transferred to the ligand. If $\partial q > 0$, the atom loses charge by bonding to a more electronegative ligand and the initial state energy decreases, if $\partial q < 0$, the atom gives charge by bonding to a less electronegative ligand and the initial state energy increases.

- ΔE_R is the final state shift. It is due to the screening capacity of the core-hole by the environment (extra-atomic relaxation). In a solid, the extra-atomic relaxation energy is approximated by the electrostatic polarization energy around the hole. Indeed, the creation of a punctual charge (hole) in a dielectric will polarize the surrounding volume (inducing an oriented array of dipoles). [72, 73] ΔE_R, that takes the same mathematical form as the solvation energy of an ion in the Born model, [74] is proportional to the square of the charge e:

  $$\Delta E_R = \frac{1}{4\pi\epsilon_0}\frac{1}{2}\left(1 - \frac{1}{\epsilon_r}\right)\frac{e^2}{R_{eff}} \tag{I.2}$$

  where ϵ_0, ϵ_r, R_{eff} are the vacuum dielectric constant, the relative dielectric constant, and the effective screening radius, respectively.

- ΔE_F considers the modification of the Fermi level position.

Chemical shifts are readily observable and interpretable in XPS spectra as core levels are discrete and generally of a well-defined energy. Atoms of a higher positive oxidation state exhibit a higher BE due to the extra coulombic interaction between the photoemitted electron and the ion core. This ability to discriminate between different oxidation states and chemical environments is one of the major strengths of the XPS technique.

Finally, the KE_{CO} measurement ($KE = 0$) is used to determine the work function (Φ) of the sample. In this case, Equation (I.1) gives:

$$\begin{aligned} 0 &= h\nu - BE - \Phi \\ h\nu - \Phi &= BE \\ h\nu - \Phi &= E_F - KE_{CO} \\ \Phi &= h\nu - (E_F - KE_{CO}) \end{aligned}$$

As already described, the energy level alignment at a metal/organic interface can be determined via the work function measurement. In this way, Φ is a key parameter for a better understanding of the interface.

I.3.2 Sampling depth

While probing surfaces with XPS, a useful signal is obtained from a depth of around 10 to 100 Å. The thickness of the layer that can be analysed is called the sampling depth which is related to the inelastic mean free path (IMFP) of the generated photoelectrons. As described previously, electrons can undergo inelastic collisions before they escape the surface. The IMFP λ is defined as follows: the probability of suffering an inelastic scattering over an infinitesimal distance $\mathrm{d}x$ is $\frac{\mathrm{d}x}{\lambda}$. λ is also the average distance travelled by the electron before it suffers an inelastic loss.

The probability of the electron travelling a distance d through the solid without undergoing scattering is:

$$P(d) = \exp\left(\frac{-d}{\lambda}\right)$$

λ can be theoretically determined using Jablonski *et al.* works. [75, 76] The variation curve of the inelastic mean free path versus the kinetic energy of the photoelectron was calculated for ITO and the DIP molecules using TPP-2M method. We thus plotted in Figure I.16 the results for the different DIP derivatives and compared then to the theoretical curve for every chemical elements.

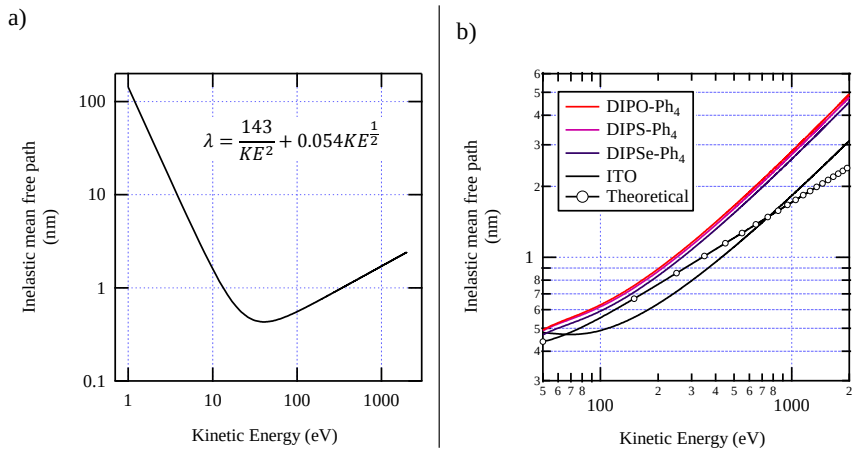

Figure I.16 – Theoretical inelastic mean pathway: a) for the chemical elements; b) ITO and DIP derivative material obtained from TPP-2M method.

At a given KE, $\lambda_{\mathrm{DIP}} > \lambda_{\mathrm{ITO}}$: for one given element for a specific photon energy, the depth analyse is thus bigger in an organic material in comparison with an inorganic one. Note that minimum IMFP, observed for a photoelectron KE of about 50 eV, can be obtained thanks to the synchrotron radiation tunability.

X-ray experiments have been described here as a tool to analyse chemical environment (chemical shift) and electronic properties (work function measurement) to determine the energy level alignment. Yet, X-ray experiments can also be used as a tool to analyse the molecular orientation, a key parameter for organic electronics.

I.3.3 X-ray absorption

X-ray absorption spectroscopy (XAS) is a well-established analytical technique used extensively for the characterization of semiconductors in solid or liquid, crystalline or amorphous, bulk or nanoscale form. If X-rays of intensity I_0 are incident on a sample, the extent of absorption depends on the photon energy $h\nu$ and the sample thickness l (Figure I.17). According to Beer's Law, the transmitted intensity I_t is:

$$I_t = I_0 \exp^{-\mu(h\nu)\rho l}$$

where $\mu(h\nu)$ is the energy-dependent X-ray absorption coefficient, and ρ the material density.

Over large energy regions, the absorption coefficient ($\mu(h\nu)$) is a smooth function of the photon energy, varying approximately as $\frac{Z^4}{m(h\nu)^3}$. [77] Here Z and m are the atomic number and mass, respectively. Thus, $\mu(h\nu)$ decreases with increasing photon energy.

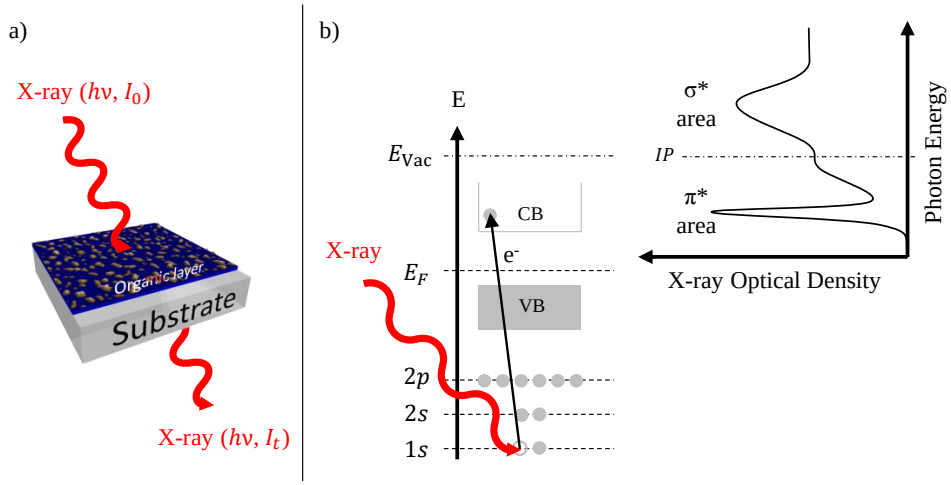

Figure I.17 – a) Schematic representation of X-ray absorption via transmission process; b) Energetic diagram and typical absorption spectrum.

Note that for multi-atom material, $\mu(h\nu)$ is determined using:

$$\mu(h\nu) = \frac{1}{M}\sum x_i \mu(h\nu)_i M_i$$

where M is the molecular weight of the compound, x_i is the stoichiometric number, $\mu(h\nu)_i$ the photoabsorption cross section ($\mathrm{cm}^2 \cdot \mathrm{g}^{-1}$) and M_i the molecular weight of atom i.

If $\mu(h\nu)$ equals or exceeds the core electron BE a new absorption channel is available in which the photon is annihilated, thereby creating a photoelectron and a core-hole. This leads to a sharp increase in the absorption coefficient. The photoelectron will be excited to the unoccupied bound states of the absorbing atom depending on the photon energy.

Experimentally, we measured the optical density (OD) defined as:

$$\begin{aligned} OD &= \ln\left(\frac{I_0}{I_t}\right) \\ OD &= \mu(h\nu)\,\rho l \end{aligned} \tag{I.3}$$

OD is thus directly proportional to $\mu(h\nu)$.

In addition to the information on the molecule electronic structure, XAS can also reveal information about their orientation. To do so, the polarization characteristics of synchrotron radiation are exploited. By taking absorption spectra measurements at two or more angles of incidence of the X-rays, the spatial orientation of an orbital can be extracted. Synchrotron radiation is almost linearly polarized in the plane. Figure I.18 shows the absorption for σ^* and π^* bond formed by 3 atoms parallelly aligned to the surface.

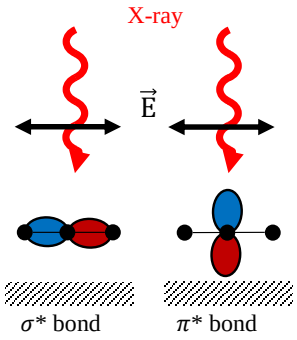

Figure I.18 – Absorption efficiency for a σ^* bond and a π^* bond with 3 atoms parallelly aligned to the surface.

Bonds, and the associated molecular orbitals, are highly directional, and the spatial orientation of an orbital, *i.e.* the direction of maximum orbital amplitude on the excited atom, determines the angular dependence of the K-shell spectra. Therefore, the transition intensities depend on the orientation of the electric field vector relative to the orientation of the molecule. Note that σ^*-orbitals have a maximum orbital amplitude along the bond axis while π^*-orbitals have maximum amplitude normal to the bond direction.

I.3 X-ray characterizations

Chapter II

DIPO-Ph_4 layer on ITO substrate: morphology and molecular orientation

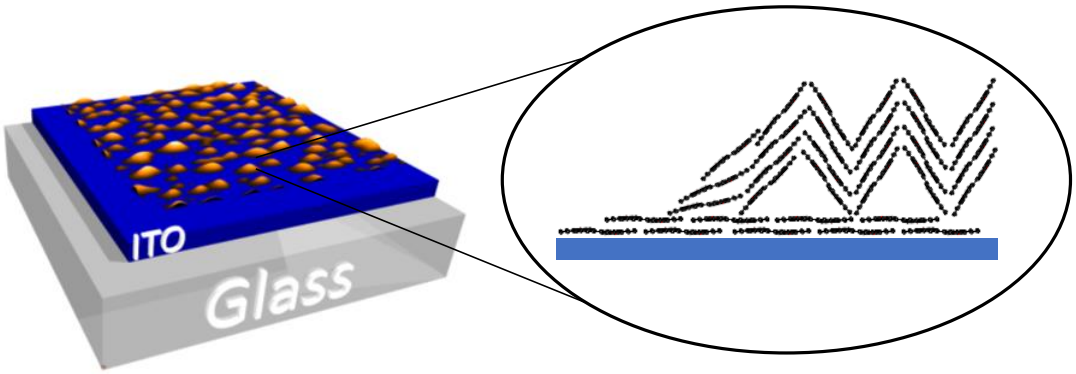

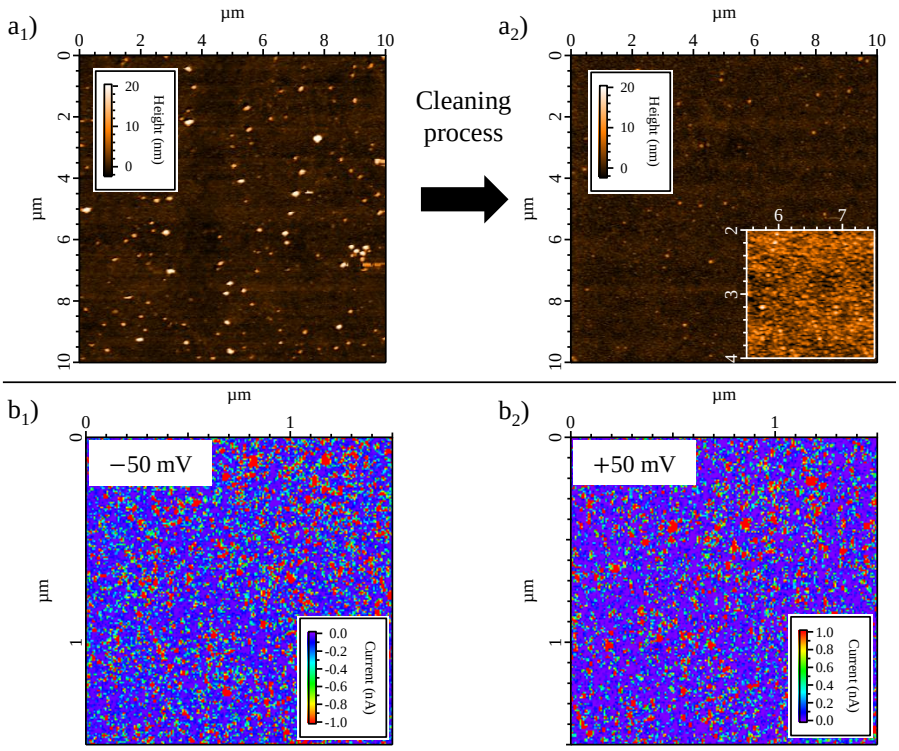

Figure II.1 – AFM images: a$_1$) Bare-ITO; a$_2$) Chemically cleaned ITO, insert: $1\times1\,\mu m^2$ zoom showing granular surface; CS-AFM images: current mapping showing conduction via ITO grains b$_1$) −50 mV; b$_2$) +50 mV.

II.1 ITO/DIPO-Ph$_4$ layer morphology

II.1.1 DIPO-Ph$_4$ growth mode on indium tin oxide

As it was previously described, the interactions between the substrate and the organic layer, and inside the layer itself, lead to three different growth modes.

To understand the ITO/DIPO-Ph$_4$ interface, it is important to characterize the electrode surface: roughness, contaminations, defaults. Before all further analyses, atomic force microscopy (AFM) was used to characterize both the ITO substrates and the organic layer morphology on ITO (Appendix B.3.1). In this first part, we will present the morphology of the ITO surface and the efficiency of the used cleaning process (Appendix A.1).

AFM images of the bare ITO show many light dots, which are attributed to contamination clusters. After the cleaning process, no cluster appears on the ITO surface. The chemical cleaning is efficient as the ITO surface appears without particle contamination. The ITO roughness is 1 nm and the surface shows a granular morphology. This was al-

ready observed in the literature for sputtered ITO. [78, 79] Besides, we performed some current-sensing AFM (CS-AFM). The sample is biased and the AFM tip is grounded. This means that for a negative bias, electrons are travelling from the substrate to the tip, and in the opposite direction for a positive bias. Concerning the current image color appearance, the color scale for the negatively biased image has been reversed in comparison to the positively biased image so that the current minimum is blue in each case and the absolute current maximum is red. The current images are represented between 0 and $(-)1\,\mathrm{nA}$ to correlate the observation with the ITO granular morphology, but the observed maximum current is $+25\,\mathrm{nA}$ and $-25\,\mathrm{nA}$ for the positively and the negatively biased image, respectively. CS-AFM images show that the conduction is clearly happening through the ITO grains.

We are thus able to get a cleaned ITO surface with a small roughness despite a granular surface. The CS-AFM experiments confirm the metallic behaviour of the ITO although it is a doped n-type SC. The Sn doping of the commercial ITO is efficient to make ITO conductive. We will now focus the analysis of DIPO-Ph$_4$ on ITO samples in order to investigate the organic layer morphology.

Several samples were prepared with a change in the deposited organic material DIP amount. The weight, followed by a quartz balance (QB), increases per surface unit during the time evaporation (Appendix B.1). It is then converted into a molecular surface density using the density given by XRD experiment. [58] The different samples are named by their QB-coverage We studied three different samples: a "thin" layer of $0.5 \times 10^{15}\,\mathrm{molecule \cdot cm^{-2}}$, an intermediate layer of $2 \times 10^{15}\,\mathrm{molecule \cdot cm^{-2}}$, and a "thick" layer $10 \times 10^{15}\,\mathrm{molecule \cdot cm^{-2}}$. AFM images were used to determine the real value of the coverage and make correlations with the QB-coverage.

After the deposition of $0.5 \times 10^{15}\,\mathrm{molecule \cdot cm^{-2}}$, the AFM image (Figure II.2a)) shows that 3D clusters cover 20 % of the ITO surface. The average cluster height is 20 nm, with an average diameter of 200 nm. Given the cluster density, an average volume of DIPO-Ph$_4$ per surface unit is obtained, leading to a molecular surface density of $0.55 \times 10^{15}\,\mathrm{molecule \cdot cm^{-2}}$ (using the density of Ref. 58), in excellent agreement with the QB-coverage. The clusters are homogeneously distributed on the surface. For the $2 \times 10^{15}\,\mathrm{molecule \cdot cm^{-2}}$ deposit (Figure II.2b)), the DIPO-Ph$_4$ layer now covers 55 % of the ITO surface. The 3D growth of slightly elongated mounds increases, and their average diameter is now 300 nm. Their average height increases to ∼30 nm. The molecular coverage deduced from the AFM image is $1.8 \times 10^{15}\,\mathrm{molecule \cdot cm^{-2}}$, also in agreement with the QB-coverage. Finally, for the "thickest" layer (Figure II.2c)), corresponding to a deposit of $10 \times 10^{15}\,\mathrm{molecule \cdot cm^{-2}}$ (QB-coverage), the film covers more than 95 % of the ITO surface and its average thickness is ∼50 nm. The AFM molecular coverage was

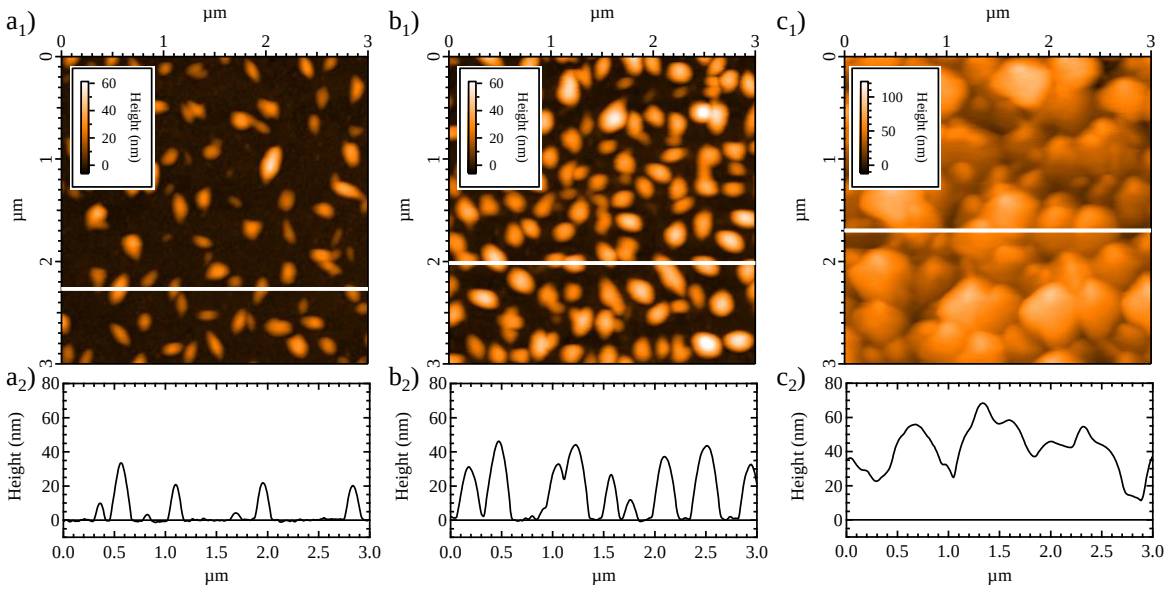

Figure II.2 – AFM images for DIPO-Ph_4: a_1) 0.5×10^{15} molecule $\cdot$ cm^{-2}; b_1) 2×10^{15} molecule $\cdot$ cm^{-2}; c_1) 10×10^{15} molecule $\cdot$ cm^{-2}; a_2), b_2), and c_2) are the corresponding profiles indicated by the white straight lines in a_1), b_1), and c_1) respectively. The molecular coverage, expressed in molecule $\cdot$ cm^{-2} (QB-coverage), is obtained from the quartz balance monitor.

estimated at 7.1×10^{15} molecule $\cdot$ cm^{-2} which is less than the QB-coverage. For this layer set, AFM measurements agree quite well with QB-coverages. An increasing error is observed with the increasing coverage, which may be due to an approximate QB parameter set up.

In the following, we will describe the growth mode. As presented in Chapter I.2.1, when layers are deposited over homogeneous substrates, like single crystals, three types of growth are classically considered. [62] The first one is the Franck Van der Merwe one which leads to a layer-by-layer growth. Our results show that this is not the case for the DIPO-Ph_4 layers. In the second one, the Volmer-Weber growth, the organic molecules clusters are islands, leaving bare substrate areas. That is what is seen for the DIPO-Ph_4-Ph layers. It arises from the fact that the interactions between molecules (π-stacking) is much stronger than the interaction between the DIPO-Ph_4 molecule and the ITO substrate. In the third mode, the Stranski-Krastanov growth, the molecule-molecule interaction competes with the molecule-substrate interaction. A thin wetting layer covers all the substrate, on top of which the 3D island growth mode takes place. If a Stranski-Krastanov mode stands, the wetting layer, if present, should not exceed $\sim$2 nm. The AFM resolution does not allow concluding in this section. Note that X-ray photoemission

spectroscopy will help us to conclude on the growth mode (see Chapter III.2.1).

For the DIPO-Ph$_4$ layers, as soon as deposited, islands are formed with an average height $> 10\,\text{nm}$. The molecule/interface is thus seen only at the island rings. To perform a deeper analysis, it would be interesting to decrease the average cluster height. We were also interested in increasing the material crystallization speed. To do so, we performed some thermal annealing treatments.

II.1.2 Access to the first deposited layer and to the crystallized material

Two kinds of treatment were performed:

- One after the evaporation, in ambient pressure condition at a temperature near the evaporation temperature of the DIPO-Ph$_4$ ($T \geq 170\,°\text{C}$) to perform some molecular desorption and access to the first deposited layers (ITO/DIPO-Ph$_4$ interface).
- One during the evaporation, *i.e.* evaporation on hot substrate ($T = 100\,°\text{C}$), to bring some energy to the system and increase the growth speed (thermodynamic equilibrium).

This study was performed while replacing the ITO substrate by a very thin (100 nm) nitride silicon (Si_3N_4) substrate. No cleaning treatment has been performed on these substrates before the molecular evaporation. The interface was then studied via XAS absorption measurements to determine the molecular orientation. AFM results are presented in Figure II.3.

First, it is important to notice that the layer morphology on a Si_3N_4 is similar to the one on ITO substrate (no thermal annealing, presented in Figure II.3). The un-annealed sample morphologies are the same as the ones presented in the previous section: slightly elongated clusters with an average height of 30 nm for the $1 \times 10^{15}\,\text{molecule} \cdot \text{cm}^{-2}$ sample. AFM-calculated coverages are $1.1 \times 10^{15}\,\text{molecule} \cdot \text{cm}^{-2}$ (25 % of the Si_3N_4 covered) and $11 \times 10^{15}\,\text{molecule} \cdot \text{cm}^{-2}$ for the 1×10^{15} and the $10 \times 10^{15}\,\text{molecule} \cdot \text{cm}^{-2}$ samples, respectively. A similar morphology between the two substrates may result from a similar surface energy.

After a post-annealing treatment at $T \geq 170\,°\text{C}$ on the $1 \times 10^{15}\,\text{molecule} \cdot \text{cm}^{-2}$ sample (post thermal annealing, presented in Figure II.3a)), the average height of the clusters decreases to 13 nm. The mounds still cover 20 % of the Si_3N_4 surface, with an average diameter of 230 nm. The molecular surface density calculated, from the AFM image, is divided by 3 ($0.3 \times 10^{15}\,\text{molecule} \cdot \text{cm}^{-2}$). The crystallization on a hot substrate (under thermal annealing, presented in Figure II.3a)) leads to the formation of twinned DIPO-Ph$_4$ structures that are more elongated than in the previous cases.

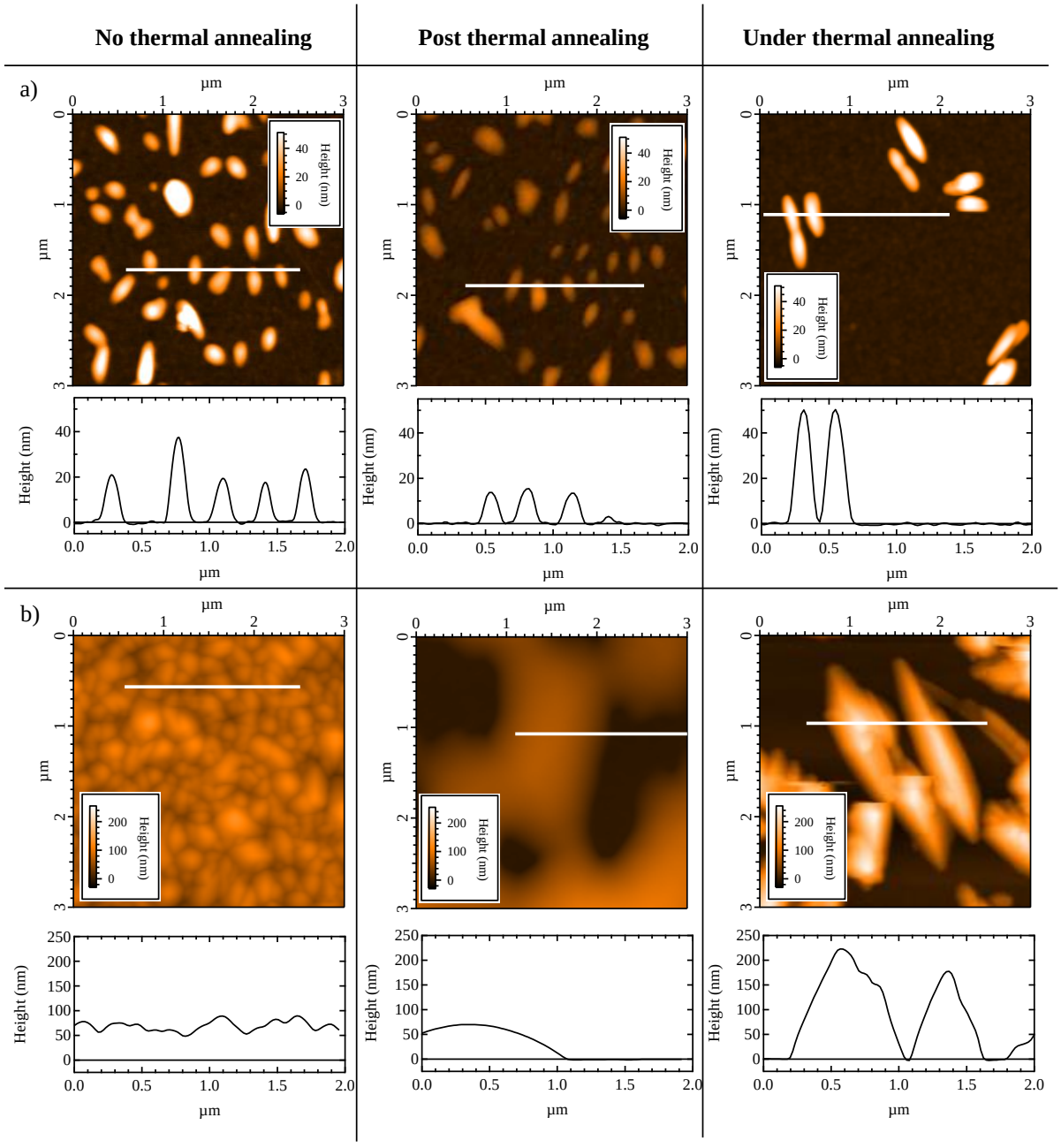

Figure II.3 – AFM images for DIPO-Ph$_4$: a) 1×10^{15} molecule $\cdot$ cm^{-2}; b) 10×10^{15} molecule $\cdot$ cm^{-2} deposited under no-thermal annealing, after a post-thermal annealing, and under a thermal annealing. The molecular coverage, expressed in molecule $\cdot$ cm^{-2} (QB-coverage), is obtained from the quartz balance measurement.

Concerning the 10×10^{15} molecule $\cdot$ cm^{-2} sample, after a post-annealing treatment (post thermal annealing, presented in Figure II.3b)), large islands are observed with an average step of 80 nm. The DIPO-Ph_4 layer does not cover the entire substrate. In the case of an under-annealing treatment (under thermal annealing, presented in Figure II.3b)), the twinned clusters continuously grow to form large molecular crystals on top of the Si_3N_4 substrate. During an under-annealing treatment, the energy brought via the hot substrate, changes the molecular growth by increasing the molecule diffusion on the surface.

In the case of well-separated 3D-clusters, post-annealing treatment leads to molecular desorption. This is the case for the 1×10^{15} molecule $\cdot$ cm^{-2}. The average height of the clusters decreases while the overall area coverage and the average cluster diameter stay constant. With such a treatment, we can access the first deposited layers which are representative of the initial stages of the evaporation. As far as the 10×10^{15} molecule $\cdot$ cm^{-2} sample is concerned, there is no homogeneous desorption as the intermolecular interaction compete with the desorption effect. In this case, the post-annealing treatment leads to the formation of large DIPO-Ph_4 islands which do not entirely cover the substrate. Note that, the 10×10^{15} molecule $\cdot$ cm^{-2} sample prepared under thermal annealing can be used as a reference sample for crystallized DIPO-Ph_4 structure.

II.2 Molecular orientation

II.2.1 Molecular description

To perform XAS spectroscopy, it is important to understand the electronic mechanisms which take place during the absorption process. Density functional theory (DFT) calculations were used to describe the empty molecular states (LUMOs) localized on the carbon and the oxygen atoms of DIPO-Ph_4 structure (Figure II.4). Furthermore, it was useful to visualize the concerned molecular orbital (MO) to obtain information on the molecular orientation. Indeed, to determine the molecular orientation inside the clusters, we must be sure that there is a MO with one main direction in the molecule geometry.

For C 1s transitions (Figure II.4a)), the lowest unoccupied molecular orbital (LUMO) and unoccupied MOs of higher energy (LUMO+1 to LUMO+6) are described via DFT calculations. LUMOs are mainly composed of π^* MOs which are perpendicular to the DIP core or to the phenyl (Ph) groups. They can be divided in 3 groups. The first one is centred at $\sim$0.3 eV above the LUMO and composed of LUMO, LUMOs +1, and +2. The second one is centred at 1.3 eV above the LUMO and composed of LUMOs +3 and +4. The last one is centred at 2.5 eV above the LUMO and is composed of LUMOs +5

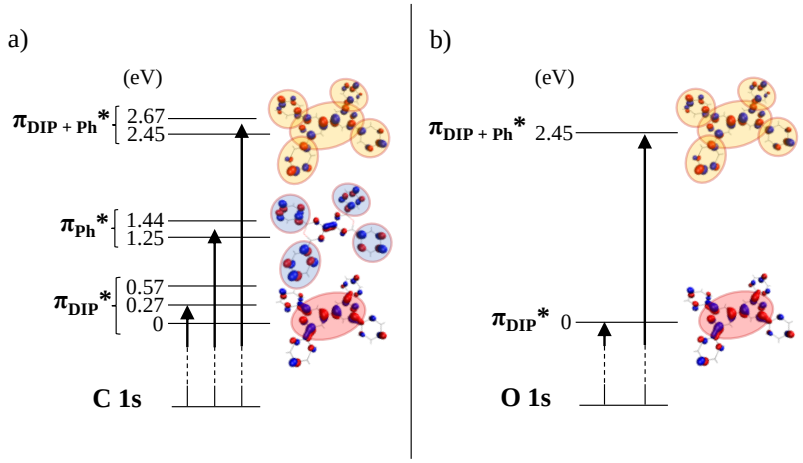

Figure II.4 – Electronic scheme of the a) C 1s and b) O 1s transition for DIPO-Ph$_4$. Indicated energies are related to the LUMO and three MOs are represented with an isovalue of 0.04 (LUMO, LUMO+3 and LUMO+5). The principal weight localization of the MOs is emphasized with ellipses.

and +6. Looking at the localization of these groups, it appears that the first one is more localized on the DIP core, whereas the second one is more localized on the Ph groups. For the last one, the MOs are localized, with the same weight, on the DIP core and on the Ph groups. These three groups will be now called π^*_{DIP}, π^*_{Ph}, and $\pi^*_{\text{DIP+Ph}}$. Concerning the O 1s transitions (Figure II.4b)), there are two main transitions as only LUMO and LUMO+5 are localized on O atoms.

The geometry of the free molecule was previously described: four Ph groups almost parallel to the DIP core. Consequently, there is one main plane following the DIP core and four other planes following each of the four Ph groups. Thus, for the π^*_{DIP} MOs there is one main direction which is perpendicular to the DIP core. On the contrary, for the π^*_{Ph} MOs, there is no main direction. Finally, the $\pi^*_{\text{DIP+Ph}}$ MOs have no main orientation because they are localized both on the DIP core and on the Ph groups.

In the following, we will describe the absorption transition. The X-ray absorption results in the electron transition from the core level to the empty state. Thus, the absorption efficiency depends on the energy level of the empty states. It will also rely on the relative geometry between the electrical component of the X-ray beam and the direction of the MOs. Therefore, for the DIPO-Ph$_4$ structure, the absorption will be high if the polarization is parallel to the π^*_{DIP}, *i.e.* perpendicular to the molecule. In other terms, with an X-ray beam normal to the surface (polarization parallel to the surface) there will be a high absorption at π^*_{DIP} energy if DIPO-Ph$_4$ molecules are perpendicular to the surface (π^*_{DIP} parallel to the surface).

II.2.2 Absorption spectroscopy

Thanks to absorption spectroscopy we saw that we can access the molecular orientation inside the layer. Such information will be important to know, as a good crystallization can lead to a better charge conduction. In this context, we can stress upon the significance of an adapted characterization tool, such as scanning transmission X-ray microscopy (STXM) that has the potential to disentangle molecular domain orientation information in thin films. [80] STXM, and other synchrotron based soft X-ray characterization tools, such as resonant soft X-ray scattering, are already been widely used in conjunction with other laboratory based techniques to investigate the complex morphology of organic devices. [81, 82, 83, 84, 85, 86, 87]

Absorption analyses were performed at the PolLux beamline (SLS synchrotron) on 4 samples (Appendix B.3.2):

- Sample A: $1 \times 10^{15}\,\text{molecule} \cdot \text{cm}^{-2}$ QB-coverage with no thermal treatment.
- Sample B: $1 \times 10^{15}\,\text{molecule} \cdot \text{cm}^{-2}$ QB-coverage with a post-annealing treatment.
- Sample C: $10 \times 10^{15}\,\text{molecule} \cdot \text{cm}^{-2}$ QB-coverage with no thermal treatment.
- Sample D: $10 \times 10^{15}\,\text{molecule} \cdot \text{cm}^{-2}$ QB-coverage with an under-annealing treatment.

The STXM results have been used to confirm the thickness of the layers (using Equation) and thus to confirm the AFM results.

The obtained image at $h\nu = 285\,\text{eV}$, corresponding to the maximum absorption at the C-K edge, is extracted from the $[X;Y;h\nu]$ image stack to obtain the optical density (OD) images ($[X;Y]$) at 285 eV. This image is used to calculate the corresponding thickness using (Equation (I.3)). In Figure II.5, images are STXM images obtained from the absorption measurements, but are presented in the same way as AFM images for comparison purpose.

For the Sample A, the STXM image shows slightly elongated clusters with an average height of 30 nm. This agrees with the AFM results. There is also a great agreement between the STXM and the AFM images for the Sample C (no thermal annealing in Figure II.5a) and b)). For the post-annealed sample (Sample B), STXM image (post thermal annealing in Figure II.5a)) shows clusters with an average height of ∼10 nm, which was already seen in the AFM image. Finally, we also have the same conclusion for the under-annealing treatment sample (Sample D) where the average cluster height is found to be 250 nm and the morphology is as large molecular crystallized cluster (under

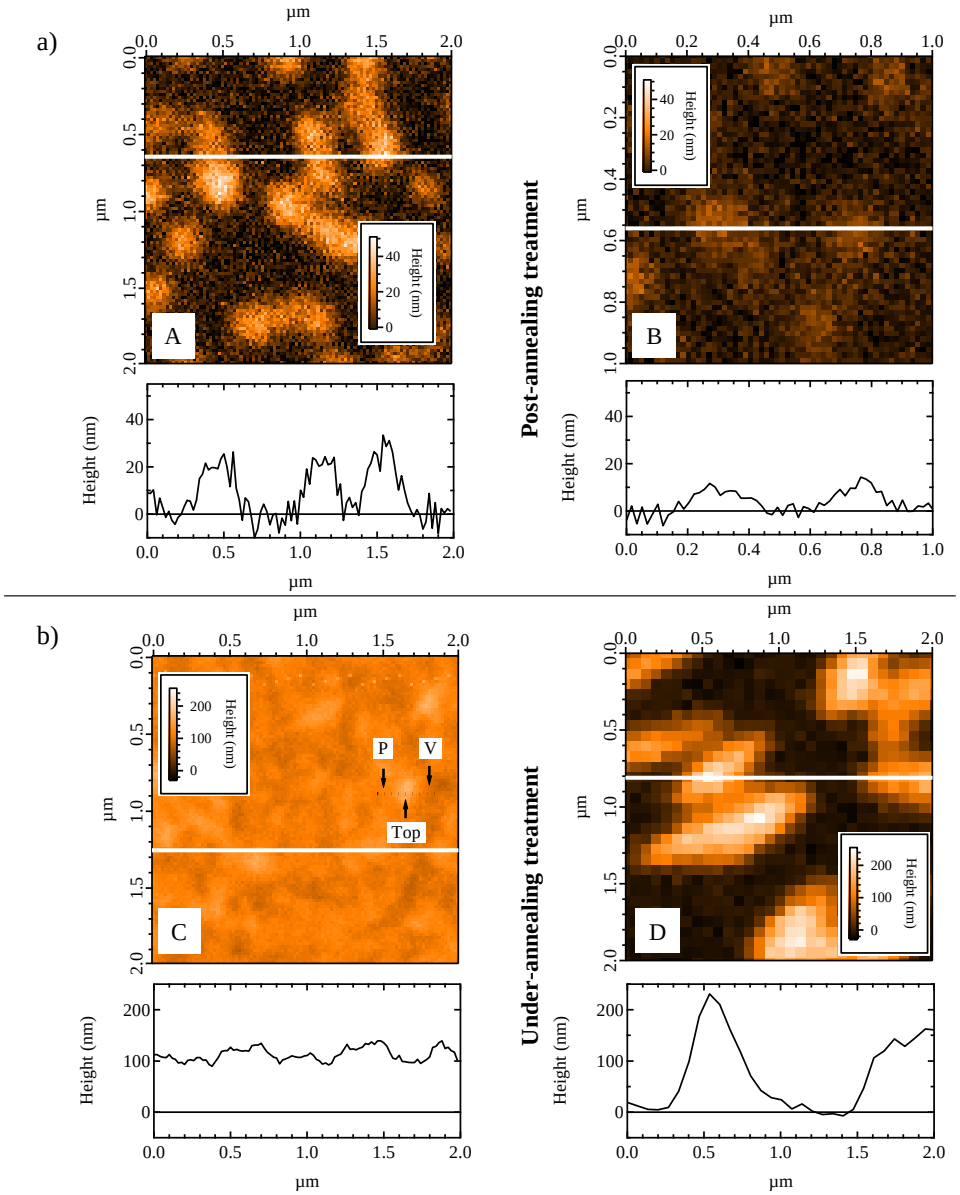

Figure II.5 – STXM images for DIPO-Ph$_4$: a) 1×10^{15} molecule $\cdot$ cm^{-2} (Samples A & B); b) 10×10^{15} molecule $\cdot$ cm^{-2} (Samples C & D); for A & C: no thermal annealing; for B: post thermal annealing and for C: under thermal annealing. The molecular coverage, expressed in molecule $\cdot$ cm^{-2} (QB-coverage), is obtained from the quartz balance measurement. The dotted line for Sample C indicates the position for the absorption linescan.

II.2 Molecular orientation

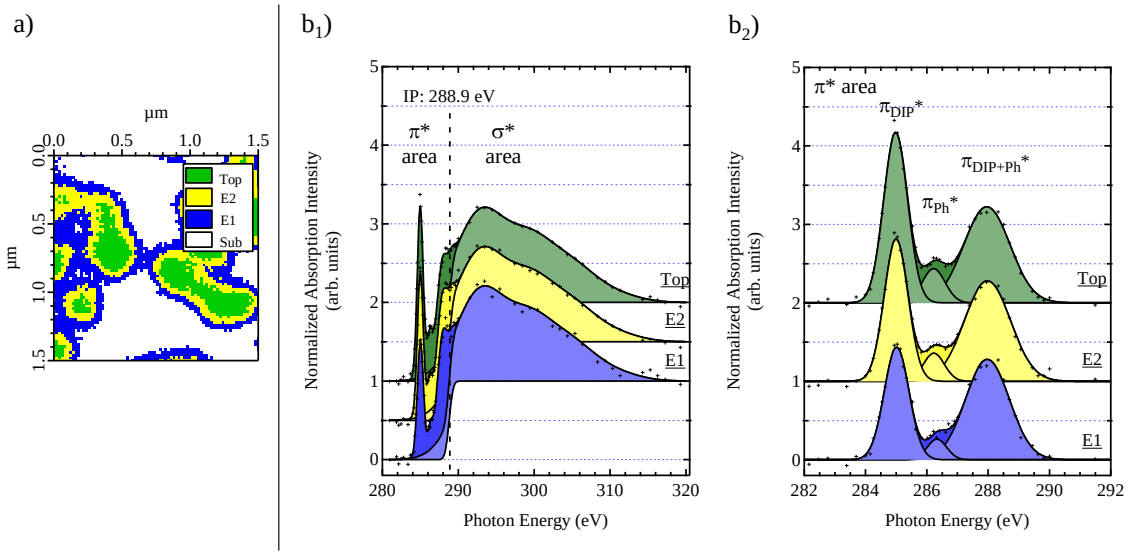

Figure II.6 – Sample A: a) STXM decomposition mapping; b_1) Absorption spectra extracted for each region (the substrate (Sub) spectrum is not represented as there is no absorption from this region); b_2) π^* area after subtraction of the step function background and the σ^* area.

thermal annealing in Figure II.5b)). $[X;Y]$ STXM analyses are in great agreement with AFM results.

Further investigations of the $[X;Y;h\nu]$ stacks were performed with respect to the photon energy related variation (spectroscopy). Using principal component analyses (PCA), we determined the main components (absorption spectra) of the stacks. Then, the first four principal components have been used to decompose the STXM stacks in four main regions. For each region, the absorption spectra were then extracted. These spectra are the average one for the found regions. After normalization, spectra have been fitted as described in the Appendix B.5.1. The potential ionization ($IP = 288.9\,\text{eV}$) value was determined from the XPS C 1s binding energy and the measurement from the work function (see next section, Chapter III.2). Results for Sample A are presented in Figure II.6 and Table II.1.

The decomposition of the $[X;Y;h\nu]$ stack for Sample A (Figure II.6a)) leads to four regions precisely localized on the sample. The main region is the one localized between the organic clusters. There is no absorption (or at least too low to be detected with the STXM thickness resolution). This corresponds to the response from the substrate. The organic mounds are decomposed in three regions: one at the top and two on the edge. These regions will now be named Top, E2, and E1 respectively.

Absorption spectra have been extracted for these regions and edge-jump normalized

Table II.1 – Experimental π^* transitions, FWHM of the Gaussian contribution and π^*/σ^* ratio from Figure II.6, Figure II.8, and Figure II.9. For Sample B there were not enough signals to determine π^*_{Ph} contribution.

Sample /region		Energy (eV)			G-FWHM (eV)			π^*/σ^* (%)			
		π^*_{DIP}	π^*_{Ph}	π^*_{DIP+Ph}	π^*_{DIP}	π^*_{Ph}	π^*_{DIP+Ph}	π^*_{DIP}	π^*_{Ph}	π^*_{DIP+Ph}	$\sum$
A	Top	284.98	286.22	287.96	0.92	0.88	1.77	11	2	12	26
	E2	285.00	286.23	287.98	0.92	0.81	1.76	10	2	13	24
	E1	285.01	286.33	287.97	0.95	0.75	1.68	8	1	12	21
A' tilted	Top	284.96	286.22	288.02	0.87	1.00	1.89	12	3	15	30
	E2	284.98	286.22	288.03	0.87	0.75	1.91	11	2	16	29
	E1	284.97	286.16	288.07	0.84	1.17	1.80	9	3	15	28
B' tilted	Top	284.94	_	287.74	0.93	_	2.10	6	_	5	11
	E	284.95	_	287.58	0.93	_	1.34	4	_	3	7

for comparison (Figure II.6b$_1$)). A clear distinction of the π^* and the σ^* regions is evident in the figure. After subtraction of the background and the σ^* region, the π^* region is emphasized in Figure II.6b$_2$) for clarity. It has been fitted with three Gaussian curves (G-FWHM values are indicated in Table II.1). The first one, entered at $\sim$ 285 eV is attributed to the first transition group π^*_{DIP}. π^*_{Ph} is at $\sim$286 eV, and π^*_{DIP+Ph} is centred at $\sim$288 eV. DFT calculations for a free molecule gives a $\pi^*_{Ph} - \pi^*_{DIP}$ of $\sim$1.3 eV and a $\pi^*_{DIP+Ph} - \pi^*_{DIP}$ of $\sim$2.3 eV (see Figure II.4a)). Experimentally, the value of the $\pi^*_{Ph} - \pi^*_{DIP}$ is $\sim$1.2 eV, which is very close to the theoretical calculation. For the π^*_{DIP+Ph} transition, the difference with the π^*_{DIP} is $\sim$3 eV. This value is 1 eV higher than the theoretical one. More LUMOs than the 2 calculated ones (+5 and +6) must thus participate to the π^*_{DIP+Ph} transition.

In the absorption spectra, we also focused on the contribution of the π^* transition in comparison to the σ^* one (Table II.1). The intensity of the σ^* transition remains identical between spectra extracted from Top to E1 regions. This intensity was used as a reference to evaluate the π^* transition in the different regions. The π^*/σ^* ratio decreases from Top to E1 (from 26 % to 21 %). This evolution is mainly due to a decrease of the π^*_{DIP} transition (from 11 % to 8 %). This transition is the only one which can be used to access the molecular orientation. Thus, in the organic layer, there is an evolution in this orientation from the edge to the top of the cluster. In the latter (top region), molecules are perpendicularly oriented to a higher degree than in the edge. This implies a change in the orientation between the layer near the substrate and the top layers.

The analysis of the post-annealed sample (Sample B) could allow us to extract information on the first evaporated layers. Unfortunately, the small amount of organic

II.2 Molecular orientation

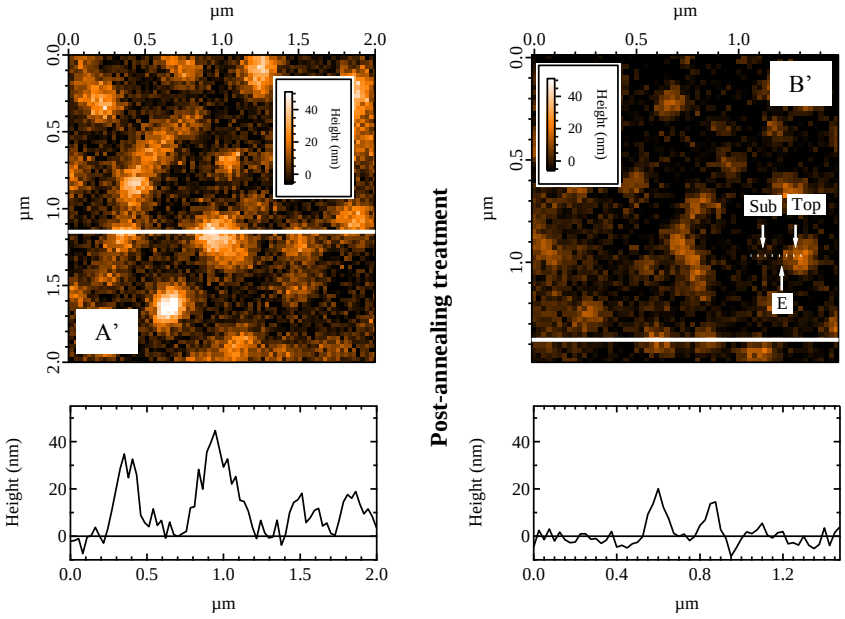

Figure II.7 – STXM images for 1×10^{15} molecule $\cdot$ cm^{-2} DIPO-Ph$_4$ with a 30° tilted angle (A': no thermal annealing; B': post thermal annealing). The molecular coverage, expressed in molecule $\cdot$ cm^{-2} (QB-coverage), is obtained from the quartz balance measurement. The dotted line for Sample B' indicates the position for the absorption linescan.

material in this sample makes the analysis harder, due to a weak signal at normal X-ray incidence. To overcome this issue, we tilted the sample (30° between the normal and the sample surface). To limit beam damage, we only performed a linescan along the organic clusters (see Figure II.7). From this line, we extracted the edge (E) and Top spectra. The values of the π^* transitions are given in Table II.1. To compare the two samples, we performed the same tilted incidence angle experiments on Sample A. Results are presented in Figure II.7, Figure II.8, and Figure II.9.

From the thickness STXM images of Sample A and B with a tilted X-ray incidence angle (A' & B'), we observe that 3D clusters appear with a bigger average height: 40 nm and 20 nm, for A' and B', respectively. Indeed, in this case there is a bigger depth penetration in the molecular material. It results in a bigger absorption which leads to an increase of the apparent thickness.

The analysis of Sample A analysis with the tilted incidence angle leads to the same results as with the normal incidence angle (see Table II.1). There are no big changes from the previous results as we chose a small tilt angle.

For Sample B, the σ^* transition is much higher than in Sample A, and a decrease from the top to the edge of the π^* is also observed (from 11 % to 7 %). The change from edge

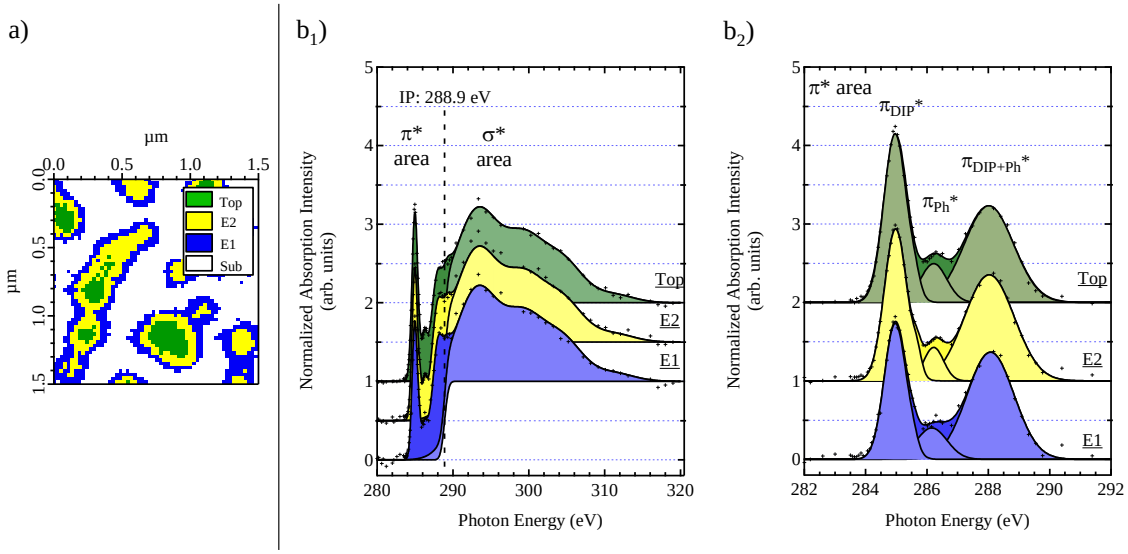

Figure II.8 – Sample A': a) STXM decomposition mapping; b$_1$) Absorption spectra extracted for each region (the substrate (Sub) spectrum is not represented as there is no absorption from this region); b$_2$) π^* area after subtraction of the step function background and the σ^* area.

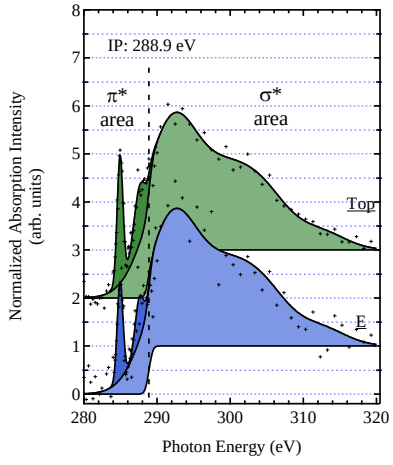

Figure II.9 – Sample B': Absorption spectra extracted for the top and the edge region (the substrate (Sub) spectrum is not represented as there is no absorption from this region).

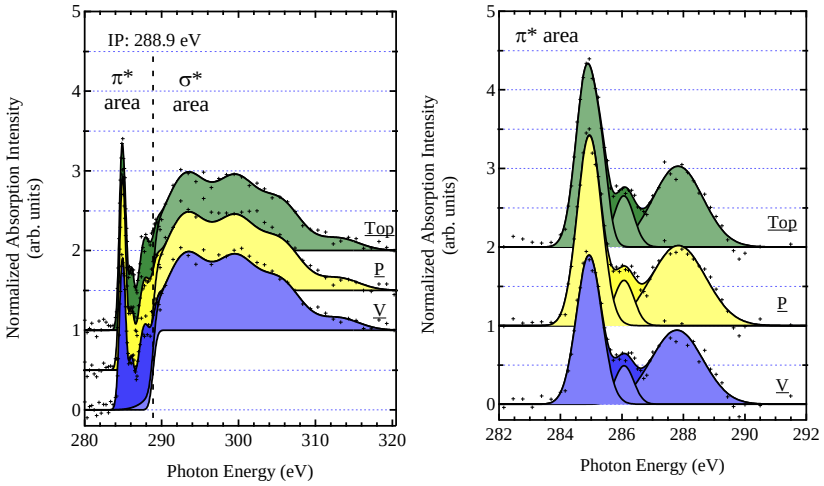

Figure II.10 – Sample C: Absorption spectra extracted for the top, plateau, and valley areas. π^* area after subtraction of the step function background and the σ^* area. (P and V referred to the points on the dotted line in STXM images Figure II.5b)).

to top agrees with the change of molecular orientation inside the organic cluster. Besides, the high σ^* transition results from the several DIPO-Ph_4 molecules that are parallel to the surface.

Therefore, at the beginning of the evaporation on substrates kept at room temperature, molecules remain parallel to the substrate. Substrate-molecule interactions are minimized in this configuration. In this case, there is a small π^* absorption and a greater σ^* absorption. After a few layers, molecules start to straighten and crystallize, driven by the π-stacking interaction. There is a change in the molecular orientation resulting in an increase of the π^* absorption. The edges of the mounds reflect this change, as they are close to the first deposited layers. Besides, crystallization leads to molecular orientation as described in Figure I.7a). It shows that molecules are not all parallel to each other: they are V-shaped. Consequently, σ^* transition is still present and the Top absorption spectrum is equivalent to that of the crystallized organic material.

To pursue the analysis, we performed the experiments on the 10×10^{15} molecule $\cdot$ cm^{-2} QB-coverage (Sample C). Linescan was performed across a high cluster and results are presented in Figure II.10. Points P and V are localized respectively on a plateau and on a valley, as depicted in STXM image (Figure II.5b)) along the dotted line.

In this sample, π^* absorption is greater at the Top and on the plateau (P). However, in a valley (V), the π^* absorption decreases from 30 % to 26 %. This confirms the change of morphology.

Let us focus now on Sample D to get the absorption spectra of a crystallized cluster.

Table II.2 – Experimental π^*/σ^* ratio from Figure II.10 and Figure II.11.

Sample /region		π^*/σ^* (%)			
		π^*_{DIP}	π^*_{Ph}	π^*_{DIP+Ph}	$\sum$
C	Top	14	3	12	30
	P	14	3	13	30
	V	12	2	12	26
D	Top	12	4	11	27
	E2	11	4	10	26
	E1	13	4	11	29

The absorption spectra were obtained following a similar treatment than Sample A (PCA). As there is a better energy resolution due to a better absorption, spectra have been fitted with more structures related to the LUMOs. Results are presented in Figure II.11 and in Table II.2.

For Sample D, there is no difference between the edge and the top of the organic mounds. The π^* transition is as high as that of the Top region of the not-annealed sample (27–29 %), with a π^*_{DIP} which remains high (11–13 %). The mounds are totally

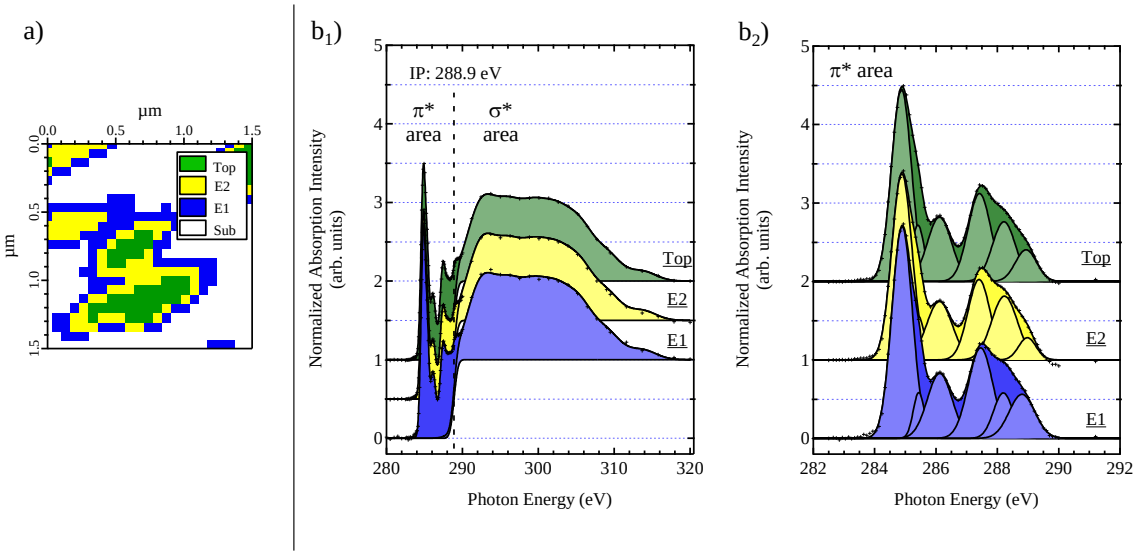

Figure II.11 – Sample D: a) STXM decomposition mapping; b_1) Absorption spectra extracted for each region (the substrate (Sub) spectrum is not represented as there is no absorption from this region); b_2) π^* area after subtraction of the step function background and the σ^* area.

II.2 Molecular orientation

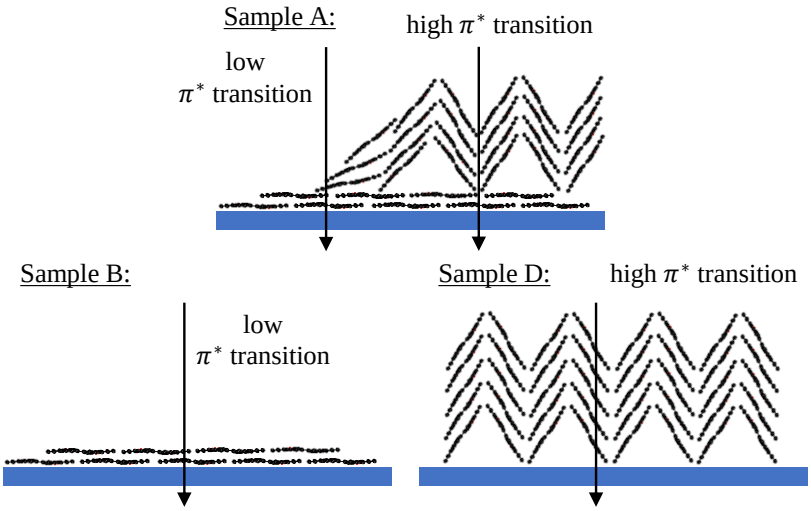

Figure II.12 – Schematic representation of the molecular orientation for Samples A, B & D.

crystallized from the first deposited layers. The substrate temperature brings enough energy to start crystallization and overcome molecule-substrate interaction. We present in Figure II.12, the schematic molecular orientation inside the organic cluster.

With these samples, we obtained two opposed molecular orientations: one which present parallel molecules on top of the surface (Sample B) and another in which the organic mounds are directly crystallized as soon as deposited on the substrate (Sample D). We are thus able to tailor the molecular orientation thanks to the evaporation conditions. With the perspective of organic electronics, it is important to control the morphology and the molecular orientation to enhance, for example, the charge mobility through the organic layer.

We assume that on ITO, the same observation would be seen. Indeed, the surface energy between an oxide and an air exposed silicon nitride must be similar. To verify this hypothesis, STXM experiments on Si_3N_4/ITO/DIPO-Ph_4 samples have been planned but the proposal was not yet accepted.

Chapter III

ITO/DIPO-Ph_4 interface: energy level alignment and exciton lifetime description

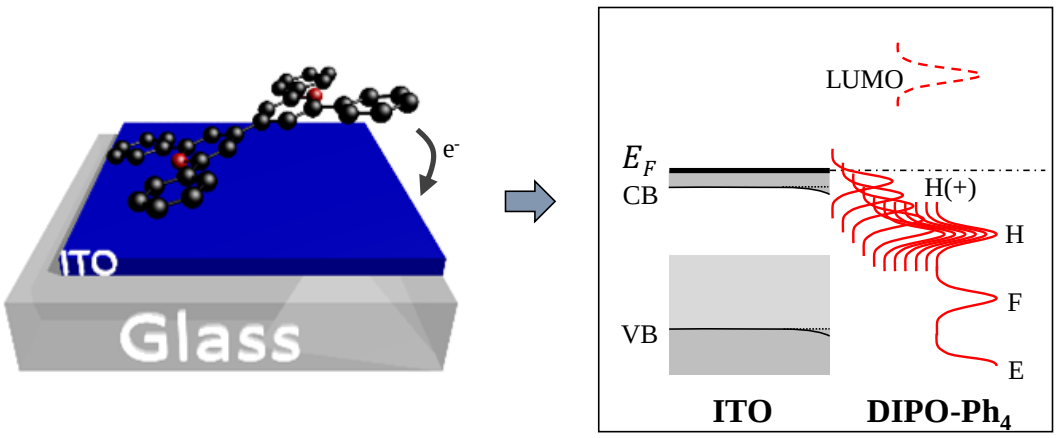

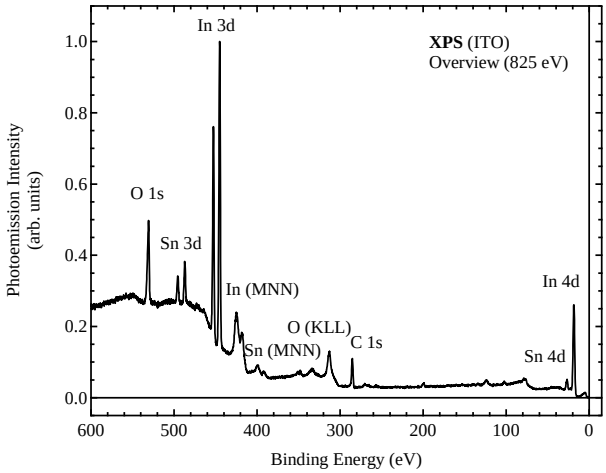

Figure III.1 – ITO overview spectrum for $h\nu = 825\,\text{eV}$. The labels refer to the core levels peak and In (MNN), Sn (MNN), and O (KLL) refer to the Auger decays.

III.1 ITO characterization

It is important to fully characterize and confirm the electronic properties of ITO substrate: it must be metallic with a partially filled CB. For this measurement, the ITO substrate has been cleaned right before its introduction in the analyse chamber of the TEMPO beamline (Appendix B.3.3 and Appendix B.5.2).

III.1.1 Electronic properties

The ITO XPS overview (Figure III.1) shows all the different core levels that can be analysed. The C 1s peak due to carbon contamination is small in comparison with the indium peak. We will further discuss this point in the study of the ITO/DIPO-Ph$_4$ interface.

The In $3d_{5/2}$ spectra of the bare, chemically cleaned surface are presented in Figure III.2a). To reach "surface sensitive" conditions, a photon energy of 600 eV is used, corresponding to a photoelectron kinetic energy (KE) of ∼155 eV and a calculated IMFP λ_{ITO} of ∼0.56 nm (see Figure I.16). More "bulk sensitive" conditions are obtained with photons of energy 825 eV, corresponding to a photoelectron KE of ∼380 eV and a λ_{ITO} ∼0.92 nm. Both spectra present an asymmetry towards higher binding energy (BE), but the spectrum measured in more 'bulk sensitive" conditions at $h\nu = 825\,\text{eV}$ is more asymmetric. This indicates that the electronic structure changes from the surface to the inner layers. The observed asymmetry is related to the electronic structure of the material and not to surface contamination. Indeed the In 3d spectra, unlike the O 1s ones, are not

III.1 ITO characterization

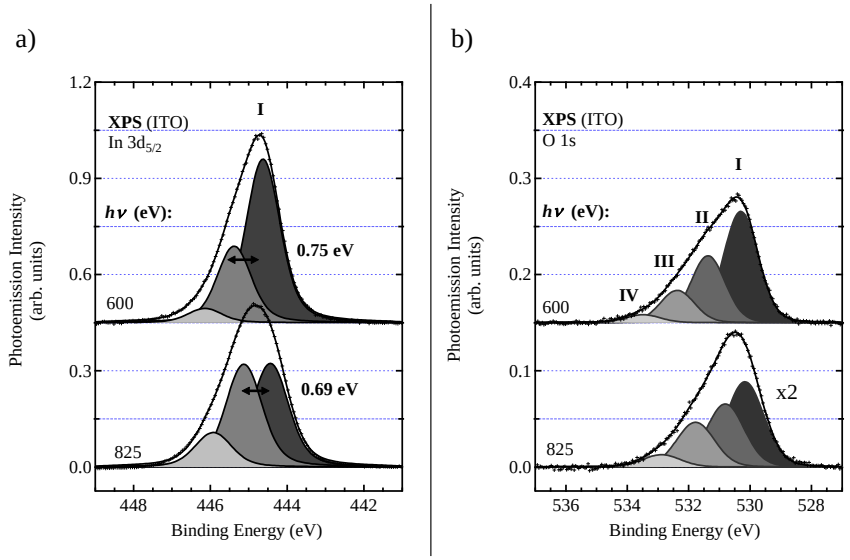

Figure III.2 – a) In $3d_{5/2}$; b) O 1s spectra of the chemically cleaned ITO sample. The photon energy is indicated. The spectra were recorded at the TEMPO beamline.

sensitive to adsorbed species. [88] The attribution of the observed asymmetry to plasmon losses has now gained wide acceptance. [38, 89] The plasmon frequencies (below 1 eV) in ITO are significantly smaller than that of classical metals, due to the lower electron density. Fitting procedures, however, differ according to authors. Christou *et al.* [89] and Körber *et al.* [52] fit the In $3d_{5/2}$ spectrum with two Voigt components. The Voigtian is a weighted sum of a Gaussian and of a Lorentzian (the Lorentzian fraction as a free parameter), the low binding energy component being prevalently Gaussian. On the other hand, Gassenbauer *et al.* [46] use three Voigt functions, constrained to have the same width and the same Gaussian/Lorentzian ratio, one main peak and two plasmon losses ($\hbar\omega_p$ and $2\hbar\omega_p$). Naturally the value of $\hbar\omega_p$ depends on the procedure. Here we adopt the same procedure as that used by Gassenbauer *et al.*, [46] *i.e.* a fit with three Voigt components of equal widths (Table III.1), corresponding to the well-screened peak (at lower BE) and to the first and second plasmon peaks.

The fact that the first plasmon peak intensity increases in more bulk sensitive conditions, can be related to a decrease in the carrier concentration n within the bulk layers. [38] This should be accompanied by a reduction of the plasmon energy, which is indeed observed ($\hbar\omega_p$ decreases from 0.75 eV to 0.69 eV). Note that an increased doping at the surface, leading to a higher carrier concentration, may be related to the segregation of Sn at the surface.

The O 1s core-level spectra of the chemically cleaned bare ITO surface (Figure III.2b)) are measured at $h\nu = 825$ eV (KE O 1s ~295 eV, λ_{ITO} ~0.79 nm) and at $h\nu = 600$ eV (KE

Table III.1 – Experimental In $3d_{5/2}$ and O 1s principal peak value, FWHM of the Gaussian contribution and plasmon structure from the spectra given in Figure III.2.

Core level	Photon Energy	G-FWHM	Peak I BE (eV)	$\hbar\omega_p$ (eV)
In $3d_{5/2}$	825 eV	0.907 eV	444.44	0.69
	600 eV	0.837 eV	444.63	0.75
O 1s	825 eV	1.370 eV	530.17	0.64
	600 eV	1.239 eV	530.30	1.07

O 1s ~70 eV, λ_{ITO} ~0.47 nm). In both cases, spectra are fitted with four components of equal widths. In more bulk sensitive conditions ($h\nu = 825$ eV) the BE of peak I (42 % of the spectra weight), II (31 %), III (22 %), and IV (6 %) are 530.17 eV, 530.81 eV, 531.78 eV and 532.89 eV, respectively. Peak II (0.6 eV from peak I) can be attributed to a plasmon loss, as also observed in the In $3d_{5/2}$ spectra (Figure III.2a)). Peak III (1.6 eV from peak I) could correspond to the second plasmon loss or to organic contamination. [90] Finally peak IV may be attributable to surface hydroxyls, that are expected in the range 532.5 – 532.9 eV. [88, 90] In more surface sensitive conditions ($h\nu = 600$ eV), peaks I (51 %), II (31 %), III (15 %), and IV (3 %) are found at 530.30, 531.38, 532.37, and 533.48 eV, respectively. The second observation is the increased BE shift (1.07 eV instead of 0.75 eV) between peak I and peak II. This is reminiscent of what is observed for the plasmon loss energy in the In $3d_{5/2}$ spectra that is greater at the surface than in the bulk. However, 1.07 eV is a too large value for the plasmon energy. It is likely that peak II encompasses both the plasmon peak and a component due to defects (*e.g.* suboxides [90]), the latter being more abundant at the surface. Surface contamination by oxygenated species can be estimated from the atomic ratio $r_{O/In}$ (λ_{ITO} ~0.47 – 0.56 nm). The latter is calculated from O 1s intensity and In 3d at $h\nu = 600$ eV, corrected from cross-section variations. $r_{O/In}$ is ~1.8, very close to 1.7, the value expected for the In_2O_3 stoichiometry. This indicates that the contribution of the oxygen contamination is small.

III.1.2 Carrier concentration

The In 3d peak highlights that there would be a tin segregation at ITO surface. As the carrier concentration depends on the Sn doping, it is crucial to probe a possible in-depth variation of the Sn concentration (see Ref. 46). We present Sn 4d and In 4d spectra of the chemically cleaned samples recorded at different photon energies, 60, 825, and 1486.6 eV (Figure III.3), corresponding to calculated λ values of ~0.5 nm, ~1.5 nm, and ~2.5 nm respectively, see Ref. 75.

III.1 ITO characterization

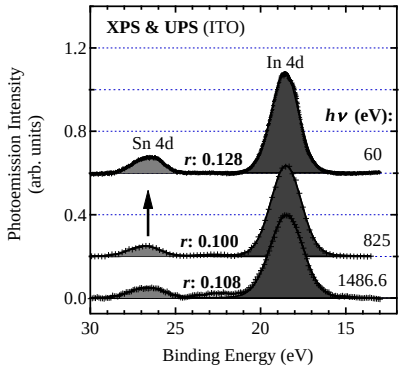

Figure III.3 – Sn 4d and In 4d spectra of the chemically cleaned ITO substrate. The photon energies were 60 and 825 eV (TEMPO beamline). A spectrum was also recorded with a non-monochromatized laboratory X-ray source Al (Al K_α 1486.6 eV) at the LCPMR (the contribution of the Al $K_{\alpha_{3,4}}$), satellites is suppressed).

Table III.2 – Experimental Sn 4d/In 4d intensity ratios from the spectra given in Figure III.3 and calculated atomic ratio. The calculated inelastic mean free paths (λ_{ITO}) are also given. A Synchrotron source and a non-monochromatized Al K_α source (the contribution of the Al $K_{\alpha_{3,4}}$) satellites is suppressed).

Photon Energy	λ_{ITO} **(nm)**	$I_{Sn/In}$	$r_{Sn/In}$
60 eV	0.5	0.164	0.128
825 eV	1.5	0.115	0.100
1486.6 eV	3.0	0.127	0.108

The In 4d and Sn 4d peaks, found at 18.5 eV and 26.5 eV respectively, flank a smaller peak at 22.5 eV (hardly visible at $h\nu = 60$ eV) attributed to O 2s, considering the local density of state (LDOS) given in Ref. 91. The O 2s contribution cannot affect the measurement of the Sn/In atomic ratio $r_{Sn/In}$) for two reasons: (i) the calculated photoemission cross-section [92] ratio $\sigma_{In\ 4d}/\sigma_{O\ 2p}$ is 34 at $h\nu = 60$ eV and 16 for photon energies of 825 eV and 1486.6 eV; (ii) the admixture of O 2s states with the In 4d level is almost negligible judging from the LDOS given in Ref. 91. Taking into account the photon energy variation of the cross-sections and asymmetry parameters of In 4d and Sn 4d, [92] we have calculated the $r_{Sn/In}$ values reported in Table III 2.

For the chemically cleaned ITO, we find a value of 0.100 – 0.108 in surface sensitive conditions ($h\nu \geq 825$ eV), in excellent agreement with the $r_{Sn/In}$ value of 0.102 calculated

for tin oxide weight of 10 % in indium oxide. The higher $r_{\mathrm{Sn/In}}$ value of 0.128 obtained in surface sensitive conditions ($h\nu = 60\,\mathrm{eV}$), indicates Sn segregation at the substrate surface. This segregation was already reported by Gassenbauer. [46]

An estimate of the charge carrier concentration n of the chemically cleaned sample can be deduced from the plasmon energy $\hbar\omega_p$: [93]

$$n = \frac{\hbar{\omega_p}^2 \epsilon_0 \epsilon_\infty m_c^*}{e^2}$$

where m_c^* is the reduced mass of the electrons localized in the CB ($0.35 m_{e^-}$ with m_{e^-} electron mass [38, 89]), ϵ_0 the vacuum permittivity, ϵ_∞ the relative dielectric constant at high frequency (∼4) [38, 89] and e the elementary charge. The $\hbar\omega_p$ value of 0.69 eV leads to a concentration of charge carrier of about $4 \times 10^{20}\,\mathrm{cm}^{-3}$ at the surface. This value is an order of magnitude smaller than the Sn concentration of $4 \times 10^{21}\,\mathrm{cm}^{-3}$. This is usually explained by the fact that Sn-donors can form neutral clusters with oxygen interstitial acceptors. [51] As a complement, from the concentration value, we calculated the difference between the Fermi level and the conduction band minimum (E_{CBm}):

$$E_F - E_{\mathrm{CBm}} = \frac{\hbar^2}{2m_{vc}^*}\left(3\pi^2 n\right)^{\frac{2}{3}}$$

where:

$$\frac{1}{m_{vc}^*} = \frac{1}{m_v^*} + \frac{1}{m_c^*}$$
$$(m_{vc}^* = 0.55 m_{e^-})$$

The magnitude of the shift depends on both m_c^* and m_v^* (reduced mass of the electrons localized in the VB). Note that in that case, m_v^* is negative, i.e. the valence band shows upward rather than downward dispersion. However, this analysis ignores the fact that doping leads to a shrinkage or renormalization of the gap between the bottom of the conduction band and the top of the valence band. [94, 95] The Fermi level is found to be 0.3 eV above the minimum of the CB. As the magnitude of the shift of the valence band edge in a photoemission experiment depends only on m_c^*, the measurement of the valence spectra at Fermi level will give a higher value. [38, 78]

III.1.3 Electron energy level scheme

The valence band spectra of the chemically cleaned ITO substrate measured at a photon energy of 60 eV is presented in Figure III.4a), corresponding to a short IMFP λ_{ITO} of ∼0.5 nm. Valence spectroscopy measures the LDOS weighted by the photoemission cross-sections of the O 2p, In 4d, In 5s, and In 5p levels, $\sigma_{\mathrm{O\ 2p}}$, $\sigma_{\mathrm{In\ 4d}}$, $\sigma_{\mathrm{In\ 5s}}$, and $\sigma_{\mathrm{In\ 5p}}$,

respectively. One should note that at $h\nu = 60\,\text{eV}$ the calculated ratios $\sigma_{\text{In 4d}}/\sigma_{\text{O 2p}}$, $\sigma_{\text{In 5s}}/\sigma_{\text{O 2p}}$, $\sigma_{\text{In 5p}}/\sigma_{\text{O 2p}}$ are 8.3, 3.1×10^{-2}, 4.8×10^{-3}, respectively. DFT calculations of the local density of states for In_2O_3 in bixbyite structure indicates that the top of the valence band is mainly constituted of O 2p related states, with some admixture (13 %) of In 4d states. [52, 91]

From the valence band edge, at a BE about 3 eV, a "tail" extends into the oxide gap. The origin of these gap states, that we observe up to about 1.2 eV (see Figure III.4a)) is yet unclear: mixed 5s/5p states of surface In^+ lone pairs on the one hand, bulk oxygen vacancies and oxygen interstitials on the other hand. [38, 48, 96] The valence band maximum energy (E_{VBM}) can be determined by fitting the valence band with two broad Gaussians, one representing the O 2p valence band edge and one the gap states, [46] see Figure III.4a). A value of 3.14 eV for the O 2p E_{VBM} is determined. A comparison with the UPS and XPS measurements made by Gassenbauer *et al.* is relevant for the discussion on the band level scheme. The E_{VBM} value we find is bracketed between an E_{VBM} of 3.54 eV for a magnetron-deposited reduced film (sputtering in argon, emission at Fermi level) and an E_{VBM} of 2.94 eV for a film grown in more oxidative conditions (sputtering in 1 % O_2/Ar, no emission at Fermi level). [46] With an E_G value of ∼2.8 eV, the $E_F - E_{\text{VBM}}$ in the range 3.0 – 3.2 eV points to a Fermi level in the conduction band. This is consistent with the In $3d_{5/2}$ peak maximum at 444.63 eV that falls in between that of the film sputtered in pure Ar (444.93 eV, emission at Fermi level) and the one sputtered in the 1 % O_2/Ar mixture (444.63 eV, no emission at Fermi level). Therefore, the In 5s states forming the conduction band should be occupied, considering the small E_G value that is now adopted. At $h\nu = 60\,\text{eV}$ (Figure III.4a)), we see an extremely weak photoemission signal at the Fermi level due to the low $\sigma_{\text{In 5s}}/\sigma_{\text{O 2p}}$ ratio. We only see an appreciable density of state at E_F when $h\nu$ is equal to 850 eV (Figure III.4b)), confirming the metallicity of the substrate. Cross sections decrease dramatically with increasing photon energy; we can thus anticipate a higher difficulty to probe conduction band states at higher photon energies. However, the cross section for In 5s states (and to a lesser extent In 5p and In 4d states) decreases much less rapidly than the cross section for O 2p states with increasing photon energy. At 850 eV the $\sigma_{\text{In 5s}}/\sigma_{\text{O 2p}}$ ratio is 1.5. Consequently, the intensity of conduction band states relative to the background coming from valence band states improves with increasing photon energy. As mentioned in previous paragraph, the In 5s width which is > 0.3 eV cannot be used to determine the position of the CB minimum. In photoemission experiments, the XPS spectra depend only on m_c^*. [38, 78]

To complete the electronic level scheme of the ITO substrate, work function (Φ) measurements are performed via the measurement of the cut-off of secondary electron

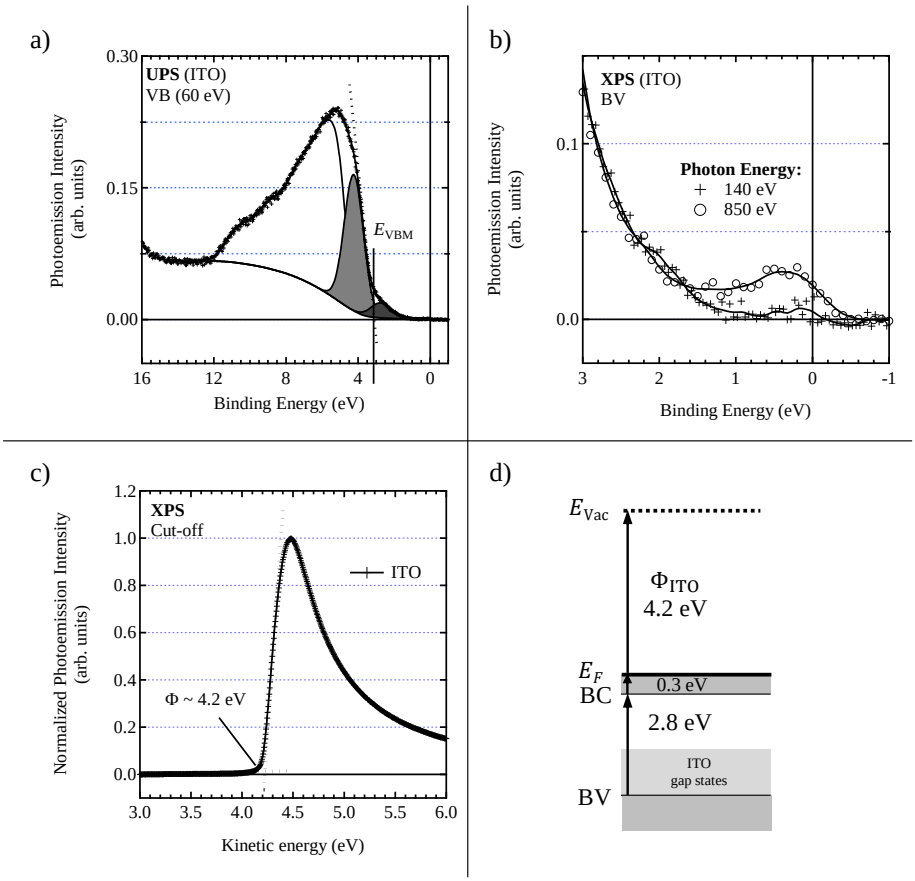

Figure III.4 – a) UV photoemission of ITO valence band and the maximum valence band determination; b) Soft X-ray valence band photoemission of the bare ITO surface at a photon energy of 140 and 850 eV (measurement performed at the ALOISA beamline, ELETTRA synchrotron, Italy): states appear at Fermi Level due to the increase in the $\sigma_{\text{In 5s}}/\sigma_{\text{O 2p}}$ ratio; c) Secondary electron energy distribution curve (SEEDC) of ITO (as the kinetic energy scale is referenced to the Fermi level, the work functions correspond to the SEEDC cut-off energies); d) Energetic diagram for ITO substrate.

energy distribution curves (SEEDC). We find Φ equal to 4.20 eV for the bare substrate (see Figure III.4c)). We also present in Figure III.4d), the electron energy level scheme of ITO. The important parameters are the work function (Φ_{ITO}), the Fermi level position in the conduction band, and the maximum valence band level. We found a valence ionization energy IP_v^{ITO} of 7.3 eV by adding Φ to the $E_F - E_{\mathrm{VBM}}$ energy difference of 3.1 eV. IP_v^{ITO} is independent of doping, but is sensitive to the surface termination (surface dipole). In fact, the literature indicates that IP_v^{ITO} values are scattered around an average of 7.6 eV (7.6 ± 0.4 eV). [51] The value we find is therefore a lower bound one. The possible presence of surface hydroxyls and carbon contaminants may indeed affect the work function.

III.2 ITO/DIPO-Ph$_4$ interface

The present study examines the growth of an ITO/DIPO-Ph$_4$ interface. The evaporation of 1×10^{15}, 2×10^{15}, and 3×10^{15} molecule $\cdot$ cm^{-2} (QB-coverage) samples described in this chapter was done in the preparation chamber of the TEMPO beamline (SOLEIL) on freshly cleaned ITO substrates (Appendix C.1). Then, the samples were directly transferred to the analyse chamber without breaking vacuum. The morphology is slightly different due to a change in the molecular beam incidence and distance to the ITO substrate. Besides, 1×10^{15}, 8×10^{15}, and 10×10^{15} molecule $\cdot$ cm^{-2} samples were also prepared in our well-controlled evaporation system and then introduced in the XPS analyse chamber after air exposure. We compared the samples prepared *in situ* and *ex situ* to see the air exposure effects (Appendix C.2). As no differences were observed, we present here the results for the *in situ* samples and, as a "thick" reference, the 10×10^{15} molecule $\cdot$ cm^{-2} samples. The 8×10^{15} molecule $\cdot$ cm^{-2} sample was used for the study of beam damage effects on the O core level.

III.2.1 Core levels XPS spectroscopy

a) Indium and tin core levels

The deposition of the DIPO-Ph$_4$ molecule affects the In 3d$_{5/2}$ BE. After the first deposit (1×10^{15} molecule $\cdot$ cm^{-2}, see Figure III.5a)), the In 3d$_{5/2}$ peak ($h\nu = 600$ eV) moves to higher binding energy by 100 meV (Table III.3).

Note that the same shift is observed on the Sn 3d$_{5/2}$ peak although fitting was processed with two Voigts as the small intensity does not allow us to detect the 3rd plasmon component (Figure III.5b)).

The shift indicates that the energy difference between the Fermi level and the conduction band minimum increases. According to the AFM images, DIPO-Ph$_4$ is in the

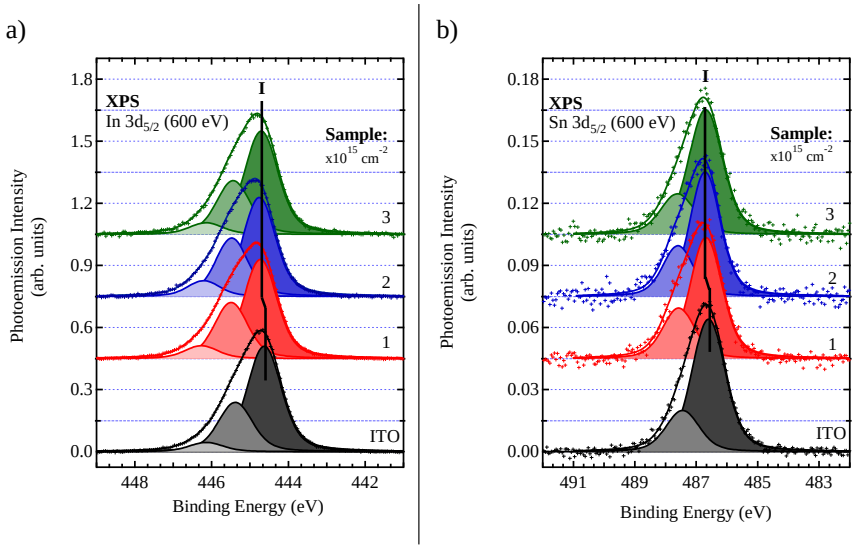

Figure III.5 – a) In $3d_{5/2}$ and b) Sn $3d_{5/2}$ spectra of the chemically cleaned ITO sample and covered with increasing layers of DIPO-Ph_4. The photon energy is indicated. The spectra were recorded at the TEMPO beamline. Coverages are obtained from QB-coverage.

Table III.3 – Experimental In $3d_{5/2}$ and Sn $3d_{5/2}$ principal peak value for $h\nu = 600\,\text{eV}$, FWHM of the Gaussian contribution and BE energy difference with the ITO peak (from Figure III.5).

Core level	**Sample**	**G-FWHM (eV)**	**Peak I BE (eV)**	**Δ^{ITO} (eV)**
In $3d_{5/2}$	1×10^{15} molecule $\cdot$ cm^{-2}	0.808	444.73	0.10
	2×10^{15} molecule $\cdot$ cm^{-2}	0.778	444.72	0.09
	3×10^{15} molecule $\cdot$ cm^{-2}	0.815	444.71	0.08
Sn $3d_{5/2}$	1×10^{15} molecule $\cdot$ cm^{-2}	0.994	486.68	0.08
	2×10^{15} molecule $\cdot$ cm^{-2}	0.924	486.71	0.11
	3×10^{15} molecule $\cdot$ cm^{-2}	1.066	486.69	0.09

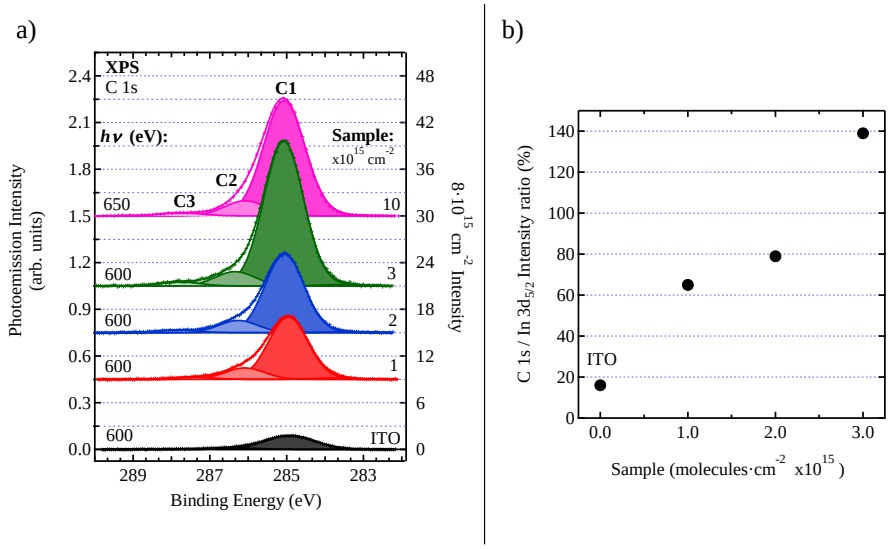

Figure III.6 – a) C 1s spectra of the chemically cleaned ITO substrate, bare and covered with increasing QB-coverages of DIPO-Ph$_4$ (1×10^{15}, 2×10^{15}, 3×10^{15}, and 10×10^{15} molecule $\cdot$ cm^{-2}); b) C 1s/In 3d$_{5/2}$ intensity evolution with the increase of QB-coverage. The C 1s intensity is normalized according to In 3d$_{5/2}$ intensity.

form of mounds, of thickness ∼30 nm, separated by inter-mound areas. Thus, given the IMFP (∼0.56 nm), most of the In 3d signal comes from the inter-mound areas (75 % of the surface) and from thin aureoles around the mounds. The observed BE shift means that molecules interacting with ITO surface change slightly the surface charge density. [19] An electronic transfer from the molecule to the substrate could explain the motion of the Fermi with respect to conduction band minimum. For subsequent depositions (for which the inter-mound area recedes down to 40 %), the position of the In 3d$_{5/2}$ peak does not change any more, showing that the Fermi level remains anchored at the position reached after the first deposit.

b) Carbon and oxygen levels

The C 1s XPS spectra of the ITO surface, bare and covered by the molecule are shown in Figure III.6. The C 1s of the bare sample is due to contamination. It presents the characteristic peak of an aliphatic carbon at 284.9 eV. [97] The C 1s/In 3d$_{5/2}$ intensity ratio (Figure III.6b)), measured at $h\nu = 600$ eV (KE C 1s ∼315 eV, $\lambda_{\text{DIPO-Ph}_4}$ ∼1.19 nm) is 16 % for the chemically cleaned ITO. Then it rises to 65, 79, 139, and 2364 % for the QB-coverages of 1×10^{15}, 2×10^{15}, 3×10^{15}, and 10×10^{15} molecule $\cdot$ cm^{-2}, respectively. These ratio values indicate that the C 1s spectra are characteristic of the deposited film. Key figures are shown in Table III.4.

Table III.4 – C 1s main component BE and Gaussian FWHM (G-FWHM) obtained from fits of the spectra given in Figure III.6. The core-hole lifetime Lorentzian FWHM (L-FWHM) is 80 meV for C 1 s. DIPO-Ph$_4$ coverages are obtained from QB-coverage. The C 1s to In 3d$_{5/2}$ intensity ratio is also given.

Sample	Phot. Energy	G-FWHM	Peak C1 BE (eV)	Peak C2 BE (eV)	$r_{\frac{C2}{C1+C2}}$	C 1s/In 3d$_{5/2}$ ratio
Chemically cleaned ITO	825 eV	1.657 eV	284.91	_	_	8 %
	600 eV	1.488 eV	284.92	_	_	16 %
1×10^{15} molecule $\cdot$ cm^{-2}	600 eV	1.168 eV	284.96	286.09	0.15	65 %
2×10^{15} molecule $\cdot$ cm^{-2}	600 eV	1.156 eV	284.96	286.26	0.13	79 %
3×10^{15} molecule $\cdot$ cm^{-2}	600 eV	1.180 eV	285.08	286.34	0.09	139 %
10×10^{15} molecule $\cdot$ cm^{-2}	650 eV	1.222 eV	285.06	286.00	0.11	2364 %

The C 1s spectra do not exhibit any BE shift, from 1×10^{15} to 3×10^{15} molecule $\cdot$ cm^{-2}, indicating that the position of the Fermi level remains constant in the organic material while the mounds are laterally growing. The C 1s spectra are fitted with three Voigt components: one main component labelled C1 at BE ∼285 eV, with a FWHM of 1.2 eV and two weaker peaks, one labelled C2 at BE ∼286 eV and one labelled C3 at 287.5 eV. Peak C1 has the typical BE expected for aryl carbons. A more thorough examination of the BEs will be made after the discussion of the O 1s spectra, here below. The C2 peak is attributed to C bonded to oxygen atoms and the C3 one at 1.5 eV higher BE that is likely a shake-up. The spectral weight of the C–O component is 0.15, 0.13, 0.09, and 0.11 for the 1×10^{15}, 2×10^{15}, 3×10^{15}, and 10×10^{15} molecule $\cdot$ cm^{-2} respectively. Note that the aryl carbons and core carbons not bonded to O atoms represent 70.5 % and 17.6 % of the carbon atoms (88 % in all), while the carbons in ether bonds amount to 12 %.

We now consider the changes induced on the O 1s spectrum by the deposition of DIPO-Ph$_4$. The O 1s spectrum measured at $h\nu = 600$ eV in "surface sensitive conditions" (KE O 1s ∼70 eV, λ_{ITO} ∼0.47 nm and $\lambda_{\text{DIPO-Ph}_4}$ ∼0.55 nm) are given in Figure III.7a). As the substrate contains oxygen, the spectra of the DIPO-Ph$_4$ covered ITO surface are fitted by a sum of Voigt components that reproduces the bare ITO spectral shape, to which two new components, due to the DIPO-Ph$_4$ molecule, are added. As shown in Figure III.7, the O1 and O2 components appear at 532.2 eV and 533.6 eV, respectively. We have also verified that the appearance of O2 is not trivially due to beam damage (see Figure III.8) during the XPS measurements.

The subtraction of the bare ITO contribution emphasizes the molecular solid contribution. In Figure III.7c) we present the difference spectra obtained in surface sensitive

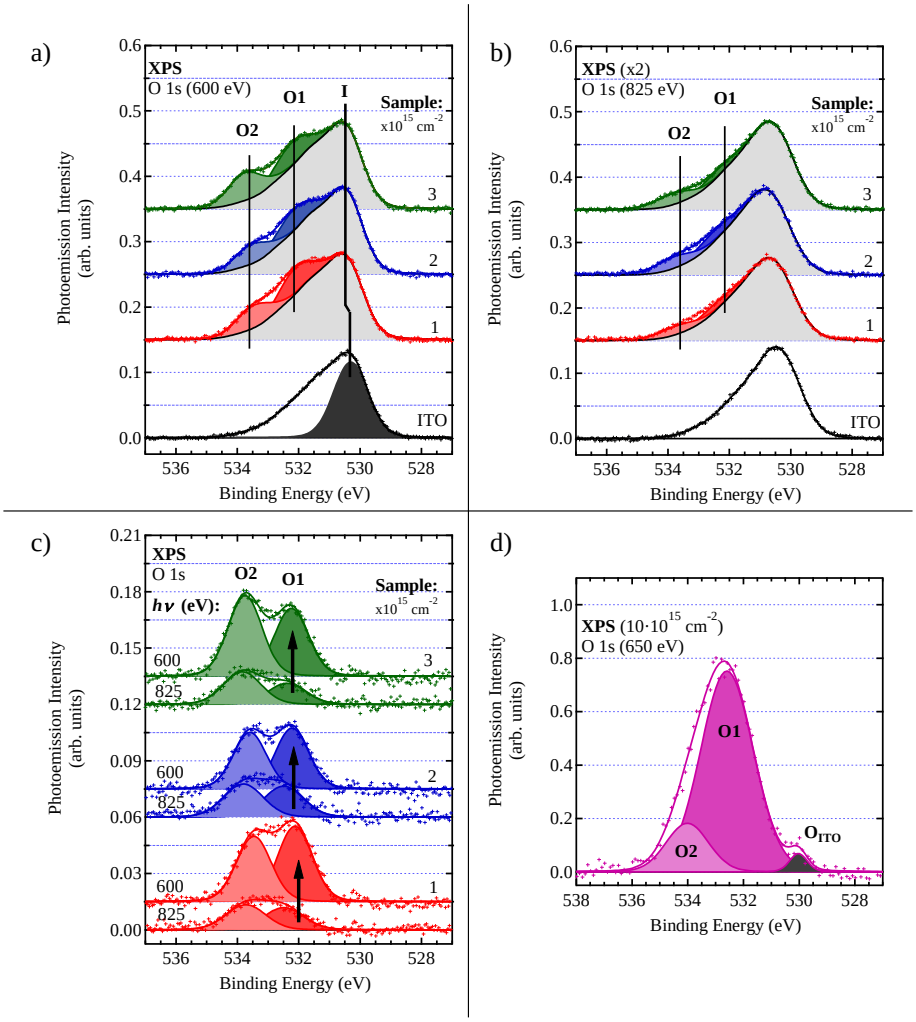

Figure III.7 – O 1s spectra of the chemically cleaned ITO substrates, bare and covered with increasing QB-coverages of DIPO-Ph$_4$ (1×10^{15}, 2×10^{15}, and 3×10^{15} molecule $\cdot$ cm^{-2}). a) $h\nu = 600$ eV; b) $h\nu = 825$ eV. The molecular solid contribution comprises two new components O1 and O2 added to the "synthesized" bare ITO spectrum. The spectra shown in c) are obtained by subtraction of the ITO substrate contribution to the spectra shown in a) and b), emphasizing the contribution of DIPO-Ph$_4$. Coverages are obtained from QB-coverage. d) The O 1s spectrum of the thickest deposit measured at photon energy of 650 eV. The grey shaded component arises from the ITO substrate.

Table III.5 – O 1s BE and Gaussian FWHM (G-FWHM) of the main peaks obtained by fitting the spectra given in Figure III.7. The Lorentzian width (L-FWHM) is 150 meV for the O 1s peaks. $r_{O2/(O1+O2)}$ measures the O2 (BE 533.6±0.1 eV) contribution weight in the molecule-related spectral intensity Coverages are obtained from QB-coverage.

Sample	Phot. Energy	G-FWHM	Peak I BE (eV)	Peak O1 BE (eV)	Peak O2 BE (eV)	$r_{\frac{O2}{O1+O2}}$
1×10^{15} molecule · cm^{-2}	825 eV	1.436 eV	530.39	532.48	533.72	0.53
	600 eV	1.252 eV	530.46	532.13	533.47	0.46
2×10^{15} molecule · cm^{-2}	825 eV	1.433 eV	530.43	532.40	533.70	0.52
	600 eV	1.196 eV	530.42	532.12	533.50	0.48
3×10^{15} molecule · cm^{-2}	825 eV	1.378 eV	530.39	532.39	533.84	0.61
	600 eV	1.227 eV	530.48	532.24	533.75	0.54
10×10^{15} molecule · cm^{-2}	650 eV	_	_	532.84	534.27	0.16

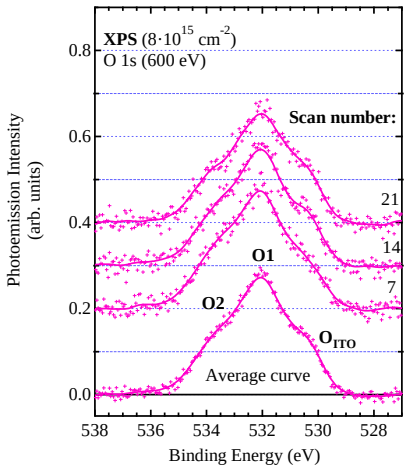

Figure III.8 – O 1s spectra of an ITO substrate covered with DIPO-Ph$_4$ of QB-coverage 8×10^{15} molecule · cm^{-2}. The curves above are the different sweeps obtained under X-ray radiation. We see no effect due to beam damage.

condition (KE ∼70 eV, $\lambda_{\text{DIPO-Ph}_4}$ ∼0.55 nm) and in bulk sensitive ones (KE ∼293 eV, $\lambda_{\text{DIPO-Ph}_4}$ ∼1.14 nm, the original spectra are given in Figure III.7b)). In fact, in DIPO-Ph$_4$ the two oxygen atoms are chemically equivalent (see Figure I.6a)), and thus one single O 1s contribution should be observed. Peak O1 is found at the typical BE of the C–O–C ether bond, in the range 531.5 – 532 eV, predicted by literature. [98] The O 1s spectrum ($h\nu = 650$ eV, $\lambda_{\text{DIPO-Ph}_4}$ ∼0.6 nm) of thick DIPO-Ph$_4$ deposit (10×10^{15} molecule $\cdot$ cm^{-2}) is the one for which the contribution of the substrate (the grey shaded component) is the least, see Figure III.7d). It exhibits the O1 and the O2 components at 534.27 eV (with $r_{\text{O2/(O1+O2)}} = 0.16$, see Table III.5).

The observation of two oxygen components can find various explanations. Let us examine the more trivial explanations. The used material introduced in the crucible may contain a high proportion of oxygen containing molecules co-evaporated with DIPO-Ph$_4$. This must be discarded as the purity of the material was checked by NMR and elementary analysis (Appendix A.2). There is no contamination detected. The presence of background impurities co-adsorbed with DIPO-Ph$_4$, is not realistic as the evaporation was carried out in a UHV system. Therefore, we must consider that the molecule is present in two different forms, one corresponding to the unaltered molecule, with an ether O 1s component labelled O1, and one corresponding to an altered form, characterized by the O2 component. Any interpretation of the O2 component should be consistent with the fitting of the C 1s spectrum into two components (attributed to ester carbons and carbons not bonded to oxygen) that corresponds to the DIPO-Ph$_4$ stoichiometry.

The molecule can be altered by a chemical reaction with species released by the ITO substrate. Indeed, aggressive oxygenated species on the ITO substrate (*e.g.* generated by UV ozone treatments) can break the bonds of organic molecules and oxidize them. [18] The C–O bond of the ether moiety may break leading to the insertion of further oxygen. Indeed, BE of 532.2 and 533.7 eV are found for the carbonyl and ether type oxygens in ester groups of polymers, respectively. [98] Against this view, there is no indication for a carboxylic/carboxylate peak at ∼289 eV in the C 1s spectrum as shown in Figure III.6a), and the $r_{\text{O2/(O1+O2)}}$ ratio is not fixed at 0.5. Other species could diffuse away from the substrate. For instance indium atoms are reported to penetrate deeply into molecular solids such as PTCDA when an indium metal layer is deposited upon it. [99] Tin atoms are less prone to diffuse into PTCDA. [100] The presence of indium in the molecular solid should be noticed by new components appearing in the In 3d$_{5/2}$ spectrum when the DIPO-Ph$_4$ is added, which is not the case. The same observation can be made for the Sn 3d peak that is not affected by DIPO-Ph$_4$ deposition (Figure III.5b)), apart from the +100 meV BE shift after deposition of the first layer (1×10^{15} molecule $\cdot$ cm^{-2}).

The alternative hypothesis to the chemical reaction is that of a charge transfer from

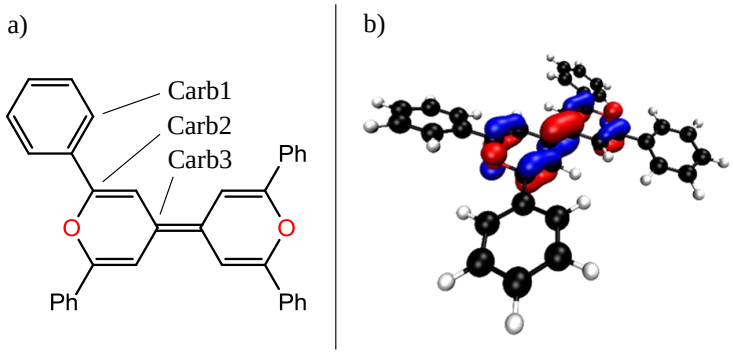

Figure III.9 – a) DIPO-Ph$_4$ structure and carbons place used for DFT calculation; b) HOMO representation.

the molecule (a good donor [25]) to the ITO substrate or to some acceptor species present in the deposited films. This leads to the formation of the radical cation [DIPO-Ph$_4$]$^{\bullet+}$.

c) DFT calculation correlation

This hypothesis is further explored by calculating the O 1s BE shift between the cationic and the neutral molecule in the gas phase (we consider a single molecule) using density functional theory (DFT). Details on the method are given in previous papers by our group (Appendix B.4). [101, 102, 103] Calculations of C and O 1s ionization potentials of a series of molecules were shown to be precise to better than 0.1 eV when compared to the experimental gas-phase values. [101, 102, 104, 105] The first step consists in calculating the energy of the optimized geometries of the neutral (see Figure I.6b)) and cationic states. Then the core-ionized state energy is calculated, keeping the same geometry as that of the initial state (Franck-Condon approximation).

The 1s ionization energies (IP) are calculated as the difference between the energy of the species having a 1s core-hole (final state) and the energy of the species in its ground state (initial state). For the neutral molecule ($IP_{\text{core}}^{\text{neutral,gas}}$), the final state is a doublet. For the cation ($IP_{\text{core}}^{\text{cation,gas}}$), the final state (one hole in the HOMO and one hole in the O 1s or C 1s state) can be a triplet (lowest energy state) or a singlet. Within the DFT framework, only the triplet can be calculated. To estimate the singlet-triplet energy difference, Hartree-Fock (HF) calculations are thus performed. For the cation core-level ionization energies, the singlet-triplet energy difference is 0.08 eV. The triplet and singlet states should be merged into one in the experimental spectra. Besides, the singlet state contributes to 1/3 of the ionized population. Therefore, the spectra curve is mainly due to triplet-state. Also as Table III.6 shows that the DFT and HF ionization energies for the triplet state are very close (0.01 eV), IP_{core} will be taken from DFT calculations.

Table III.6 – Comparison of DFT and HF ionization energies for O 1s.

O 1s $IP_{\text{core}}^{\text{cation,gas}}$	Singlet	Triplet	$\Delta_{\text{Singlet}-\text{Triplet}}^{\text{HF}}$
DFT	_	541.47 eV	_
HF	541.56 eV	541.48 eV	0.08 eV
$\Delta_{\text{HF}-\text{DFT}}^{\text{Triplet}}$	_	0.01 eV	

The calculated O 1s ionization energy (IP_{core}, *i.e.* the BE referenced to the vacuum level) of the neutral molecule ($IP_{\text{core}}^{\text{neutral,gas}}$) is 537.64 eV, while that of the molecular cation ($IP_{\text{core}}^{\text{cation,gas}}$) in the triplet state is 541.42 eV. The difference of ∼3.8 eV between the cationic (triplet) and neutral state DFT ionization energies is much larger than the O2−O1 BE difference of 1.5 eV measured for the molecular solid. In fact, a simple dielectric response model describes the relaxation energy effects via the polarization energy ΔE_R of a unit charge. Then the cationic-neutral BE shift is reduced in the solid state with respect to the gas phase due to core-hole screening by the dielectric medium in the final state.

For the cation immersed in the dielectric medium, the relaxation energy is ΔE_R in the initial state (charge $+e$) and $4\Delta E_R$ in the core ionized state (charge $+2e$) (see Equation (I.2)), assuming that the initial state and the final state ϵ_r constants are the same.

Then

$$IP_{\text{core}}^{\text{cation,gas}} - IP_{\text{core}}^{\text{cation,solid}} = 3\Delta E_R \tag{III.1}$$

If one now considers the IP of the neutral species, the IP difference between the gas phase and the solid writes:

$$IP_{\text{core}}^{\text{neutral,gas}} - IP_{\text{core}}^{\text{neutral,solid}} = \Delta E_R \tag{III.2}$$

Combining Equations (III.1) and (III.2) one obtains:

$$IP_{\text{core}}^{\text{cation,solid}} - IP_{\text{core}}^{\text{neutral,solid}} = \left(IP_{\text{core}}^{\text{cation,gas}} - IP_{\text{core}}^{\text{neutral,gas}}\right) - 2\Delta E_R$$

Considering that the ionization energy measure from the vacuum level is the sum of the binding energy measured from the Fermi level plus the work function, it comes that:

$$BE_{\text{core}}^{\text{cation,solid}} - BE_{\text{core}}^{\text{neutral,solid}} = \left(IP_{\text{core}}^{\text{cation,gas}} - IP_{\text{core}}^{\text{neutral,gas}}\right) - 2\Delta E_R \tag{III.3}$$

where $BE_{\text{core}}^{\text{cation,solid}}$ and $BE_{\text{core}}^{\text{neutral,solid}}$ are the binding energies (measured from the Fermi level) in the solid state of the cation and the neutral species, respectively, and $IP_{\text{core}}^{\text{cation,solid}}$

Table III.7 – Calculated DFT $IP^{\text{neutral,gas}}_{\text{core or valence}}$ and $IP^{\text{cation,gas}}_{\text{core or valence}}$ values for the neutral and cationic DIPO-Ph$_4$ molecule. For the cationic form, core-ionized energies are calculated for the triplet final state. In the estimation of $BE^{\text{cation,solid}}_{\text{core or valence}} - BE^{\text{neutral,solid}}_{\text{core or valence}}$, the polarization energy ΔE_R is taken as 1.2 eV (see Equation (III.3)).

Core/valence level Energy (eV)	**O 1s**	**C 1s Carb1 (phenyl)**	**C 1s Carb2 (ether)**	**C 1s Carb3 (central)**	**HOMO**
$IP^{\text{neutral,gas}}_{\text{core or valence}}$	537.67	289.25	290.70	289.14	5.14
$IP^{\text{cation,gas}}_{\text{core or valence}}$	541.47	292.00	294.27	293.02	8.49
$IP^{\text{cation,gas}}_{\text{core or valence}} - IP^{\text{neutral,gas}}_{\text{core or valence}}$	3.80	2.75	3.57	3.88	3.35
$BE^{\text{cation,solid}}_{\text{core or valence}} - BE^{\text{neutral,solid}}_{\text{core or valence}}$	1.40	0.35	1.2	1.5	1

and $IP^{\text{neutral,solid}}_{\text{core}}$ are the ionization energies (measured from the vacuum level) in the solid of the cation and the neutral species, respectively.

A polarization energy ΔE_R of ∼1.2 eV explains why the calculated energy difference of 3.8 eV between the cationic and neutral species calculated in the gas phase can be reduced to 1.5 eV in the solid state. Therefore, the charge transfer hypothesis must be regarded as likely. Nevertheless, we must check the consistency of two "charge state" model for the C 1s spectra.

In the DFT framework, we also theoretically calculated the C 1s $IP^{\text{neutral,gas}}_{\text{core}}$ and triplet-state $IP^{\text{cation,gas}}_{\text{core}}$ of selected atoms in the molecule. We distinguish three atoms, one labelled Carb1 pertains to the phenyl ring and the two others, Carb2 (central atoms) and Carb3 (ether bond), pertain to the dipyranylidene core, see Figure III.9a). The calculated energies are reported in Table III.7.

For the neutral molecule, the triplet-state DFT IP of the central atoms is slightly shifted with respect to that of the phenyl carbons (by −0.1 eV), while that of the ether carbon is 1.5 eV higher, as experimentally observed. In contrast, for the cationic species, the IP of the central atoms is distinct from that of the phenyl by +1 eV. Physically, this means that the central carbons have lost charge, as it can be guessed from a representation of the HOMO (Figure III.9b)). The ether carbon is found +2.3 eV higher than the phenyl, a sizeable increase when one considers the neutral molecule case.

Considering a polarization energy ΔE_R of ∼1.2 eV that accounts for the solid effects, the energy difference $BE^{\text{cation,solid}}_{\text{core}} - BE^{\text{neutral,solid}}_{\text{core}}$ is reduced to ∼0.35 eV for the phenyl carbon. Consequently, peak C1 in Figure III.6a) can correspond to the phenyl carbons of both the neutral and cationic species. Component C2 at 1.2 eV from C1 can be attributed to the ether carbons of the neutral molecule and to the central carbons of the molecular cation, as $BE^{\text{cation,solid}}_{\text{core}} - BE^{\text{neutral,solid}}_{\text{core}}$ is worth ∼1.5 eV for the latter ones. Component

C3 at 2.5 eV from C1 can be attributed to the ether carbons of the cation given that $BE_{\text{core}}^{\text{cation,solid}} - BE_{\text{core}}^{\text{neutral,solid}}$ is worth ∼1.2 eV. Consequently, the hypothesis of a mixture of neutral and cationic species in similar proportions consistently explains both the O 1s and C 1s spectra. Note that the O1/O2 proportions do not depend on the sample coverage as the island aureoles probed via XPS have the same area for the different samples from 1×10^{15} to 3×10^{15} molecule $\cdot$ cm^{-2}. Thus, no DIPO-Ph$_4$ material is deposited is deposited between the islands. Therefore, the DIPO-Ph$_4$ growth follows a Volmer-Weber mode.

III.2.2 Valence band energy level

We now focus on changes in the electronic structure of the valence band. With respect to the substrate spectrum prior to deposition, the valence band spectra measured at $h\nu = 60$ eV (Figure III.10a)) exhibit new features (red-, blue-, green-, and violet-shaded components) related to the occupied molecular orbitals of DIPO-Ph$_4$ superimposed onto the ITO valence band contribution. Note that the valence band photoelectrons measured at this energy and the O 1s photoelectrons measured at $h\nu = 600$ eV correspond to the same probing depth, as their KE (∼60 eV and ∼70 eV, respectively) are very close. Therefore, the two chemical states associated to the O1 and O2 components in the O 1s spectrum contribute in nearly equal weights to the molecular valence band spectrum.

For deposits $\leq 3 \times 10^{15}$ molecule $\cdot$ cm^{-2}, a grey-shaded synthetic spectrum represents the ITO contribution. This is the major one in the valence spectrum. At $h\nu = 60$ eV, the IMFP $\lambda_{\text{DIPO-Ph}_4}$ of the photoelectron in the molecular solid is only ∼0.55 nm. Considering the morphology of the deposit, the photoemission signal comes from the top of the molecular mounds and from the inter-mound areas, which still represents 40 % of the surface for a deposit of 3×10^{15} molecule $\cdot$ cm^{-2}. The probed ITO still shows its metallic character (there is a weak Fermi level emission for the 3×10^{15} molecule $\cdot$ cm^{-2} deposit). The valence band spectrum of the thickest deposit (10×10^{15} molecule $\cdot$ cm^{-2}) is more characteristic of the organic material as the ITO contribution in the O 1s spectrum (see Figure III.7d)) is minimal and the neutral state corresponds to 70 % of the molecular spectral weight. We observe the growth of six strong components, labelled A to F, that show up at BE 14.06, 10.97, 9.36, 6.99, 4.30, and 3.29 eV, respectively, plus two molecular states appearing in the ITO gap centred at 2.5 and 1.4 eV, that we label H(+) and H, respectively.

As the measured spectrum results from the combination of two different chemical states (neutral versus cationic) of the molecule, the respective molecular levels are mixed up in the experimental spectrum. Let us now start with the two molecular levels with

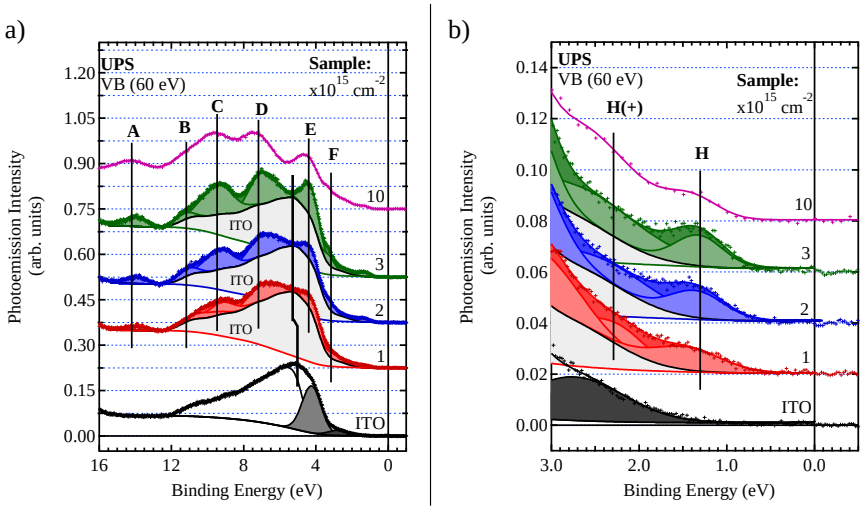

Figure III.10 – a) UV photoemission: ITO and DIPO-Ph$_4$ maximum valence band with HOMO levels of DIPO-Ph$_4$; b) Zoom on the a) image. Coverages in molecule $\cdot$ cm^{-2} are obtained from QB-coverage. The ITO contribution for all samples, except the thickest deposit of 10×10^{15} molecule $\cdot$ cm^{-2}, is represented by the grey-shaded area (labelled ITO). H is the HOMO of the neutral molecule and H(+) indicates the binding energy of the cation singly occupied molecular orbital (SOMO).

lower BE, H(+) and H that appear in the gap of ITO. Using DFT, we have calculated the vertical valence ionization energy of the highest occupied molecular orbital (HOMO, neutral) and singly occupied molecular orbital (SOMO, cationic), $IP^{\text{neutral,gas}}_{\text{HOMO}}$ and $IP^{\text{cation,gas}}_{\text{SOMO}}$, respectively. We find $IP^{\text{neutral,gas}}_{\text{HOMO}} = 5.14\,\text{eV}$ and $IP^{\text{cation,gas}}_{\text{SOMO}} = 8.49\,\text{eV}$. The DFT energy difference $IP^{\text{cation,gas}}_{\text{SOMO}} - IP^{\text{neutral,gas}}_{\text{HOMO}}$ (Table III.7) is close to that calculated for the C 1s core-levels (triplet state) of atoms in the dipyranylidene core. The estimated BE energy difference in the solid state $BE^{\text{cation,solid}}_{\text{SOMO}} - BE^{\text{neutral,solid}}_{\text{HOMO}}$ is reduced $\sim$1 eV with ΔE_R equal to $\sim$1.2 eV (see (III 7)). Therefore, the components H(+) and H, whose measured BE difference is also $\sim$1 eV, are attributed to the SOMO level of the cationic species and to the HOMO of the neutral molecule, respectively.

We have tried to calculate the DFT ionization energy of molecular orbitals (neutral and cationic state) that are essentially localized on phenyls. The calculation of the doubly ionized states does not converge, because the phenyl localized orbitals pertain to a manifold of levels with very close energies. Nevertheless, the difference in the ionization energies between the neutral state and the cationic state may be expected to be lower than in the case of the highest energy levels (HOMO and SOMO), since the charge appearing on the phenyl is spatially remote from the electron vacancy localized on the core of the molecule. The latter point is clearly demonstrated by the valence band spectra of

DIPS-Ph$_4$ films we present in Figure V.8.

III.2.3 Electron energy level scheme

The SEEDC of the deposits 1×10^{15}, 2×10^{15}, and 3×10^{15} molecule $\cdot$ cm^{-2} give a Φ value of 3.90 eV, independent of coverage. Considering that charge transfer occurs at the ITO/DIPO-Ph$_4$ interface, the value of Φ gives the value of Φ^+ (3.9 eV) and the slight decrease in work-function is attributed to the formation of cationic species at the ITO/DIPO-Ph$_4$ interface. [10] The ionization energy of the HOMO (neutral species) obtained by adding Φ to the HOMO edge binding energy measured from the Fermi level is 4.6 eV. The value agrees with the ionization energy measured thanks to the Forrest relationship. [56]

We present in Figure III.11, the electron energy level scheme of the ITO/DIPO-Ph$_4$ interface. The important parameters are the $E_F -$HOMO (neutral) energy offset of 0.7 eV (leading edge)/1.4 eV (centroid), the molecular solid work function Φ (3.90 eV), and the valence ionization energy of DIPO-Ph$_4$ is obtained by adding Φ to the HOMO binding energy measured from the Fermi level to give 4.6 eV (HOMO leading edge)/5.3 eV (centroid). The SOMO level of the cationic species H(+) has a higher binding energy (referenced to the Fermi level) and thus a higher ionization energy (referenced to the vacuum level) that of the neutral HOMO level, as demonstrated by the DFT calculation of the isolated molecule. As emphasized in Ref. 106, UPS generates photoemitted electrons that carry away with them the relaxation energies (electronic polarization and structural relaxation) of the valence ionized molecule. This is entirely true for molecules in the neutral ground state, and therefore the measured HOMO binding energies are relevant to discuss transport properties, in particular the transport gap of molecular solids, when inverse photoemission spectroscopy data about the lowest unoccupied molecular orbital (LUMO) energy are also available. However, as E_F approaches the HOMO, this molecular level is partly emptied due to a charge transfer to the substrate, but the spectroscopic level H(+) (a doubly ionized final state) will appear below the HOMO due to the strong hole-hole interaction. This is a common observation in UPS spectroscopy, when SOMOs are concerned (a good example is the valence band spectroscopy of copper phthalocyanine [107]).

Let us first consider the $E_F -$HOMO (neutral) energy offset. As the HOMO (neutral) is below the Fermi level by at least 0.7 eV (edge), there is no barrier to collect holes from the DIPO-Ph$_4$ layer into the ITO substrate, as expected. It is also worth noticing that $E_F -$ HOMO (neutral) is also the hole injection barrier (Δ_h) from ITO to the molecular solid. The low value of 0.7 eV (edge) make it interesting for organic light-emitting diodes,

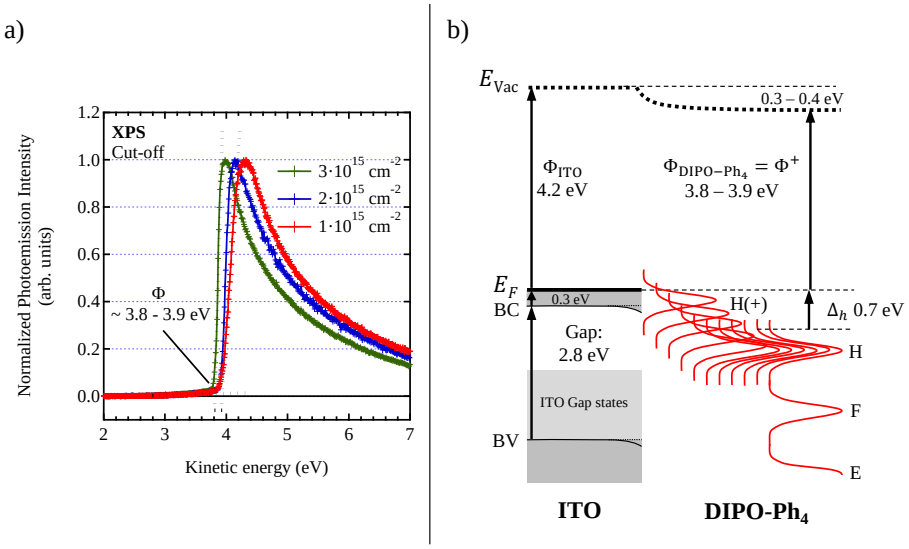

Figure III.11 – a) Secondary electron energy distribution curve (SEEDC) of various deposits indicated in inset (as the kinetic energy scale is referenced to the Fermi level, the work functions correspond to the SEEDC cut-off energies); b) Expected energy level scheme of the ITO/DIPO-Ph_4 system.

and very competitive with other organic hole-transport materials such as TPD and α-NPD deposited on ITO. [108]

As discussed before, given the UHV deposition conditions, DIPO-Ph_4 should be undoped and moderately conductive. It is only when it meets the substrate that it can transfer electronic charge and become a cation. This is a particular case of doping, different from the classical molecular doping, [109, 110, 111] where acceptor or donor molecules are inserted into the organic semiconductor host. A significant difference with molecular doping is the absence of negatively charged recombination centres in the film itself. Thin layers in contact with the substrate may have a high hole conductivity.

III.3 Charge transfer from DIPO-Ph_4 to ITO

Finally, we were interested in charge-transfer dynamics between ITO and the DIPO-Ph_4 layer. In fact, the performance of organic-based electronic devices relies on efficient charge transport across hybrid interfaces where electronically different materials couple; such interfaces often represent a bottleneck in the overall performance of organic electronic and photovoltaic devices. [112] Charge transfer (CT) across interfaces is most easily studied using small aromatic molecules that can form ordered molecular films on a variety of substrates. Often, such systems exhibit rather uniform coupling schemes to metal electrodes,

as well as to other molecules, thereby minimizing structural disorder, which is a major limiting factor in the device performance. [14, 113] Such ordered prototypical systems open the possibility to experimentally address charge transport phenomena on the molecular level using X-ray based spectroscopy techniques. [114, 115, 116, 117, 118, 119, 120]

III.3.1 Resonant photoemission spectroscopy

Auger or valence photoemission in the so-called resonant regime are observed when the photon energy is set at, or scanned across, a resonance in the X-ray absorption spectrum, *i.e.* when the core electron is lifted to unoccupied levels of antibonding π nature, forming bound states below the ionization potential. These states were previously described via STXM study (π^*_{DIP}, π^*_{Ph}, and $\pi^*_{\mathrm{DIP+Ph}}$). Before entering into the details of the resonant spectroscopy and the information it brings about the fate of the lifted electron, we devote a few words to describing the operating mode of resonant photoemission electron spectroscopy (ResPES), that we carried out at the TEMPO beamline (SOLEIL synchrotron) dedicated to such experiments.

The X-ray absorption coefficient measurements can be carried in transmission, but this technique requires sufficiently thin materials. This technique is obviously not convenient to use in the present case (we cannot use detached DIPO-Ph$_4$ thin films and the interface ITO/molecule is of high interest). We must rely on electron yield techniques by placing a detector collecting electrons emitted from the sample surface. The idea is that the absorption coefficient is proportional to the electron yield. The detector can be very cheap and simple (a channeltron, a microchannel plate) or much more sophisticated (an electron analyser). The total electron yield (TEY) detection can be used when the detection does not require the knowledge of the electron energies. All emitted electrons are collected: photoelectrons, Auger electrons (see below) and secondary electrons. The yield being dominated by the very low energy secondary electrons, and the probed material thickness being large, a few tens of nm, [121] this is not a surface sensitive technique.

The Auger yield measurement needs a sophisticated electron analyser, as the Auger kinetic energy window is recorded. First, we recall what the Auger process is. X-rays are absorbed through excitations of core electrons to empty states above the Fermi level. In the Auger decay, after a short time of the order of 10^{-15} s, the core-hole is filled by an electron from a higher energy state. Using an energy electron analyser, the Auger energy window can be recorded, and integrated, to give the Auger electron yield (AEY). The AEY is made of electrons with kinetic energies in the 240 – 280 eV energy range for C (KLL) and in the 480 – 520 eV for O (KLL), corresponding to relatively short inelastic mean free path of 1.0 – 1.7 nm. In comparison with the TEY, the AEY can be considered

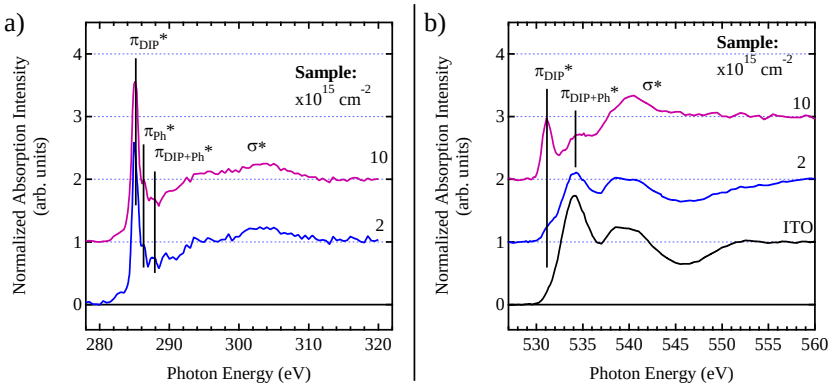

Figure III.12 – Absorption transitions for DIPO-Ph_4: a) C core level; b) O core level for QB-coverage 2×10^{15} and 10×10^{15} molecule $\cdot$ cm^{-2} samples and the ITO substrate.

as surface sensitive.

We present in Figure III.12, the absorption spectra obtained from AEY experiments and the transitions already observed via STXM measurements.

Let us discuss in more detail the spectroscopic aspects of the experiment. When the energy of a photon is much higher than the ionization potential, the electron is ejected from the material, which leads to a one core-hole (h) state. In the Auger decay process, the initial state is the core-ionized state. The "normal" Auger channel leading to a 2h (two holes) final state. Then the emitted Auger electron is characterized by a specific KE (see left part of Figure III.13) that is simply equal to the difference between the energy of the initial (h) core-ionized state and that of the final (2h) state.

When the photon energy is smaller than the ionization threshold, the electron is lifted to an unoccupied level, creating a bound state. There, it may remain as a spectator of the Auger process. Then the initial state is the "excitonic state", one core-hole one electron state (1h1e) and the final state is a two-hole one-electron (2h1e) final state. The KE of the spectator Auger is simply the energy difference between the former and the latter. The electron may also transfer out of the unoccupied state, before the normal Auger decay leading to a 2h final state. At a given resonance photon energy, the 2h1e spectator Auger is found shifted to higher KE with respect to the normal Auger. The energy difference is termed "spectator shift". It is due to the screening by the extra electron (see center part of Figure III.13).

The excited electron in the unoccupied bound state may also participate to the Auger decay, leaving the system with one hole in the occupied valence band, hence it is termed participator. This one-hole (1h) final state is equally reached via direct valence band photoemission, although the selection rules are different (see center part of Figure III.13).

III.3 Charge transfer from DIPO-Ph$_4$ to ITO

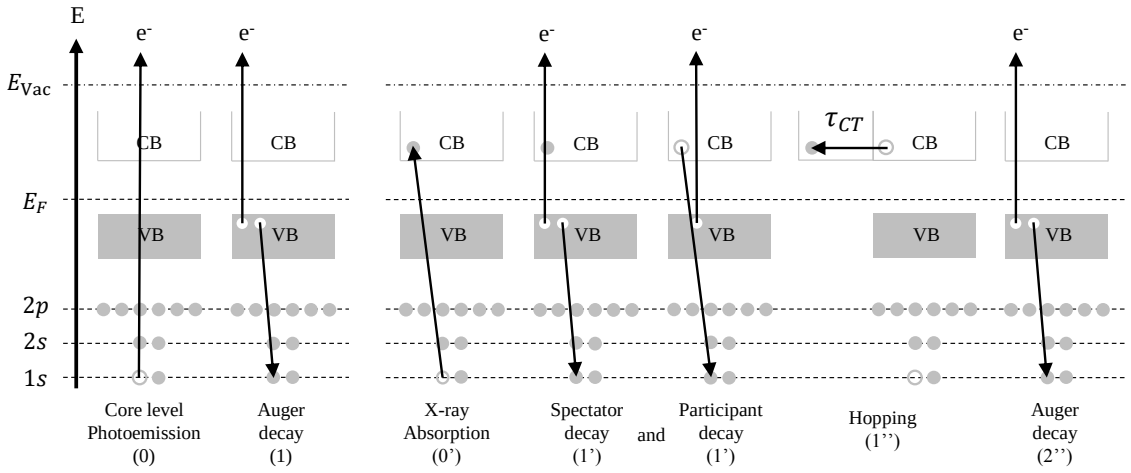

Figure III.13 – Auger processes after core level photoemission.

Because the two final states are identical, although stemming from two different channels, the wave functions can interfere. Therefore, valence states can resonate and their intensity can be exalted.

To introduce the concept of measuring charge-transfer dynamics via core excitation, also called the core-hole clock method, we also present in Figure III.13 (right part) the case in which the excited state of a small system is coupled to a larger system (the substrate or the molecular material itself). Consider that the lifted-up electron is removed before the Auger decay occurs with a charge transfer time of τ_{CT} (in other words the probability of being removed during an interval of time dt is dt/τ_{CT}). Once the electron is transferred out of its level, a "normal" 2h final state Auger decay is observed. Any process that entails the effective removal of the excited electron from the vicinity of the core hole (coupling to the greater environment) leads to a quenching of the resonant channels. Therefore, if the charge transfer time is neither infinitely small (normal Auger, plus resonant valence band state) nor infinitely long (pure spectator Auger), the result will be a mixture of both normal and resonant Auger (affected by the spectator shift). To observe such a mixture, the charge transfer time must be of the order of the core-hole lifetime, *i.e.* a few femtoseconds for C and O 1s levels.

Figure III.14 presents the schematic Auger spectrum decomposition at a resonance with a fraction of the promoted electrons which go to a continuum (material or substrate).

It can be shown easily that the intensity of the "normal" Auger (I_{Aug}) spectrum and of resonant spectrum intensity (spectator and participant, I_{Res}) are related to the core lifetime energy broadening Γ_C, and to the tunneling bandwidth Γ_{CT} by the relation: [114]

$$\frac{\Gamma_{CT}}{\Gamma_C + \Gamma_{CT}} = \frac{I_{\mathrm{Aug}}}{I_{\mathrm{Res}} + I_{\mathrm{Aug}}}$$

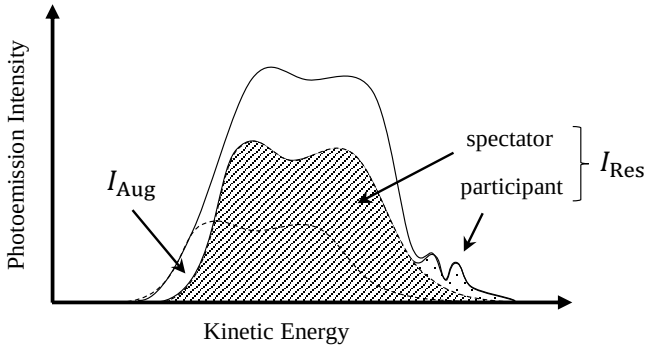

Figure III.14 – Auger spectrum decomposition at resonant transition.

As bandwidths Γ are related to the lifetimes τ via the Heisenberg relation $\Gamma = \frac{\hbar}{\tau}$ relation, one gets:

$$\tau_{CT} = \frac{I_{\text{Res}}}{I_{\text{Aug}}} \tau_C$$

III.3.2 ITO/DIPO-Ph$_4$ interface

To gain information on the charge transfer time from the organic materials to either the ITO substrate or the molecular solid itself, two different DIPO-Ph$_4$ samples were studied. To be sensitive to the metal/organic interface, we studied a 2×10^{15} molecule $\cdot$ cm^{-2} (QB-coverage) deposit with a 50 % coverage and an average cluster height of 20 nm. Such deposits present appreciable contributions of aureoles around the mounds, where the films are thin enough to observe modifications of the organic molecules by the TCO. For the sake of comparison, we studied a "thicker" 10×10^{15} molecule $\cdot$ cm^{-2} sample characteristic of the unaltered film. In this case, the DIPO-Ph$_4$ layer almost entirely covers the ITO substrate with an average height of 50 nm.

a) C K-edge

First, we will focus on the C transitions and then on the O ones. The results are presented as ResPES mapping from which Auger areas are extracted for different photon energies corresponding to main absorption transitions (Figure III.15). Mappings are presented as a function of binding energy while Auger spectra are presented as a function of kinetic energy. On the mapping, the absorption intensity is superimposed, to highlight resonance areas.

For the thicker layer (10×10^{15} molecule $\cdot$ cm^{-2}), ResPES mapping (Figure III.15a$_1$)) shows a main resonance at a photon energy corresponding to π^*_{DIP} transition (∼285 eV).

III.3 Charge transfer from DIPO-Ph$_4$ to ITO

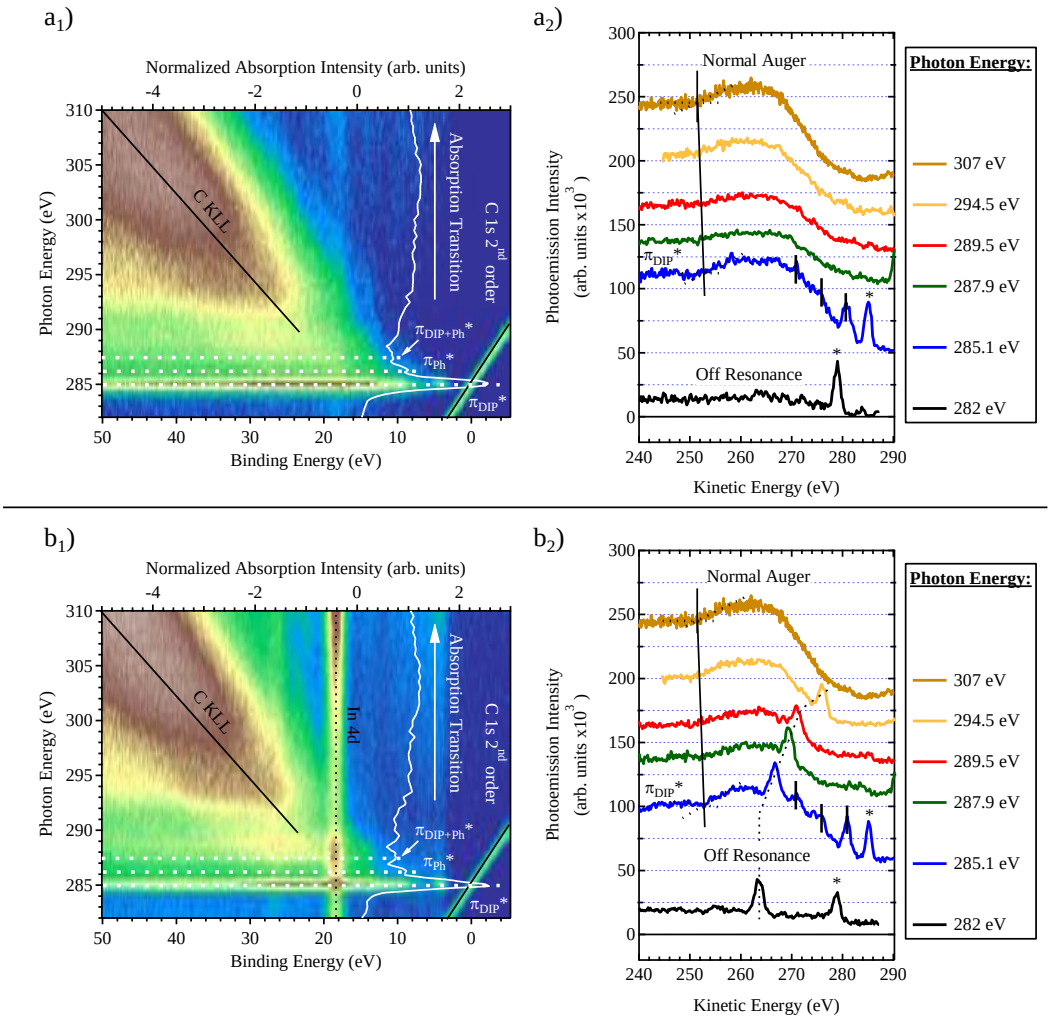

Figure III.15 – DIPO-Ph$_4$ at C-K edge: a$_1$), b$_1$) ResPES mapping; a$_2$), b$_2$) Extracted C KLL Auger for the QB-coverage a) 10×10^{15} and b) 2×10^{15} molecule $\cdot$ cm^{-2}. On the Auger spectra, the asterisk (*) indicates the C 1s 2nd order peak position; the dotted line indicates In 4d peak position, the long continuous line the spectator shift, and small ticks (|) indicate the participant decays.

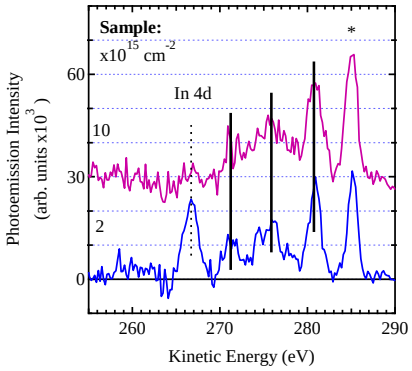

Figure III.16 – DIPO-Ph$_4$: participant decay after subtraction of a shifted "normal" Auger to the resonant Auger spectra. The asterisk (*) indicates the C 1s 2nd order peak position, the dotted line indicates In 4d peak position, the long continuous line the spectator shift, and ticks (|) indicate the participant decays.

From this mapping, the C KLL Auger areas are extracted (Figure III.15a$_2$)) for different photon energy (near absorption transitions and far from resonances). The C KLL Auger is clearly shifted for $h\nu = 285.1\,\text{eV}$ in comparison to the "normal" Auger taken at $h\nu = 307\,\text{eV}$. This shift results from a spectator decay. Besides, new structures appear at the π^*_{DIP} resonance, which correspond to participant decays. The latter have been emphasized after subtraction of a shifted "normal" Auger to the resonant Auger spectrum (Figure III.16).

Finally, the Auger spectrum does not show any "normal" Auger decay around the π^*_{DIP} transition, which indicates that the lifted electron remains in the π^*_{DIP} level for much longer times than the core-hole decay characteristic time (8 fs). [92] There is no observable charge transfer to the molecular continuum.

Let us now focus on the "thinner" deposit ($2 \times 10^{15}\,\text{molecule} \cdot \text{cm}^{-2}$). For this sample, the In 4d signal is detected as the organic layer does not cover the entire ITO surface (Figure III.15b)). Yet, the results and the conclusion are identical to those drawn from the study of the thickest deposit. A spectator shift is also observed and we found 3 participant decays (Figure III.16). Therefore, there is no charge transfer: neither to the molecular continuum, as it was already observed with the bulk sensitive sample, nor to the ITO substrate continuum.

b) O K-edge

To confirm the C K-edge results, we also performed the measurements at the O K-edge. The O 1s spectrum for this sample shows two O components (O1 and, at 1.2 eV above, O2)

attributed to the neutral and the cationic DIPO-Ph$_4$ form, respectively (see Figure III.7). The absorption intensity increases at the π^*_{DIP} and the $\pi^*_{\mathrm{DIP+Ph}}$ levels on top of the ITO absorption (Figure III.12b)). There is no absorption at the π^*_{Ph} level as the unoccupied states at this level are not localized on the oxygen atoms (see Figure II.4). Note that for the "thinner" deposit (2×10^{15} molecule $\cdot$ cm^{-2}), we cannot distinguish, in the absorption spectrum, the signal from the cationic DIPO-Ph$_4$. The ITO substrate signal is too high as the probed surface is mainly the ITO surface between the DIPO-Ph$_4$ mounds. For the thicker layer (10×10^{15} molecule $\cdot$ cm^{-2}), probed DIPO-Ph$_4$ molecules are mainly neutral.

We will now consider the Auger/VB spectrum of the bare ITO substrate, recorded while scanning the O K edge (the blank spectrum), before discussing the ResPES spectrum of DIPO-Ph$_4$ deposited on ITO.

For the bare ITO sample, we see neither spectator nor participant decay channel (Figure III.17a)). The O 1s2p2p Auger main peak remains at the same energetic position all through the O K edge. Being a conductor, the electron lifted in the conduction band of the ITO is delocalized. On the contrary, for the two DIPO-Ph$_4$ covered samples (Figure III.17b) and c)), the O Auger is shifted up in kinetic energy with respect to the "normal" Auger. This indicates a spectator Auger. At the π^*_{DIP} transition, there is no charge transfer to the molecular extended states or to the ITO substrate, as already seen in C K-edge ResPES. However, in contrast to the C K-edge case, no participant channels are observed. We are inclined to think that the unoccupied MO to which the participator electron is promoted, and the occupied MOs localized on the O site have very different spatial extent. [116]

The morphology of the "thinner" deposit (2×10^{15} molecule $\cdot$ cm^{-2} QB-coverage) is dominated by high 3D clusters (20 nm), characteristic of the unaltered molecular film, thus ultra-thin layers, in which possible charge transfer phenomena in the core-excited state could be observed, do not contribute enough. Remember that the Auger analysis is rather surface sensitive due to the kinetic energy of the electrons. In further analyses, we plan to study samples prepared with a post annealing treatment with lower-height clusters as it was described in the morphology section (Chapter II.1.2).

Besides, the BE of the C 1s (DIP core) carbons is 285 eV, corresponding to an IP_{core} of $285 + 3.9 = 289.9$ eV. Therefore, (i) the resonance energy with respect to vacuum level of the π^*_{DIP} is 3.9 eV as the absorption transition energy C 1s to π^*_{DIP} is 285 eV; (ii) the core-exciton state is within the HOMO−LUMO gap ($IP_v - EA_c = 4.6 - 2.6$ eV, with a gap of 2 eV). The absence of delocalization is thus understandable as the energy needed to remove an electron from the π^*_{DIP} to an unoccupied level far away is at least $3.9 - 2.6 = 1.3$ eV. No intermediate hoping level near the excited molecule, at lower in energy due to the hole-electron Coulomb interaction, has been created. [114] Concerning

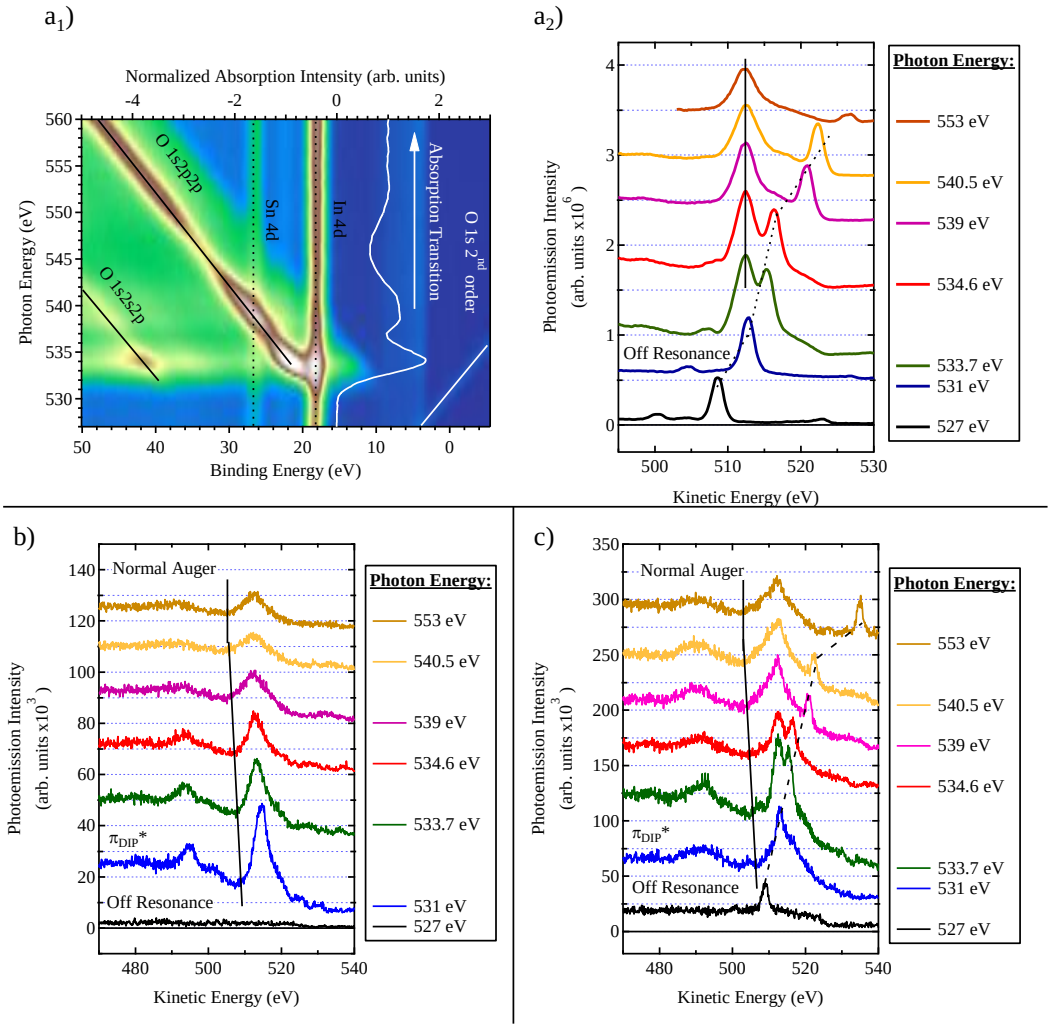

Figure III.17 – O K-edge: a$_1$) ResPES mapping, dotted lines indicate In 4d and Sn 4d peak positions; a$_2$) Extracted O 1s2p2p Auger for ITO substrate; Extracted O Auger for the QB-coverage b) 10×10^{15}; c) 2×10^{15} molecule $\cdot$ cm^{-2}. On the Auger spectra, the dotted line indicates In 4d peak position and the long continuous line indicates the spectator shift.

III.3 Charge transfer from DIPO-Ph$_4$ to ITO

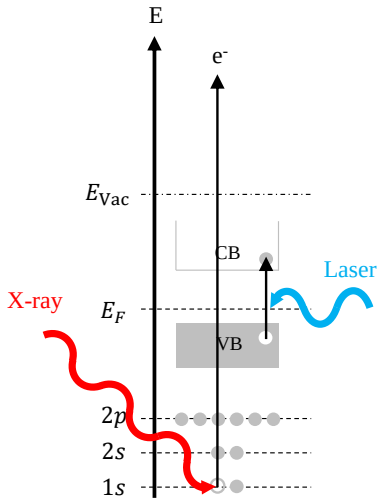

Figure III.18 – Energetic diagram of the photoemission process during laser impulsion.

the relation with the ITO electronic structure, the absorption state is practically located at the Fermi level. The transfer to the unoccupied part of the conduction band (according to the Pauli principle) could be envisaged.

In these core-hole clock experiments, we observe a core-exciton with an electron charge transfer time much longer than the femtosecond. However, in opto-electronic devices, excitations are valence excitations not core excitations. Do valence excitons in DIPO-Ph$_4$ present the same energy and spatial characteristics of core excitons? For large conjugated molecules (this is the case of DIPO-Ph$_4$), or more generally for well screened systems, one considers it to be true. [122] This makes the core-hole clock method a method of simple implementation compared with the pump-probe approach, especially at a fs time-scale that cannot be addressed with the time structure of 3rd generation synchrotrons. However, other longer time-scales are crucial to examine in the molecular crystals, especially when transport is concerned. This was the aim of a pump (laser)-probe (synchrotron radiation) experiment we carried out at SOLEIL.

III.3.3 Pump-probe experiments

To determine the valence exciton time-scales in DIPO-Ph$_4$, we performed pump-probe experiments at the TEMPO beamline, SOLEIL. We used a laser impulsion (400 nm; 500 ms; 5 mW) to promote a valence electron to the unoccupied states and thus fabricate a valence electron-hole (e-h) pair in DIPO-Ph$_4$ (Figure III.18). Such a combination was already implemented several decades ago with a combination of visible laser (pump) and synchrotron radiation (probe) in C_{60} and polymerized C_{60} to observe the population

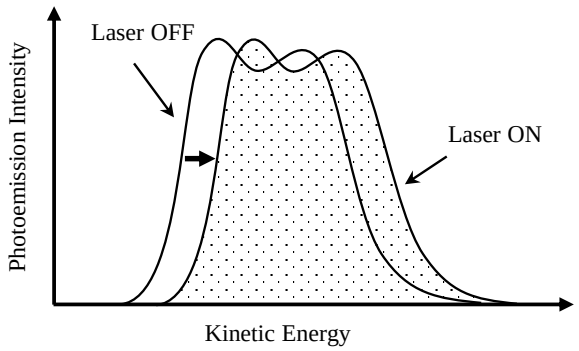

Figure III.19 – Core level shift due to photoconductivity.

of new valence states (*i.e.* the LUMO) and estimate the characteristic lifetimes of the excited states. [123] Probing the core levels is performed most of the time in relation with photovoltage studies. Here we also examine changes in the C 1s core level during ON/OFF laser cycles. Our idea was that the core level could be sensitive (i) to changes brought by photoconductivity (small charging effects in the material could be eliminated by the creation of carriers under illumination), (ii) to photovoltage (changes in "band bending") and (iii) to changes brought by the excited e-h state itself. In cases (i) and (ii), the shape of the C 1s peak is not affected, only its binding energy position varies. In case (iii) we bet on a change in the C 1s spectral shape due to the formation of the exciton. The rationale was the following: the binding energies of the various chemically inequivalent carbon atoms (*e.g.* DIP core, phenyl wings, *etc.*) could indeed be perturbed by the formation of the excited valence state. Indeed we already know (see Chapter III.2.1c)) from DFT calculations that the binding energies of the C 1s components of the valence ionized molecule (HOMO) are at different positions with respect to those of the ground state neutral molecule. In any case we hoped to see something interesting, case (iii) being a novelty in the field of pump-probe experiments.

The laser power was set up at 5 mW to avoid any damage under laser illumination.

We now focus on the photoconductivity effect that we mentioned earlier. It is an optical and electrical phenomenon in which a material becomes more conductive due to photon absorption. When light is absorbed, the number of free electrons and electron holes increases and raises its electrical conductivity. Intrinsic molecular solids are normally relatively poor conductive materials, as the number of free carriers is small. [7] Therefore, under X-ray irradiation, all holes cannot be replenished, even if the material is grounded, and a (small) charging effect can be expected for films deposited on conductive substrate, when their thicknesses are greater than 50 nm.

III.3 Charge transfer from DIPO-Ph$_4$ to ITO

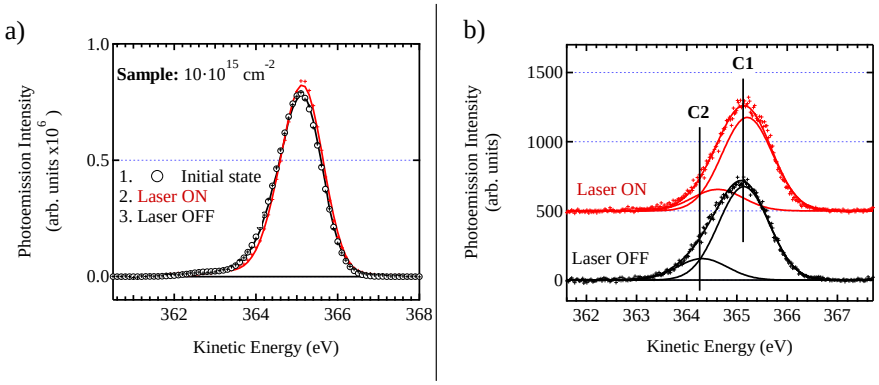

Figure III.20 – C 1s spectra: a) Laser impulsion ON & OFF effect; b) Decomposition fitting with C1 and C2 components.

The photoemission core-level in charging materials are pushed to lower kinetic energy (the escaping electrons are retained by the positive charge), that is, to higher binding energy. When the laser is ON, the photoconductivity effect eliminates this electrical charging. Figure III.19 presents the effect of laser illumination on the XPS spectrum of a charging sample, *i.e.* a rigid shift of the spectrum to lower binding energy. This will be naturally the case when a strong differential charging deforming the spectra is absent. Point (ii), *i.e.* band bending, may be not relevant to present study, as surface layers of the organic material are essentially probed. "Band bending" could indeed appear at the interface between ITO and DIPO-Ph$_4$.

Finally, point (iii), *i.e.* the exciton-induced shift in core binding energies, must be considered. In the case of the DIPO-Ph$_4$ structure, the LUMO is mainly localized on the DIP core. When a HOMO electron is promoted to the LUMO, one can expect changes in the relaxation energy of the C 1s components of the DIP carbons. A screening effect results in an increase (decrease) of the kinetic energy (binding energy). Previous C 1s spectra analysis for an all-covered substrate show two main components C1 and C2 attributed to Ph carbons and core DIP carbons respectively. Thus, the exciton may affect the C2 component.

Our first experiment was to observe possible changes in the C 1s spectra under laser illumination, and verify they are not due to irreversible photolytic damages. The C 1s spectra were recorded "laser OFF", then "laser ON" and finally "laser OFF" to be sure that the system comes back to its initial state (Figure III.20a)).

The C 1s spectra exhibit no rigid shift but an increase of the maximum height is observed and the asymmetry to higher binding energy diminishes. In the "Laser OFF" state, the system comes back to its initial state, showing no laser damage. Peak fitting

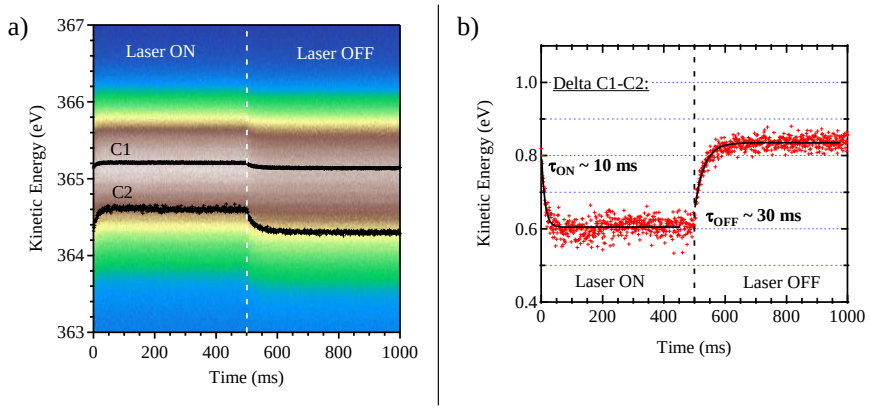

Figure III.21 – a) Mapping of C 1s spectra during Laser ON & OFF; b) Extracted difference between C1 and C2.

(Figure III.20b)) shows that the C1 (phenyl and DIP core) and C2 (ether) components behave differently. Under illumination, the C1 component BE slightly shifts by -70 meV. The C2 component BE shifts by -300 meV. The maximum height increase is due to the smaller energy difference between C1 and C2 under illumination.

To determine the time-scale of the spectral change, we looked at the energetic difference between C1 and C2 during the pump-probe experiments. The results are mapped out in Figure III.21a) on which the C1 and C2 peak positions are represented. To eliminate the possible charge/photoconductivity effects, the lifetime is deduced from the energetic difference between C1 and C2 positions (Figure III.21b)).

Two characteristic times are found: τ_{ON} and τ_{OFF} which correspond to the response time of the molecular system during excitation and de-excitation time, respectively. τ_{ON} is smaller than τ_{OFF} as the absorption process is faster than de-excitation one. The de-excitation time is quite long (30 ms).

The absence of a rigid shift eliminates the photovoltage hypothesis. The photoconductivity/charging hypothesis remains if differential charging occurs. A careful examination of a possible charging effect should be realized, using efficient compensation methods. [124] Finally, if one considers the excitonic hypothesis that remains when the other two possibilities are eliminated, the typical times are those of a phosphorescence process via a triplet state. DFT C 1s ionization energies should be calculated in the triplet state. Only then, the long-life time of the valence exciton might be put in relation with to the absence of fs charge transfer in the excitonic absorption state.

III.3 Charge transfer from DIPO-Ph_4 to ITO

Chapter IV

DIPO-Ph_4 as interfacial layer for organic photovoltaic devices

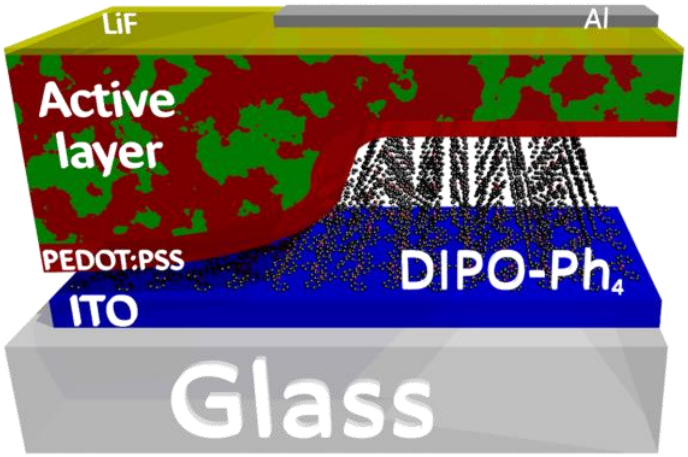

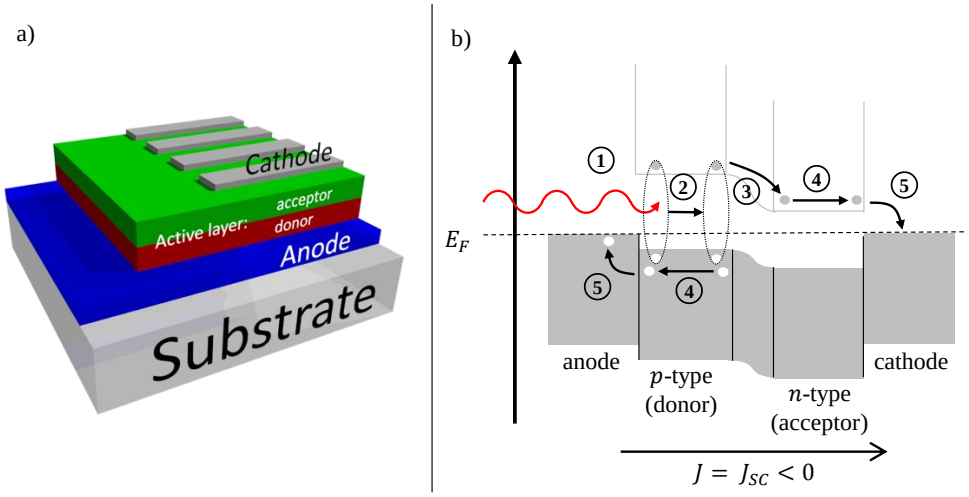

Figure IV.1 – a) Typical solar cell stack; b) Energetic representation of the photovoltaic process in a solar cell.

IV.1 Solar devices

As DIP is a good donor molecule, we made some organic solar cells to see the effect of the DIP molecule on the cell efficiency. The rapid depletion of conventional energy sources and increasing energy demand, have encouraged intensive research for renewable and sustainable energy sources. [125] Renewable energy sources mainly consist of sunlight, wind, tides, waves, and geothermal heat. [126] As one of cleanest energy resources, solar energy has been developed into three significant technologies, such as solar heating, solar photovoltaic (PV) and concentrating solar power. Among these technologies, solar PV technology has attracted numerous interest and research all over the world. [127, 128]

A typical solar structure consists of cathode and anode electrodes, a cathode interfacial layer (cIFL)/an anode interfacial layer (aIFL), and an active layer (p-n junction). Aiming at achieving a higher efficiency, extensive efforts have been focused on the developments of active layer materials, device architectures and interfacial layers. Before explaining in more details the interface layers, it is vital to understand the physical processes occurring from the active layer to the electrodes under illumination.

IV.1.1 Photovoltaic mechanism

To understand the photovoltaic effect, the operation of a solar cell can be described in five steps (Figure IV.1).

1. Photon ionization:

IV.1 Solar devices

Any incident photon with an energy $h\nu$ greater than the semiconductor gap (E_G) of the active layer is absorbed. This process is particularly efficient in materials with very high molar extinction coefficient (ϵ_0). Since the molar extinction coefficient of the donor is generally much greater than that of the acceptor, the latter is neglected in most of cases. The photon energy allows an electron to go from the VB to the CB of the p-type material. Once the electron-hole pairs, called excitons, are formed, they have a very limited lifetime ($\sim$1 ns) and can recombine according to different radiative processes (fluorescence or phosphorescence) or to non-radiative ones (heat).

2. Excitons diffusion:

With an anisotropic nature, all the excitons will not diffuse to the donor-acceptor interface and therefore do not participate in the photovoltaic process. Furthermore, the presence of trapping sites within the material (impurity) limit the effective excitons number. However, diffusion can be promoted within a highly organized material, which increases their diffusion length.

3. Excitons dissociation:

This process takes place at the donor-acceptor interface, where the existence of the internal field (V_{bi}) allows the dissociation of the exciton. During the dissociation of the exciton, the electron can be transferred from the p-type CB to the n-type CB while the hole remains in the p-type VB. Negative and positive polarons are created in materials.

4. Carrying the charges:

The polarons scatter to their respective electrodes by a "jump" mechanism. This mechanism is more efficient for high carrier mobility material. This mechanism may also be affected by the defects existence within the material.

5. Collection of charges:

This should be improved due to the ohmic contact between the semiconductors and the metal. The existence of trapping sites at the electrodes also limit the step efficiency.

A density-voltage (J-V) curve is a direct and significant characterization method to express the solar cell performance. Figure IV.2 is a typical J-V curve under dark and light illumination.

As important parameters of the solar cells, power conversion efficiency (PCE), open-circuit voltage (V_{OC}), short-circuit current density (J_{SC}), and field-factor (FF) play significant roles in defining the photovoltaic performance (Appendix C.3).

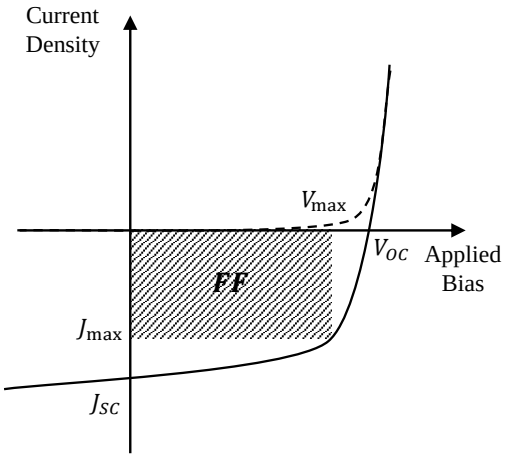

Figure IV.2 – Typical *J-V* curve: under dark (dashed line) and under illumination (continuous line).

IV.1.2 Photovoltaic devices

a) Photovoltaic generations

Different generation PV technologies have been developed, i.e. crystalline/polycrystalline silicon solar cell (1st generation solar cells), thin film solar cells (2nd generation solar cells), polymer solar cells (3rd generation solar cells) and perovskite solar cells (4th generation solar cells).

1st generation solar cells

So-called 1st generation solar cells, which are based on crystalline and polycrystalline or amorphous silicon, are still dominating the PV market. Their PCE range from 18 to 25 %. Even though they have higher PCE and stability, but they remain expensive and the fabrication process is complicated [129]

2nd generation solar cells

They are also called thin film solar cells based on II-VI semiconductors, such as cooper indium gallium selenide (CIGS, $PCE = 22\,\%$), cadmium telluride (CdTe, $PCE = 20\,\%$), amorphous silicon ($PCE = 20\,\%$), and gallium arsenide (GaAs, $PCE = 38\,\%$). [129, 130, 131, 132] However, CdTe technology requires the manipulation of highly toxic material. Moreover, the recycling life is not well enough controlled to limit environment pollution. GaAs remains expensive. Development of amorphous silicon yields to lower cost processes compared to 1st generation solar cells, but it has poor stability. From a general point of view the achievement of inorganic solar cell allows reaching high and stable performances,

but requires complicated fabrication processes.

3rd generation solar cells

To balance PCEs and low costs, organic solar cells (OSCs), dye-sensitized solar cells (DSSCs), and organic-inorganic hybrid solar cells, have been developed. These solar cells are easy to fabricate at large-scale with low cost, but the main challenges are their low PCEs (maximum ∼10 %) in comparison with 1st and 2nd solar cells, along with the chemical stability in front of dioxygen from air. [133, 134, 135]

4th generation solar cells

Lead halide perovskite solar cells (PSCs) have increased rapidly in recent years with PCE of ∼19 % and ultimately low-cost and stability. [136] However, because of the toxicity of lead and solubility of perovskites in water, they can cause human health and environmental problems. Therefore, scientists try to use other metals, such as tin, to replace lead. Nevertheless, the photovoltaic performances of lead-free halide PSCs are less effective than lead-based ones. [137, 138]

b) Organic solar cells

The development of organic solar cells followed the development of organic electronics with organic light-emitting diode (OLED) technology [139] and organic field-effect transistor (OFET). [140, 141] Organic photovoltaics really took off in 1986, when for the first time Tang *et al.* achieved a PCE of 1 %. [142] This performance, carried out using a copper phthalocyanine and 3,4,8,10-perylene tetracarboxylic bisbenzimidazole as two-layered p-n system, was not overcome before the early 2000s. In the last decade, yield improvement has accelerated. Shaheen *et al.* achieved 2.5 % as PCE with a bulk heterojunction (BHJ) of MDMO-PPV and PCBM. [143]

Pursuing more effective active layer materials is not the only solution. Indeed, the device architecture plays a significant role in obtaining high performance OSC devices. A conventional single BHJ structure (see Figure IV.3) is considered as the best candidate for OSCs with easy fabrication and low cost. To further enhance photon harvesting in single junction solar cells, a second donor or acceptor material is embedded into the active layer and forms a ternary structure, named organic ternary solar cells. [144, 145] The fundamental limitations of the OSC performance are significantly based on thermodynamical losses, such as the sub-band gap transmission and the thermalization of hot charge carrier issues. To avoid both effects simultaneously, tandem, or multi-junction solar cells have been developed in the past decades. [144, 146, 147]

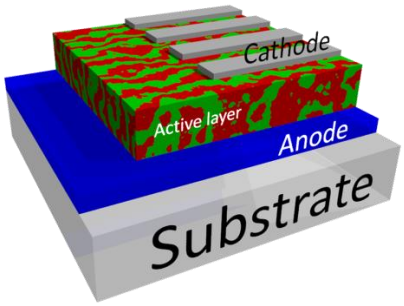

Figure IV.3 – Bulk heterojunction solar cell.

Therefore, yields have steadily increased with a PCE greater than 10 % on a 1 cm^2 cell. Heliatek, with a PCE record of 13.2 %, brought photovoltaics to the marketing door. [148] From an industrial point of view, organic-based devices have numerous advantages: the possibility of obtaining large modules, low cost processes and flexibility. The industrial objective to be achieved is the production of 1 W $\cdot$ m^{-2} for 1 \$.

In organic solar cells, the typical active layer materials consist of a low bandgap polymer (a donor) and an acceptor. The significant research of active materials has been mainly undertaken on developing relatively low bandgap donor materials to extend absorption and harvest more solar energy. [149] Currently, one of the most widely used donor materials is poly(3-hexylthiophene) (P3HT) but lot of thiophene derivatives have been developed (PCPDTBT, PCDTBT, PBDTTT-C: see donors in Figure IV.4). [150, 151, 152, 153] Concerning the acceptors, [6,6]-phenyl-C61-butyric acid methyl ester (PCBM) is widely used but its CB energy level limits the V_{OC} for OSC performance. To get higher V_{OC} and maximum absorption, other fullerene derivatives and non-fullerene acceptors (see acceptors in Figure IV.4) have been synthesized and applied to OSC devices. [154, 155, 156, 157]

Besides the pursuit of improved new active materials and device architectures, the long-time stability of OSC devices simultaneously requires much attention for successful commercialization. [158] The degradation of OSC devices are highly associated with humidity, oxygen, heat, or light. [159, 160] The strategies to stabilize OSC devices have involved insertion of interface layers (IFLs), encapsulation materials development and active layer purity optimization. [161, 162, 163, 164]

c) Interfacial layer

Among the stability strategies and charge collection improvement, much efforts have been dedicated to the insertion of interfacial layers between active layers and electrodes, due to the simultaneous ability of stabilizing OSCs and maximizing PCEs. [165]

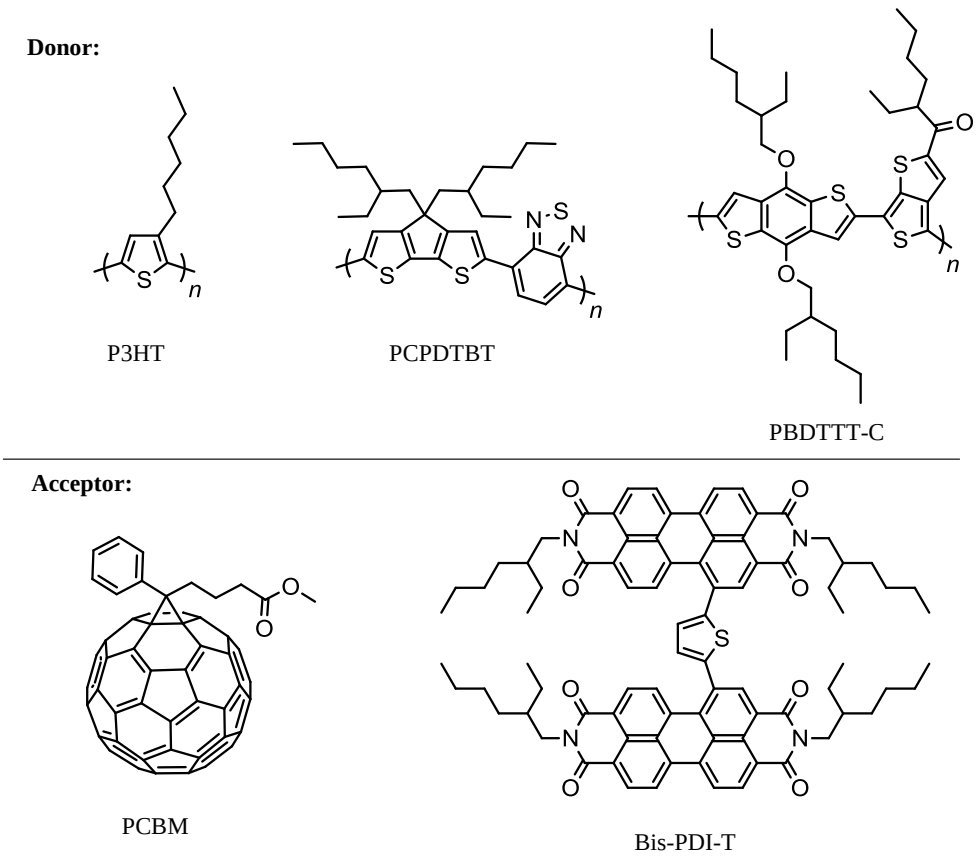

Figure IV.4 – Examples of used molecules for donor and acceptor materials in organic solar cells.

The main functions of the interfacial layers can be summarized as follows

- Inhibit a chemical/physical reaction between the active layer and electrodes.
- Form an optional contact for some types of carriers.
- Determine the polarity of the photovoltaic device.
- Adjust the barrier height between the active layer and electrodes.
- Play the role of an optical spacer.

With the respect to these functions, interfacial materials can be mainly divided into two types, hole (anode IFL) and electron (cathode IFL) interfacial layers.

In the conventional OSC devices, poly(3,4-ethylenedioxythiophene) polystyrene sulfonate (PEDOT:PSS) is widely used as an anode IFL to break the energetic barrier between electrodes and active layers. However, the acidic and hydrophilic properties of

PEDOT:PSS make it sensitive to oxygen and moisture, leading to a rapid degradation and short lifetime in OSCs. [159, 166, 167] Hence, it is essential to discover new anode interface materials to replace PEDOT:PSS.

Numerous inorganic metal oxides have been developed and used as anode/cathode interfacial layers, due to their high stability in comparison with organic interfacial layers. Among the family of cathode IFLs, *n*-type semiconductor metal oxides (*e.g.* titanium oxide [168] and zinc oxide [169]) exhibit excellent performances, due to their ambient stability, high optical transparency, outstanding solution process ability and superior capability of extracting/transporting electron carriers. On the other way, anode interfacial layers such as *p*-type semiconductor transition metal oxides (*e.g.* vanadium oxides, [170] tungsten oxide, [171] and molybdenum oxide [172]) have demonstrated good device performance by promoting hole transport process and stability of devices. The oxygen vacancies of *p*-type metal oxides play an important role in their electronic properties. Tuning the oxygen level (valence band) allows creating filled gap states in the gap, and finally enhancing hole transport between active layers and anode electrodes. [173]

Small molecules have also been developed for hole transport layers. This has already shown its efficiency in the field of OLEDs and photo-detectors. Hains and Marks have shown that cross-reactions with silanes can form an effective hopper-conveying layer. [174] TPDSi2, PABTSi2 or TPDB were proved to be successfully used as selective layers for extraction of holes. TPA-PFCB is also used as a hole transport layer with PEDOT:PSS to form an interface bilayer. In addition to an improvement of the J_{SC} of the cells, IFL protects the anode from PEDOT:PSS corrosion. Our team has explored the benefit of depositing hole-transport molecular solid of the DIP family. [57] DIPS-Ph$_4$ has been used on ITO to finally form an ITO/DIPS-Ph$_4$/P3HT:PCBM/LiF/Al cell in which the J_{SC} is efficiently increased. [26] Current sensing contact mode atomic force microscopy (CS-AFM) shows that there is an increase in the total number of hole-carrying pathways with respect to a PEDOT:PSS IFL. [26]

IV.2 Organic electronics application

Now, could the DIPO-Ph$_4$ layer be an efficient interfacial hole collecting layer per se in the context of the state-of-the-art bulk heterojunctions (BHJ) of organic photovoltaic?

IV.2.1 Energetic alignment

The BHJ are blends of P3HT donor and PCBM acceptor. Some predictions can be made from the present data and from already published UPS results [175] and inverse

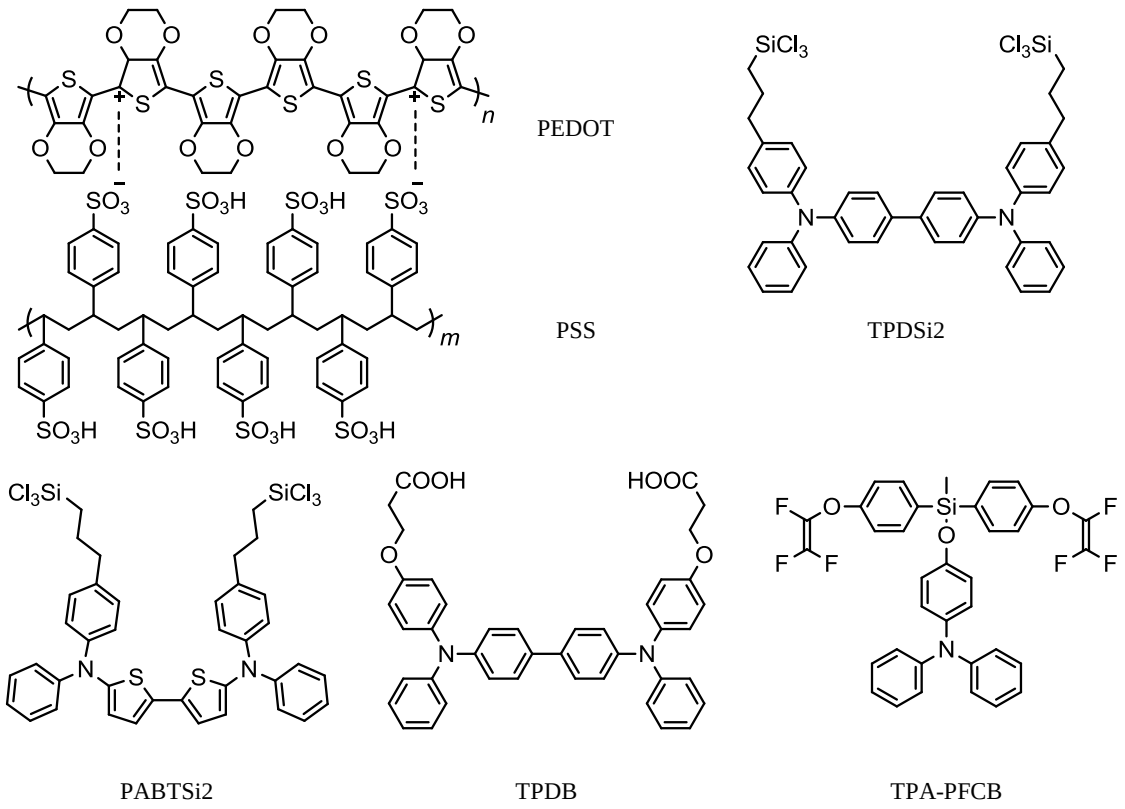

Figure IV.5 – Examples of used molecules for anode IFL in organic solar cells.

photoemission spectroscopy (IPES) works. [176] The expected energy level schemes of the interfaces are given in Figure IV.6.

Vacuum-level alignment should be obeyed at the DIPO-Ph_4/P3HT interface. Indeed, the work function of P3HT is 3.9 eV [175] (identical to that of DIPO-Ph_4) and its ionization energy (HOMO edge) is 4.65 eV. [176] As the ionization energy (HOMO edge) of DIPO-Ph_4 is 4.6 eV, the HOMOs of the two materials are practically coincident. Therefore, the injection of holes from P3HT to ITO via the DIPO-Ph_4 interfacial layer remains barrierless.

The interfacial DIPO-Ph_4 may also come into contact with PCBM. Figure IV.6 shows the expected energy level scheme at the DIPO-Ph_4/PCBM interface. The work function of DIPO-Ph_4 donor (3.9 eV) is smaller than that of the PCBM acceptor, 4.3 eV. [175] Therefore electron charge should be transferred from DIPO-Ph_4 to PCBM. After level alignment, an energy offset Δ of $\sim$ +0.4 eV appears. [175, 177] This offset (generally ignored in most depictions of the energy schemes of these photovoltaic materials) will bring up the PCBM LUMO in energy and make it closer to that of DIPO-Ph_4. Considering that the transport gap in DIPO-Ph_4 is greater than 2 eV (the value of the optical gap, see

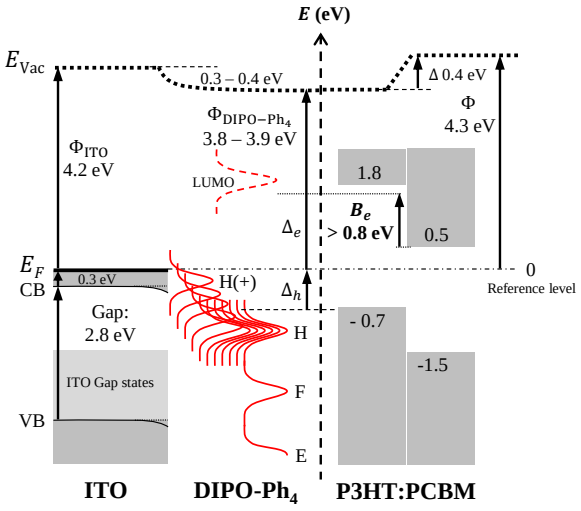

Figure IV.6 – Expected energy level scheme of the ITO/DIPO-Ph$_4$/P3HT:PCBM system. The work functions of DIPO-Ph$_4$ and of P3HT [175] are both equal to 3.9 eV (and coincidentally the vacuum levels are aligned). The HOMO energy versus E_{Vac} (vacuum level) in P3HT is from Ref. 176. The Fermi level in metallic ITO, P3HT, and PCBM [175] are assumed to be aligned. Δ is the energy offset. The LUMO/HOMO energies versus vacuum are from Ref. 176. As the LUMO – HOMO gap in DIPO-Ph$_4$ is greater than 2 eV (see Figure I.6) the minimum electron blocking barrier B_e^{min} is 0.8 eV. E_F and E_{Vac} are the Fermi and vacuum level, respectively (E_F is the zero of energies).

Figure I.6), and considering that the PCBM LUMO is 3.8 eV below the vacuum level, [176] then the LUMO (DIPO-Ph$_4$)/LUMO (PCBM) energy difference is greater than 0.8 eV. Therefore DIPO-Ph$_4$ should remain an efficient blocking barrier (B_e) to electrons coming from PCBM, despite the positive value of Δ.

To sum up, the DIPO-Ph$_4$ interfacial layer presents a favourable energy level scheme to collect holes from P3HT and to block electrons from PCBM. However, if this condition is necessary, it is not sufficient for the material to behave as an efficient hole collector, and to improve the performances of the BHJ cells. The conductivity of the DIPO-Ph$_4$ material and the number of good "contact" points with the ITO substrate (per surface unit) must be also high. In the case of the parent molecule DIPS-Ph$_4$, CS-AFM points to a sizeable increase in hole-carrying pathways with respect to PEDOT:PSS. [26]

IV.2.2 Photovoltaic response

We prepared three OSCs with an active layer of P3HT:PCBM (see Appendix B.2), with a "thin" (0.3×10^{15} molecule $\cdot$ cm^{-2}), a "thick" (1×10^{15} molecule $\cdot$ cm^{-2}) layers of

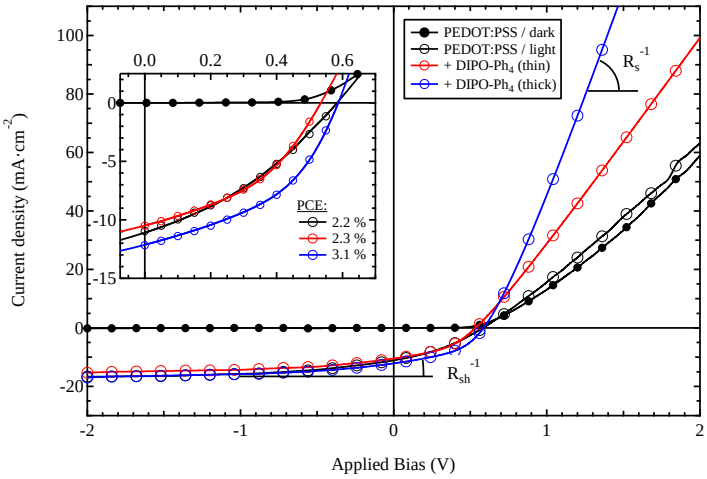

Figure IV.7 – Photovoltaic characterization with 3 different IFLs under $100\,\mathrm{mW \cdot cm^{-2}}$, with a zoom on the interesting area in inset.

DIPO-Ph_4 and a reference based on PEDOT:PSS (5 nm), all three as interfacial layers. Prior to characterization of the photovoltaic cells, we ensured that the structuration obtained onto ITO was comparable to the Si_3N_4. It is worth noticing that on top of the DIPO-Ph_4 layer, a thin layer (5 nm) of PEDOT:PSS was deposited to prevent the organic solvent of P3HT:PCBM deposition from modifying the DIPO-Ph_4 morphology.

Table IV.1 – PV parameters ($100\,\mathrm{mW \cdot cm^{-2}}$) of devices with different IFLs and P3HT:PCBM as active layer.

Anodic IFLs	PCE (%)	V_{OC} (mV)	J_{SC} ($\mathrm{mA \cdot cm^{-2}}$)	FF (%)	R_{sh} ($\Omega \cdot \mathrm{cm^2}$)	R_s ($\Omega \cdot \mathrm{cm^2}$)
PEDOT:PSS	2.2	583	11.1	34	174	22
DIPO-Ph_4, thin	2.3	534	10.5	41	191	14
DIPO-Ph_4, thick	3.1	586	12.1	44	191	7

The photovoltaic cell performances are given in Figure IV.7 and in Table IV.1. The thick DIPO-Ph_4 layer reaches a maximum power conversion efficiency (PCE) of 3.1 %, using a solar simulator calibrated at $100\,\mathrm{mW \cdot cm^{-2}}$. The open circuit voltage (V_{OC}) and the fill factor (FF) are 586 mV and 44 %, respectively. The current density (J_{SC}) is $12.1\,\mathrm{mA \cdot cm^{-2}}$. These results were compared to a reference cell using only 5 nm PEDOT:PSS as interfacial layer, prepared in the same conditions, and which shows a lower PCE at 2.2 %. The increase of the fill factor revealed not only better electronic processes but also an increase in the ratio of the charge carrier collection. A smaller number

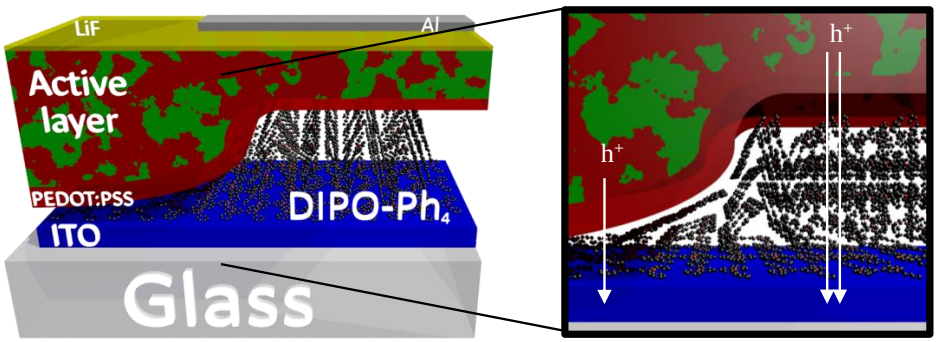

Figure IV.8 – Schematic representation of the solar cell morphology. A better hole collection occurs through crystallized DIPO-Ph$_4$ layer than through PEDOT:PSS.

of holes are recombined to be collected at the ITO electrode. Consequently, the short circuit current increases and the overall yield rises by 47 %.

In addition to the performance, the physical constants extracted from the current density versus voltage under illumination described the same phenomena as the one presented in STXM. Indeed, the DIPO-Ph$_4$ layer demonstrates a favourable hole transport collection at the ITO anode which is consistent with the electronic behaviour of DIPO-Ph$_4$. The series resistance decreases to $7\,\Omega \cdot \mathrm{cm}^2$ when for the reference cell the value was measured at $22\,\Omega \cdot \mathrm{cm}^2$ and $14\,\Omega \cdot \mathrm{cm}^2$ for the thinnest IFL based on DIPO-Ph$_4$. Despite the increase of the thickness of the organic interface, the resistance decreases. On the other side, the shunt resistance (R_{sh}), which reflects the electrical short-cut and more generally the overall electronical recombination at the interface, remained the same for the three layers, high enough to avoid short-cut losses. The small decrease of the series resistance leads to a 50 % increase of performance.

The DIPO-Ph$_4$ layer has no effect on the V_{OC}. This parameter mainly depends on the LUMO donor/HOMO acceptor difference in the active layer. On the contrary, we observe a J_{SC} increase of $1\,\mathrm{mA} \cdot \mathrm{cm}^{-2}$ due to the lowering of the series resistance. [26, 178] As hole transport layer and compared to PEDOT:PSS, DIPO-Ph$_4$ increases the efficiency of charge collection at the ITO anode (Figure IV.8). On thick DIPO-Ph$_4$, it is worth noticing that the fill factor increases significantly despite the surface mounds. Often a highly-structured surface is frequently associated to a rough surface and a bad layer contact. [179] However, the STXM investigations demonstrated that it was possible to form a bulk structure that maximizes the orbital interaction to reach the best electronic performance.

Chapter V

DIP heteroatom effect: morphology and electronic description

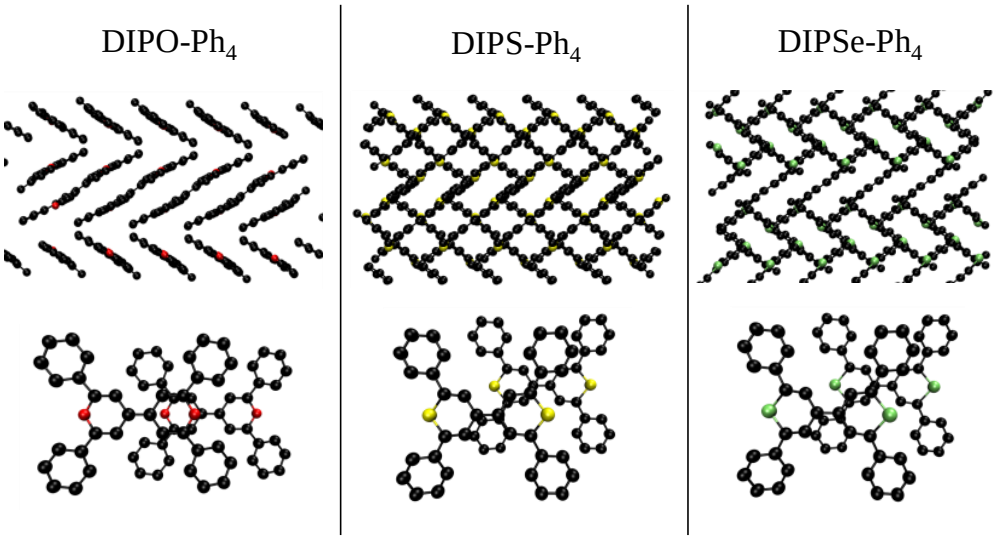

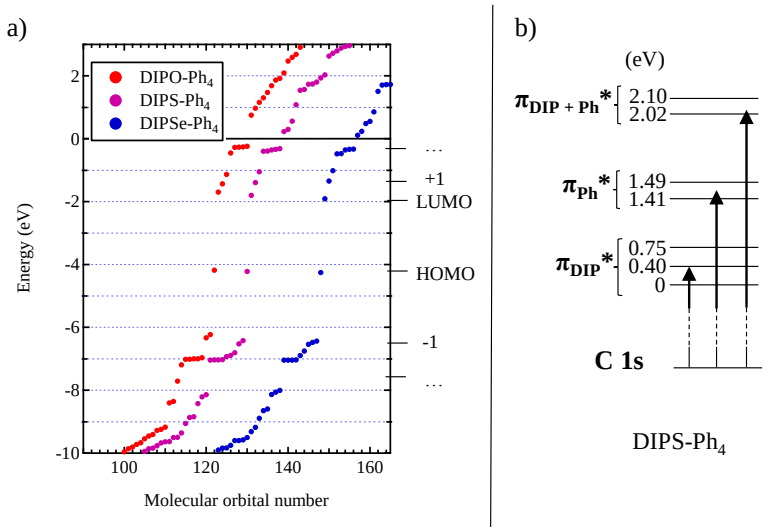

Figure V.1 – a) DFT calculated molecular orbital levels; b) Electronic scheme of the C 1s of DIPS-Ph_4. Indicated energies are related to the LUMO.

V.1 ITO/DIP layer morphology

V.1.1 Molecular description

The ITO/DIPO-Ph_4 interface leads to a charge transfer from the first organic layer to the metal substrate. The alignment mode (LUMO pinning, Schottky-Mott mode or HOMO pinning) depends on the value of the metal work function in comparison to the Φ^+ and Φ^- values for the organic material. We decided to keep working with ITO but we changed the dipyranylidene structure. We studied the sulphur and the selenium derivatives. Note that the electronegativity decreases from O to Se atoms. [180]

Between the DIP derivatives (DIPO-Ph_4, DIPS-Ph_4, and DIPSe-Ph_4), the major difference, beside the atomic element, comes from the increasing dihedral angle between the DIP core and the Ph groups. As a free molecule, the angle increases from ∼17° (DIPO-Ph_4) to ∼39° (DIPS-Ph_4), and ∼42° (DIPSe-Ph_4). We perform DFT calculations for the neutral (Figure V.1a)) to determine the OM energy levels.

Calculated DFT molecular orbital energies are close for the three DIP derivatives. As a difference, we can notice that the energy gap (LUMO−HOMO difference) decreases from DIPO-Ph_4 (2.48 eV), to DIPS-Ph_4(2.42 eV), and to DIPSe-Ph_4 (2.35 eV). This observation agrees with the diminishing optical gap along the O, S, and Se series (see Figure I.6c)) for the DIP derivatives deposited as thin solid films.

The free-molecule description does not predict any spectacular change in the electronic structure apart from the sizeable increase in the dihedral angle. However, the latter has

a strong impact in the molecular stacking in the solid state and on the adsorption mode on the substrate. As a reminder, in the solid state, the dihedral angle measured via XRD are 7.8, 12.4, and 14° for DIPO-Ph_4, DIPS-Ph_4, and DIPSe-Ph_4, respectively, but the packing mode is completely different (see Figure I.7). Therefore, we performed AFM, STXM, and XPS measurements on ITO/DIPS-Ph_4 and DIPSe-Ph_4 samples.

V.1.2 DIPS-Ph_4 and DIPSe-Ph_4 growth mode

For each DIP derivatives, three samples have been prepared, the QB-coverages being 0.5×10^{15}, 2×10^{15}, and 10×10^{15} molecule $\cdot$ cm^{-2}. We characterized the layer morphology (the organic layer on ITO substrate) via AFM and performed STXM on the DIPS-Ph_4 layers to study the molecular orientation and growth mode (the organic layer on Si_3N_4 substrate). Concerning the absorption transitions for the DIPS-Ph_4 structure, unoccupied state energies (Figure V.1b)) are found to be similar as for the DIPO-Ph_4 (Figure II.4) and thus the description of the C 1s transitions is the same as the one for the DIPO-Ph_4 structure.

Concerning DIPS-Ph_4 3D clusters are observed from the 0.5×10^{15} molecule $\cdot$ cm^{-2} (Figure V.2a_1)). Molecules cover only 5 % of the ITO surface, with an average diameter of 100 nm. The AFM measurement reveals a molecular coverage of only 0.18×10^{15}. The average height of the clusters is 15 nm. For the 2×10^{15} molecule $\cdot$ cm^{-2} sample (Figure V.2b_1)), the clusters cover 20 % of the ITO surface and the molecular coverage is 0.65×10^{15} molecule $\cdot$ cm^{-2}. The average height increases to 20 nm. In comparison with the DIPO-Ph_4 layers, clusters are more elongated. Besides, this growth leads to the formation of twinned clusters. In the case of the DIPO-Ph_4 layer, to obtain twinned clusters, energy was brought to the system via a under annealing treatment. For DIPS-Ph_4, the diffusion may be easier at room temperature. The 10×10^{15} molecule $\cdot$ cm^{-2} sample confirms the observation (Figure V.2c_1)). Molecules are forming a continuous film covering the entire ITO surface. AFM measurements show that 13×10^{15} molecule $\cdot$ cm^{-2} have been evaporated.

For the DIPSe-Ph_4 structure (Figure V.2d), e), and f)), the 3D clusters are square-shaped. They cover 10, 60 % and the entire ITO surface for the 0.5×10^{15}, 2×10^{15}, and 10×10^{15} molecule $\cdot$ cm^{-2} (QB-coverage), respectively. AFM measurements show coverage of 0.29×10^{15}, 1.6×10^{15}, and 10×10^{15} molecule $\cdot$ cm^{-2}.

The difference between the DIP structures lies in the shape of the clusters: slightly elongated for the DIPO-Ph_4, elongated and twinned for the DIPS-Ph_4, and nearly squared for DIPSe-Ph_4. As the crystallization inside the layer is different between the three structures (see Figure I.7), it leads to different cluster shapes.

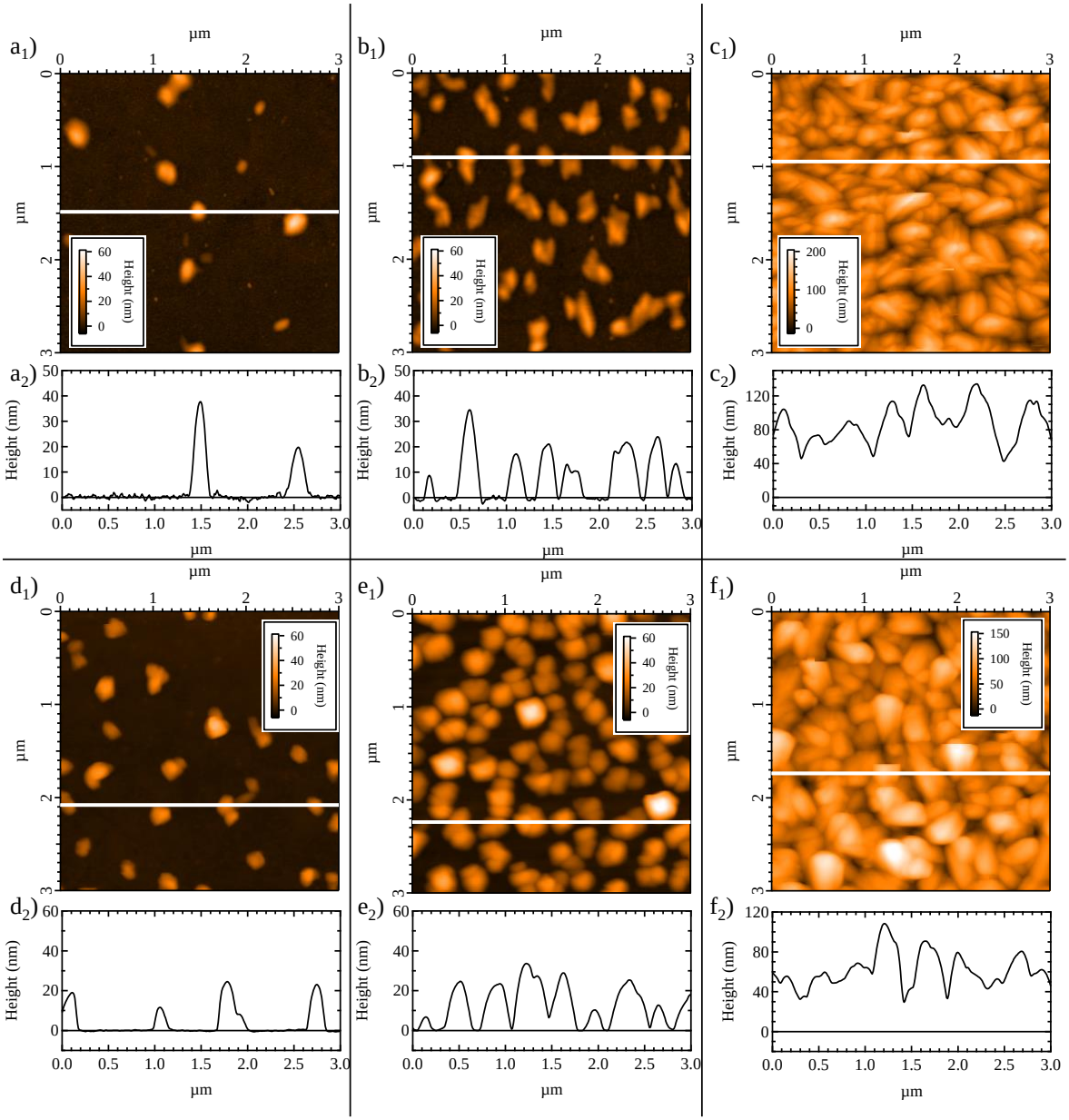

Figure V.2 – AFM images for DIPS-Ph_4 (a), b), and c)) and DIPSe-Ph_4 (d), e), and f)): a_1) d_1) QB-coverage of 0.5×10^{15} molecule $\cdot$ cm^{-2}; b_1) e_1) QB-coverage 2×10^{15} molecule $\cdot$ cm^{-2}; c_1) f_1) QB coverage 10×10^{15} molecule $\cdot$ cm^{-2}; a_2), b_2), c_2), d_2), e_2), and f_2) are the profiles indicated by the white straight lines in a_1), b_1), c_1), d_1), e_1), and f_1) respectively.

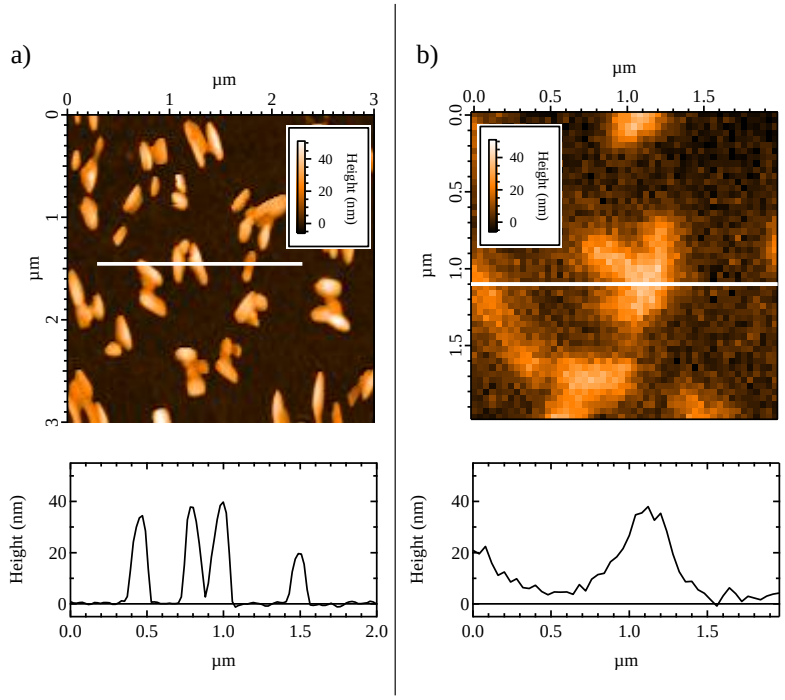

Figure V.3 – a) AFM image for DIPS-Ph_4: QB-coverage of 2×10^{15} molecule $\cdot$ cm^{-2}; b) Corresponding STXM image in thickness.

In the following, we will describe the molecular orientation of the DIP derivatives. We completed the STXM measurements for the DIPS-Ph_4 structure. An AFM/STXM correlation and a PCA (principal component analysis) decomposition have been performed (Figure V.3 and Figure V.4). Note that for DIPS-Ph_4 the IP_{core} for the C 1s core level has been taken as equal to the DIPO-Ph_4 one.

The DIPS-Ph_4 layer morphology on Si_3N_4 is similar than the one on ITO: twinned, elongated structure with an average height of 30 nm. The STXM measurement agrees with the AFM image: twinned clusters with an average cluster height of 40 nm. Let us now focus on the absorption spectra.

Results and discussions are the same to the DIPO-Ph_4 ones. π^* absorption decreases from the top to the edge, which means that first deposited layers are more parallel to the surface, and then there is a growth change (see Figure II.12). For the DIPS-Ph_4 structure, π^*_{Ph} absorption is less intense than in the case of the DIPO-Ph_4. The greater dihedral between Ph groups and DIP core results in a less efficient π^*_{Ph} absorption at normal incidence.

Therefore, the DIPS-Ph_4 layer grows as the DIPO-Ph_4 one. The first deposited molecules are parallel to the surface. Then, as intermolecular interactions are greater,

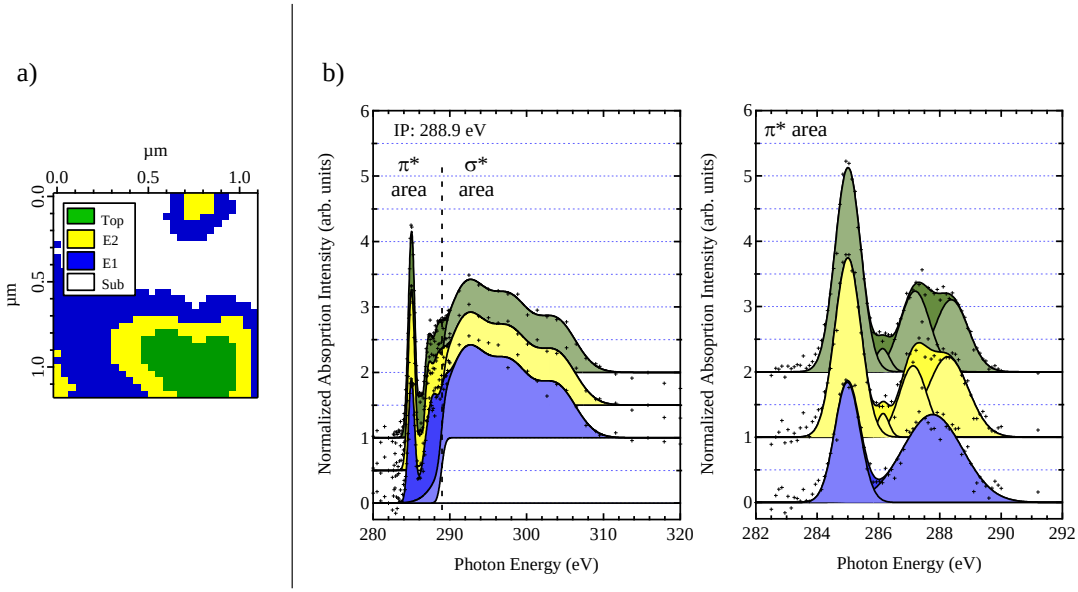

Figure V.4 – DIPS-Ph_4: a) STXM decomposition mapping; b) Absorption spectra extracted for each region (the substrate (Sub) spectrum is not represented as there is no absorption from this region). π^* area after subtraction of the step function background and the σ^* area.

DIPS-Ph_4 crystallizes and a change in the orientation is seen.

V.2 Electronic properties

Two samples of DIPS-Ph_4 and two samples of DIPSe-Ph_4 were prepared in our well-controlled evaporation system. Before measurements at the ALOISA beamline (ELETTRA synchrotron in Trieste, Italy), [181] samples were subjected to a long-time air exposure. To see the air exposure effect on the O 1s peak, an ITO substrate has been chemically cleaned and then air exposed during the same time as the DIP samples.

V.2.1 Core levels XPS spectroscopy

As a preliminary result of this part, we will present here the XPS characterization of the air exposed ITO starting with the overview spectrum (Figure V.5a)) to determine the carbon contamination.

The C 1s peak intensity is relatively small, which indicates a low carbon contamination. The C 1s/In $3d_{5/2}$ atomic ratio is 20 eV, which is slightly higher than the one of the previously presented ITO (see Chapter III.2.1b)). Concerning the O 1s spectra (Figure V.5b)), for $h\nu$ = 1100 eV (KE O 1s ~570 eV, λ_{ITO} ~1.21 nm), the bulk ITO

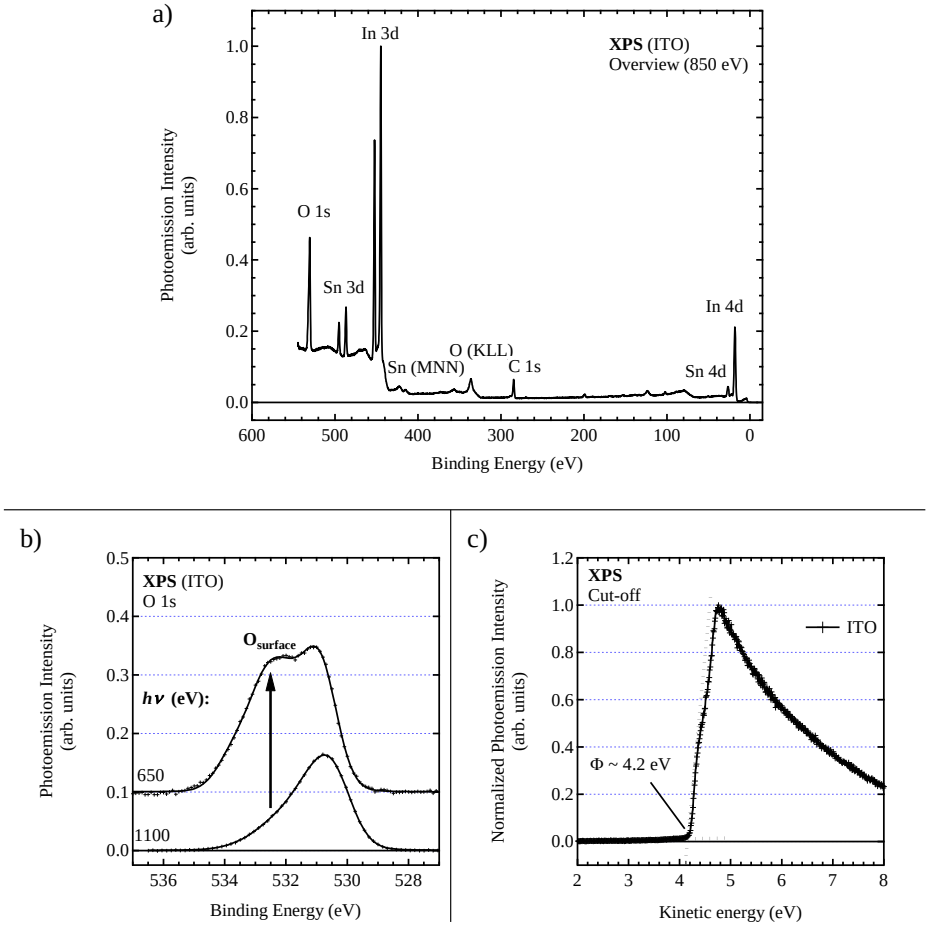

Figure V.5 – a) ITO overview spectrum for $h\nu = 850\,\text{eV}$. The labels refer to the core level peaks, Sn (MNN) and O (KLL) refer to the Auger decays; b) O 1s spectra of the air exposed ITO sample; c) SEEDC of ITO (as the kinetic energy scale is referenced to the Fermi level, the work functions correspond to the SEEDC cut-off energies). Coverages are obtained from QB-coverage. The spectra were recorded at the ALOISA beamline.

Table V.1 – Experimental In $3d_{5/2}$ principal peak value for $h\nu = 650\,eV$, FWHM of the Gaussian contribution and BE energy difference with the ITO peak. Coverages are obtained from QB-coverage.

Sample		G-FWHM (nm)	Peak I BE (nm)	Δ^{ITO} (nm)
Air exposed ITO		0.835	444.63	_
DIPS-Ph_4	2×10^{15} molecule $\cdot$ cm^{-2}	0.830	444.96	0.33
	10×10^{15} molecule $\cdot$ cm^{-2}	0.815	444.88	0.25
DIPSe-Ph_4	2×10^{15} molecule $\cdot$ cm^{-2}	0.942	444.63	0.00
	10×10^{15} molecule $\cdot$ cm^{-2}	0.895	444.66	0.03

oxygen structure is the same as the one previously described (see Chapter III.1.1). In more "surface sensitive conditions" ($h\nu = 650\,eV$, KE O 1s ~120 eV, λ_{ITO} ~0.51 nm), a new component is seen ($O_{surface}$). This component is attributed to oxygen contamination at the substrate surface. During air exposure, pollutants are deposited on the surface. Concerning the work function, the value is found at 4.20 eV (Figure V.5c)) which is the same as the ITO electronic properties previously described. Contaminants affect the work function as it was observed for the ITO presented in Chapter III.1.3.

We now consider the changes induced on the O 1s spectrum by the deposition of DIPS-Ph_4 and DIPSe-Ph_4. The O 1s spectrum measured at $h\nu = 650\,eV$ in "surface sensitive conditions" are given in Figure V.6a). The oxygen ITO structure is present but the $O_{surface}$ component is also observed. Contaminants are deposited on the DIP samples. Note that as the evaporation was done under UHV conditions on freshly chemically cleaned ITO substrates, there is no contamination between the ITO substrate and DIP layers. Nevertheless, considering this contaminants at the surface, we already plan to characterize *in situ* prepared ITO/DIPS-Ph_4 and DIPSe-Ph_4 to avoid too long-time air exposure (TEMPO beamline, September 2017).

Figure V.6b) and c) and Table V.1 present the DIPS-Ph_4 and DIPSe-Ph_4 deposition effects on In $3d_{5/2}$ spectra. The In $3d_{5/2}$ peak ($h\nu = 650\,eV$) moves to higher binding energy by 300 meV for the DIPS-Ph_4 samples, while no shift is observed for the DIPSe-Ph_4 samples. This shift, bigger than the one observed at ITO/DIPO-Ph_4 interface, indicates that DIPS-Ph_4 molecules interacting with the ITO surface slightly change the surface charge density. [19] This may be related to charge transfer at the interface for DIPO-Ph_4 and DIPS-Ph_4 but not for DIPSe-Ph_4.

Concerning DIPSe-Ph_4 for which no In $3d_{5/2}$ shift has been observed, we present in Figure V.7a) the Se 3d spectra. For 2×10^{15} and 10×10^{15} molecule $\cdot$ cm^{-2}, only one

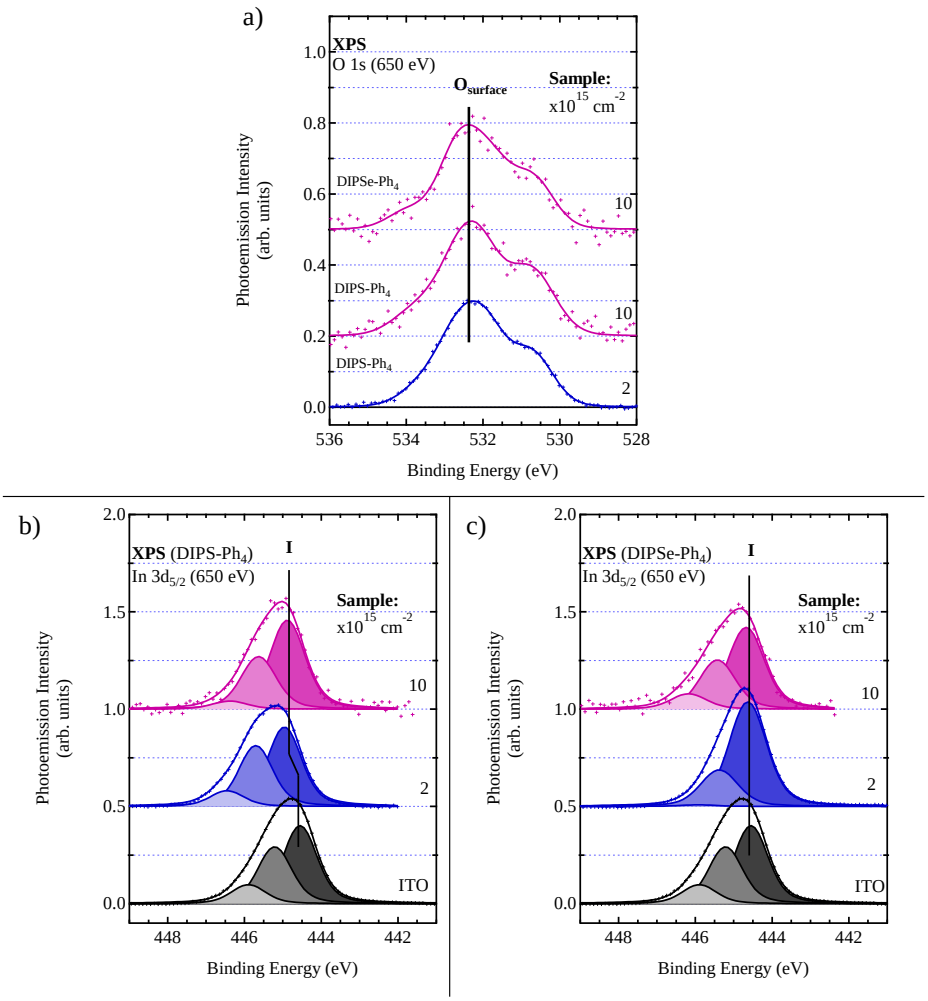

Figure V.6 – a) O 1s spectra of the air exposed DIPS-Ph_4 (2×10^{15} and 10×10^{15} molecule $\cdot$ cm^{-2}) and DIPSe-Ph_4 (10×10^{15} molecule $\cdot$ cm^{-2}); In $3d_{5/2}$ spectra of the chemically cleaned ITO sample and covered with increasing layers of b) DIPS-Ph_4 and c) DIPSe-Ph_4. The photon energy is indicated. The spectra were recorded at the ALOISA beamline. Coverages are obtained from QB-coverage.

component is observed with an atomic ratio Se/C equal to 6 %, which agrees with the theoretical ratio. There is no cationic form at higher (BE) which means that there may not be a charge transfer for the Se derivatives DIP.

For DIPS-Ph_4 the heteroatom (S 2p) core levels spectra would confirm the cationic formation (Figure V.7b_1)). For the 2×10^{15} molecule $\cdot$ cm^{-2} DIPS-Ph_4 sample, there are two components S1 and S2 at ∼164 eV and ∼169 eV, respectively. The atomic ratio (S1 + S2) /C is 6 % which is close to the theoretical ratio for the DIPS-Ph_4 molecule (5.9 %). The S2 component completely disappears for the 10×10^{15} molecule $\cdot$ cm^{-2} sample while S/C atomic ratio is still 6 %. The S2 peak is attributed to the cationic form of the sulphur DIP Yet, the S2 − S1 BE difference (∼5 eV) is much larger than the O2 − O1 BE difference (∼1.5 eV). The polarization energy ΔE_R must be similar between the oxygen and the sulphur derivatives.

In the following, we will explain the larger BE difference. One can think of a decomposition of the sulphur derivatives which must be seen on the C 1s spectra. C 1s peak (Figure V.7b_2)) does not highlight any decomposition components, and C 1s spectra look like the ones of DIPO-Ph_4 structure.

Consequently, as a good donor, [25] we think of a cationic [DIPS-Ph_4]$^{\bullet+}$ formation. In this way, DFT calculations have been performed on the S 2s IP_{core} as the S 2p spin-orbit doublet is not soluble. The S 2p IP_{core} has been determined by subtracting the S 2s − S $2p_{3/2}$ BE energy difference experimentally obtained (64.3 eV) in agreement with the literature. [182, 183] DFT results are presented in Table V.2. The calculated S $2p_{3/2}$ ionization energy (IP_{core}) of the neutral molecule ($IP_{\text{core}}^{\text{neutral,gas}}$) is 169.52 eV, while that of the molecular cation ($IP_{\text{core}}^{\text{cation,gas}}$) in the triplet state is 173.11 eV. The difference between the cationic (triplet) and neutral state DFT ionization energies is ∼3.6 eV which is lower than the S2 − S1 BE difference experimentally measured. We could think that for the DIPS-Ph_4 structure, 2 electrons are transferred to ITO. Now, when considering the dicationic state, the S $2p_{3/2}$ ionization energy $IP_{\text{core}}^{\text{dication,gas}}$ is 177.17 eV. The difference between the dicationic and the neutral state is now ∼7.7 eV which is bigger than the S2 − S1 BE difference.

The simple dielectric response model can be used for the dicationic state. Immersed in the dielectric medium, the relaxation energy is $4\Delta E_R$ in the initial state (charge $+2e$) and $9\Delta E_R$ in the core ionized state (charge $+3e$), assuming that the initial state and the final state ϵ_r constants are the same.

Then

$$IP_{\text{core}}^{\text{dication,gas}} - IP_{\text{core}}^{\text{dication,solid}} = 5\Delta E_R \tag{V.1}$$

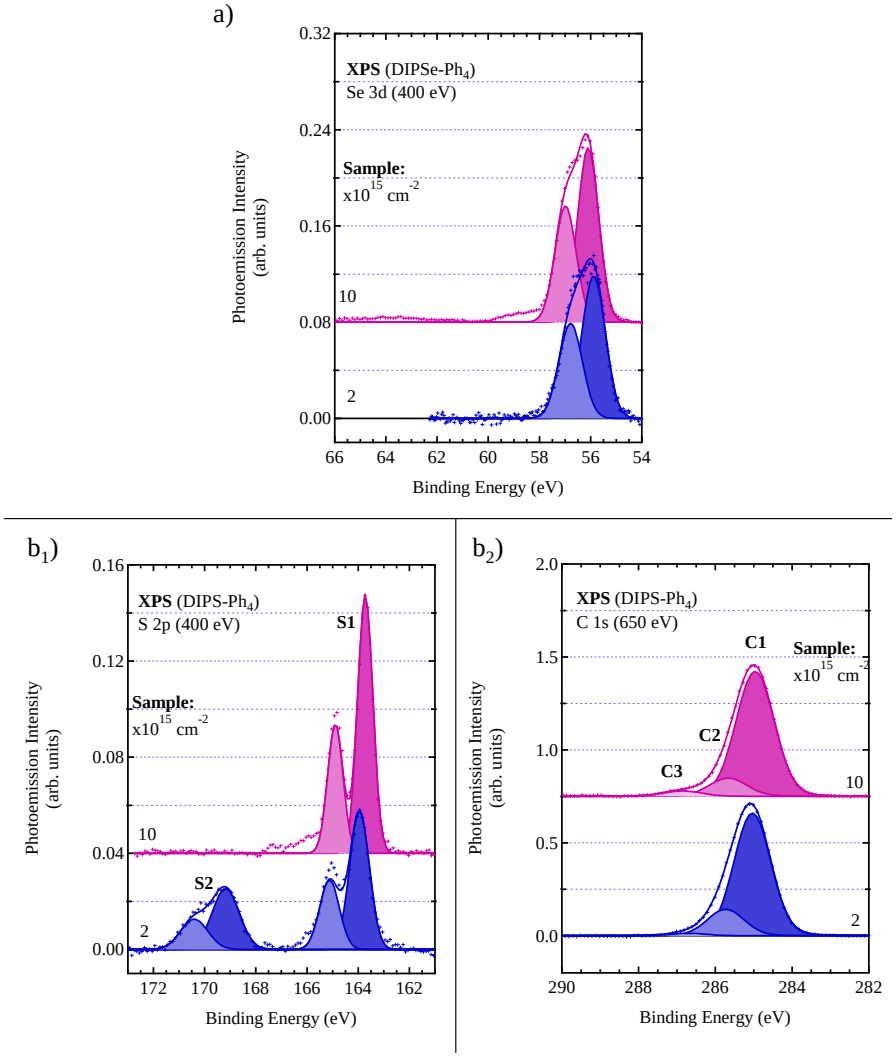

Figure V.7 – a) Se 3d spectra of the air exposed DIPSe-Ph_4 (2×10^{15} and 10×10^{15} molecule $\cdot$ cm^{-2}); b_1) S 2p and b_2) C 1s spectra of the air exposed DIPS-Ph_4 (2×10^{15} and 10×10^{15} molecule $\cdot$ cm^{-2}). The photon energy is indicated. The spectra were recorded at the ALOISA beamline. Coverages are obtained from QB-coverage.

Table V.2 – Calculated DFT $IP^{\text{neutral,gas}}_{\text{core or valence}}$, $IP^{\text{cation,gas}}_{\text{core or valence}}$, and $IP^{\text{dication,gas}}_{\text{core or valence}}$ values for the neutral, cationic and dicationic DIPS-Ph_4 molecule. For the cationic form, core-ionized energies are calculated for the triplet final state.

Core/valence level energy (eV)	**S 2s**	**S $2p_{3/2}$**
$IP^{\text{neutral,gas}}_{\text{core or valence}}$	233.82	169.52
$IP^{\text{cation,gas}}_{\text{core or valence}}$	237.41	173.11
$IP^{\text{cation,gas}}_{\text{core or valence}} - IP^{\text{neutral,gas}}_{\text{core or valence}}$	3.59	3.59
$IP^{\text{dication,gas}}_{\text{core or valence}}$	241.47	177.17
$IP^{\text{dication,gas}}_{\text{core or valence}} - IP^{\text{neutral,gas}}_{\text{core or valence}}$	7.65	7.65

Combining Equations (V.1) and (III.2) one obtains:

$$IP^{\text{dication,solid}}_{\text{core}} - IP^{\text{neutral,solid}}_{\text{core}} = \left(IP^{\text{dication,gas}}_{\text{core}} - IP^{\text{neutral,gas}}_{\text{core}}\right) - 4\Delta E_R$$

Considering that the ionization energy measured from the vacuum level is the sum of the binding energy measured from the Fermi level plus the work function, it comes that:

$$BE^{\text{dication,solid}}_{\text{core}} - BE^{\text{neutral,solid}}_{\text{core}} = \left(IP^{\text{dication,gas}}_{\text{core}} - IP^{\text{neutral,gas}}_{\text{core}}\right) - 4\Delta E_R$$

where $BE^{\text{dication,solid}}_{\text{core}}$ and $BE^{\text{neutral,solid}}_{\text{core}}$ are the binding energies (measured from the Fermi level) in the solid of the cation and of the neutral species, respectively, and $IP^{\text{dication,gas}}_{\text{core}}$ and $IP^{\text{neutral,gas}}_{\text{core}}$ are the ionization energies (measured from the vacuum level) in the solid state of the cation and of the neutral species, respectively.

A polarization energy ΔE_R of ∼0.7 eV explains why the energy difference of 7.65 eV between the dicationic and neutral species, calculated in the gas phase, can be reduced to 5 eV in the solid state.

Therefore, the charge transfer and dicationic hypothesis must be regarded as likely. In this case, the HOMO of the neutral will be completely empty for the dicationic state and no SOMO state should be observed in the VB spectrum.

V.2.2 Valence band energy level

We focus on the electronic structure of the valence band. The DIP derivatives valence band spectra measured at $h\nu = 140$ eV (Figure V.8a) and b)) exhibit the A – F features related to the occupied molecular orbitals (HOMOs) of DIPS-Ph_4 and DIPSe-Ph_4 as it was already described for DIPO-Ph_4.

In more details, in the case of the 10×10^{15} molecule $\cdot$ cm^{-2} (QB-coverage) DIPSe-Ph$_4$ sample, we observed the A – F series. The VB spectrum for the 2×10^{15} molecule $\cdot$ cm^{-2} sample is like an ITO VB and DIPSe-Ph$_4$ HOMO features are weak (Figure V.8a)).

Concerning DIPS-Ph$_4$, we have successfully prepared a very thick layer (10×10^{15} as QB-coverage, but 13×10^{15} molecule $\cdot$ cm^{-2} from AFM measurement), for which only the neutral state is seen, as proved by a single S1 component in the S 2p spectrum. We observe a clear narrow HOMO level well isolated from the A – F series (10×10^{15} sample, see Figure V.8b)). Note that we are also able to distinguish a new feature labelled D', thanks to a good signal/noise ratio. For the "thinner deposit" (2×10^{15} molecule $\cdot$ cm^{-2}), which exhibits two chemically shifted S 2p doublets, the H level is now strongly broadened.

We closely look at the H area for the DIPS-Ph$_4$ and DIPSe-Ph$_4$ (Figure V.8c)). For DIPSe-Ph$_4$ a single peak H is seen. It confirms the neutral DIPSe-Ph$_4$ form, and that there is no a charge transfer to ITO. Concerning the DIPS-Ph$_4$ (2×10^{15} molecule $\cdot$ cm^{-2}) a new state (G) at 2.3 eV is seen (1 eV above the HOMO state). In the hypothesis of the dicationic formation, the G state cannot come from a "dicationic HOMO" state, as this one would be empty after the double charge transfer. The HOMO-1 state for neutral DIPS-Ph$_4$ structure is 2 eV below the HOMO state (see Figure V.1a)). The G $-$ H energy difference is only 1.2 eV. Such a difference has already been observed for DIPO-Ph$_4$ with the H(+) and H states. Thus, G is attributed to the SOMO of the cationic DIPS-Ph$_4$.

How to explain the large S2 $-$ S1 BE difference with a S2 component coming from the cationic [DIPS-Ph$_4$]$^{\bullet+}$? DFT calculations for the cationic form lead to a too small difference. We thus consider sulphur reaction at the surface after the charge transfer. With the oxygen from the ITO substrate, sulphur could react and form a S$^+-$O bond. The chemical environment of the cationic sulphur is modified and the binding energy increases. In this case, we should see some modification in the oxygen structure of ITO. But, due to the oxygen contamination, we are not able to distinguish any significant modification. To do so, the future synchrotron experiment (September 2017) will include an *in situ* sample preparation to avoid a long-time air exposure.

V.2.3 Electron energy level scheme

Finally, to complete the study, we measured for the DIPS-Ph$_4$ and DIPSe-Ph$_4$ samples the work function to draw the electronic energy diagram (Figure V.9).

The SEEDC of the DIPS-Ph$_4$ deposits 2×10^{15}, 10×10^{15} molecule $\cdot$ cm^2 give a Φ value of 3.8 eV, independent of coverage. Considering that charge transfer occurs at the ITO/DIPS-Ph$_4$ interface, the value of Φ gives Φ^+ (3.8 eV). [10] On the contrary, there is no charge transfer at the ITO/DIPSe-Ph$_4$ and Φ is equal to Φ_{ITO} (4.2 eV).

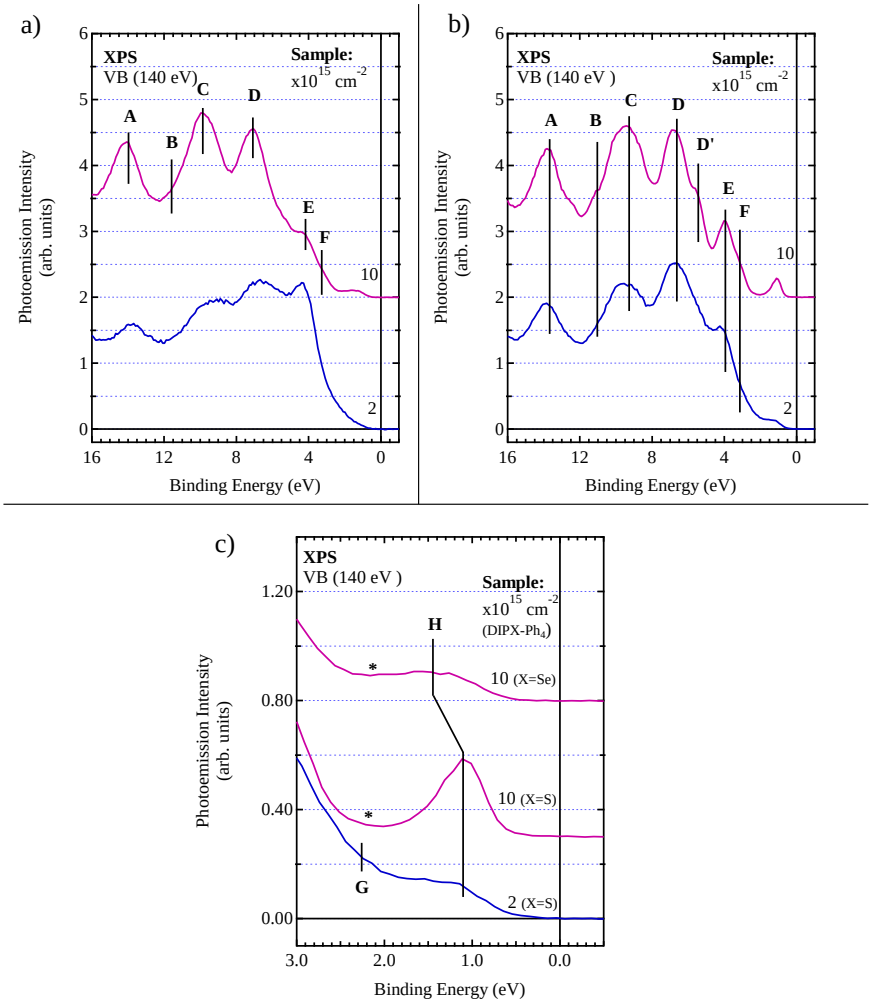

Figure V.8 – UV photoemission: a) DIPS-Ph_4 and b) DIPSe-Ph_4 valence band with HOMO levels; c) Zoom on the a) and b) image. Coverages in molecule $\cdot$ cm^{-2} are obtained from QB-coverage. H is the HOMO of the neutral molecule, G that of the cation (SOMO), and the asterisk (*) indicates that there is no SOMO observed.

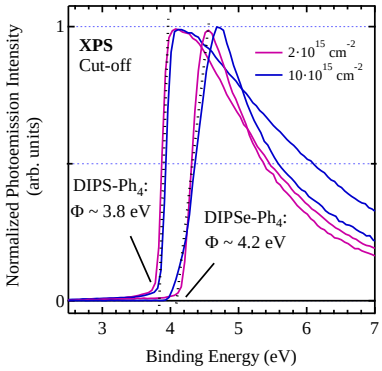

Figure V.9 – Secondary electron energy distribution curve (SEEDC) of various deposits indicated in inset (as the kinetic energy scale is referenced to the Fermi level, the work functions correspond to the SEEDC cut-off energies)

In Figure V.10, we present the energy level alignment of the ITO/DIPS-Ph_4 and ITO/DIPSe-Ph_4 interfaces.

From the VB spectra, we get the value of the hole barrier (Δ_h) which is the H edge position. The value is determined by withdrawing 0.6 eV to the H centroid position. This is what was done in the case of DIPO-Ph_4. Δ_h is found to be at 0.5 eV for DIPS-Ph_4 and 0.9 eV for DIPSe-Ph_4. Adding to the latter the respective work functions, the IP_v values for the DIP derivatives are thus, 4.3 and 5.1 eV for DIPS-Ph_4 and DIPSe-Ph_4, respectively. The ionization potential for DIPS-Ph_4 is similar to the one for DIPO-Ph_4 (4.6 eV). On the contrary, the DIPSe-Ph_4 IP_v is ∼0.5 eV bigger than the two other studied

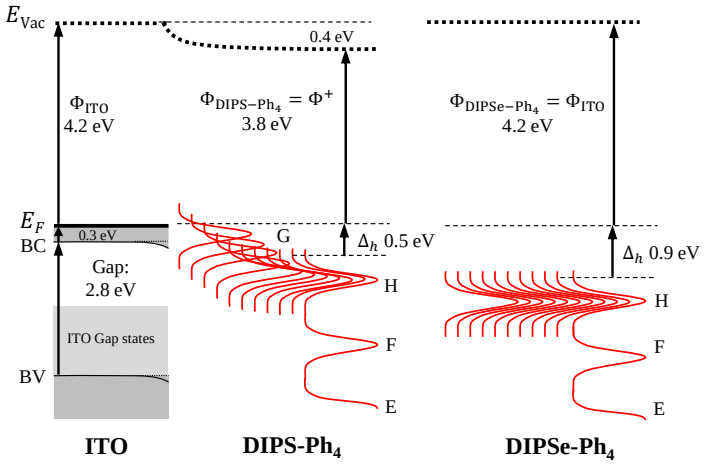

Figure V.10 – Expected energy level scheme of the ITO/DIPS-Ph_4 and the ITO/DIPSe-Ph_4 systems.

DIP derivatives studied.

We obtained, with the sulphur and the selenium DIP derivatives, two different alignment modes. For DIPS-Ph_4, a HOMO pinning mode occurs ($\Phi_{ITO} > \Phi^+$), with a charge transfer to ITO. In the case of DIPSe-Ph_4, the alignment follows the Schottky-Mott limit ($\Phi_{ITO} < \Phi^+$, *i.e.* vacuum level alignment). This results from a large difference between the IP_v values of the two DIP derivatives.

Conclusion

We combine AFM and synchrotron radiation XPS/UPS to elucidate the formation the DIPO-Ph_4/ITO interface, DIPO-Ph_4 has appeared as a very promising interfacial layer for hole collection in organic photovoltaic. The DIPO-Ph_4/ITO morphology of the deposits otherwise characterized by XPS/UPS, is examined by AFM. For coverages in the 1×10^{15} - 8×10^{15} molecule $\cdot$ cm^{-2} range, we do not observe a layer-by-layer growth mode. Molecular mounds are formed, starting from ITO macroscopic surface defects. In the 1×10^{15} - 3×10^{15} molecule $\cdot$ cm^{-2} range the height of the mounds is typically 30 nm, leaving inter-mound area bare or covered by an ultra-thin layer that remains unobservable by AFM. Only at 8×10^{15} molecule $\cdot$ cm^{-2} does the mounds tend to coalesce, and their height reaches an average value of 50 nm.

Synchrotron radiation XPS and UPS give unique information on the electronic properties of both the substrate and the film. The fact that the film thickness is not uniform, as shown by AFM, is crucial to interpret the photoemission spectra. Indeed, for coverages $\leq 3 \times 10^{15}$ molecule $\cdot$ cm^{-2}, a sizeable ITO contribution is always observed in the O 1s and valence band spectra, even in highly surface sensitive conditions. The ITO-related signal originates from the inter-mound areas (and the aureoles of the mound) where the deposit thickness is very thin. All substrate related components (*e.g.* In 3d) increase their binding energies when the molecule is deposited, indicating that the Fermi level moves up in energy due to the interaction with the molecule. This may be interpreted as a filling of the conduction band by electrons coming from the deposited molecules.

For all the deposits studied, we detect the presence of two components in the O 1s spectra, indicating that the molecule is in two different states. One state corresponds to an ether oxygen of an otherwise unaltered molecule. The second one at higher binding energy originates from an altered molecule interacting with the substrate. These two molecular states are in comparable amounts until the DIPO-Ph_4 mounds almost coalesce. Then the relative weight of the altered state at high binding energy diminishes. The fact that the altered species gives a sizeable spectra contribution, even in surface sensitive conditions, is due to the growth mode: its signal comes from the inter-mound areas and from the

flanks of the mounds, where the layer thickness become comparable to the probed length. Given than the DIPO-Ph_4 is an excellent donor, the possibility of a molecular cation is examined. O 1s core-ionized state DFT calculations of isolated molecules in the neutral and cationic state give a reasonable explanation for the observed O 1s binding energy difference when the core-hole relaxation energy in dielectric media is accounted for. The C 1s spectra can also be interpreted in a similar way.

The UPS valence band of the bare substrate is characteristic of metallic ITO, with a density of state observable at Fermi level. When the molecule is deposited, new states appear. The corresponding molecular levels are also interpreted within the framework of the two molecular states, neutral and cationic. The HOMO of the neutral molecule shows up, centred at 1.4 eV below the Fermi level with its edge only 0.7 eV below the Fermi level. The HOMO of the cationic species is found shifted to higher binding energy by ∼1.1 eV (centroid at ∼2.5 eV below the Fermi level). The work function of the ITO surface is affected by a slight decrease when the molecule is deposited (∼0.3 eV), due to the charge transfer from the molecule to the substrate. The work function of the deposit (3.9 eV) is therefore the integer charge transfer energy.

Finally, we draw the electron level the DIPO-Ph_4/ITO interface, and discuss the implications in devices, as a hole conducting layer in organic light emitting diodes and as an anode interfacial layer in organic solar cells.

Appendix A

Materials

A.1 Indium tin oxide

Commercial ITO substrates (SOLEMS) used have a sheet resistance of $25\,\Omega \cdot \mathrm{sq}^{-1}$. As solar cells efficiency relies on the good quality of the layers and of the interfaces, ITO is firstly cleaned before being exposed to the first organic layer. Wet cleaning was achieved by sequential ultrasonic baths using alkaline detergent solution (5 vol% in deionized water), dichloromethane, ethanol, and isopropanol, each for 10 minutes. The chemically cleaning procedure leaves a weak carbon contamination and gives a relatively low work function. [184] The dried surface is then exposed to UV-ozone treatment for 10 minutes. A too long UV ozone cleaning could result in the degradation of the molecular layer deposition due to the formation of active oxygens. [185]

In some samples, ring-shaped structures remain on the ITO surface, despite the cleaning process. They are characterized by an average height of 2 nm and an average diameter of 100 nm (Figure A.1). They cover 20 % of the surface. Away from these "craters", the roughness remains low (1 nm). These defaults origin is not yet determined but for organic layer growth on top of ITO they will be more favourable nucleation point.

A.2 Dipyranylidenes

The final DIP compounds were characterized via Nuclear Magnetic Resonance (NMR) and via elementary analysis (see Table A.1). There is no contamination detected.

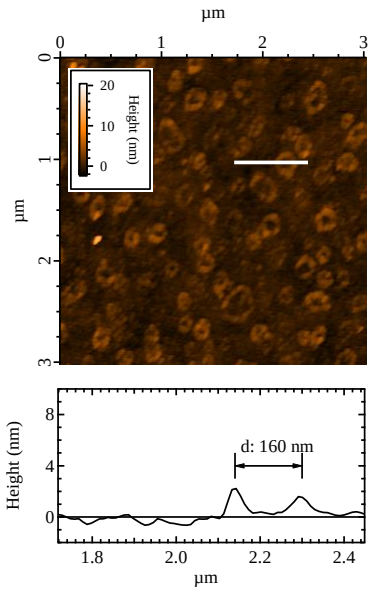

Figure A.1 – AFM image of chemically cleaned ITO presenting ring-shaped features.

Table A.1 – Elementary analysis of DIPX-Ph_4 (X = O, S, Se).

DIPX-Ph_4	**Atom**	**1st measurement**	**2nd measurement**	**Theoretical value**
X = O	Carbon (%)	86.45	86.17	87.90
	Hydrogen (%)	5.12	5.22	5.21
X = S	Carbon (%)	80.15	_	82.22
	Hydrogen (%)	5.03	_	4.87
	Sulphur (%)	12.42	_	12.91
X = Se	Carbon (%)	68.43	_	69.16
	Hydrogen (%)	3.80	_	4.10

Appendix B

Experimental setups

B.1 Deposition

Deposition of organic materials can be performed either via liquid or via gaseous phase. Spin-coating has been developed to rapidly form thin films, with a thickness control depending on the speed rotation. In liquid phase methods, the molecules must have a good solubility in any solvent. Consequently, for immiscible materials, thin films are formed using thermal evaporation. All DIP deposits are prepared on commercial ITO substrate (SOLEMS) with a sheet resistance of $25\,\Omega \cdot \mathrm{sq}^{-1}$. After a DECON 90 treatment, the ITO substrates are cleaned ultrasonically in bathes of dichloromethane and propan-2-ol (10 min each) without any further treatment before DIP deposition.

DIP layers are prepared via thermal evaporation under vacuum. A quartz balance (QB) controls the evaporation speed rate ($\sim 1\,\text{Å} \cdot \mathrm{min}^{-1}$) and the deposited DIP amount. The different prepared samples are named by the average number of deposited molecules per cm^2 (QB-coverage).

For *in situ* prepared samples on the TEMPO beamline, the ITO substrate is exposed to a molecular beam of DIPO-Ph_4, using a Knudsen cell positioned at 4 cm from it, after its introduction into the ultra-high vacuum ($\sim 10^{-10}$ mbar) preparation chamber. The molecular beam is slightly tilted. The DIP covered substrates are then introduced in the XPS analysis chamber in a pressure better than $\sim 10^{-8}$ mbar.

For *ex situ* samples prepared at CEA laboratory, a molybdenum (Mo) crucible with the DIP molecules is positioned at 30 cm from the used substrate. The molecular beam is perpendicular to the sample holder. A QB monitor allows us to follow the deposition rate. The substrate can be kept at room temperature or heated thanks to two lamps. Once prepared, the samples are air exposed and brought to the different synchrotron beamlines.

B.2 Fabrication of photovoltaic devices

The device structure is ITO/DIPO-Ph_4/PEDOT:PSS/P3HT:PCBM/LiF. The cleaned ITO substrates are immediately transferred into nitrogen glove box and then used to build the devices. PEDOT:PSS is spin-coated and heated at 140 °C for 10 minutes in nitrogen glove box and a thickness of approximately 5 nm is achieved.

The 100 – 150 nm active layer consisting of P3HT:PCBM ($15\,\mathrm{mg \cdot mL^{-1}}$ for P3HT, $12\,\mathrm{mg \cdot mL^{-1}}$ for PCBM, blended in ortho-dichlorobenzene) is spin-coated and subsequently annealed at 80 °C for 15 minutes in nitrogen glove box. Then, we transport samples into high vacuum chamber to evaporate LiF (1.0–1.5 nm, at rates of $0.01\,\mathrm{Å \cdot s^{-1}}$) and Al (100–150 nm, at rates of $0.5\,\mathrm{Å \cdot s^{-1}}$) through a shadow mask to define the active area of $6\,\mathrm{mm^2}$ or $12\,\mathrm{mm^2}$. Then samples are transferred back to nitrogen box and post annealing is performed. The post-annealing treatment consists in firstly heating at 100 °C for 10 minutes and then at ∼150 °C for 5 minutes.

The photo-electrical characterization of OPVs is performed using a xenon lamp, with an AMG 1.5 filter. The calibration demonstrates an incident light of $100\,\mathrm{mW \cdot cm^{-2}}$.

B.3 Spectroscopy and microscopy analysis

B.3.1 AFM

The surface morphology of the DIP films is investigated via atomic force microscopy (AFM) at CEA (IRAMIS group). The AFM used is a Molecular Imaging from Agilent, PicoLE, used in contact mode using a conductive Pt/Ir tip of radius 20 nm. The spring constant of the cantilever is $0.2\,\mathrm{N \cdot m^{-1}}$. The vertical resolution in contact mode is 0.5 nm. The sample roughness is determined thanks to the root mean square method (RMS).

B.3.2 STXM

STXM has been performed on the PolLux beamline (Switzerland Light Source). Samples are introduced in the analysis chamber which is then pumped down to $\sim 10^{-3}$ mbar. The absorption stacks are recorded at the C 1s edge (280 to 340 eV) with an X-ray beam normal to the surface and horizontally polarized. A zone plate with an outer ring spacing of 25 nm is used, allowing a spatial resolution of ∼30 nm. We also obtain spectra via stacks and via linescans to minimize X-ray dosage to the molecular clusters.

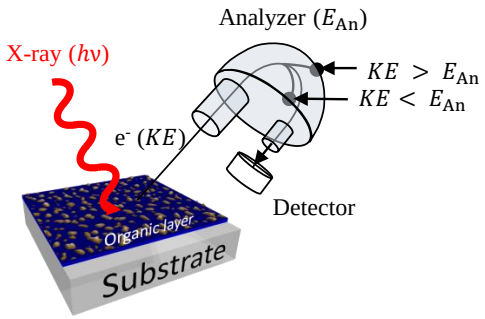

Figure B.1 – Schematic representation of photoelectron emission and analyser process.

B.3.3 XPS

The basic elements of a spectroscopy instrument are a light source, an electron energy analyser, and an electron detector.

In a laboratory system, an X-ray tube (usually with Al or Mg cathode) for XPS analysis and a He gas-discharge lamp for UPS analysis are used. Development of synchrotrons made available the whole range of excitation energies between X-ray tubes and He lamps. Furthermore, use of synchrotron light has several advantages in comparison with common laboratory X-ray sources. Besides higher photon flux and the possibility of focusing an X-ray or UV beam into a small spot, synchrotron light has the property of excitation energy tunability, which allows modulating the information depth and the photoelectron cross section.

Magnetic electron energy analysers were used on early stages of photoelectron spectroscopy development. Later they were completely replaced by electrostatic analysers because of easier construction and handling. Among the different types of electrostatic analysers, including the retarding field analyser, the cylindrical mirror or deflection analysers, and the hemispherical analyser. Only the last one is widely used nowadays for XPS, because of better resolution characteristics. A schematic diagram of a hemispherical electrostatic electron energies analyser is shown on Figure B.1.

The difference in voltages on the hemispherical electrodes corresponds to a selection of electrons of the kinetic energy E_{An}. The pass energy PE will define the window of the filtered electrons with $E_{\mathrm{An}} - \frac{PE}{2} < KE < E_{\mathrm{An}} + \frac{PE}{2}$. Thus, the photoelectrons are registered in a small kinetic energy range (PE); this width determines the analyser resolution. A spectrum is obtained by sweeping voltages of the hemispherical electrodes. Electrons are usually detected by an electron multiplier of the channeltron type and electronics in the pulse counting mode. Sometimes channeltrons are replaced by a microchannel plate, or a video camera of CCD type with a fluorescent screen, or other detectors for

space-resolved spectroscopic measurements.

The photoemission data for ITO/DIPO-Ph_4 interface was collected at the TEMPO beamline, SOLEIL synchrotron, France. The synchrotron light spot of the TEMPO beamline is defocused to 1 mm×2 mm purposely to decrease the photon flux, and to avoid beam damage, without losing photoelectron count rate. The electron analyser is a modified SCIENTA200 machine fitted with a delay line detector. All photoemission spectra are taken with a take-off angle of 0° with respect to the surface normal. Valence band spectra and shallow core-levels (Sn 4d, In 4d) are recorded at $h\nu = 60\,\text{eV}$ in surface sensitive conditions. The In 4d and Sn 4d spectra are also recorded in more bulk sensitive conditions at 825 eV to profile out the Sn distribution in the material. In 3d core-levels are measured at 600 eV. C 1s, O 1s core-level XPS spectra are respectively recorded at $h\nu = 340\,\text{eV}$ and $h\nu = 600\,\text{eV}$ with an overall experimental resolution better than 100 meV.

The photoemission data for ITO/DIPS-Ph_4 and ITO/DIPSe-Ph_4 interface was collected at the ALOISA beamline, ELETTRA synchrotron, Italy, with the same parameters as the TEMPO beamline ones. Complementary XPS characterization of the bare ITO surface was also carried at Laboratoire de Chimie Physique Matière et Rayonnement (LCPMR, Paris), where a standard laboratory setup was used (a PHOIBOS 150 analyser from SPECS and a non-monochromatized Al K_α source).

B.4 Theoretical calculation

DFT was performed using the GAMESS (general atomic and molecular electronic structure system) package. The cationic state is obtained by creating a hole in the HOMO. We use the Becke three-parameter exchange functional, along with the Lee Yang-Parr gradient-corrected correlation functional (the so-called Becke three-parameter Lee-Yang-Parr (B3LYP) functional). The 6-311G* basis sets are used for carbon and oxygen and the 6-31G* basis set for hydrogen atoms.

B.5 Data analysis

B.5.1 STXM stack analysis

The image stacks were post processed using aXis2000. [186] The optical density (OD) was obtained using the I_0 on the area between the DIP clusters (absorption of the Si_3N_4 substrate) and the decomposition of the stacks into main spectral components was performed via principal component analysis (PCA). Absorption spectra were normalized to the edge jump and were fitted using an error function curve as background, [121] cen-

tred at 288.9 eV (IP). Energy calibration of the beamline was checked by measuring a reference PCBM film. Main transitions have been fitted with Gaussian.

B.5.2 Core levels analysis

After subtraction of a Shirley background, the spectra are reconstructed with sums of Voigt functions, with respectively a 340, 380, 80, 150, 199, and 210 meV Lorentzian full widths at half maximum (FWHM, corresponding to the core-hole lifetime) for Sn 3d, In 3d, C 1s, O 1s, In 4d and Sn 4d, respectively, according to the literature. [187] The Gaussian contribution, which may change according to the chemical environment, is indicated in the text. It is worth noticing that the value of the core/valence level width σ_i can be determined according to Hwang *et al.* work: [188]

$$\sigma_i = \sqrt{{\sigma_{\mathrm{XPS/UPS}}}^2 - {\sigma_{\mathrm{inst}}}^2 - {\sigma_{\mathrm{surf}}}^2 - {\sigma_{\mathrm{vib}}}^2}$$

Surface relaxation processes (σ_{surf}) and vibrational coupling (σ_{vib}) are estimated to be both in the range of 0.05–0.2 eV. [188] The instrumental resolution (σ_{inst}) is measured at the Fermi edge of a clean metal sample ($\sigma_{\mathrm{inst}}\,(\mathrm{Au}) = 0.08\,\mathrm{eV}$). σ_i can be then used as a key value for the determination of the effective injection barrier. [189]

Binding energies (BE) are referenced with respect to the Fermi level (E_F) determined from a scrapped area of the copper sample holder in electrical contact with the ITO substrate. The work function is determined by measuring the kinetic energy (KE) of the secondary electron cut-off (KE_{CO}). To avoid truncating the spectrum by the analyser work-function, the sample is negatively biased (to -20 V) with respect to the analyser. The knowledge of KE_{CO}, that of the kinetic energy of the Fermi level (KE_{FL}) measured on the metallic contact, and the precise determination of the photon energy $h\nu$ (using 1$^{\mathrm{st}}$ and 2$^{\mathrm{nd}}$ order core level peaks), enables the determination of the work function Φ of the sample as $\Phi = h\nu - (KE_{FL} - KE_{CO})$.

Appendix C

Complementary results

C.1 Morphology at the TEMPO beamline

For the study of metal/organic interface electronic properties, we had to prepare samples and bring them to synchrotron facilities, which means air exposure and thus contaminations. Consequently, we also prepared samples directly in the preparation chamber of the X-ray experiments. From an evaporation system to another, there could be a change in the global geometry. We present in this point the effect of the molecular beam incidence on the molecular shapes. Let us see what happens for a molecular source located at 4 cm to the ITO surface and which is slightly tilted (Figure C.1).

In this case, 3D growth of nearly circular mounds switches to that of recumbent, elongated (needle-like) mounds. Their average height is 30 and 40 nm for the 1×10^{15} and the 3×10^{15} molecule $\cdot$ cm^{-2} samples, respectively. For this coverage, the typical

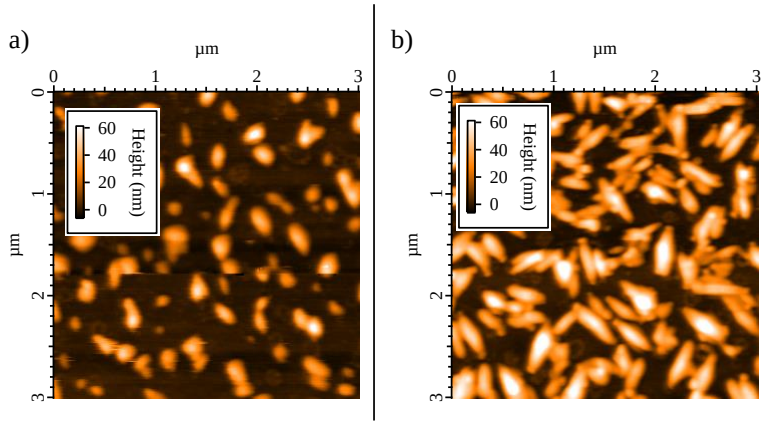

Figure C.1 – AFM images for DIPO-Ph$_4$, tilted molecular beam: a) QB-coverage of 1×10^{15} molecule $\cdot$ cm^{-2}; b) QB-coverage 3×10^{15} molecule $\cdot$ cm^{-2}.

lateral and longitudinal needle dimensions are ∼150 and ∼400 nm.

C.2 Electronic properties after air exposure

Two DIPO-Ph_4 samples (1×10^{15} and 8×10^{15} molecule $\cdot$ cm^{-2} as QB-coverage) have been air exposed after being prepared in our well-controlled evaporation system. The objective was to compare the results with in situ prepared samples and to see if there is any difference with the *ex situ* prepared samples.

In both case, ITO substrates are chemically cleaned and are immediately introduced in the vacuum chamber. The intimate ITO/DIPO-Ph_4 interface is thus identical for the *ex situ* and *in situ* samples. Yet, after an air exposure (during the travel to the synchrotron for example), some oxygen contaminants can deposit on the surface and change the electronic properties.

Consequently, we perform XPS measurements on the two *ex situ* samples. The In 3d DIPO-Ph_4 spectrum shows a rigid shift to higher binding energy in comparison to ITO In 3d spectrum (Figure C.2a)). It is similar as for the *in situ* samples: a rigid shift that can be attributed to a charge transfer from the organic layer to the oxide substrate.

The O 1s spectra (Figure C.2b)) show two components for DIPO-Ph_4. O1 and O2 are the O components for the neutral and the cationic DIPO-Ph_4 forms, respectively. This is further proved by looking at the VB states (Figure C.2c) and d)). H (HOMO) and H(+) (SOMO) states are seen in the VB spectra.

As a consequence, results for the *ex situ* samples are strictly identical to the ones of the *in situ* samples. We thus decided to prepare the samples in our well-controlled evaporation system. The layer morphology is thus unchanged and well-known before the synchrotron experiments.

C.3 Solar cell characterization

The main parameter of solar cell performance is the power conversion efficiency (PCE). The PCE of a solar cell is defined as the ratio of maximum output power density (P_{out}) to the intensity of incident light (P_{in}). P_{out} depends on open circuit voltage (V_{OC}), short circuit current density (J_{SC}) and fill factor (FF) (see Figure C.3). The PCE formula can be expressed as the following:

$$PCE = \frac{P_{\text{out}}}{P_{\text{in}}} = \frac{V_{\text{max}} J_{\text{max}}}{P_{\text{in}}} = FF \frac{V_{OC} J_{SC}}{P_{\text{in}}}$$

where V_{max} and J_{max} are respectively the voltage and the current density at P_{out}.

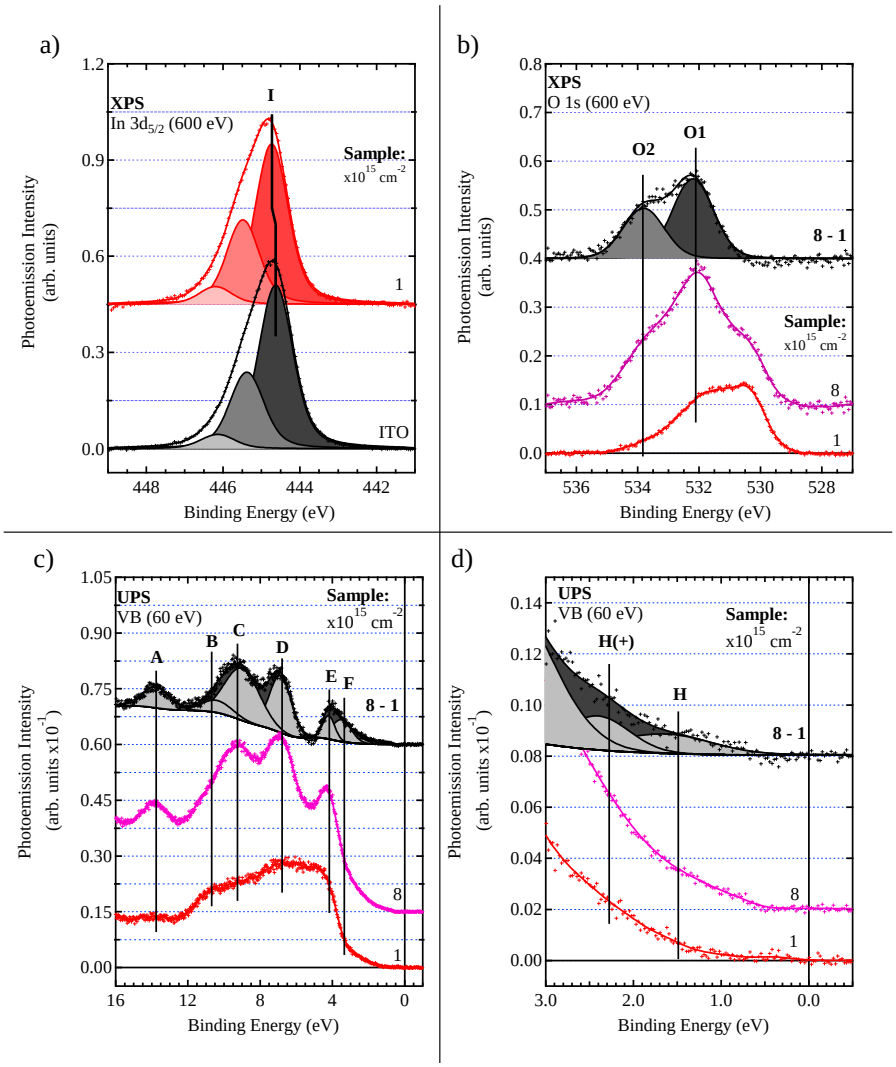

Figure C.2 – a) In $3d_{5/2}$ spectra of the chemically cleaned ITO and 1×10^{15} molecule $\cdot$ cm^{-2} air exposed samples; b) O 1s spectra and c) valence band with HOMO levels for the 1×10^{15} and 8×10^{15} molecule $\cdot$ cm^{-2} air exposed samples; d) Zoom of the c) image. The $8 - 1$ difference curve is used to highlight DIPO-Ph$_4$ components. The photon energy is indicated. The spectra were recorded at the TEMPO beamline.

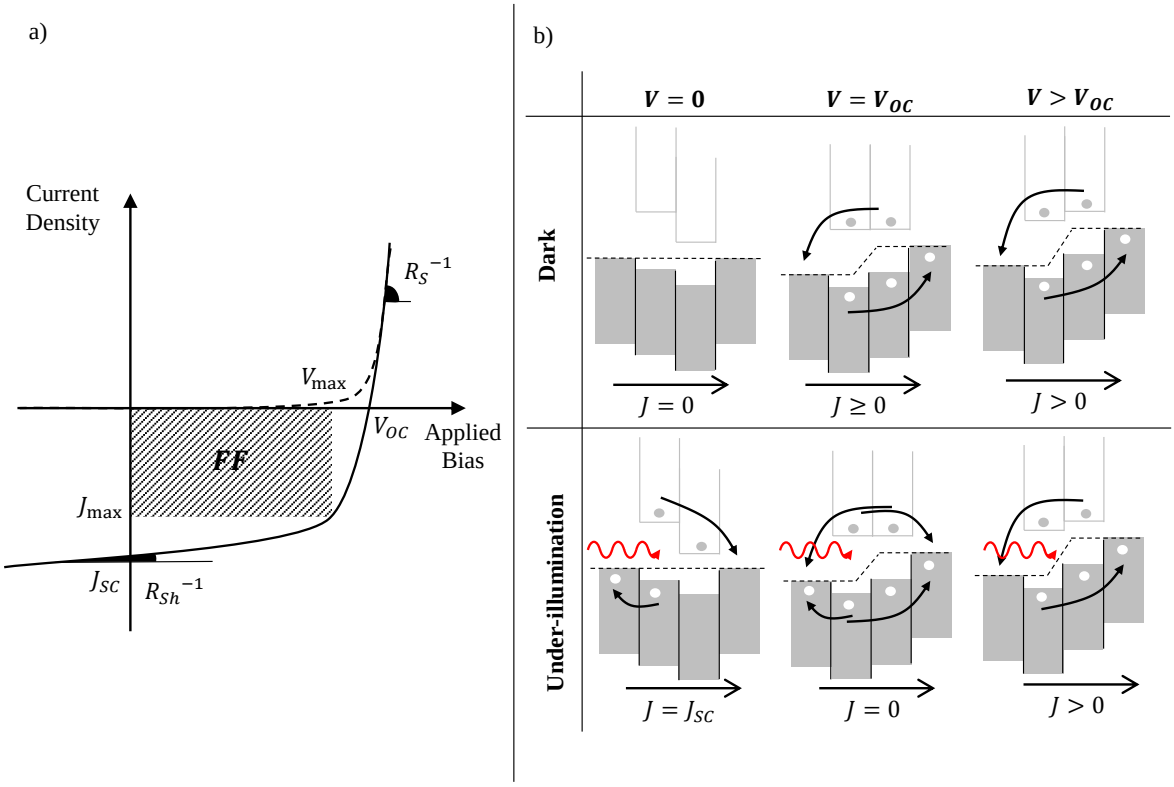

Figure C.3 – a) Typical J-V curve: under dark (dashed line) and under illumination (continuous line); b) Energetic diagram for different applied bias. Dark points are electrons and light points are holes.

Open circuit voltage (V_{OC}):

Open circuit voltage is the maximum voltage that a p-n solar cell could provide to external circuit, deriving from the splitting of hole and electron by light illumination. In this case, the expression is described as following:

$$V_{OC} = \frac{1}{e}\left(E_{E_F,n} - E_{E_F,p}\right)$$

where e is the elementary charge, $E_{E_F,n}$ and $E_{E_F,p}$ are the Fermi levels of the n-type and p-type SCs, respectively.

Short circuit current density (J_{SC}):

Short circuit current density is the maximum photocurrent density that could be achieved in a solar cell. If no saturation effect appears, J_{SC} is mainly dependent on the number of absorbed photons. In addition, the surface area of the active layer, the device thickness and the charge transport also influence J_{SC}.

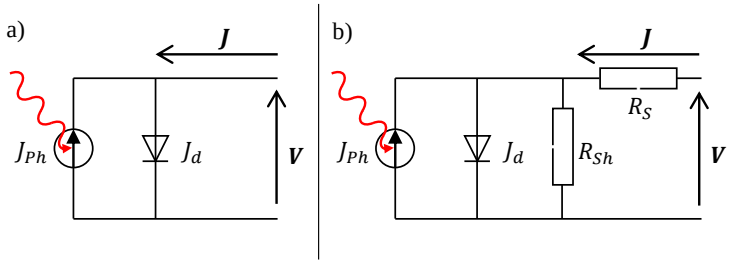

Figure C.4 – Electrical circuit of: a) an ideal solar cell; b) a practical solar cell. J_{Ph} is the current density from the photo-generator (provided by illumination), J_d is the current density from the diode (forward bias through p-n junction).

Fill factor (FF):

The fill factor is the ratio of the maximum power output (P_{out}) of a solar cell to the product of the V_{OC} and J_{SC}, describing the quality of the photovoltaic devices. The equation is expressed as:

$$FF = \frac{V_{\text{max}} J_{\text{max}}}{V_{OC} J_{SC}}$$

FF demonstrates the ability of extracting charge carriers from active layers. An ideal FF J-V characteristic is rectangle.

Series and shunt resistance (R_S and R_{Sh}):

As a photo-generator, a SC can be also described as an electrical circuit which includes a series resistance (R_S) and a shunt resistance (R_{Sh}) (see Figure C.4).

In a first approximation, the equivalent circuit cell is shown Figure C.4a). In this description, the two electrodes are decoupled and only the efficiency of the active layer to convert the photon can describe the electrical processes. A better comprehension of the working steps into the device lead to a more complex description. Indeed, the exciton recombination/de-excitation, charge losses due to material defaults, layer arrangement defaults, and electronical losses can be highlighted by the J-V curve and a more complex equivalent electrical circuit (Figure C.4b)). In this schema, R_S is the total resistance of all the layers. R_{Sh} represents current leakage, such as impurity induced or p-n junction leakage. From a graphical point of view, the value of R_S can be approximated from the inverse slope of the J-V curve at forward bias, while R_{Sh} is the inverse slope of the J-V curve at reverse bias (see Figure C.3a)).

Caractérisations structurales et électroniques d'une interface oxyde transparent conducteur/organique

Introduction

Les dispositifs d'électronique et d'optoélectronique organique ont été étudiés ces dernières années comme de potentielles alternatives aux technologies actuelles de semi-conducteurs inorganiques. Les semi-conducteurs organiques sont aujourd'hui utilisés dans les diodes électroluminescentes (OLED), [1] on les retrouve aussi dans les transistors à effet de champ (OFET), [2] dans les cellules solaire (OSC), [3, 4] ou dans les capteurs chimiques. [5] Alors que certains de ces dispositifs sont déjà sur le marché (OLED, OFET), d'autres sont encore loin d'être développés, malgré les progrès enregistrés au cours des dernières décennies (hétérojonction en volume). [6]

Pour augmenter l'efficacité de ces dispositifs, il faut maîtriser de nombreux paramètres, tels que la nature chimique et la structure électronique des solides moléculaires, la présence d'impuretés et de dopants ou la morphologie à l'échelle de la nanomètre des films organiques. [7] L'interface entre la couche organique active et les contacts métalliques est d'une importance primordiale dans la détermination de l'efficacité du dispositif. Par exemple, l'alignement des niveaux énergétiques de la couche organique avec le niveau de Fermi des substrats métalliques détermine les barrières d'injection des électrons ou des trous. [8, 9, 10] Aux côtés des effets purement électroniques, l'organisation moléculaire à l'interface permettra également de déterminer la morphologie et la structure des molécules organiques dans des films plus épais et, ainsi, jouera un rôle important dans le comportement physique du dispositif. [11]

Pour cette raison, au cours de ces dernières années, de nombreux groupes de recherche ont attiré leur attention sur la structure d'espèces donneuses ou acceptrices organiques déposées sur des surfaces métalliques. Les résultats ont montré beaucoup de nouveaux

phénomènes. [17, 18, 19, 20, 21] L'origine des effets observés est dû, mais ne se limite pas uniquement, au réarrangement de charge à l'interface et au réalignement concomitant des niveaux d'énergie. Le transfert d'électrons à travers l'interface organique/inorganique conduit à la formation d'états délocalisés d'électrons [22] ou peut même conférer des propriétés magnétiques à la couche organique. [23, 24]

Au cours de ce projet de 3 ans, nous avons étudié une interface métal/organique. Celle-ci est formée par un oxyde d'indium dopé à l'étain (ITO), le métal et d'un dipyranylidene (DIP), la matière organique. Plusieurs expériences de synchrotron ont été réalisées sur des lignes de lumière synchrotron : TEMPO (SOLEIL, France), ALOISA (ELETTRA, Italie) et PolLux (SLS, Suisse).

Dans la partie S.1, nous discuterons du processus de transfert de charge pour comprendre l'alignement des niveaux électroniques à l'interface entre les métaux et les donneurs et accepteurs organiques. La morphologie de l'interface ITO/DIPO-Ph_4 est présentée dans la partie S.2.

La microscopie à force atomique (AFM) et la microscopie à rayons X (STXM) ont été utilisées pour déterminer le mode de croissance et l'orientation moléculaire. Les traitements thermiques de recuit nous permettent de moduler la morphologie de la couche organique. Cette étude nous aidera à comprendre les mesures effectuées par la spectroscopie de photoémission de rayons X (XPS) présentée dans la partie S.3.

En effet, dans ce dernier, nous allons faire une description complète des propriétés électroniques de l'interface ITO/DIPO-Ph_4 obtenues grâce à l'XPS. Ces résultats ont été confrontés à des calculs théoriques (DFT). On observe un transfert de charge de la matière organique au substrat. Pour terminer ce chapitre, nous présenterons les résultats de spectroscopie de photoémission résonnant (ResPES) et les résultats de pompe-sonde qui ont été obtenus.

Une fois l'interface ITO/DIPO-Ph_4 complément caractérisée, nous avons intégré le système dans des dispositifs photovoltaïques. Nous présenterons dans la partie S.4, l'alignement énergétique d'une cellule solaire organique typique avec du DIPO-Ph_4 comme couche interfaciale.

Dans la dernière partie, partie S.5, nous présenterons l'effet d'un changement dans l'hétéroatome du DIP sur la morphologie et les propriétés électroniques. Dans cette thèse, ces données seront présentées comme les résultats préliminaires et d'autres expériences XPS et calculs DFT seront effectués afin de permettre une discussion complète sur les dérivés DIP.

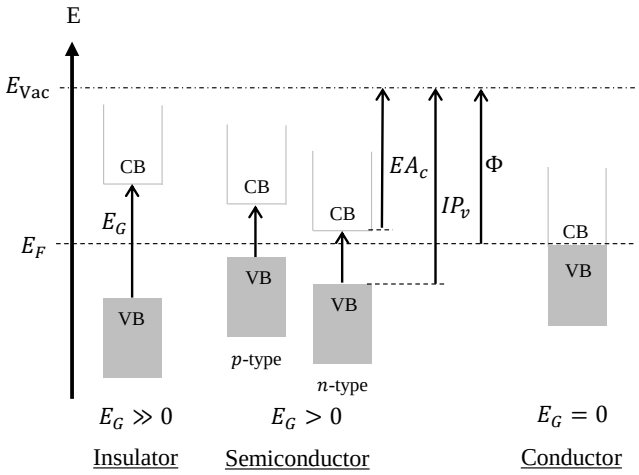

Figure S.1 – Représentation énergétique d'un isolant, d'un semi-conducteur et d'un matériau métallique.

S.1 Interfaces métal/organique : morphologie et propriétés électroniques

Pour comprendre l'électronique moléculaire, il faut d'abord considérer les propriétés électroniques d'un semi-conducteur et la façon dont les molécules se déposent sur une surface. Dans ce premier point, nous rappelons les fondamentaux du placement d'énergie dans un solide et le mode de croissance de la couche organique.

Les propriétés électroniques d'un matériau dépendent en particulier de la valeur du gap énergétique (E_G) (Figure S.1) :

- $E_G \gg 0$: isolant
- $E_G > 0$: semi-conducteur (SC)
- $E_G = 0$: conducteur (C)

E_G est la différence entre le bas de la bande de conduction (première bande inoccupée ; CB) et le maximum de la bande de valence (dernière bande pleine ; VB). Cette description est aussi appliquée au solide moléculaire.

Parmi les semi-conducteurs organiques, les dipyranylidenes (DIP) sont des molécules prometteuses (structure présentée dans la Figure S.2a)). La structure quinoïde du noyau DIP est équivalente à celle du tétrathiafulvalène (TTF), une famille bien connue de donneurs d'électrons. Cependant, contrairement au TTF et ses analogues, dont les propriétés ont été largement étudiées, les dérivés DIP restent presque inexplorés aujourd'hui. Alizon

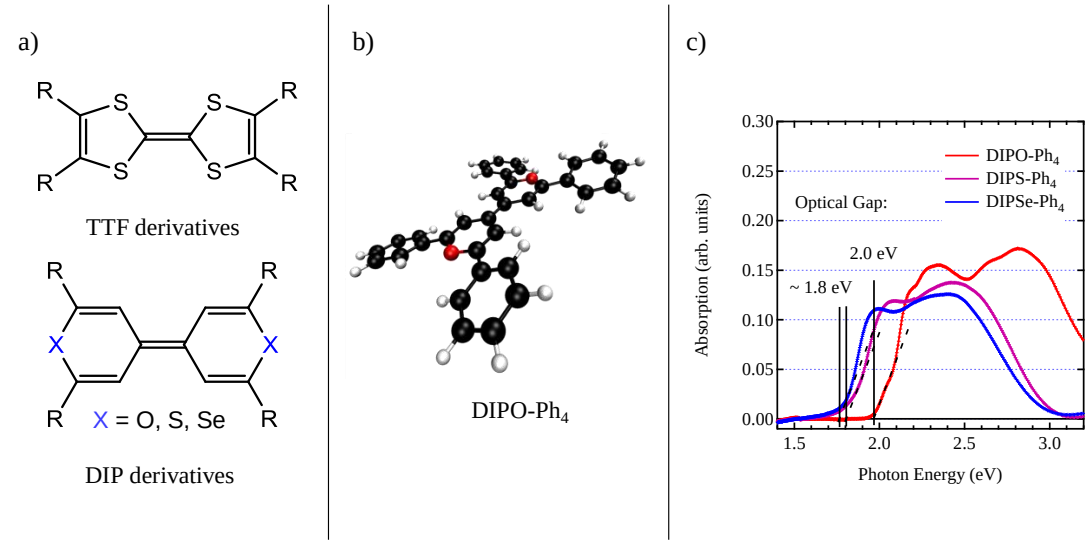

Figure S.2 – a) Comparaison de la structure entre la famille des TTF et celle des DIP ; b) Géométrie optimisée du dérivé DIPO-Ph_4.

et coll. ont montré que les DIP forment des complexes à transfert de charge (donneur-accepteur) avec le tétracyanoquinodiméthane (TCNQ) dont la conductivité est élevée. [25] Le potentiel d'oxydation des DIP est d'environ 0,2 V, ce qui les rend meilleurs donneurs d'électrons que le TTF (0,34 V les deux par rapport à l'électrode Ag/AgCl dans l'acétonitrile). Cette valeur conduit à un potentiel d'ionisation de 4,6 V, selon la relation de la Forrest. [56]

Dans cette étude, nous nous concentrerons sur les dérivés DIPX-Ph_4 avec X = O, S ou Se. Concernant la géométrie de la molécule (Figure S.2b), dérivé oxygéné), les quatre phényl forment un angle dièdre d'environ 17° pour le dérivé oxygéné. Cette valeur augmente à 39° pour le dérivé soufré et 42° pour le séléné. A l'état solide, par diffraction des rayons X (XRD), il a été mesuré un angle dièdre réduit à 7,8° pour le dérivé oxygéné. [58] Pour le DIPS-Ph_4, l'angle est de 12,4° et pour le DIPSe-Ph_4, il est de 14°. [59, 60] Cet angle ,entre le noyau DIP et les groupes Ph, peut conduire à un changement dans le comportement électronique des matériaux moléculaires.

Les dérivés DIP ont déjà été utilisés dans des dispositifs organiques tels que les cellules solaires organiques (OSC) [27, 26] ou les transistors à effet de champ organique (OFET) [61, 28] mais les processus électroniques et les propriétés n'ont pas été clairement démontrées. Au cours de ce travail, nous visons ainsi à acquérir une meilleure compréhension de l'interface formée par des couches DIP sur des substrats de ITO, qui sont typiquement des interfaces métal/organique.

Les niveaux électroniques d'un matériau moléculaire déposé sur un métal sont le plus

souvent placés en alignant les niveaux de vide (la limite dite de Schottky-Mott). Une vaste littérature sur les interfaces métal/organique montre que c'est loin d'être toujours le cas. [9, 10, 17, 21, 63, 64, 65, 66] Divers modèles ont été proposés pour décrire la situation réelle.

Oehzelt et ses collaborateurs [10] ont proposé un modèle permettant de regrouper tous les modèles développés précédemment. S'appuyant fortement sur la densité d'État (DOS) du film organique, le profil spatial du potentiel électrostatique dans la couche organique a été calculé par l'équation de Poisson. Les différents régimes d'alignement des niveaux énergétiques sont présentés dans la Figure S.3. Trois régimes sont possibles :

- Alignement par la HOMO.
- Limite de Schottky-Mott.
- Alignement par la LUMO.

En cas de transfert de charge la HOMO, cas du donneur (ou la LUMO, pour le cas de l'accepteur) s'aligne avec le niveau de Fermi du métal pour les premières couches déposées. Pour les couches suivantes une «courbure de bande»apparaît. Le modèle électrostatique de la Réf. 10 reproduit le comportement expérimental des barrières d'injection des électrons ou des trous par rapport au travail de sortie du métal, distinguant les cas obéissant à la limite de Schottky-Mott de ceux où la HOMO ou la LUMO du solide moléculaire s'alignent.

Pour déterminer l'alignement niveau énergique, des caractérisations aux rayons X peuvent être effectuées.

S.2 Couche de DIPO-Ph_4 sur ITO : morphologie et orientation moléculaire

Pour comprendre l'interface ITO/DIPO-Ph_4, il est important de caractériser la surface de l'électrode : rugosité, contaminations, défauts de surface. Avant toutes autres analyses, la microscopie à force atomique (AFM) a été utilisée pour caractériser les substrats d'ITO et la morphologie de la couche organique sur ITO.

Plusieurs échantillons ont été préparés avec un changement dans la quantité de DIP déposée. Le suivi du dépôt est obtenu par une balance à quartz (QB). Les différents échantillons sont nommés par leur recouvrement nominal (QB-coverage). Nous avons étudié trois échantillons différents : une couche «mince»de $0{,}5 \times 10^{15}$ molécule $\cdot$ cm^{-2}, une couche intermédiaire de 2×10^{15} molécule $\cdot$ cm^{-2} et une couche «épaisse»dont le QB-coverage est de 10×10^{15} molécule $\cdot$ cm^{-2}.

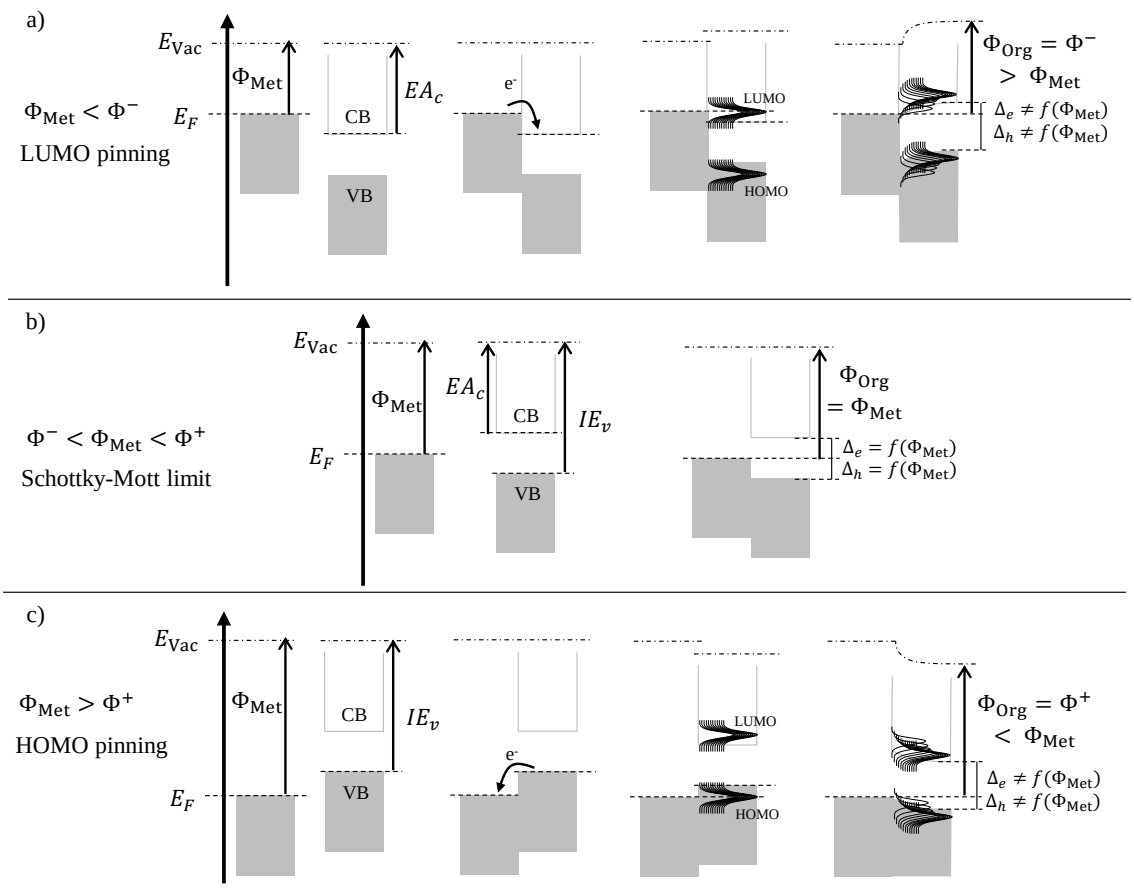

Figure S.3 – Représentation énergétiques d'une interface métal/organique après a) alignement par la LUMO, b) limite de Schottky-Mott et c) alignement par la HUMO.

Après nettoyage chimique, nous obtenons un ITO qui présente une surface granulée et une rugosité de l'ordre de 1 nm (root mean square, RMS). Après le dépôt de $0{,}5 \times 10^{15}$ molécule $\cdot$ cm^{-2}, l'image AFM (Figure S.4a)) montre que des îlots recouvrent 20 % de la surface d'ITO. Leur hauteur moyenne est de 20 nm, avec un diamètre moyen de 200 nm. Les îlots sont distribués de façon homogène sur la surface. Pour le dépôt de 2×10^{15} molécule $\cdot$ cm^{-2} (Figure S.4b)), la couche de DIPO-Ph$_4$ couvre désormais 55 % de la surface de l'ITO. Les îlots s'allongent légèrement, et leur diamètre moyen est maintenant de 300 nm. La hauteur moyenne augmente de 10 nm. Enfin, pour la couche «épaisse»(S.4c)), le film couvre plus de 95 % de la surface d'ITO et son épaisseur moyenne est de $\sim$50 nm.

Dans ce qui suit, nous allons décrire le mode de croissance. Lorsque les couches sont déposées sur des substrats, trois types de croissance sont classiquement considérés. [62] Le premier est le type Franck Van der Merwe qui conduit à une croissance couche par

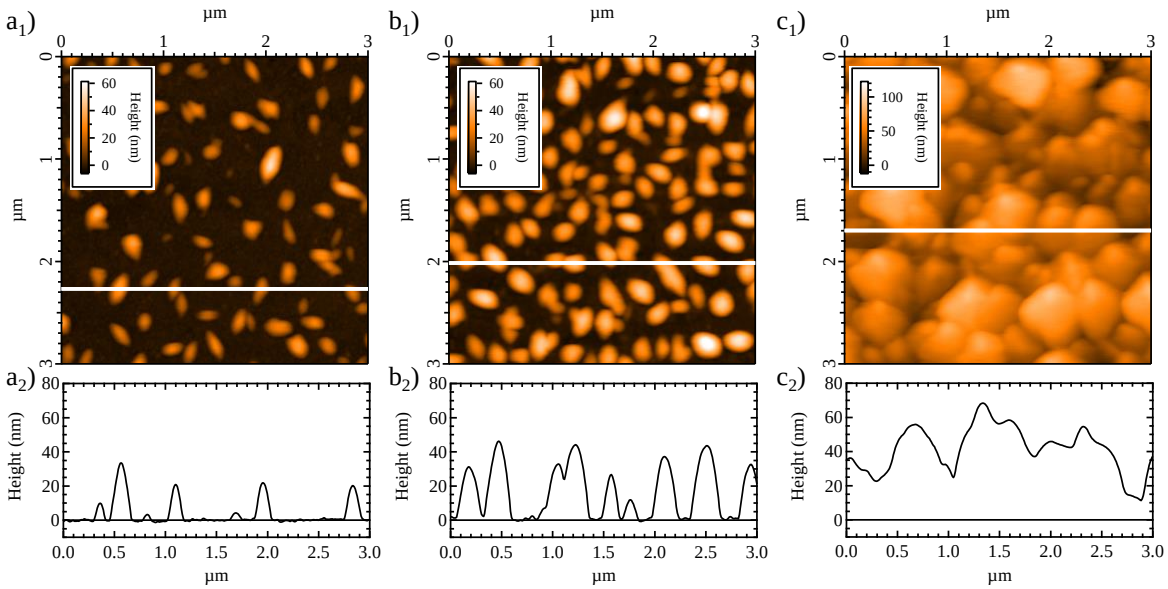

Figure S.4 – Images AFM des couches de DIPO-Ph_4 : a_1) $0{,}5 \times 10^{15}$ molécule $\cdot$ cm^{-2} ; b_1) 2×10^{15} molécule $\cdot$ cm^{-2} ; c_1) 10×10^{15} molécule $\cdot$ cm^{-2} ; a_2), b_2), et c_2) correspondent aux profils indiqués par une ligne blanche dans les images a_1), b_1), et c_1) respectivement. Le recouvrement moléculaire, exprimé en molécule $\cdot$ cm^{-2} (QB-coverage), est mesuré par la balance à quartz.

couche. Nos résultats montrent que ce n'est pas le cas pour les couches de DIPO-Ph_4. Dans le second, la croissance type Volmer-Weber, le matériau organique se dépose sous la forme d'îlots, laissant des zones de substrat nu. C'est ce qu'on voit pour les couches de DIPO-Ph_4. L'origine provient du fait que les interactions entre molécules est beaucoup plus forte que l'interaction entre la molécule de DIPO-Ph_4 et le substrat d'ITO. Dans le troisième mode, la croissance type Stranski-Krastanov, l'interaction molécule-molécule est en concurrence avec l'interaction entre les molécules du substrat. Une couche mince de mouillage couvre tout le substrat, au-dessus de laquelle le mode de croissance 3D se déroule. Si un mode Stranski-Krastanov a lieu, la couche de mouillage ne doit dépasser 2 nm. La résolution de l'AFM ne permet pas de conclure dans cette section.

Pour effectuer une analyse plus approfondie nous avons effectué des traitements de recuit. En effet, il serait intéressant de diminuer la hauteur moyenne des îlots grâce à de la désorption moléculaire. Nous voulions également, en chauffant le substrat lors de l'évaporation du matériau moléculaire, augmenter la vitesse de cristallisation. Deux types de traitement ont été réalisé :

- Un après l'évaporation, à pression ambiante et à une température voisine de la tem-

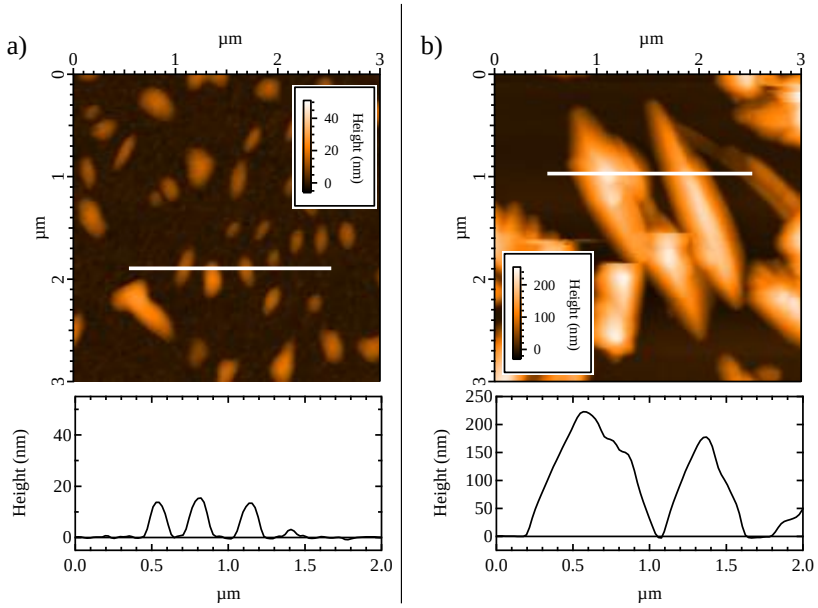

Figure S.5 – Images AFM des couches de DIPO-Ph_4 : a) 1×10^{15} molécule $\cdot$ cm^{-2} après recuit ; b) 10×10^{15} molécule $\cdot$ cm^{-2} déposé sur substrat chaud. Le recouvrement moléculaire, exprimé en molécule $\cdot$ cm^{-2} (QB-coverage), est mesuré par la balance à quartz.

pérature d'évaporation du DIPO-Ph_4 ($T \geq 170\,°C$) pour effectuer de la désorption moléculaire et accéder aux premières couches déposées.

- Un lors de l'évaporation, *i.e.* évaporation sur substrat chaud ($T = 100\,°C$), pour apporter de l'énergie au système et augmenter la vitesse de croissance.

Après un recuit à $T \geq 170\,°C$ sur un échantillon de 1×10^{15} molécule $\cdot$ cm^{-2} (Figure S.5a)), la hauteur moyenne des îlots diminue jusqu'à 13 nm. Les monticules recouvrent encore 20 % de la surface du substrat, avec un diamètre moyen de 230 nm. La hauteur moyenne des îlots diminue alors que la couverture globale et le diamètre moyen restent constants. Le recuit après dépôt permet donc de désorber du matériau organique et avec un tel traitement, nous pouvons accéder aux premières couches de dépôts qui sont représentatives des premières phases de l'évaporation.

Dans le cas d'une évaporation sur substrat chaud (Figure S.5b)), des structures jumelées croissent formant des cristaux moléculaires. L'énergie apportée par le substrat chaud, modifie la croissance moléculaire en augmentant la diffusion de la molécule sur la surface. L'échantillon alors obtenu peut être utilisé comme référence pour la structure cristallisée du DIPO-Ph_4.

Pour déterminer l'orientation moléculaire au sein de la couche organique, de la spectroscopie d'absorption des rayons X (XAS) a été effectuée. Il est important de comprendre

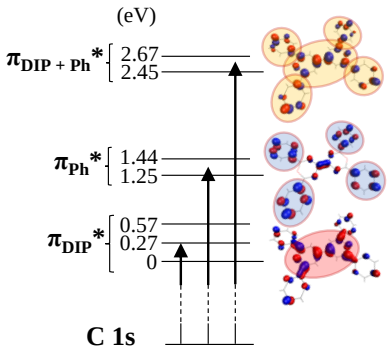

Figure S.6 – Schéma électronique des transitions C 1s pour le DIPO-Ph_4. La référence des énergies indiquées est le niveau de la LUMO. Trois MOs sont représentées avec une isovaleur de 0,04 (LUMO, LUMO+3 et LUMO+5). La localisation des orbitales est représentée par des ellipses.

les mécanismes électroniques qui ont lieu pendant le processus d'absorption. Des calculs théoriques (DFT) ont été effectués pour décrire les états moléculaires vides (LUMOs) localisée sur les carbones de la structure du DIPO-Ph_4 (Figure S.6). En effet, il est primordial de visualiser les orbitales moléculaires (MO) pour obtenir des informations sur l'orientation moléculaire.

Les LUMOs sont composées principalement de MOs qui sont perpendiculaires au cœur DIP ou aux groupes phényls (Ph). Elles peuvent être divisées en 3 groupes. Le premier est centré à ∼0,3 eV au-dessus la LUMO et composé de la LUMO et des LUMOs +1 et +2. Le second est centré à ∼1,3 eV au-dessus de la LUMO et composé des LUMOs +3 et +4. Le dernier d'entre eux est centré à ∼2,5 eV au-dessus de la LUMO et se compose des LUMOs +5 et +6. En regardant la localisation de ces groupes, il semble que le premier est principalement localisé sur le noyau DIP, tandis que le second est plus localisé sur les groupes Ph. Pour le dernier d'entre eux, les MOs sont localisés, avec le même poids, sur le noyau DIP et les groupes Ph. On appellera désormais ces trois groupes π^*_{DIP}, π^*_{Ph}, et $\pi^*_{\mathrm{DIP+Ph}}$. Seule la première transition pourra être utilisé pour répondre à la question de l'orientation puisque qu'il s'agit de la seule transition avec une direction globale dans la géométrie de la molécule (perpendiculaire au noyau DIP).

De la microscopie d'absorption X (microscopie par transmission des rayons X, STXM) a été effectuée sur la ligne PolLux (SLS) sur trois échantillons différents : pas de recuit sur l'un, recuit sur un deuxième et évaporation sur substrat chaud pour le dernier. Les stacks $[X; Y; h\nu]$ ont été analysée grâce à la décomposition en éléments principaux (PCA). Les quatre premières composantes ont été utilisés pour décomposer les stacks en quatre régions. Pour chacune, les spectres d'absorption ont été ensuite extraits. Ces spectres sont

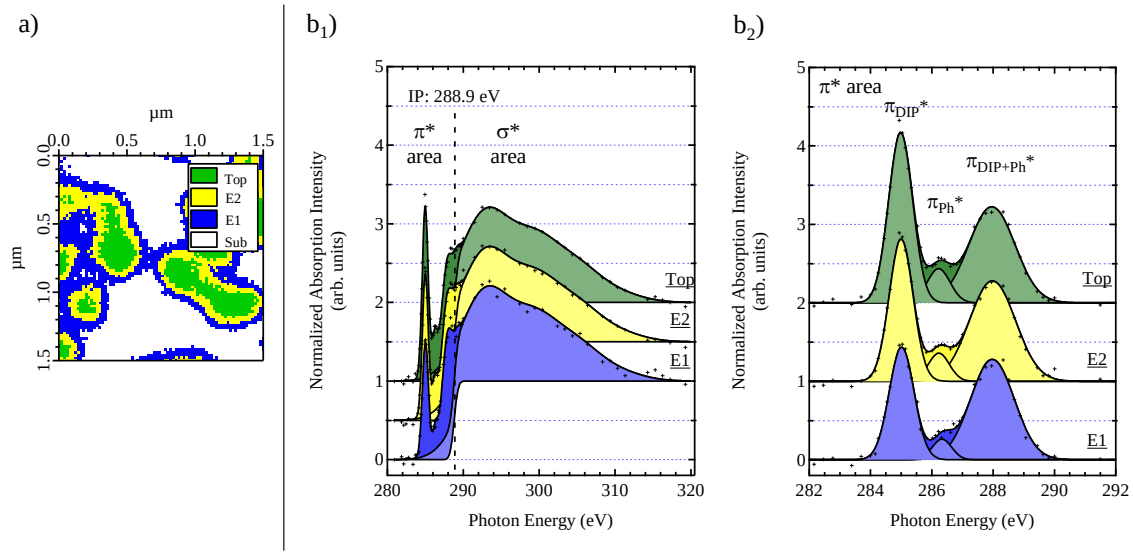

Figure S.7 – Echantillon sans recuit : a) carte de décomposition du stack ; b_1) spectres d'absorption extraits des régions (le spectre provenant du substrat (Sub) n'est pas représenté car il n'y a pas d'absorption provenant de cette région) ; b_2) transition π^* après soustraction du fond et de la transition σ^*.

la moyenne des spectres de la région.

La décomposition du stack pour l'échantillon sans recuit (Figure S.7a)) conduit à quatre régions précisément localisées sur l'échantillon. La région principale est celle localisée entre les îlots organiques. Il n'y a pas d'absorption (ou du moins trop faible pour être détectée avec la résolution du STXM). Cela correspond au substrat. Les monticules organiques sont quant à eux décomposés en trois régions : une sur le sommet et deux sur le bord. Ces régions seront désormais nommées Top, E2 et E1 respectivement.

Les spectres d'absorption ont été extraits de ces régions et normalisées (Figure S.7b_1)). On distincte clairement les transitions π^* et σ^*. Après soustraction du fond et de la transition σ^*, on peut décomposer la transitionπ^* avec plus de clarté (Figure S.7b_2). La première composante, centrée à ∼285 eV est attribuée à la transition π^*_{DIP}. π^*_{Ph} est à ∼286 eV, et $\pi^*_{\mathrm{DIP+Ph}}$ est centrée à ∼288 eV. L'intensité de la transition σ^* reste identique entre les spectres du sommet et du bord des îlots. Cette intensité a été utilisée comme référence pour évaluer la transition π^* dans les différentes régions. Le ratio π^*/σ^* diminue du sommet vers le bord. Cette évolution est principalement due à une diminution de la transition π^*_{DIP} (de 11 à 8 %). Cette transition est la seule qui peut être utilisée pour accéder à l'orientation moléculaire. Ainsi, dans la couche organique, il semble y avoir un changement entre les premières couches déposées et les dernières couches.

L'analyse de l'échantillon recuit (premières couches évaporées) permettrait de confir-

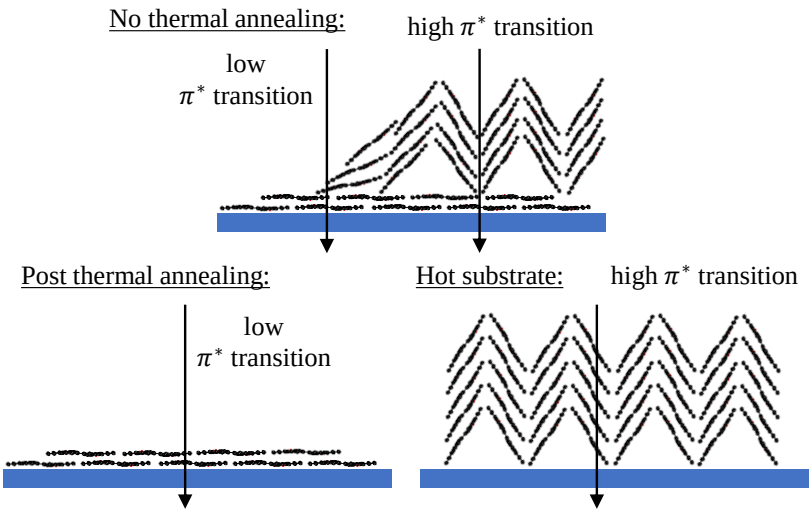

Figure S.8 – Représentation schématique de l'orientation moléculaire pour les différents échantillons.

mer cette évaporation. Dans le cas de cet échantillon, la transition σ^* est beaucoup plus élevée que dans l'échantillon précédent. On observe aussi une diminution depuis le sommet de la transition π^* (de 11 à 7 %).

Par conséquent, au début de l'évaporation sur substrat maintenu à température ambiante, les molécules se déposent parallèlement au substrat. Les interactions molécule-substrat sont minimisées dans cette configuration. Après quelques couches, les molécules commencent à se redresser et à cristalliser, piloté par le π-stacking. Il y a un changement dans l'orientation moléculaire, ce qui entraîne une augmentation de l'absorption au niveau π^*.

Pour confirmer la structure du matériau cristallisé nous avons étudié par STXM un échantillon déposé sur substrat chaud. Pour cet échantillon, il n'y a aucune différence entre le bord et le sommet des îlots organiques. La transition π^* est plus élevée que celle de l'échantillon non recuit (27–29 %). Les îlots sont totalement cristallisés depuis les premières couches déposées. La température du substrat apporte suffisamment d'énergie pour démarrer la cristallisation et surmonter l'interaction molécule-substrat.

Avec ces échantillons, nous avons obtenu deux orientations moléculaires opposées : un qui présente les molécules parallèles sur le dessus de la surface (échantillon avec recuit) et un autre avec des îlots organiques cristallisés (échantillon préparé sur substrat chaud). Nous sommes donc en mesure de moduler l'orientation moléculaire (Figure S.8). Pour des applications en électronique organique, il est important de contrôler la morphologie et l'orientation moléculaire afin d'améliorer, par exemple, la mobilité des charges à travers

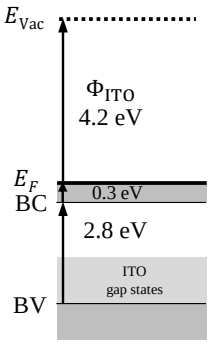

Figure S.9 – Diagramme énergique du substrat d'ITO.

la couche organique.

S.3 Interface ITO/DIPO-Ph_4 : alignement énergétique et durée de vie excitonique

L'ITO commercial que nous utilisons a tout d'abord été caractérisé en détails pour vérifier ses propriétés électroniques (concentration en porteur de charge, ségrégation en étain à la surface). Le diagramme énergétique récapitulatif de l'ITO est donné en Figure S.9

En ce qui concerne l'interface ITO/DIPO-Ph_4, on observe un shift rigide de +100 meV des énergies de liaison (BE) des niveaux de cœur de l'ITO. Ce shift indique que les molécules interagissent avec la surface de l'ITO et changent ainsi légèrement la densité de charge de surface. [19] Un transfert électronique de la molécule vers le substrat pourrait expliquer le mouvement du niveau de Fermi par rapport au minimum de la bande de conduction.

Nous allons maintenant examiner les modifications induites sur le spectre O 1s. Comme le substrat contient de l'oxygène, les spectres du DIPO-Ph_4 sont présentés comme la somme de la contribution de l'ITO et de nouvelles composantes. Comme illustré sur la Figure S.10, les composantes O1 et O2 apparaissent à 532,2 et 533,6 eV, respectivement.

Un transfert de charge de la molécule (DIPO-Ph_4 est un bon donneur [25]) vers le substrat d'ITO permet d'expliquer la formation des deux composantes pour le DIPO-Ph_4. En effet, un tel transfert conduit à la formation du cation radicalaire $[\text{DIPO-Ph}_4]^{\bullet+}$ et des calculs DFT corrélés à un modèle de relaxation dans le solide moléculaire ont montré que la distance entre O1 et O2 et de l'ordre de celle trouvée expérimentalement.

Concernant la bande de valence (Figure S.11), pour les dépôts dont le QB-coverage est $\leq 3 \times 10^{15}$ molécule $\cdot$ cm^{-2}, un spectre synthétique gris correspondant à la contribution de l'ITO est ajouté. Nous observons la croissance de six nouvelles composantes, marqués

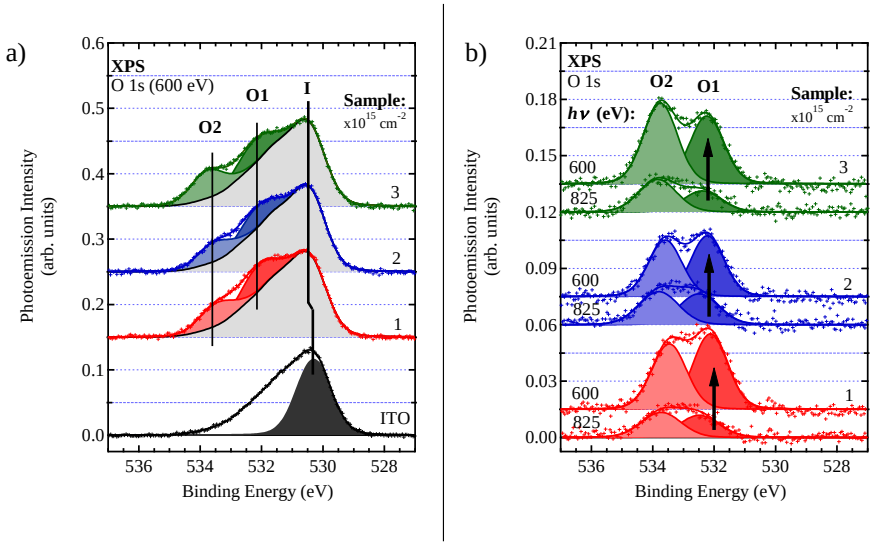

Figure S.10 – Spectres O 1s du substrat d'ITO chimiquement nettoyé, nu et couvert avec une augmentation du QB-coverage (1×10^{15}, 2×10^{15} et 3×10^{15} molécule $\cdot$ cm^{-2}). a) $h\nu = 600$ eV ; b) soustraction de la contribution du substrat d'ITO aux spectres montrés en a) et à $h\nu = 825$ eV, mettant l'accent sur la contribution du DIPO-Ph$_4$.

de A à F, qui se trouvent à 14,06, 10,97, 9,36, 6,99, 4,30 et 3,29 eV, respectivement. Deux nouveaux états apparaissent aussi à 2,5 et 1,4 eV, que nous étiquetons H(+) et H, respectivement. Ces composantes sont la SOMO et la HOMO de la molécule cationique et neutre respectivement.

La courbe d'émission des électrons secondaires (SEEDC) des dépôts 1×10^{15}, 2×10^{15}

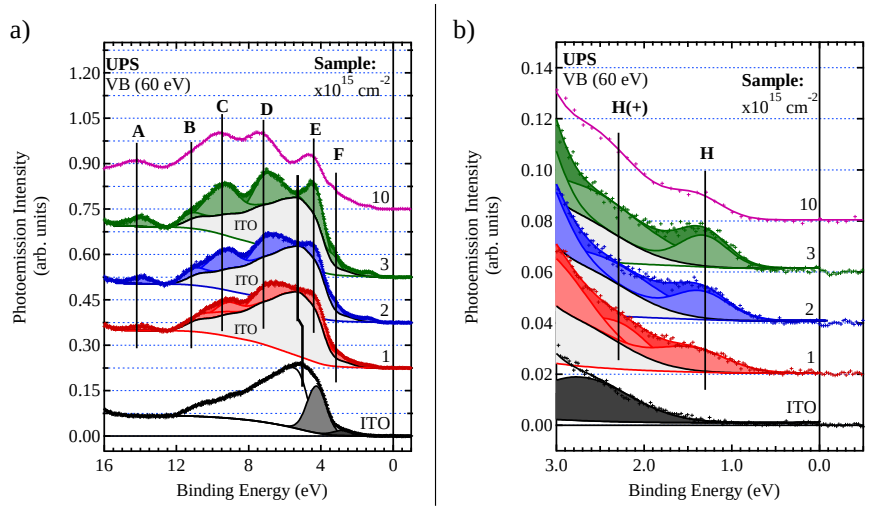

Figure S.11 – a) Photoémission UV : ITO et DIPO-Ph$_4$; b) Zoom de l'image a).

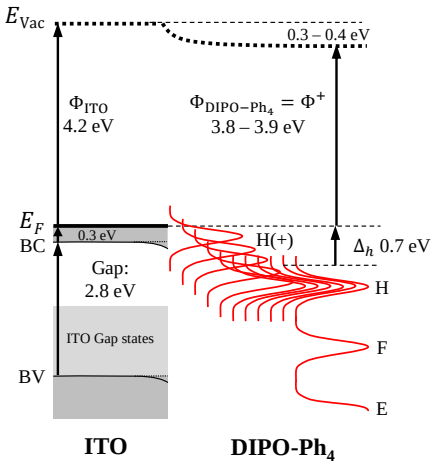

Figure S.12 – Diagramme énergétique de l'interface ITO/DIPO-Ph$_4$.

et 3×10^{15} molécule $\cdot$ cm^{-2} donne une valeur de 3,90 eV pour le travail de sortie. Étant donné qu'un transfert de charge a lieu de la couche organique vers le substrat, la valeur du travail de sortie (Φ) donne la valeur de Φ^+ (3,9 eV) et la légère baisse du travail de sortie par rapport à l'ITO nu est attribuée à la formation d'espèces cationiques à l'interface ITO/DIPO-Ph$_4$. [10] L'énergie d'ionisation de la HOMO (espèces neutres) obtenue en additionnant Φ à l'énergie de liaison du bord de la HOMO est de 4,6 eV. La valeur est en accord avec l'énergie d'ionisation mesurée grâce à la relation de Forrest. [56]

Nous présentons dans la Figure S.12, le diagramme énergétique de l'interface métal/organique ITO/DIPO-Ph$_4$.

Compte tenu de l'évaporation sous ultra-vide, le DIPO-Ph$_4$ ne doit pas être dopé et est moyennement conducteur. C'est seulement quand il rencontre le substrat qu'il peut transférer des charges électroniques et former un cation. Il s'agit d'un cas particulier de dopage, différent du dopage moléculaire classique, [109, 110, 111] où des molécules acceptrices ou donneuses sont insérés dans le semi-conducteur organique. Une différence significative avec le dopage moléculaire est l'absence de centres de recombinaison chargés négativement dans le film lui-même. Les couches minces en contact avec le substrat peuvent avoir une conductivité de trous importante.

Enfin pour caractériser la dynamique de transfert de charge, nous avons réalisé des expériences de photoémission résonnante (ResPES). Deux échantillons de DIPO-Ph$_4$ différents ont été étudiés. Pour être sensible à l'interface métal/organique, nous avons étudié un dépôt de 2×10^{15} molécule $\cdot$ cm^{-2} et à titre de comparaison, nous avons étudié un dépôt «épais»de 10×10^{15} molécule $\cdot$ cm^{-2} caractéristique du film inaltéré.

Pour les deux dépôts, le ResPES (Figure S.13a$_1$) et b$_1$)) montre une résonance princi-

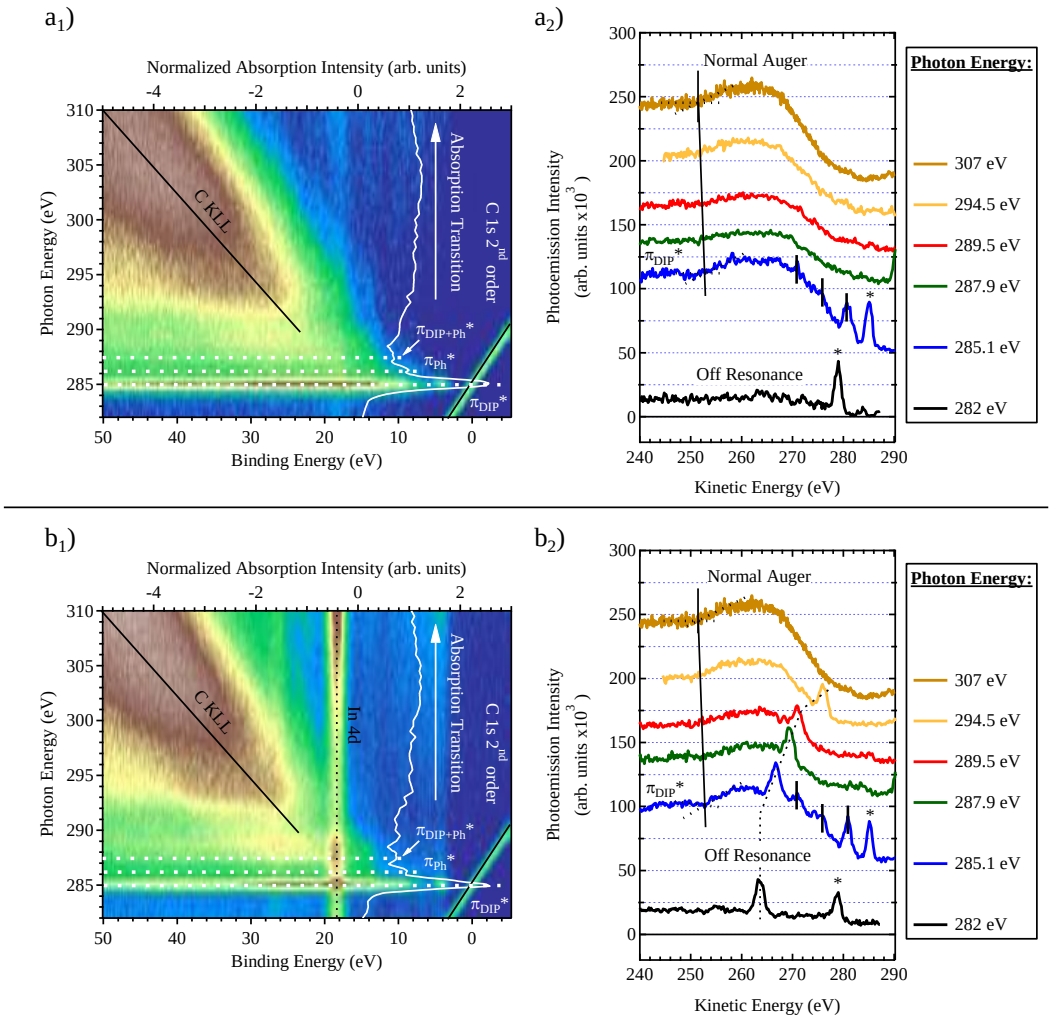

Figure S.13 – Niveau du carbone pour le DIPO-Ph_4 : a_1), b_1) ResPES ; a_2), b_2) Auger C KLL extraits pour les dépôts a) 10×10^{15} et b) 2×10^{15} molécule $\cdot$ cm^{-2}. Sur les spectres Auger, L'astérisque (*) indique la position du C 1s de second ordre ; la ligne pointillée indique la position du pic In 4d ; la ligne continue indique le shift dû à l'Auger spectateur ; et les petits traits (|) indiquent les Auger participants.

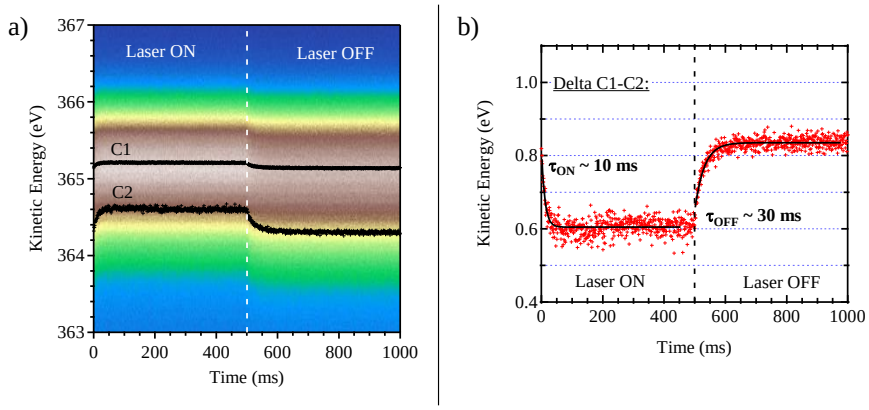

Figure S.14 – a) Spectres C 1s sous éclairement et sans laser ; b) Différence C1 − C2 extraite de a).

pale pour la transition π^*_{DIP} (285 eV). De ces cartographies, les Auger C KLL Auger sont extraits (Figure S.13a$_2$) et b$_2$)) à des énergies de photon correspondant aux différentes transitions d'absorption. L'Auger C KLL est clairement décalée pour une énergie de photon de 285,1 eV par rapport à l'Auger «normal»obtenu à 307 eV. Ce changement provient d'un Auger spectateur. Par ailleurs, de nouvelles structures apparaissent à la résonance correspondant aux Auger participants. Cependant, le spectre résonant ne présente pas de composantes de l'Auger «normal», ce qui indique que l'électron excité dans la CB reste à ce niveau pendant un temps beaucoup plus long que le temps caractéristique de la desexcitation électronique (8 fs). [92] Il n'y a aucun transfert de charge observé vers le substrat ou dans le continuum moléculaire. Un temps de vie excitonique long est donc suggéré.

Afin de déterminer le temps de vie excitonique du DIPO-Ph$_4$, nous avons effectué des expériences de pompe-sonde [123] sur la ligne de lumière TEMPO, SOLEIL. Nous avons utilisé une impulsion laser (400 nm ; 500 ms ; 5 mW) pour promouvoir un électron de valence dans les états inoccupés et donc fabriquer une paire électron-trou.

Le spectre C 1s ne présente aucun shift de l'énergie de liaison mais on observe une augmentation de la hauteur maximale et de l'asymétrie. Sous excitation, la décomposition du spectre C 1s montre que la composante C1 (phényl et DIP essentiellement) et la composante C2 (éther) se comportent différemment. Sous illumination, la composante C1 se décale légèrement de +70 meV. La composante C2 se décale elle de +300 meV. L'augmentation de la hauteur maximale est due à la plus petite différence d'énergie entre C1 et C2 sous illumination.

On trouve alors (Figure S.14) deux temps caractéristiques τ_{ON} et τ_{OFF} qui correspondent au temps de réponse du système moléculaire au cours du temps d'excitation et de désexcitation, respectivement. τ_{ON} est plus petit que τ_{OFF} comme le processus d'ab-

sorption est plus rapide que la désexcitation. Celui-ci est alors de l'ordre de 30 ms. Ces temps typiques sont ceux d'un processus de phosphorescence via un état triplet.

S.4 DIPO-Ph_4 comme couche interfaciale pour les dispositifs photovoltaïques organiques

Comme les DIPs sont de bons donneurs moléculaires, nous avons ajouté une couche de DIPO-Ph_4 dans une cellule solaire organique. L'épuisement rapide des sources d'énergie conventionnelles et la demande énergétique croissante, ont encouragé des recherches intensives sur les sources d'énergie renouvelable et durable. [125] Les sources d'énergie renouvelables se composent principalement du solaire, du vent, des marées, des vagues et de la géothermie. [126] Comme l'une des sources d'énergie les plus propres, l'énergie solaire a largement été développé dans trois technologies importantes : le solaire thermique, le solaire photovoltaïque (PV) et l'énergie solaire à concentration.

Une structure solaire typique se compose d'électrodes, cathode et l'anode, de couches interfaciales, une couche interfaciale cathodique (cIFL) et anodique (aIFL), et une couche active (jonction *p*-*n*). Visant à atteindre un rendement plus élevé, des efforts considérables se sont concentrés sur les matériaux de la couche active, les architectures des dispositifs et les couches interfaciales.

La couche de DIPO-Ph_4 peut-elle être une bonne couche interfaciale anodique (transporteur de trous) au sein d'une cellule photovoltaïque organique ? L'hétérojonction en volume (BHJ) typique pour une cellule solaire organique est un mélange de P3HT donneur et de PCBM accepteur. Il est possible de prédire l'alignement des différentes couches à partir des résultats déjà publiés de UPS [175] et de spectroscopie de photoémission inverse (IPES). [176] Cette alignement est présenté en Figure S.15.

La couche interfaciale de DIPO-Ph_4 présente un alignement favorable à la collecte des trous du P3HT et de bloquer les électrons du PCBM. Toutefois, si cette condition est nécessaire, elle n'est pas suffisante pour que le matériau se comporte comme un collectionneur de trou efficace et pour que les performances de la cellule soient améliorées. La conductivité du DIPO-Ph_4 et son recouvrement avec le substrat d'ITO (par unité de surface) doivent être aussi élevés. Dans le cas de la molécule de DIPS-Ph_4, le CS-AFM montre une augmentation notable de la conduction des trous. [26]

Les performances des cellules photovoltaïques sont données dans la Figure S.16. Avec la couche «épaisse»de DIPO-Ph_4, on atteint une efficacité de conversion de puissance (PCE) de 3,1 %. La tension de circuit ouvert (V_{OC}) et le facteur de remplissage (FF) sont 586 mV et 44 %, respectivement. La densité de courant (J_{SC}) est de 12,1 $mA \cdot cm^{-2}$. Ces résultats

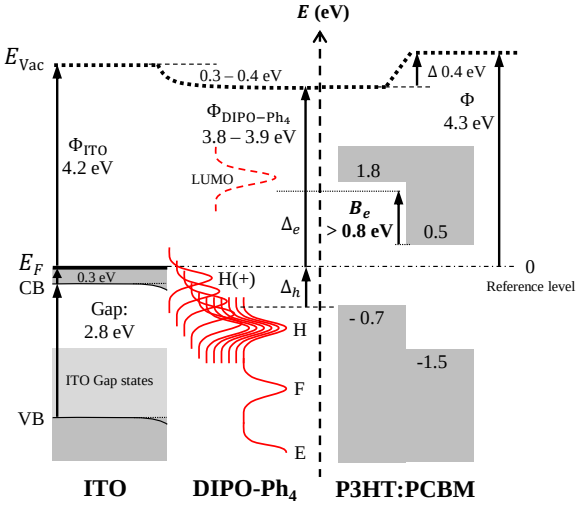

Figure S.15 – Schéma énergétique attendue du système ITO/DIPO-Ph_4/P3HT:PCBM. Les travaux de sortie du DIPO-Ph_4 et du P3HT [175] sont tous deux égaux à 3,9 eV (et les niveaux de vide sont alignés). Comme le gap LUMO/HOMO du DIPO-Ph_4 est supérieur à 2 eV (voir Figure S.2) la barrière de blocage électronique minimale est de 0,8 eV.

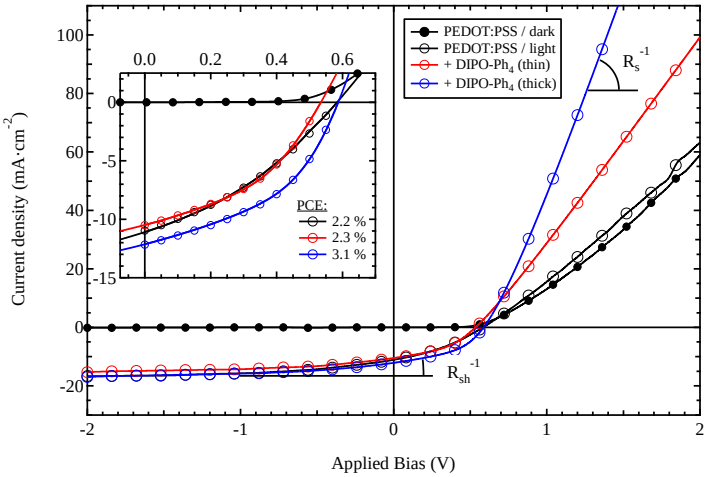

Figure S.16 – Caractérisation photovoltaïque avec 3 IFL différentes sous un éclairement de 100 $mW \cdot cm^{-2}$ et zoom sur la zone d'intérêt.

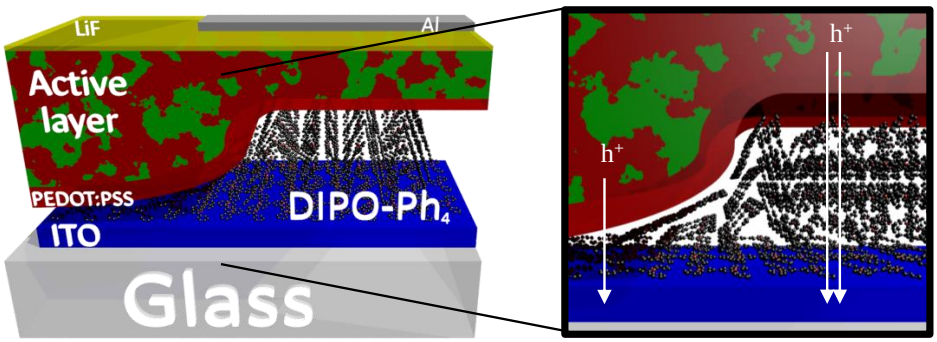

Figure S.17 – Représentation schématique de la morphologie de la cellule solaire. Une meilleure collecte des trous se fait par la couche de DIPO-Ph_4 que par le PEDOT:PSS.

ont été comparés à une cellule de référence avec seulement 5 nm de PEDOT:PSS comme couche interfaciale qui montre une PCE inférieure à 2,2 %.

Comme couche conductrice de trous et comparativement au PEDOT:PSS, la couche de DIPO-Ph_4 augmente l'efficacité de la collecte des charges à l'anode d'ITO (Figure IV.8). L'étude STXM a démontré qu'il était possible de former une structure en îlots qui maximise l'interaction orbitalaire pour atteindre les meilleures performances électroniques.

S.5 Effet de l'hétéroatome du DIP : morphologie et description électronique

Le mode d'alignement (alignement par la LUMO, limite de Schottky-Mott ou alignement par la HOMO) dépend de la valeur du travail de sortie du métal par rapport aux valeurs Φ^+ et Φ^- du matériau organique. Nous avons alors changé la structure de dipyranylidene en remplaçant l'oxygène par le soufre et le sélénium. L'électronégativité diminue de O à atomes de Se. [180]

D'un point de vue morphologique, la différence entre les structures DIP réside dans la forme des îlots : légèrement allongés pour DIPO-Ph_4, allongés et jumelés pour DIPS-Ph_4 et presque carrés pour DIPSe-Ph_4. Comme la cristallisation à l'intérieur de la couche est différente entre les trois structures, elle conduit à des formes d'îlot différents.

De plus, des études XAS ont été faites sur DIPS-Ph_4 et ont monté que la couche du dérivé soufré croît comme celle du DIPO-Ph_4. Les premières molécules déposées sont parallèles à la surface, puis, comme les interactions intermoléculaires deviennent importantes, le matériau cristallise et on observe par STXM un changement dans l'orientation.

En ce qui concerne les propriétés électroniques des interface ITO/DIP, on observe par XPS un shift en énergie de liaisons des niveaux de cœurs de l'ITO pour le dérivé soufré

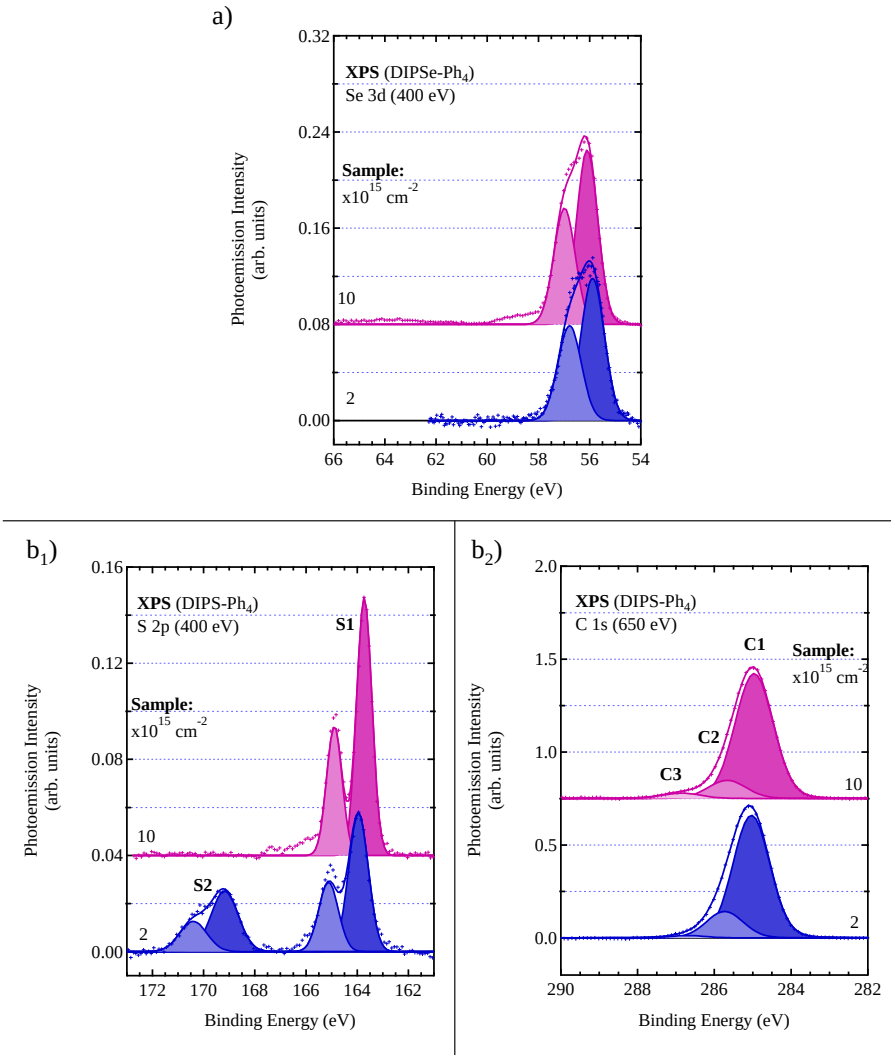

Figure S.18 – a) Spectre du Se 3d pour DIPSe-Ph_4 ; b_1) du S 2p et b_2) du C 1s pour DIPS-Ph_4. Les spectres ont été enregistrés à ALOISA.

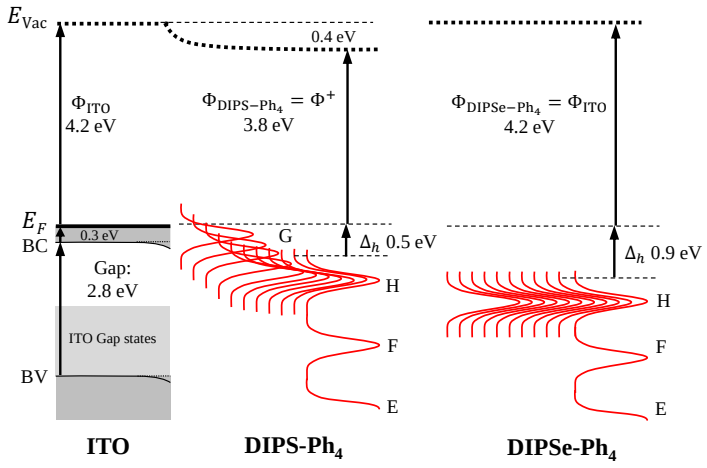

Figure S.19 – Alignement des niveaux énergétiques pour les interfaces ITO/DIPS-Ph$_4$ et ITO/DIPSe-Ph$_4$.

mais pas pour le dérivé séléné ce qui tend à penser à un transfert de charge dans le premier cas mais pas dans le second.

En regardant les niveaux S 2p et Se 3d (Figure S.18), on voit la présence de deux composantes S2 et S1 pour le dérivé soufré alors que sur le sélénium une seule composante est présente. L'étude de la bande de valence permet de conclure sur la formation d'un cation à l'interface pour le dérivé soufré et pas de transfert de charge pour le dérivé séléné.

Cependant, la différence en énergie entre S2 et S1 est plus large que dans le cadre du dérivé oxygéné. Comment expliquer la différence en énergie entre S1 et S2 ? Les calculs DFT et le modèle de relaxation pour la forme cationique conduisent à une trop petite différence. Nous considérons donc que le soufre réagit après le transfert de charge avec l'oxygène de surface et forme une liaison $S^+ - O$. L'environnement chimique du soufre cationique est modifié et l'énergie de liaison de la composante S2 est supérieure à celle d'un cationique pur.

Finalement, nous avons déterminer le diagramme énergétique et l'alignement des niveaux pour les différents DIP (Figure S.19). Nous avons obtenu, avec le dérivé soufré et le dérivé séléné deux modes d'alignement différents : pour DIPS-Ph$_4$, un alignement par la HOMO, avec un transfert de charge vers l'ITO et pour DIPSe-Ph$_4$, un alignement des niveaux du vide (limite de Schottky-Mott). Cela résulte d'une différence importante entre les énergies d'ionisation des deux dérivés DIP.

Conclusion

Cette thèse présente une description structurale et électronique d'une interface ITO/DIP. Nous avons caractérisé en détail le substrat d'ITO, puis l'interface ITO/DIPO-Ph_4. Nous avons ensuite appliqué ces résultats à l'étude du dérivé soufré et séléné. Les expériences de synchrotron ont montré être des techniques puissantes pour accéder à l'organisation moléculaire (STXM), à l'environnement chimique et l'alignement du niveau d'énergie (XPS), au transfert de charge (ResPES) et aux temps de la désexcitation des molécules DIP (pompe-sonde). Des calculs DFT (niveaux d'énergie moléculaires et énergies d'ionisation) nous permettent de traiter les données, mais aussi de corréler les résultats expérimentaux.

La morphologie des couches DIP peut être qualifiée d'îlots sur la surface couvrant partiellement la surface d'ITO. En décomposant les stacks d'absorption obtenus par STXM, nous avons été en mesure de distinguer les changements dans l'orientation moléculaire depuis les premières couches déposées jusqu'au au sommet des îlots. Au début de l'évaporation, les molécules se posent parallèles à la surface. Lorsque les interactions intramoléculaires deviennent plus énergétiquement favorables, la matière organique se cristallise, entraînée par le π-stacking.

Le rayonnement synchrotron nous a donné des informations sur les propriétés électroniques du substrat et des films DIP. Le fait que l'épaisseur du film n'est pas uniforme, tel qu'illustré par l'AFM et le STXM, est essentiel pour interpréter les spectres de photoémission. Les énergies de liaison des composants de l'ITO augmentent lorsque la molécule est déposée, à l'exception du dérivé de DIPSe-Ph_4. Ceci est interprété comme un remplissage de la bande de conduction par les électrons provenant des molécules déposées.

Pour le DIPO-Ph_4 et le DIPS-Ph_4, nous détectons la présence de deux composantes dans les spectres de O 1s et S 2p, ce qui indique que la molécule est dans deux états différents. Un état correspond à la molécule intacte. L'autre, à une énergie de liaison supérieure, provient d'une molécule altérée en interaction avec le substrat après transfert de charge. Pour DIPSe-Ph_4, aucun transfert de charge n'est observé dû à une énergie d'ionisation plus élevé que les deux autre DIPs.

Grâce à des expériences de pompe-sonde, nous avons pu mesurer la durée de vie de l'exciton qui est de l'ordre de plusieurs dizaines de millisecondes et qui est à l'origine des observations faite en photoémission résonante.

Enfin, nous avons utilisé le DIPO-Ph_4 dans un dispositif de cellule organique. L'efficacité augmente en raison d'une meilleure collecte de trou. La densité de courant est significativement plus élevée que celui de la cellule de référence. Ce résultat a été corrélé aux précédentes études structurales et électroniques. Les molécules de DIP sont donc bien prometteuses pour les applications en électronique organique.

Nous nous sommes donc efforcés de décrire précisément les résultats afin d'établir un protocole d'étude pour les interfaces métal/organique. D'autres expériences sont déjà prévues pour achever l'étude Néanmoins, nous avons posé notre brique sur le mur du monde de l'électronique organique.

Bibliography

[1] S. Reineke, F. Lindner, G. Schwartz, N. Seidler, K. Walzer, B. Lüssem & K. Leo; "White organic light-emitting diodes with fluorescent tube efficiency"; Nature **459**, p. 234–238 (2009); ISSN 0028-0836; URL http://dx.doi.org/10.1038/nature08003. 1, 2, S-1

[2] M. Małachowski & J. Żmija; "Organic field-effect transistors"; Opto-Electronics Review **18**, p. 121–136 (2010); ISSN 1896-3757; URL http://dx.doi.org/10.2478/s11772-010-0008-9. 1, S-1

[3] P. W. M. Blom, V. D. Mihailetchi, L. J. A. Koster & D. E. Markov; "Device Physics of Polymer: Fullerene Bulk Heterojunction Solar Cells"; Advanced Materials **19**, p. 1551–1566 (2007); ISSN 09359648; URL http://dx.doi.org/10.1002/adma.200601093. 1, S-1

[4] M. Grätzel; "Applied physics: Solar cells to dye for"; Nature **421**, p. 586–587 (2003); ISSN 0028-0836; URL http://dx.doi.org/10.1038/421586a. 1, S-1

[5] P. Lin & F. Yan; "Organic Thin-Film Transistors for Chemical and Biological Sensing"; Advanced Materials **24**, p. 34–51 (2012); ISSN 09359648; URL http://dx.doi.org/10.1002/adma.201103334. 1, S-1

[6] M. Scharber & N. Sariciftci; "Efficiency of bulk-heterojunction organic solar cells"; Progress in Polymer Science **38**, p. 1929–1940 (2013); ISSN 00796700; URL http://dx.doi.org/10.1016/j.progpolymsci.2013.05.001. 1, 2, S-1

[7] W. Brütting, C. Adachi & R. J. D. Holmes; *Physics of organic semiconductors* (Wiley-VCH) (2012); ISBN 3527410538. 1, 79, S-1

[8] H. Ishii & K. Seki; "Energy level alignment at organic/metal interfaces studied by UV photoemission: breakdown of traditional assumption of a common vacuum level at the interface"; IEEE Transactions on Electron Devices **44**, p. 1295–1301 (1997); ISSN 00189383; URL http://dx.doi.org/10.1109/16.605471. 1, 15, S-1

[9] S. Braun, W. R. Salaneck & M. Fahlman; "Energy-level alignment at organic/metal and organic/organic interfaces"; Advanced Materials **21**, p. 1450–1472 (2009); ISSN 09359648; URL http://dx.doi.org/10.1002/adma.200802893. 1, 11, 17, S-1, S-5

[10] M. Oehzelt, N. Koch & G. Heimel; "Organic semiconductor density of states controls the energy level alignment at electrode interfaces"; Nature Communications **5**, p. 4174–4181 (2014); ISSN 2041-1723; URL http://dx.doi.org/10.1038/ncomms5174. 1, 17, 19, 68, 110, S-1, S-5, S-14

[11] C. Dimitrakopoulos & P. Malenfant; "Organic Thin Film Transistors for Large Area Electronics"; Advanced Materials **14**, p. 99–117 (2002); ISSN 0935-9648; URL http://dx.doi.org/10.1002/1521-4095(20020116)14:2<99::AID-ADMA99>3.0.CO;2-9. 1, S-1

[12] S. De Feyter & F. C. De Schryver; "Self-assembly at the liquid/solid interface: STM reveals"; Journal of Physical Chemistry B **109**, p. 4290–4302 (2005); ISSN 15206106; URL http://dx.doi.org/10.1021/jp045298k. 1, 2

[13] J. V. Barth, G. Costantini & K. Kern; "Engineering atomic and molecular nanostructures at surfaces"; Nature **437**, p. 671–679 (2005); ISSN 0028-0836; URL http://dx.doi.org/10.1038/nature04166. 1, 2

[14] J. V. Barth; "Molecular Architectonic on Metal Surfaces"; Annual Review of Physical Chemistry **58**, p. 375–407 (2007); ISSN 0066-426X; URL http://dx.doi.org/10.1146/annurev.physchem.56.092503.141259. 1, 2, 70

[15] L. Bartels; "Tailoring molecular layers at metal surfaces"; Nature Chemistry **2**, p. 87–95 (2010); ISSN 1755-4330; URL http://dx.doi.org/10.1038/nchem.517. 1, 2

[16] J.-M. Lehn; *Supramolecular chemistry : concepts and perspectives* (VCH) (1995); ISBN 3527293116. 1

[17] A. Kahn, N. Koch & W. Gao; "Electronic structure and electrical properties of interfaces between metals and Pi-conjugated molecular films"; Journal of Polymer Science, Part B: Polymer Physics **41**, p. 2529–2548 (2003); ISSN 08876266; URL http://dx.doi.org/10.1002/polb.10642. 2, 17, S-2, S-5

[18] Y. Gassenbauer & A. Klein; "Electronic and chemical properties of tin-doped indium oxide (ITO) surfaces and ITO/ZnPc interfaces studied in-situ by photo-

electron spectroscopy"; Journal of Physical Chemistry B **110**, p. 4793–4801 (2006); ISSN 15206106; URL http://dx.doi.org/10.1021/jp056640b. 2, 62, S-2

[19] D. Qi, W. Chen, X. Gao, L. Wang, S. Chen, P. L. Kian & A. T. S. Wee; "Surface transfer doping of diamond (100) by tetrafluoro- tetracyanoquinodimethane"; Journal of the American Chemical Society **129**, p. 8084–8085 (2007); ISSN 00027863; URL http://dx.doi.org/10.1021/ja072133r. 2, 58, 105, S-2, S-12

[20] P. Borghetti, A. El-Sayed, E. Goiri, C. Rogero, J. Lobo-Checa, L. Floreano, J. E. Ortega & D. G. de Oteyza; "Spectroscopic Fingerprints of Work-Function-Controlled Phthalocyanine Charging on Metal Surfaces"; ACS Nano **8**, p. 12 786–12 795 (2014); ISSN 1936-0851; URL http://dx.doi.org/10.1021/nn5060333. 2, S-2

[21] A. Khaliq, J. J. Gallet, F. Bournel, D. Pierucci, H. Tissot, M. Silly, F. Sirotti & F. Rochet; "Charge transfer and energy level alignment at the interface between cyclopentene-modified Si(001) and tetracyanoquinodimethane"; Journal of Physical Chemistry C **118**, p. 22 499–22 508 (2014); ISSN 19327455; URL http://dx.doi.org/10.1021/jp502680b. 2, 17, S-2, S-5

[22] N. Gonzalez-Lakunza, I. Fernández-Torrente, K. J. Franke, N. Lorente, A. Arnau & J. I. Pascual; "Formation of Dispersive Hybrid Bands at an Organic-Metal Interface"; Physical Review Letters **100**, p. 156 805–156 808 (2008); ISSN 0031-9007; URL http://dx.doi.org/10.1103/PhysRevLett.100.156805. 2, S-2

[23] I. Fernández-Torrente, K. J. Franke & J. I. Pascual; "Vibrational Kondo Effect in Pure Organic Charge-Transfer Assemblies"; Physical Review Letters **101**, p. 217 203–217 206 (2008); ISSN 0031-9007; URL http://dx.doi.org/10.1103/PhysRevLett.101.217203. 2, S-2

[24] T. Choi, S. Bedwani, A. Rochefort, C.-Y. Chen, A. J. Epstein & J. A. Gupta; "A Single Molecule Kondo Switch: Multistability of Tetracyanoethylene on Cu(111)"; Nano Letters **10**, p. 4175–4180 (2010); ISSN 1530-6984; URL http://dx.doi.org/10.1021/nl1024563. 2, S-2

[25] J. Alizon, J. Blanc, J. Gallice, H. Robert, C. Fabre, H. Strzelecka, J. Rivory & C. Weyl; "Investigations of high conductivity of dipyranylidene and dithiadipyranylidene — TCNQ complexes"; in "Organic Conductors and Semiconductors", p. 563–569 (Springer-Verlag, Berlin/Heidelberg) (1977); URL http://dx.doi.org/10.1007/BFb0012411. 3, 13, 63, 107, S-4, S-12

[26] S. Berny, L. Tortech, M. Véber & D. Fichou; "Dithiapyrannylidenes as efficient hole collection interfacial layers in organic solar cells"; ACS Applied Materials & Interfaces **2**, p. 3059–3068 (2010); ISSN 19448244; URL http://dx.doi.org/10.1021/am1005546. 3, 14, 91, 93, 95, S-4, S-17

[27] M. Courté, S. G. Surya, R. Thamankar, C. Shen, V. R. Rao, S. G. Mhaisalkar, D. Fichou, T. Qi, T. Liu, K. Lu, C. Du, Z. Shuai, G. Yu & D. Zhu; "A non-volatile resistive memory effect in 2,2',6,6'-tetraphenyl-dipyranylidene thin films as observed in field-effect transistors and by conductive atomic force microscopy"; RSC Adv. **7**, p. 3336–3342 (2017); ISSN 2046-2069; URL http://dx.doi.org/10.1039/C6RA26876E. 3, 14, S-4

[28] M. Courté, M. Alaaeddine, V. Barth, L. Tortech & D. Fichou; "Structural and electronic properties of 2,2',6,6'-tetraphenyl-dipyranylidene and its use as a hole-collecting interfacial layer in organic solar cells"; Dyes and Pigments **141**, p. 487–492 (2017); ISSN 01437208; URL http://dx.doi.org/10.1016/j.dyepig.2017.03.002. 3, 14, S-4

[29] S. M. Sze & K. K. Ng; *Physics of semiconductor devices* (Wiley-Interscience) (2007); ISBN 0471143235. 7, 8

[30] A. Klein; "Transparent conducting oxides: Electronic structure-property relationship from photoelectron spectroscopy with in situ sample preparation"; Journal of the American Ceramic Society **96**, p. 331–345 (2013); ISSN 00027820; URL http://dx.doi.org/10.1111/jace.12143. 9

[31] C. Brabec, V. Dyakonov & U. Scherf; *Organic Photovoltaics* (Wiley-VCH Verlag GmbH & Co. KGaA, Weinheim, Germany) (2008); ISBN 9783527623198; URL http://dx.doi.org/10.1002/9783527623198. 9

[32] A. W. Hains, Z. Liang, M. A. Woodhouse & B. A. Gregg; "Molecular semiconductors in organic photovoltaic cells"; Chemical Reviews **110**, p. 6689–6735 (2010); ISSN 00092665; URL http://dx.doi.org/10.1021/cr9002984. 9

[33] J. Meiss, C. L. Uhrich, K. Fehse, S. Pfuetzner, M. K. Riede & K. Leo; "Transparent Electrode Materials for Solar Cells"; in P. Schelkens, A. Gombert, F. Berghmans, A. Tervonen, R. M. De La Rue, D. L. Andrews, K. Kalli, J. Popp, N. P. Johnson, H. Urey, K. P. Panajotov, P. L. Heremans, H. Thienpont, J. A. Terry, J. T. Sheridan, G. C. Righini, C. Gorecki, A. K. Asundi, S. K. Honkanen, F. Wyrowski, T. Graf, P. Van Daele, M. Muccini, M. Sciamanna, W. Drexler, W. Urbanczyk, J.-M. Nunzi, C. López, F. Möllmer,

E. Özbay, A. G. Mignani, T. Ebrahimi, G. Cristóbal, A. Cutolo, N. I. Zheludev, M. Midrio, A. Ostendorf, V. V. Tuchin, A. A. Valle, E. A. Meulenkamp, J. Mohr, H. Jelínková, L. Pavesi, W. Osten, L. Vivien, M. R. Taghizadeh, D. L. Matthews, R. Michalzik, P. Viktorovitch, R. W. Ziolkowski, P. P. Meyrueis, F. Truchetet & T. P. Pearsall (editors), "Photonics Europe, Photonics for solar Energy Systems II", , volume 7002p. 700 210–700 218 (2008); ISBN 9780819472007; ISSN 0277786X; URL http://dx.doi.org/10.1117/12.781275. 9

[34] P. Hyesung, J. A. Rowehl, K. Ki Kang, V. Bulovic & K. Jing; "Doped Graphene Electrodes for Organic Solar Cells"; Nanotechnology **21**, p. 505 204–505 209 (2010); ISSN 0957-4484; URL http://dx.doi.org/10.1088/0957-4484/21/50/505204. 9

[35] Y. Zhu, Z. Sun, Z. Yan, Z. Jin & J. M. Tour; "Rational design of hybrid graphene films for high-performance transparent electrodes"; ACS Nano **5**, p. 6472–6479 (2011); ISSN 19360851; URL http://dx.doi.org/10.1021/nn201696g. 9

[36] D. Johnson; "Graphene Still Trying to Replace ITO in Organic Solar Cells"; (2013); URL spectrum.ieee.org. 9

[37] H. M. Mirletz, K. A. Peterson, I. T. Martin & R. H. French; "Degradation of transparent conductive oxides: Interfacial engineering and mechanistic insights"; Solar Energy Materials and Solar Cells **143**, p. 529–538 (2015); ISSN 09270248; URL http://dx.doi.org/10.1016/j.solmat.2015.07.030. 9

[38] R. G. Egdell; "Dopant and Defect Induced Electronic States at In2O3 Surfaces"; in J. Jupille & G. Thornton (editors), "Springer Series in Surface Sciences", , *Springer Series in Surface Sciences*, volume 58p. 351–400 (Springer International Publishing) (2015); ISBN 978-3-319-14366-8 978-3-319-14367-5; URL http://dx.doi.org/10.1007/978-3-319-14367-5_12. 9, 50, 53, 54

[39] Y. Jia, C. Chen, D. Jia, S. Li, S. Ji & C. Ye; "Silver Nanowire Transparent Conductive Films with High Uniformity Fabricated via a Dynamic Heating Method"; ACS Applied Materials & Interfaces **8**, p. 9865–9871 (2016); ISSN 1944-8244; URL http://dx.doi.org/10.1021/acsami.6b00500. 9

[40] X. Guo, X. Liu, F. Lin, H. Li, Y. Fan & N. Zhang; "Highly Conductive Transparent Organic Electrodes with Multilayer Structures for Rigid and Flexible Optoelectronics"; Scientific Reports **5**, p. 10 569–10 577 (2015); ISSN 2045-2322; URL http://dx.doi.org/10.1038/srep10569. 9

[41] G. Gruner, M.-H. Yoon, A. Gaur, M. Shim, A. Facchetti, T. J. Marks, J. A. Rogers, L. Wang, T. J. Marks, J. R. Ireland & C. R. Kannewurf; "Carbon nanotube films for transparent and plastic electronics"; Journal of Materials Chemistry **16**, p. 3533–3539 (2006); ISSN 0959-9428; URL http://dx.doi.org/10.1039/b603821m. 9

[42] J.-Y. Hong, W. Kim, D. Choi, J. Kong & H. S. Park; "Omnidirectionally Stretchable and Transparent Graphene Electrodes"; ACS Nano **10**, p. 9446–9455 (2016); ISSN 1936-0851; URL http://dx.doi.org/10.1021/acsnano.6b04493. 9

[43] M. Marezio; "Refinement of the crystal structure of In2O3 at two wavelengths"; Acta Crystallographica **20**, p. 723–728 (1966); ISSN 0365-110X; URL http://dx.doi.org/10.1107/S0365110X66001749. 9

[44] S. Nishikawa; "The influence of substrate temperature and sputtering gas atmosphere on the electrical properties of reactively sputtered indium tin oxide films"; Thin Solid Films **135**, p. 219–228 (1986); ISSN 00406090; URL http://dx.doi.org/10.1016/0040-6090(86)90129-X. 9

[45] H. K. Müller; "Electrical and Optical Properties of Sputtered In2O3 films. I. Electrical Properties and Intrinsic Absorption"; Physica Status Solidi (B) **27**, p. 723–731 (1968); ISSN 15213951; URL http://dx.doi.org/10.1002/pssb.19680270229. 10

[46] Y. Gassenbauer, R. Schafranek, A. Klein, S. Zafeiratos, M. Hävecker, A. Knop-Gericke & R. Schlögl; "Surface states, surface potentials, and segregation at surfaces of tin-doped In2O3"; Physical Review B - Condensed Matter and Materials Physics **73**, p. 245 312–245 322 (2006); ISSN 10980121; URL http://dx.doi.org/10.1103/PhysRevB.73.245312. 10, 50, 51, 53, 54

[47] A. Walsh, J. L. F. Da Silva, S. H. Wei, C. Körber, A. Klein, L. F. J. Piper, A. Demasi, K. E. Smith, G. Panaccione, P. Torelli, D. J. Payne, A. Bourlange & R. G. Egdell; "Nature of the band gap of In2O3 revealed by first-principles calculations and X-ray spectroscopy"; Physical Review Letters **100**, p. 167 402–167 405 (2008); ISSN 00319007; URL http://dx.doi.org/10.1103/PhysRevLett.100.167402. 10

[48] D. Braun, V. Scherer, C. Janowitz, Z. Galazka, R. Fornari & R. Manzke; "In-gap states of In2O3 single crystals investigated by scanning tunneling spectroscopy"; Physica Status Solidi (A) Applications and Materials Science **211**, p. 59–

65 (2014); ISSN 18626300; URL http://dx.doi.org/10.1002/pssa.201330089. 10, 54

[49] E. Burstein; "Anomalous optical absorption limit in InSb4"; Physical Review **93**, p. 632–633 (1954); ISSN 0031899X; URL http://dx.doi.org/10.1103/PhysRev.93.632. 10

[50] T. S. Moss; "The Interpretation of the Properties of Indium Antimonide"; Proceedings of the Physical Society. Section B **67**, p. 775–782 (1954); ISSN 0370-1301; URL http://dx.doi.org/10.1088/0370-1301/67/10/306. 10

[51] A. Klein, C. Körber, A. Wachau, F. Säuberlich, Y. Gassenbauer, S. P. Harvey, D. E. Proffit & T. O. Mason; "Transparent conducting oxides for photovoltaics: Manipulation of fermi level,work function and energy band alignment"; Materials **3**, p. 4892–4914 (2010); ISSN 19961944; URL http://dx.doi.org/10.3390/ma3114892. 10, 53, 56

[52] C. Körber, V. Krishnakumar, A. Klein, G. Panaccione, P. Torelli, A. Walsh, J. L. F. Da Silva, S.-H. Wei, R. G. Egdell & D. J. Payne; "Electronic structure of In2O3 and Sn-doped In2O3 by hard X-ray photoemission spectroscopy"; Physical Review B **81**, p. 165 207–165 215 (2010); ISSN 1098-0121; URL http://dx.doi.org/10.1103/PhysRevB.81.165207. 10, 50, 54

[53] K. Sugiyama, H. Ishii, Y. Ouchi & K. Seki; "Dependence of indium–tin–oxide work function on surface cleaning method as studied by ultraviolet and X-ray photoemission spectroscopies"; Journal of Applied Physics **87**, p. 295–298 (2000); ISSN 00218979; URL http://dx.doi.org/10.1063/1.371859. 10

[54] D. P. McMahon & A. Troisi; "Evaluation of the External Reorganization Energy of Polyacenes"; The Journal of Physical Chemistry Letters **1**, p. 941–946 (2010); ISSN 1948-7185; URL http://dx.doi.org/10.1021/jz1001049. 11

[55] W. E. Hatfield (editor); *Molecular Metals* (Springer US, Boston, MA) (1979); ISBN 978-1-4684-3482-8; URL http://dx.doi.org/10.1007/978-1-4684-3480-4. 13

[56] B. W. D'Andrade, S. Datta, S. R. Forrest, P. Djurovich, E. Polikarpov & M. E. Thompson; "Relationship between the ionization and oxidation potentials of molecular organic semiconductors"; Organic Electronics: physics, materials, applications **6**, p. 11–20 (2005); ISSN 15661199; URL http://dx.doi.org/10.1016/j.orgel.2005.01.002. 13, 68, S-4, S-14

[57] S. Berny, L. Tortech & D. Fichou; "Derives de type dipyrannylidene comme couche interfaciale anodique dans des dispositifs electroniques"; (2011). 13, 91

[58] D. Chasseau, J. Gaultier, C. Hauw, R. Fugnitto, V. Gianis & H. Strzelecka; "Tétraphényldipyranylidène (Dip-Ph4)"; Acta Crystallographica Section B **38**, p. 1629–1631 (1982); ISSN 1600-5740; URL http://dx.doi.org/10.1107/S0567740882006645. 14, 32, S-4

[59] H. R. Luss & D. L. Smith; "The structure of tetraphenyldithiapyranylidene"; Acta Crystallographica Section B Structural Crystallography and Crystal Chemistry **36**, p. 986–989 (1980); ISSN 05677408; URL http://dx.doi.org/10.1107/S0567740880005110. 14, S-4

[60] A. Leclaire, C. Regnault du Mottier, G. Le Coustumer & IUCr; "Structure du tétraphényl-2,2',6,6' bisélénapyrannylidène-4:4'"; Acta Crystallographica Section C Crystal Structure Communications **42**, p. 312–314 (1986); ISSN 01082701; URL http://dx.doi.org/10.1107/S0108270186096361. 14, S-4

[61] A. Bolag, M. Mamada, J.-i. Nishida & Y. Yamashita; "Field-Effect Transistors Based on Tetraphenyldipyranylidenes and the Sulfur Analogues"; Chemistry of Materials **21**, p. 4350–4352 (2009); ISSN 0897-4756; URL http://dx.doi.org/10.1021/cm902037w. 14, S-4

[62] J. A. Venables, G. D. T. Spiller & M. Hanbucken; "Nucleation and growth of thin films"; Reports on Progress in Physics **47**, p. 399–459 (1984); ISSN 0034-4885; URL http://dx.doi.org/10.1088/0034-4885/47/4/002. 15, 16, 33, S-6

[63] X. Crispin, V. Geskin, A. Crispin, J. Cornil, R. Lazzaroni, W. R. Salaneck & J. L. Brédas; "Characterization of the interface dipole at organic/metal interfaces"; Journal of the American Chemical Society **124**, p. 8131–8141 (2002); ISSN 00027863; URL http://dx.doi.org/10.1021/ja025673r. 17, S-5

[64] S. Braun, W. Osikowicz, Y. Wang & W. R. Salaneck; "Energy level alignment regimes at hybrid organic-organic and inorganic-organic interfaces"; Organic Electronics: physics, materials, applications **8**, p. 14–20 (2007); ISSN 15661199; URL http://dx.doi.org/10.1016/j.orgel.2006.10.006. 17, S-5

[65] H. Vázquez, F. Flores & A. Kahn; "Induced Density of States model for weakly-interacting organic semiconductor interfaces"; Organic Electronics: physics, materials, applications **8**, p. 241–248 (2007); ISSN 15661199; URL http://dx.doi.org/10.1016/j.orgel.2006.07.006. 17, S-5

[66] A. Klein; "Energy band alignment at interfaces of semiconducting oxides: A review of experimental determination using photoelectron spectroscopy and comparison with theoretical predictions by the electron affinity rule, charge neutrality levels, and the common anion"; Thin Solid Films **520**, p. 3721–3728 (2012); ISSN 00406090; URL http://dx.doi.org/10.1016/j.tsf.2011.10.055. 17, S-5

[67] H. Hertz; "Ueber einen Einfluss des ultravioletten Lichtes auf die electrische Entladung"; Annalen der Physik **267**, p. 983–1000 (1887); ISSN 15213889; URL http://dx.doi.org/10.1002/andp.18872670827. 19

[68] P. D. Innes; "On the Velocity of the Cathode Particles Emitted by Various Metals under the Influence of Rontgen Rays, and Its Bearing on the Theory of Atomic Disintegration"; Proceedings of the Royal Society of London A: Mathematical, Physical and Engineering Sciences **79**, p. 442–462 (1907); URL http://rspa.royalsocietypublishing.org/content/79/532/442. 19

[69] C. Nordling, E. Sokolowski & K. Siegbahn; "Precision Method for Obtaining Absolute Values of Atomic Binding Energies"; Physical Review **105**, p. 1676–1677 (1957); ISSN 0031-899X; URL http://dx.doi.org/10.1103/PhysRev.105.1676. 20

[70] A. Taylor; "Practical surface analysis, 2nd edn., vol I, auger and X-ray photoelectron spectroscopy. Edited by D. Briggs & M. P. Seah"; Journal of Chemical Technology & Biotechnology **53**, p. 555–586 (1992); ISSN 02682575; URL http://dx.doi.org/10.1002/jctb.280530219. 20

[71] C. N. Berglund & W. E. Spicer; "Photoemission Studies of Copper and Silver: Theory"; Physical Review **136**, p. A1030–A1044 (1964); ISSN 0031-899X; URL http://dx.doi.org/10.1103/PhysRev.136.A1030. 20

[72] W. F. Egelhoff; "Core-level binding-energy shift at surface and in solids"; Surface Science Reports **6**, p. 253–415 (1987). 23

[73] B. Winter & M. Faubel; "Photoemission from liquid aqueous solutions"; Chemical Reviews **106**, p. 1176–1211 (2006); ISSN 00092665; URL http://dx.doi.org/10.1021/cr040381p. 23

[74] P. W. Atkins & A. J. MacDermott; "The Born equation and ionic solvation"; Journal of Chemical Education **59**, p. 359–360 (1982); ISSN 0021-9584; URL http://dx.doi.org/10.1021/ed059p359; ed059p359. 23

[75] C. J. Powell; "Calculations of electron inelastic mean free paths from experimental optical data"; Surface and Interface Analysis **7**, p. 263–274 (1985); ISSN 0142-2421; URL http://dx.doi.org/10.1002/sia.740070604. 24, 51

[76] A. Jablonski; "Determination of the electron inelastic mean free path in solids from the elastic electron backscattering intensity"; Surface and Interface Analysis **37**, p. 1035–1044 (2005); ISSN 01422421; URL http://dx.doi.org/10.1002/sia.2119. 24

[77] J. Als-Nielsen & D. McMorrow; *Elements of modern X-ray physics* (Wiley) (2011); ISBN 0470973943. 25

[78] I. Hamberg & C. G. Granqvist; "Evaporated Sn-doped In2O3 films: Basic optical properties and applications to energy-efficient windows"; Journal of Applied Physics **60**, p. R123–R160 (1986); ISSN 00218979; URL http://dx.doi.org/10.1063/1.337534. 32, 53, 54

[79] E. H. Morales, Y. He, M. Vinnichenko, B. Delley & U. Diebold; "Surface structure of Sn-doped In2O3 (111) thin films by STM"; New Journal of Physics **10**, p. 125 030–125 040 (2008); ISSN 13672630; URL http://dx.doi.org/10.1088/1367-2630/10/12/125030. 32

[80] B. Watts, T. Schuettfort & C. R. McNeill; "Mapping of Domain Orientation and Molecular Order in Polycrystalline Semiconducting Polymer Films with Soft X-Ray Microscopy"; Advanced Functional Materials **21**, p. 1122–1131 (2011); ISSN 1616301X; URL http://dx.doi.org/10.1002/adfm.201001918. 38

[81] S. Swaraj, C. Wang, H. Yan, B. Watts, J. Lüning, C. R. McNeill & H. Ade; "Nanomorphology of Bulk Heterojunction Photovoltaic Thin Films Probed with Resonant Soft X-ray Scattering"; Nano Letters **10**, p. 2863–2869 (2010); ISSN 1530-6984; URL http://dx.doi.org/10.1021/nl1009266. 38

[82] B. A. Collins, E. Gann, L. Guignard, X. He, C. R. McNeill & H. Ade; "Molecular Miscibility of Polymer-Fullerene Blends"; The Journal of Physical Chemistry Letters **1**, p. 3160–3166 (2010); ISSN 1948-7185; URL http://dx.doi.org/10.1021/jz101276h. 38

[83] B. A. Collins, J. E. Cochran, H. Yan, E. Gann, C. Hub, R. Fink, C. Wang, T. Schuettfort, C. R. McNeill, M. L. Chabinyc & H. Ade; "Polarized X-ray scattering reveals non-crystalline orientational ordering in organic films"; Nature

Materials **11**, p. 536–543 (2012); ISSN 1476-1122; URL http://dx.doi.org/10.1038/nmat3310. 38

[84] B. A. Collins, Z. Li, J. R. Tumbleston, E. Gann, C. R. McNeill & H. Ade; "Absolute Measurement of Domain Composition and Nanoscale Size Distribution Explains Performance in PTB7:PC71BM Solar Cells"; Advanced Energy Materials **3**, p. 65–74 (2013); ISSN 16146832; URL http://dx.doi.org/10.1002/aenm.201200377. 38

[85] L. Ye, S. Zhang, W. Ma, B. Fan, X. Guo, Y. Huang, H. Ade & J. Hou; "From Binary to Ternary Solvent: Morphology Fine-tuning of D/A Blends in PDPP3T-based Polymer Solar Cells"; Advanced Materials **24**, p. 6335–6341 (2012); ISSN 1521-4095; URL http://dx.doi.org/10.1002/ADMA.201202855. 38

[86] J. A. Bartelt, Z. M. Beiley, E. T. Hoke, W. R. Mateker, J. D. Douglas, B. A. Collins, J. R. Tumbleston, K. R. Graham, A. Amassian, H. Ade, J. M. J. Fréchet, M. F. Toney & M. D. McGehee; "The Importance of Fullerene Percolation in the Mixed Regions of Polymer-Fullerene Bulk Heterojunction Solar Cells"; Advanced Energy Materials **3**, p. 364–374 (2013); ISSN 16146832; URL http://dx.doi.org/10.1002/aenm.201200637. 38

[87] A. C. Stuart, J. R. Tumbleston, H. Zhou, W. Li, S. Liu, H. Ade & W. You; "Fluorine Substituents Reduce Charge Recombination and Drive Structure and Morphology Development in Polymer Solar Cells"; Journal of the American Chemical Society **135**, p. 1806–1815 (2013); ISSN 0002-7863; URL http://dx.doi.org/10.1021/ja309289u. 38

[88] S. P. Harvey, T. O. Mason, Y. Gassenbauer, R. Schafranek & A. Klein; "Surface versus bulk electronic/defect structures of transparent conducting oxides: I. Indium oxide and ITO"; Journal of Physics D: Applied Physics **39**, p. 3959–3968 (2006); ISSN 0022-3727; URL http://dx.doi.org/10.1088/0022-3727/39/18/006. 50, 51

[89] V. Christou, M. Etchells, O. Renault, P. J. Dobson, O. V. Salata, G. Beamson & R. G. Egdell; "High resolution x-ray photoemission study of plasma oxidation of indium–tin–oxide thin film surfaces"; Journal of Applied Physics **88**, p. 5180–5187 (2000); ISSN 00218979; URL http://dx.doi.org/10.1063/1.1312847. 50, 53

[90] V. M. Bermudez, A. D. Berry, H. Kim & A. Piqué; "Functionalization of indium

tin oxide"; Langmuir **22**, p. 11 113–11 125 (2006); ISSN 07437463; URL http://dx.doi.org/10.1021/la061578a. 51

[91] F. P. Sabino, L. N. De Oliveira & J. L. F. Da Silva; "Role of atomic radius and d -states hybridization in the stability of the crystal structure of M2O3 (M=Al, Ga, In) oxides"; Physical Review B - Condensed Matter and Materials Physics **90**, p. 155 206–155 212 (2014); ISSN 1550235X; URL http://dx.doi.org/10.1103/PhysRevB.90.155206. 52, 54

[92] J. J. Yeh & I. Lindau; "Atomic subshell photoionization cross sections and asymmetry parameters: Z from 1 to 103"; Atom. Data Nucl. Data **32**, p. 1–155 (1985). 52, 75, S-16

[93] H. Ibach & H. Lüth; *Solid-state physics: An introduction to principles of materials science* (Springer; 2nd edition) (2010); ISBN 9783540938033; URL http://dx.doi.org/10.1007/978-3-540-93804-0; arXiv:1011.1669v3. 53

[94] R. Abram, G. Rees & B. Wilson; "Heavily doped semiconductors and devices"; Advances in Physics **27**, p. 799–892 (1978); ISSN 0001-8732; URL http://dx.doi.org/10.1080/00018737800101484. 53

[95] K. F. Berggren & B. E. Sernelius; "Band-gap narrowing in heavily doped many-valley semiconductors"; Physical Review B **24**, p. 1971–1986 (1981); ISSN 0163-1829; URL http://dx.doi.org/10.1103/PhysRevB.24.1971. 53

[96] P. Ágoston, P. Erhart, A. Klein & K. Albe; "Geometry, electronic structure and thermodynamic stability of intrinsic point defects in indium oxide"; Journal of Physics: Condensed Matter **21**, p. 455 801–455 811 (2009); ISSN 0953-8984; URL http://dx.doi.org/10.1088/0953-8984/21/45/455801. 54

[97] T. L. Barr; "Nature of the use of adventitious carbon as a binding energy standard"; Journal of Vacuum Science & Technology A: Vacuum, Surfaces, and Films **13**, p. 1239–1246 (1995); ISSN 07342101; URL http://dx.doi.org/10.1116/1.579868. 58

[98] G. P. López, D. G. Castner & B. D. Ratner; "XPS O 1s binding energies for polymers containing hydroxyl, ether, ketone and ester groups"; Surface and Interface Analysis **17**, p. 267–272 (1991); ISSN 10969918; URL http://dx.doi.org/10.1002/sia.740170508. 62

[99] Y. Hirose, A. Kahn, V. Aristov & P. Soukiassian; "Chemistry, diffusion, and electronic properties of a metal/organic semiconductor contact:

In/perylenetetracarboxylic dianhydride"; Applied Physics Letters **68**, p. 217–219 (1996); ISSN 00036951; URL http://dx.doi.org/10.1063/1.116465. 62

[100] Y. Hirose, A. Kahn, V. Aristov, P. Soukiassian, V. Bulovic & S. R. Forrest; "Chemistry and electronic properties of metal-organic semiconductor interfaces: Al, Ti, In, Sn, Ag, and Au on PTCDA"; Physical Review B **54**, p. 13 748–13 758 (1996); ISSN 0163-1829; URL http://dx.doi.org/10.1103/PhysRevB.54.13748. 62

[101] S. Carniato, J. J. Gallet, F. Rochet, G. Dufour, F. Bournel, S. Rangan, A. Verdini & L. Floreano; "Characterization of hydroxyl groups on water-reacted Si (001)-2x1 using synchrotron radiation O 1s core-level spectroscopies and core-excited state density-functional calculations"; Physical Review B - Condensed Matter and Materials Physics **76**, p. 085 321–085 333 (2007); ISSN 10980121; URL http://dx.doi.org/10.1103/PhysRevB.76.085321. 63

[102] S. Carniato, F. Rochet, J. J. Gallet, F. Bournel, G. Dufour, C. Mathieu & S. Rangan; "DFT calculations of XPS/NEXAFS and IR spectra to elucidate the reaction products of acetonitrile with Si(001)-2x1"; Surface Science **601**, p. 5515–5525 (2007); ISSN 00396028; URL http://dx.doi.org/10.1016/j.susc.2007.09.039. 63

[103] R. Coustel, S. Carniato, F. Rochet & N. Witkowski; "Pyridine on Si(001)-(2x1): Density functional theory simulations compared with spectroscopic measurements"; Physical Review B - Condensed Matter and Materials Physics **85**, p. 035 323–035 331 (2012); ISSN 10980121; URL http://dx.doi.org/10.1103/PhysRevB.85.035323. 63

[104] S. Rangan, F. Bournel, J. J. Gallet, S. Kubsky, K. Le Guen, G. Dufour, F. Rochet, F. Sirotti, S. Carniato & V. Ilakovac; "Experimental and theoretical NEXAFS/XPS study of the room-temperature adsorption of acetonitrile on Si (001) -2x1"; Physical Review B - Condensed Matter and Materials Physics **71**, p. 165 319–165 329 (2005); ISSN 10980121; URL http://dx.doi.org/10.1103/PhysRevB.71.165319. 63

[105] C. Mathieu, X. Bai, J. J. Gallet, F. Bournel, S. Carniato, F. Rochet, E. Magnano, F. Bondino, R. Funke, U. Köhler & S. Kubsky; "Molecular staples on Si(001)-2x1: Dual-head primary amines"; Journal of Physical Chemistry C **113**, p. 11 336–11 345 (2009); ISSN 19327447; URL http://dx.doi.org/10.1021/jp902918j. 63

[106] D. Cahen & A. Kahn; "Electron energetics at surfaces and interfaces: Concepts and experiments"; Advanced Materials **15**, p. 271–277 (2003); ISSN 09359648; URL http://dx.doi.org/10.1002/adma.200390065. 68

[107] F. Evangelista, V. Carravetta, G. Stefani, B. Jansik, M. Alagia, S. Stranges & A. Ruocco; "Electronic structure of copper phthalocyanine: An experimental and theoretical study of occupied and unoccupied levels"; Journal of Chemical Physics **126**, p. 124 709–124 718 (2007); ISSN 00219606; URL http://dx.doi.org/10.1063/1.2712435. 68

[108] D. J. Milliron, I. G. Hill, C. Shen, A. Kahn & J. Schwartz; "Surface oxidation activates indium tin oxide for hole injection"; Journal of Applied Physics **87**, p. 572–576 (2000); ISSN 00218979; URL http://dx.doi.org/10.1063/1.371901. 69

[109] J. H. Lee & J. J. Kim; "Interfacial doping for efficient charge injection in organic semiconductors"; Physica Status Solidi (A) Applications and Materials Science **209**, p. 1399–1413 (2012); ISSN 18626300; URL http://dx.doi.org/10.1002/pssa.201228199. 69, S-14

[110] B. Lüssem, M. Riede & K. Leo; "Doping of organic semiconductors"; Physica Status Solidi (A) Applications and Materials Science **210**, p. 9–43 (2013); ISSN 18626300; URL http://dx.doi.org/10.1002/pssa.201228310. 69, S-14

[111] S. J. Yoo & J. J. Kim; "Charge transport in electrically doped amorphous organic semiconductors"; Macromolecular Rapid Communications **36**, p. 984–1000 (2015); ISSN 15213927; URL http://dx.doi.org/10.1002/marc.201500026. 69, S-14

[112] S. R. Forrest; "The path to ubiquitous and low-cost organic electronic appliances on plastic"; Nature **428**, p. 911–918 (2004); ISSN 0028-0836; URL http://dx.doi.org/10.1038/nature02498. 69

[113] F. Schreiber; "Structure and growth of self-assembling monolayers"; Progress in Surface Science **65**, p. 151–257 (2000); ISSN 00796816; URL http://dx.doi.org/10.1016/S0079-6816(00)00024-1. 70

[114] P. A. Brühwiler, O. Karis & N. Mårtensson; "Charge-transfer dynamics studied using resonant core spectroscopies"; Reviews of Modern Physics **74**, p. 703–740 (2002); ISSN 00346861; URL http://dx.doi.org/10.1103/RevModPhys.74.703. 70, 72, 76

[115] D. Menzel, N. Müller, T. Uphues, V. S. Yakovlev, A. Baltuska, B. Horvath, B. Schmidt, L. Blümel, R. Holzwarth, S. Hendel, M. Drescher,

U. Kleineberg & P. M. Echenique; "Ultrafast charge transfer at surfaces accessed by core electron spectroscopies"; Chemical Society Reviews **37**, p. 2212–2223 (2008); ISSN 0306-0012; URL http://dx.doi.org/10.1039/b719546j. 70

[116] J. J. Gallet, F. Bournel, S. Kubsky, G. Dufour, F. Rochet & F. Sirotti; "Resonant Auger spectroscopy of solid acrylonitrile at the N K-edge"; Journal of Electron Spectroscopy and Related Phenomena **122**, p. 285–295 (2002); ISSN 03682048; URL http://dx.doi.org/10.1016/S0368-2048(01)00366-8. 70, 76

[117] J. J. Gallet, F. Jolly, F. Rochet, F. Bournel, G. Dufour, P. A. Avila, F. Sirotti & P. Torelli; "Resonant Auger spectroscopy of poly(4-hydroxystyrene)"; Journal of Electron Spectroscopy and Related Phenomena **122**, p. 11–25 (2002); ISSN 03682048; URL http://dx.doi.org/10.1016/S0368-2048(01)00303-6. 70

[118] J. J. Gallet, F. Bournel, S. Carniato, G. Dufour, F. Rochet, S. Rangan & F. Sirotti; "Resonant Auger spectroscopy study of charge transfer phenomena in N 1s core-excited acetonitrile adsorbates on Si(001)-2×1"; Surface Science **601**, p. 552–561 (2007); ISSN 00396028; URL http://dx.doi.org/10.1016/j.susc.2006.10.022. 70

[119] L. Cao, X.-Y. Gao, A. T. S. Wee & D.-C. Qi; "Quantitative Femtosecond Charge Transfer Dynamics at Organic/Electrode Interfaces Studied by Core-Hole Clock Spectroscopy"; Advanced Materials **26**, p. 7880–7888 (2014); ISSN 09359648; URL http://dx.doi.org/10.1002/adma.201305414. 70

[120] D. Cvetko, G. Fratesi, G. Kladnik, A. Cossaro, G. P. Brivio, L. Venkataraman, A. Morgante, A. Santaniello, A. Verdini, F. Tommasini, G. Tondello, K. Plunkett, D. Delongchamp, C. Nuckolls, A. Morgante, D. Cvetko & I. Kymissis; "Ultrafast electron injection into photo-excited organic molecules"; Phys. Chem. Chem. Phys. **18**, p. 22 140–22 145 (2016); ISSN 1463-9076; URL http://dx.doi.org/10.1039/C6CP04099C. 70

[121] J. Stöhr; *NEXAFS Spectroscopy*; *Springer Series in Surface Sciences*, volume 25 (Springer Berlin Heidelberg, NewYork) (1992); ISBN 978-3-642-08113-2; URL http://dx.doi.org/10.1007/978-3-662-02853-7; arXiv:1011.1669v3. 70, A-6

[122] J. Schnadt, J. Schiessling & P. A. Brühwiler; "Comparison of the size of excitonic effects in molecular π systems as measured by core and valence spectroscopies"; Chemical Physics **312**, p. 39–45 (2005); ISSN 03010104; URL http://dx.doi.org/10.1016/j.chemphys.2004.11.019. 78

[123] J. P. Long, S. J. Chase & M. N. Kabler; "Excited-state photoelectron spectroscopy of excitons in C60 and photopolymerized C60 films"; Physical Review B **64**, p. 205 415–205 426 (2001); ISSN 0163-1829; URL http://dx.doi.org/10.1103/PhysRevB.64.205415. 79, S-16

[124] B. Mahler, L. Guillemot, L. Bossard-Giannesini, S. Ithurria, D. Pierucci, A. Ouerghi, G. Patriarche, R. Benbalagh, E. Lacaze, F. Rochet & E. Lhuillier; "Metallic Functionalization of CdSe 2D Nanoplatelets and Its Impact on Electronic Transport"; Journal of Physical Chemistry C **120**, p. 12 351–12 361 (2016); ISSN 19327455; URL http://dx.doi.org/10.1021/acs.jpcc.6b02101; arXiv:1011.1669v3. 81

[125] O. Ellabban, H. Abu-Rub & F. Blaabjerg; "Renewable energy resources: Current status, future prospects and their enabling technology"; Renewable and Sustainable Energy Reviews **39**, p. 748–764 (2014); ISSN 1364-0321; URL http://dx.doi.org/10.1016/j.rser.2014.07.113. 85, S-17

[126] S. R. Bull; "Renewable energy today and tomorrow"; Proceedings of the IEEE **89**, p. 1216–1226 (2001); ISSN 0018-9219; URL http://dx.doi.org/10.1109/5.940290. 85, S-17

[127] K. H. Solangi, M. R. Islam, R. Saidur, N. A. Rahim & H. Fayaz; "A review on global solar energy policy"; Renewable and Sustainable Energy Reviews **15**, p. 2149–2163 (2011); ISSN 1364-0321; URL http://dx.doi.org/10.1016/j.rser.2011.01.007. 85

[128] G. R. Timilsina, L. Kurdgelashvili & P. A. Narbel; "Solar energy: Markets, economics and policies"; Renewable and Sustainable Energy Reviews **16**, p. 449–465 (2012); ISSN 1364-0321; URL http://dx.doi.org/10.1016/j.rser.2011.08.009. 85

[129] X. Fan, M. Zhang, X. Wang, F. Yang & X. Meng; "Recent progress in organic–inorganic hybrid solar cells"; Journal of Materials Chemistry A **1**, p. 8694–8709 (2013); ISSN 2050-7496; URL http://dx.doi.org/10.1039/C3TA11200D. 87

[130] J. Ward, K. Ramanathan, F. Hasoon, T. J. Coutts, J. Keane, M. Contreras, T. Moriarty & R. Noufi; "A 21.5Cu(In,Ga)Se2 thin-film concentrator solar cell"; Progress in Photovoltaics: Research and Applications **10**, p. 41–46 (2002); ISSN 1099-159X; URL http://dx.doi.org/10.1002/pip.424. 87

[131] M. Gloeckler, I. Sankin & Z. Zhao; "CdTe solar cells at the threshold to 20% efficiency"; IEEE Journal of Photovoltaics **3**, p. 1389–1393 (2013); ISSN 21563381; URL http://dx.doi.org/10.1109/JPHOTOV.2013.2278661. 87

[132] E. D. Kosten, J. H. Atwater, J. Parsons, A. Polman & H. A. Atwater; "Highly efficient GaAs solar cells by limiting light emission angle"; Light: Science & Applications **2**, p. e45–e50 (2013); ISSN 2047-7538; URL http://dx.doi.org/10.1038/lsa.2013.1. 87

[133] Q. Zhang, X. Wan, F. Liu, B. Kan, M. Li, H. Feng, H. Zhang, T. P. Russell & Y. Chen; "Evaluation of Small Molecules as Front Cell Donor Materials for High-Efficiency Tandem Solar Cells"; Advanced Materials p. 7008–7012 (2016); ISSN 15214095; URL http://dx.doi.org/10.1002/adma.201601435. 88

[134] O. K. Varghese, M. Paulose & C. A. Grimes; "Long vertically aligned titania nanotubes on transparent conducting oxide for highly efficient solar cells"; Nature Nanotechnology **4**, p. 592–597 (2009); ISSN 1748-3387; URL http://dx.doi.org/10.1038/nnano.2009.226. 88

[135] W. R. Wei, M. L. Tsai, S. T. Ho, S. H. Tai, C. R. Ho, S. H. Tsai, C. W. Liu, R. J. Chung & J. H. He; "Above-11organic-inorganic hybrid solar cells with omnidirectional harvesting characteristics by employing hierarchical photon-trapping structures"; Nano Letters **13**, p. 3658–3663 (2013); ISSN 15306984; URL http://dx.doi.org/10.1021/nl401540h. 88

[136] C. Roldán-Carmona, P. Gratia, I. Zimmermann, G. Grancini, P. Gao, M. Graetzel & M. K. Nazeeruddin; "High efficiency methylammonium lead triiodide perovskite solar cells: the relevance of non-stoichiometric precursors"; Energy & Environmental Science **8**, p. 3550–3556 (2015); ISSN 1754-5706; URL http://dx.doi.org/10.1039/C5EE02555A. 88

[137] Y. Ogomi, A. Morita, S. Tsukamoto, T. Saitho, N. Fujikawa, Q. Shen, T. Toyoda, K. Yoshino, S. S. Pandey, T. Ma & S. Hayase; "CH3NH3SnxPb(1-x)I3 perovskite solar cells covering up to 1060 nm"; Journal of Physical Chemistry Letters **5**, p. 1004–1011 (2014); ISSN 19487185; URL http://dx.doi.org/10.1021/jz5002117. 88

[138] F. Hao, C. C. Stoumpos, D. H. Cao, R. P. H. Chang & M. G. Kanatzidis; "Lead-free solid-state organic–inorganic halide perovskite solar cells"; Nature Photonics **8**, p. 489–494 (2014); ISSN 1749-4885; URL http://dx.doi.org/10.1038/nphoton.2014.82; 0402594v3. 88

[139] N. Thejo Kalyani & S. J. Dhoble; "Organic light emitting diodes: Energy saving lighting technology - A review"; Renewable and Sustainable Energy Reviews **16**, p. 2696–2723 (2012); ISSN 13640321; URL http://dx.doi.org/10.1016/j.rser.2012.02.021. 88

[140] G. Horowitz, D. Fichou, X. Peng, Z. Xu & F. Garnier; "A field-effect transistor based on conjugated alpha-sexithienyl"; Solid State Communications **72**, p. 381–384 (1989); ISSN 00381098; URL http://dx.doi.org/10.1016/0038-1098(89)90121-X. 88

[141] B. Kumar, B. K. Kaushik & Y. S. Negi; "Organic Thin Film Transistors: Structures, Models, Materials, Fabrication, and Applications: A Review"; Polymer Reviews **54**, p. 33–111 (2014); ISSN 1558-3724; URL http://dx.doi.org/10.1080/15583724.2013.848455. 88

[142] C. W. Tang; "Two-layer organic photovoltaic cell"; Applied Physics Letters **48**, p. 183–185 (1986); ISSN 00036951; URL http://dx.doi.org/10.1063/1.96937; arXiv:1011.1669v3. 88

[143] S. E. Shaheen, C. J. Brabec, N. S. Sariciftci, F. Padinger, T. Fromherz & J. C. Hummelen; "2.5% Efficient Organic Plastic Solar Cells"; Applied Physics Letters **78**, p. 841–843 (2001); ISSN 00036951; URL http://dx.doi.org/10.1063/1.1345834. 88

[144] T. Ameri, P. Khoram, J. Min & C. J. Brabec; "Organic ternary solar cells: A review"; Advanced Materials **25**, p. 4245–4266 (2013); ISSN 09359648; URL http://dx.doi.org/10.1002/adma.201300623. 88

[145] Q. An, F. Zhang, J. Zhang, W. Tang, Z. Deng & B. Hu; "Versatile ternary organic solar cells: a critical review"; Energy Environ. Sci. **9**, p. 281–322 (2016); ISSN 1754-5692; URL http://dx.doi.org/10.1039/C5EE02641E. 88

[146] A. D. Vos; "Detailed balance limit of the efficiency of tandem solar cells"; Journal of Physics D: Applied Physics **13**, p. 839–846 (1980); ISSN 0022-3727; URL http://dx.doi.org/10.1088/0022-3727/13/5/018. 88

[147] T. Ameri, N. Li & C. J. Brabec; "Highly efficient organic tandem solar cells: a follow up review"; Energy & Environmental Science **6**, p. 2390–2413 (2013); ISSN 1754-5692; URL http://dx.doi.org/10.1039/c3ee40388b. 88

[148] "Heliatek sets new Organic Photovoltaic world record efficiency of 13.2%"; URL heliatek.com. 89

[149] D. Duché, F. Bencheikh, S. B. Dkhil, M. Gaceur, N. Berton, O. Margeat, J. Ackermann, J. J. Simon & L. Escoubas; "Optical performance and color investigations of hybrid solar cells based on P3HT:ZnO, PCPDTBT:ZnO, PTB7:ZnO and DTS(PTTh2)2:ZnO"; Solar Energy Materials and Solar Cells **126**, p. 197–204 (2014); ISSN 09270248; URL http://dx.doi.org/10.1016/j.solmat.2014.03.049. 89

[150] J. Hou, H.-Y. Chen, S. Zhang, R. I. Chen, Y. Yang, Y. Wu & G. Li; "Synthesis of a Low Band Gap Polymer and Its Application in Highly Efficient Polymer Solar Cells"; Journal of the American Chemical Society **131**, p. 15 586–15 587 (2009); ISSN 0002-7863; URL http://dx.doi.org/10.1021/ja9064975. 89

[151] Y. Liang, Z. Xu, J. Xia, S. T. Tsai, Y. Wu, G. Li, C. Ray & L. Yu; "For the bright future-bulk heterojunction polymer solar cells with power conversion efficiency of 7.4%"; Advanced Materials **22**, p. E135–E138 (2010); ISSN 09359648; URL http://dx.doi.org/10.1002/adma.200903528. 89

[152] L. Huo, X. Guo, Y. Li & J. Hou; "Synthesis of a polythieno[3,4-b]thiophene derivative with a low-lying HOMO level and its application in polymer solar cells"; Chemical Communications **47**, p. 8850–8852 (2011); ISSN 1359-7345; URL http://dx.doi.org/10.1039/c1cc12643a. 89

[153] L. Dou, W. H. Chang, J. Gao, C. C. Chen, J. You & Y. Yang; "A selenium-substituted low-bandgap polymer with versatile photovoltaic applications"; Advanced Materials **25**, p. 825–831 (2013); ISSN 09359648; URL http://dx.doi.org/10.1002/adma.201203827. 89

[154] Y. He, C. Chen, E. Richard, L. Dou, Y. Wu, G. Li & Y. Yang; "Novel fullerene acceptors: synthesis and application in low band gap polymer solar cells"; Journal of Materials Chemistry **22**, p. 13 391–13 394 (2012); ISSN 0959-9428; URL http://dx.doi.org/10.1039/c2jm31712e. 89

[155] Y. Lin, P. Cheng, Y. Li & X. Zhan; "A 3D star-shaped non-fullerene acceptor for solution-processed organic solar cells with a high open-circuit voltage of 1.18 V"; Chemical Communications **48**, p. 4773–4775 (2012); ISSN 1359-7345; URL http://dx.doi.org/10.1039/c2cc31511d. 89

[156] C. Zhang, S. Chen, Z. Xiao, Q. Zuo & L. Ding; "Synthesis of mono- and bisadducts of thieno-o-quinodimethane with C60 for efficient polymer solar cells."; Organic letters **14**, p. 1508–11 (2012); ISSN 1523-7052; URL http://dx.doi.org/10.1021/ol3002392. 89

[157] Y. Zhou, L. Ding, K. Shi, Y.-Z. Dai, N. Ai, J. Wang & J. Pei; "A Non-Fullerene Small Molecule as Efficient Electron Acceptor in Organic Bulk Heterojunction Solar Cells"; Advanced Materials **24**, p. 957–961 (2012); ISSN 09359648; URL http://dx.doi.org/10.1002/adma.201103927. 89

[158] F. C. Krebs (editor); *Stability and Degradation of Organic and Polymer Solar Cells* (John Wiley & Sons, Ltd, Chichester, UK) (2012); ISBN 9781119942436; URL http://dx.doi.org/10.1002/9781119942436. 89

[159] M. Jørgensen, K. Norrman & F. C. Krebs; "Stability/degradation of polymer solar cells"; Solar Energy Materials and Solar Cells **92**, p. 686–714 (2008); ISSN 09270248; URL http://dx.doi.org/10.1016/j.solmat.2008.01.005; 1. 89, 91

[160] C. H. Peters, I. T. Sachs-Quintana, J. P. Kastrop, S. Beaupré, M. Leclerc & M. D. McGehee; "High efficiency polymer solar cells with long operating lifetimes"; Advanced Energy Materials **1**, p. 491–494 (2011); ISSN 16146832; URL http://dx.doi.org/10.1002/aenm.201100138. 89

[161] Y. Sun, C. J. Takacs, S. R. Cowan, J. H. Seo, X. Gong, A. Roy & A. J. Heeger; "Efficient, air-stable bulk heterojunction polymer solar cells using MoOx as the anode interfacial layer"; Advanced Materials **23**, p. 2226–2230 (2011); ISSN 09359648; URL http://dx.doi.org/10.1002/adma.201100038; arXiv:1408.1149. 89

[162] T. M. Clarke, C. Lungenschmied, J. Peet, N. Drolet, K. Sunahara, A. Furube & A. J. Mozer; "Photodegradation in encapsulated silole-based polymer: Pcbm solar cells investigated using transient absorption spectroscopy and charge extraction measurements"; Advanced Energy Materials **3**, p. 1473–1483 (2013); ISSN 16146832; URL http://dx.doi.org/10.1002/aenm.201300337. 89

[163] W. R. Mateker, J. D. Douglas, C. Cabanetos, I. T. Sachs-Quintana, J. A. Bartelt, E. T. Hoke, A. El Labban, P. M. Beaujuge, J. M. J. Fréchet & M. D. McGehee; "Improving the long-term stability of PBDTTPD polymer solar cells through material purification aimed at removing organic impurities"; Energy & Environmental Science **6**, p. 2529–2537 (2013); ISSN 1754-5692; URL http://dx.doi.org/10.1039/c3ee41328d. 89

[164] S. R. Cowan, P. Schulz, A. J. Giordano, A. Garcia, B. A. Macleod, S. R. Marder, A. Kahn, D. S. Ginley, E. L. Ratcliff & D. C. Olson; "Chemically controlled reversible and irreversible extraction barriers Via stable interface modification of zinc oxide electron collection layer in polycarbazole-based organic solar

cells"; Advanced Functional Materials **24**, p. 4671–4680 (2014); ISSN 16163028; URL http://dx.doi.org/10.1002/adfm.201400158. 89

[165] H. Ma, H.-L. Yip, F. Huang & A. K.-Y. Jen; "Interface Engineering for Organic Electronics"; Advanced Functional Materials **20**, p. 1371–1388 (2010); ISSN 1616301X; URL http://dx.doi.org/10.1002/adfm.200902236. 89

[166] K. Kawano, R. Pacios, D. Poplavskyy, J. Nelson, D. D. C. Bradley & J. R. Durrant; "Degradation of organic solar cells due to air exposure"; Solar Energy Materials and Solar Cells **90**, p. 3520–3530 (2006); ISSN 09270248; URL http://dx.doi.org/10.1016/j.solmat.2006.06.041. 91

[167] E. Vitoratos, S. Sakkopoulos, E. Dalas, N. Paliatsas, D. Karageorgopoulos, F. Petraki, S. Kennou & S. A. Choulis; "Thermal degradation mechanisms of PEDOT:PSS"; Organic Electronics: physics, materials, applications **10**, p. 61–66 (2009); ISSN 15661199; URL http://dx.doi.org/10.1016/j.orgel.2008.10.008. 91

[168] D. Zhang, W. C. H. Choy, F. Xie, W. E. I. Sha, X. Li, B. Ding, K. Zhang, F. Huang & Y. Cao; "Plasmonic electrically functionalized TiO2 for high-performance organic solar cells"; Advanced Functional Materials **23**, p. 4255–4261 (2013); ISSN 1616301X; URL http://dx.doi.org/10.1002/adfm.201203776. 91

[169] M. A. Ibrahem, H. Y. Wei, M. H. Tsai, K. C. Ho, J. J. Shyue & C. W. Chu; "Solution-processed zinc oxide nanoparticles as interlayer materials for inverted organic solar cells"; Solar Energy Materials and Solar Cells **108**, p. 156–163 (2013); ISSN 09270248; URL http://dx.doi.org/10.1016/j.solmat.2012.09.007. 91

[170] K. Zilberberg, S. Trost, J. Meyer, A. Kahn, A. Behrendt, D. Lützenkirchen-Hecht, R. Frahm & T. Riedl; "Inverted organic solar cells with sol-gel processed high work-function vanadium oxide hole-extraction layers"; Advanced Functional Materials **21**, p. 4776–4783 (2011); ISSN 1616301X; URL http://dx.doi.org/10.1002/adfm.201101402. 91

[171] Z. Tan, L. Li, C. Cui, Y. Ding, Q. Xu, S. Li, D. Qian & Y. Li; "Solution-processed tungsten oxide as an effective anode buffer layer for high-performance polymer solar cells"; Journal of Physical Chemistry C **116**, p. 18 626–18 632 (2012); ISSN 19327447; URL http://dx.doi.org/10.1021/jp304878u. 91

[172] K. H. Wong, K. Ananthanarayanan, J. Luther & P. Balaya; "Origin of hole selectivity and the role of defects in low-temperature solution-processed molybde-

num oxide interfacial layer for organic solar cells"; Journal of Physical Chemistry C **116**, p. 16 346–16 351 (2012); ISSN 19327447; URL http://dx.doi.org/10.1021/jp303679y. 91

[173] M. Vasilopoulou, A. M. Douvas, D. G. Georgiadou, L. C. Palilis, S. Kennou, L. Sygellou, A. Soultati, I. Kostis, G. Papadimitropoulos, D. Davazoglou & P. Argitis; "The influence of hydrogenation and oxygen vacancies on molybdenum oxides work function and gap states for application in organic optoelectronics"; Journal of the American Chemical Society **134**, p. 16 178–16 187 (2012); ISSN 00027863; URL http://dx.doi.org/10.1021/ja3026906. 91

[174] A. W. Hains, C. Ramanan, M. D. Irwin, J. Liu, M. R. Wasielewski & T. J. Marks; "Designed Bithiophene-Based Interfacial Layer for High-Efficiency Bulk-Heterojunction Organic Photovoltaic Cells. Importance of Interfacial Energy Level Matching"; ACS Applied Materials & Interfaces **2**, p. 175–185 (2010); ISSN 1944-8244; URL http://dx.doi.org/10.1021/am900634a. 91

[175] Z. Xu, L. Chen, M. Chen, G. Li & Y. Yang; "Energy level alignment of poly(3-hexylthiophene): [6,6]-phenyl C-61 butyric acid methyl ester bulk heterojunction"; Applied Physics Letters **95**, p. 13 301–13 303 (2008); ISSN 00036951; URL http://dx.doi.org/10.1063/1.3163056. 91, 92, 93, S-17, S-18

[176] Z.-L. Guan, J. B. Kim, H. Wang, C. Jaye, D. A. Fischer, Y.-L. Loo & A. Kahn; "Direct determination of the electronic structure of the poly(3-hexylthiophene):phenyl-[6,6]-C61 butyric acid methyl ester blend"; Organic Electronics **11**, p. 1779–1785 (2010); ISSN 1566-1199; URL http://dx.doi.org/10.1016/j.orgel.2010.07.023. 92, 93, S-17

[177] Q. Chen, L. Mao, Y. Li, T. Kong, N. Wu, C. Ma, S. Bai, Y. Jin, D. Wu, W. Lu, B. Wang & L. Chen; "Quantitative operando visualization of the energy band depth profile in solar cells"; Nature Communications **6**, p. 7745–7753 (2015); ISSN 2041-1723; URL http://dx.doi.org/10.1038/ncomms8745. 92

[178] V. Barth; *Dipyrrométhènes métallés (Co,Ni,Cu) et dipyrannilidènes : de nouveaux matériaux organiques pour la conversion photovoltaïque de l'énergie solaire*; PhD thesis; Université Pierre et Marie Curie (2014); URL http://www.theses.fr/2014PA066405. 95

[179] D. Gupta, S. Mukhopadhyay & K. S. Narayan; "Fill factor in organic solar cells"; Solar Energy Materials and Solar Cells **94**, p. 1309–1313 (2010); ISSN 09270248; URL http://dx.doi.org/10.1016/j.solmat.2008.06.001. 95

[180] L. Pauling; "the Nature of the Chemical Bond. Iv. the Energy of Single Bonds and the Relative Electronegativity of Atoms"; Journal of the American Chemical Society **54**, p. 3570–3582 (1932); ISSN 0002-7863; URL http://dx.doi.org/10.1021/ja01348a011; arXiv:1011.1669v3. 99, S-19

[181] L. Floreano, G. Naletto, D. Cvetko, R. Gotter, M. Malvezzi, L. Marassi, A. Morgante, A. Santaniello, A. Verdini, F. Tommasini & G. Tondello; "Performance of the grating-crystal monochromator of the ALOISA beamline at the Elettra Synchrotron"; Review of Scientific Instruments **70**, p. 3855–3864 (1999); ISSN 00346748; URL http://dx.doi.org/10.1063/1.1150001. 103

[182] J. A. Bearden & A. F. Burr; "Reevaluation of X-ray atomic energy levels"; Reviews of Modern Physics **39**, p. 125–142 (1967); ISSN 00346861; URL http://dx.doi.org/10.1103/RevModPhys.39.125. 107

[183] M. Cardona & L. Ley; *Photoemission in Solids I - General Principles*; *Topics in Applied Physics*, volume 26 (Springer Berlin Heidelberg, Berlin, Heidelberg) (1978); ISBN 3540086854; URL http://dx.doi.org/10.1007/3-540-08685-4. 107

[184] M. G. Mason, L. S. Hung, C. W. Tang, S. T. Lee, K. W. Wong & M. Wang; "Characterization Of Treated Indium–Tin–Oxide Surfaces Used In Electroluminescent Devices"; Journal of Applied Physics **86**, p. 1688–1692 (1999); ISSN 00218979; URL http://dx.doi.org/10.1063/1.370948. A-1

[185] M. F. Lo, T. W. Ng, H. W. Mo & C. S. Lee; "Direct threat of a UV-ozone treated indium-tin-oxide substrate to the stabilities of common organic semiconductors"; Advanced Functional Materials **23**, p. 1718–1723 (2013); ISSN 1616301X; URL http://dx.doi.org/10.1002/adfm.201202120. A-1

[186] "aXis2000 source"; URL unicorn.mcmaster.ca. A-6

[187] J. Campbell & T. Papp; "Widths of the Atomic K–N7 Levels"; Atomic Data and Nuclear Data Tables **77**, p. 1–56 (2001); ISSN 0092640X; URL http://dx.doi.org/10.1006/adnd.2000.0848. A-7

[188] J. Hwang, A. Wan & A. Kahn; "Energetics of metal-organic interfaces: New experiments and assessment of the field"; Materials Science and Engineering R: Reports **64**, p. 1–31 (2009); ISSN 0927796X; URL http://dx.doi.org/10.1016/j.mser.2008.12.001. A-7

[189] J. Gassmann, S. V. Yampolskii, Y. A. Genenko, T. C. Reusch & A. Klein; "Functional interfaces for transparent organic electronic devices: consistent description of charge injection by combining in situ XPS and current voltage measurements with self-consistent modeling"; The Journal of Physical Chemistry C **120**, p. 10 466–10 475 (2016); ISSN 1932-7447; URL http://dx.doi.org/10.1021/acs.jpcc.6b02567. A-7

Quentin ARNOUX **September 15th, 2017**

Sujet : Caractérisations structurales et électroniques d'une interface oxyde transparent conducteur/organique : Vers des applications en électronique organique

Résumé : Nous avons déterminé l'alignement des niveaux énergétiques d'un solide moléculaire organique, transporteurs de trous, avec un oxyde d'indium dopé à l'étain (ITO), un conducteur transparent. Les molécules étudiées, basées sur une structure dipyranylidène (DIP), diffèrent par leur hétéroatome (O, S et Se). La spectroscopie de photoémission X a été utilisée pour déterminer cet alignement, et nous avons étudié l'orientation moléculaire par spectromicroscopie d'absorption X. Des calculs DFT ont été réalisés pour interpréter les données spectroscopiques. Nous avons constaté la présence d'un transfert de charge, au moins pour les dérivés oxygénés et soufrés. Celui-ci a lieu des molécules vers l'ITO, lorsqu'ils sont en contact intime avec le substrat. Nous avons déterminé la barrière d'injection des trous entre le niveau de Fermi de l'ITO et la HOMO du solide organique. Notre approche expérimentale met l'accent sur la relation entre les propriétés structurelles et les propriétés électroniques. Ces résultats ont été obtenus pendant des runs synchroton en France (SOLEIL), en Italie (ELETTRA) et en Suisse (SLS).

Mots clés : Cellule solaire organique, Couche interfaciale, Transporteur de trous, Interface métal/organique, Spectroscopie de photoémission, Transfert de charge, Orientation moléculaire

Subject: Electronic and structural characterizations of a transparent conductive oxide/organic interface: Towards applications for organic electronic devices

Abstract: The energy level alignment of hole-transport organic molecular solids with indium tin oxide (ITO), a transparent conducting oxide, has been characterized. The studied molecules, based on the dipyranylidene (DIP) structure, differ by the heteroatom (O, S and Se). Synchrotron photoemission electron spectroscopy has been used to determine the alignment, and we investigated the molecular orientation via X-ray absorption spectromicroscopy. By interpreting spectroscopic data in the light of DFT calculations, we found evidence of the presence of charge transfer from the molecules to the ITO, when they are in intimate contact with the substrate, at least for the O and S-DIPs. The hole injection barrier between the ITO Fermi level and the organic HOMO was obtained. Our experimental approach emphasizes the relationship between structural and electronic properties. These results were obtained during beamtimes in France (SOLEIL), Italy (ELETTRA) and Switzerland (SLS).

Keywords: Organic solar cells, Interfacial layer, Hole-transport layer, Metal/Organic interface, Photoemission spectroscopy, Charge transfer, Molecular orientation